September 2019
Report No. 19-008

Development of Load Rating Procedures for Deteriorated Steel Beam Ends

Principal Investigator
Dr. Simos Gerasimidis
Dr. Sergio Brena
University of Massachusetts Amherst

Research and Technology Transfer Section
MassDOT Office of Transportation Planning

U.S. Department of Transportation
Federal Highway Administration

Technical Report Document Page

1. Report No.	2. Government Accession No.	3. Recipient's Catalog No.
19-008	n/a	n/a

4. Title and Subtitle	5. Report Date
Development of Load Rating Procedures for Deteriorated Steel Beam Ends: Deliverable 4: Final Report.	July 2019
	6. Performing Organization Code n/a
7. Author(s) Georgios Tzortzinis, Simos Gerasimidis, Sergio Brena and Brendan Knickle	8. Performing Organization Report No. 19-008
9. Performing Organization Name and Address University of Massachusetts Amherst UMass Transportation Center 130 Natural Resources Way Amherst, MA 01003	10. Work Unit No. (TRAIS) n/a
	11. Contract or Grant No. n/a
12. Sponsoring Agency Name and Address Massachusetts Department of Transportation Office of Transportation Planning Ten Park Plaza, Suite 4150, Boston, MA 02116	13. Type of Report and Period Covered Final Report – July 2019 (August 2017 – July 2019)
	14. Sponsoring Agency Code n/a

15. Supplementary Notes
n/a

16. Abstract

This study focuses on the current strength evaluation policies for strength assessment of corroded steel girders and investigates potential improvements based on real corrosion data. The research work included in this report has three phases. First, the current deterioration condition of steel bridges is studied through MassDOT inspection reports of bridges with beam end corrosion. The topology and the extent of the phenomenon are recorded from the reports and the gathered data are processed to define the most common corrosion patterns. Second, full scale experimental testing of naturally corroded girders is performed. The beams are obtained from bridge demolition projects across the Commonwealth of Massachusetts and tested in the Brack lab at UMass Amherst. Based on the experimental test results, a numerical finite element model is appropriately calibrated to predict the failure load of corroded beam ends. Finally, combining the new corrosion patterns identified during the first part of the work with finite element modeling, an extensive parametric analysis is performed. Based on the numerical outcome, the current procedures are evaluated and improvements are proposed through a new set of equations. The report includes many important findings regarding the behavior of corroded beam ends and discusses the limitations of this study and potential future research work.

17. Key Word	18. Distribution Statement
Steel bridges, bearing load, beam end corrosion, buckling, crippling, experiments	n/a

19. Security Classif. (of this report)	20. Security Classif. (of this page)	21. No. of Pages	22. Price
unclassified	unclassified	276	n/a

Form DOT F 1700.7 (8-72) Reproduction of completed page authorized

This page left blank intentionally.

Development of Load Rating Procedures for Deteriorated Steel Beam Ends

Final Report

Prepared By:
Georgios Tzortzinis
Graduate Researcher
gtzortzinis@umass.edu

Simos Gerasimidis, Ph.D.
Principal Investigator
413-545-2521
sgerasimidis@umass.edu

Sergio Breña, Ph.D.
Co-Principal Investigator
413-545-2521
brena@umass.edu

Brendan Knickle
Graduate Researcher
bknickle@umass.edu

University of Massachusetts Amherst
130 Natural Resources Way, Amherst, MA 01003

Prepared For:
Massachusetts Department of Transportation
Office of Transportation Planning, Ten Park Plaza, Suite 4150
Boston, MA 02116

July 2019

This page left blank intentionally.

Disclaimer

The contents of this report reflect the views of the authors, who are responsible for the facts and the accuracy of the data presented herein. The contents do not necessarily reflect the official view or policies of the Massachusetts Department of Transportation or the Federal Highway Administration. This report does not constitute a standard, specification, or regulation.

This page left blank intentionally.

Executive Summary

This study of development of load rating procedures for deteriorated steel beam ends was undertaken as part of the Massachusetts Department of Transportation (MassDOT) Research Program. This program is funded with Federal Highway Administration (FHWA) State Planning and Research (SPR) funds. Through this program, applied research is conducted on topics of importance to the Commonwealth of Massachusetts transportation agencies.

According to recent estimates, more than 50,000 bridges in the US are characterized as structurally deficient *(1)*. Among the many aspects of structural deficiency, corrosion is considered a common cause for steel bridge deterioration, especially in the northern parts of the country. This condition can be primarily attributed to leaking through deck joints. The leaking water contains high concentrations of chemical substances employed seasonally to winterize the road above. The phenomenon varies significantly in topology and intensity, leading in many cases to severe thickness loss. The main challenge is the accurate assessment of the corroded end's residual capacity. This research focuses on simple span girders with unstiffened ends and uses real corrosion data to assess the current bridge manual procedures.

The research work has three phases:

- Gathering data and assessing the current condition of steel bridges (Chapters 2 and 5 of this report).
- Experimental testing of naturally corroded beam ends (Chapters 3 and 6 of this report).
- Computational parametric analysis and new proposed procedures for the bridge manual (Chapters 4, 7, and 8 of this report).

The organization of this report is as follows:

- Chapters 2 to 4 describe the methodology of this study,
- Chapters 5 to 8 present the results.
- Chapter 8 includes the implementation of the research findings and the proposed new procedures to predict better the capacity of corroded girders.
- Chapters 9 and 10 summarize the conclusions and present the limitations and opportunities for further study.

In detail, Chapter 2 presents the study on the current deterioration condition of steel bridges through MassDOT inspection reports of bridges that have experienced beam end corrosion. Real corrosion data on thickness loss, corroded area size, and location are collected from the reports. Using this data, Chapter 5 includes the statistical analysis of 808 corroded beam ends, which are described in the available inspection reports. The outcome of this analysis is the identification of the most common corrosion topologies.

Over the years, a significant amount of research has been carried out to determine the remaining capacity of corroded beam ends. Researchers have followed both experimental and computational approaches. However, to date, no study has looked at beams with natural corrosion. In all cases, the corrosion was simulated with artificial thickness reduction, which

insinuates results that are not realistic. **To our knowledge, this project is the first to perform full-scale experimental testing of natural corroded beams extracted from highway bridges.** The beams are obtained from bridge demolition projects across the Commonwealth of Massachusetts. The beam selection process, the design of the testing rig, the instrumentation configuration, and the detailed descriptions of each specimen are described in Chapter 3. Following the tests, all the measured data, including the failure load, the reaction forces' distribution at the beams' supports, the failure mode, and the developed stresses are presented in Chapter 6.

Based on the experimental results, a high-fidelity numerical finite element model is developed and calibrated, capable of predicting the capacity of beam ends. The simulation methodology and all the details about the computational modeling are included in Chapter 4. Combining the corrosion patterns identified in the first phase of the project with numerical modeling, an extensive parametric analysis is performed under the assumption of uniform section loss along the corroded area. The advantage of this assumption is twofold. First, it is in compliance with the current procedures for strength evaluation of corroded girders. Second, it is compatible with the usually limited thickness measurements performed by state inspection engineers. In Chapter 7, the bounds of the corrosion topology that significantly affect the residual strength of deteriorated girders are identified.

Finally, in Chapter 8, the current analytical expressions are evaluated and modified for three different initial imperfection amplitudes to better resemble the computational results. The new proposed set of equations are included in this chapter.

Table of Contents

This page left blank intentionally.

List of Tables

This page left blank intentionally.

List of Figures

This page left blank intentionally.

List of Acronyms

Acronym	Expansion
a	Hole Height
b	Hole Length
B_L	Bearing Length
BL/d	Bearing Length Ratio
B_0	Beam End Overhang
c	Distance From end of Beam
C_f	Flange Corrosion Length
C_H	Corrosion Height
C_L	Corrosion Length
FEM	Finite Element Model
H	Beam Depth
H_0	Web Height
LTB	Lateral Torsional Buckling
LVDT	Linear Variable Differential Transformer
MassDOT	Massachusetts Dept. of Transportation
SR	Strain Rosette
t_f	Flange thickness
t_{rem}	Remaining Web Thickness
UHPC	Ultra High-performance Concrete
UMass	University of Massachusetts, Amherst

This page left blank intentionally.

1.0 Introduction

1.1 Background Information

Infrastructure is the backbone of the nation's economy, affecting public health and prosperity and the welfare of its citizens. According to a recent evaluation *(2)*, the United States' infrastructure is classified in poor to fair condition, with many elements approaching the end of their service life. In that same report, among the many aspects of the problem, the criticality of the existing condition and the gap between the total needs and the estimated funding are highlighted. It is estimated that 53% of the nation's public schools are in poor condition, 15,500 dams are potentially hazardous, and the increasing demands at airports are not met. The nation's infrastructure funding gap is estimated to be close to $2.5 trillion.

Regarding the transportation network condition, from the 600,000+ bridges which are included in the National Bridge Inventory, 55,000 of them are characterized as structurally deficient *(1)*, with the backlog of bridge rehabilitation needs estimated at $123 billion *(2)*. A bridge can be characterized as structurally deficient if at least one of its components has a condition rating of poor or worse. The critical components are the deck, superstructure, and substructure or culvert. Among the many aspects of structural deficiency, corrosion is considered a common cause for steel bridges deterioration and affects mainly the superstructure components. This condition can be attributed primarily to malfunctioning deck expansion joints, which fail to prevent water or deicing mixtures from penetrating into the bearing area. The leaking water contains high concentrations of chemical substances employed seasonally to winterize the road above. Deterioration of the steel is most often initiated by the buildup of this runoff, triggering a corrosive process in the bottom flange and the components above it. When this condition is sustained, it can ultimately result in severe thickness loss directly affecting the load-carrying capacity of the bridge.

The phenomenon varies significantly in topology and intensity, and it is highly related to the configuration at the bearing. Parameters like the type of bearing, the existence of a diaphragm, and the position of the leaking deck joints directly affect the water flow, resulting in a significant problem as well as an extra source of difficulty for the establishment of a unified protocol to deal with the problem. Focusing on the human factor, the accessibility, the dependency on weather conditions, and in some cases lack of understanding of the phenomenon results in uncertainty during all the steps of capacity assessment, from thickness measurements to load rating.

All these factors make the accurate assessment of the corroded end's residual capacity a challenging task. So far, there have not been tests of real corroded beams that could resolve some of the above questions. This research attempts to address this problem.

1.2 Literature Review

One of the pioneering studies regarding beam capacity was by Roberts *(3)*, who proposed the plastic hinge failure mechanism to predict the capacity of undamaged stiffened girders to edge loading. An improved method was proposed more than a decade later by Johansson et al. *(4)*. One of the earliest efforts to extend the area of investigation to deteriorated bridges was performed by Kayser et al. *(5)*, who studied the effect of thickness loss to bearing capacity. In a recent work, Tohibi et al. *(6)* proposed an empirical equation based on Back-Propagation neural network (BPNN) to predict the residual bearing capacity of damaged beams. A different approach was followed by Gheitasi et al. *(7)*, whose research was not limited to the behavior of individual deteriorated components but tested the overall redundancy and operational safety of a bridge.

Van de Lindt et al. *(8)* developed guidelines for deteriorated steel beam ends. Initially, damage simulations of various sizes and shapes were performed using the finite element method (FEM). Experimental work was conducted on beams 3 ft. in length, with artificial web and flange thickness reduction above the bearing, also validating the FEM model. Ultimately, a deterioration factor was proposed as a simplified approach for calculating capacity reduction of deteriorated girders. Design charts were introduced for the deterioration factor calculation for given damage height and three options of thickness losses, for one as well as two sides of web corrosion. It should be noted that experimentally and numerically, crushing analysis was performed directly above the bearing on short specimens. This configuration is not considered to capture the in-service conditions of girders; the girders are treated more as columns without accounting for shear loading conditions.

Beam end corrosion is an issue that has received much research attention in eastern Asia, with computational and experimental work conducted by and reported from Japan and Korea (9-17). Sugimoto et al. *(9)* tested an actual railway deck plate girder constructed in the beginning of the 20th century, in an effort to evaluate the durability of railway steel bridges. Liu et al. *(10)* investigated the impact of corrosion height and thickness reduction of steel girders with stiffeners. Ahn et al. *(11)* pointed out that the pattern's shape (rectangular or triangular) affects the capacity only when it intersects with the tension field of the web panel. The same research group performed experiments on stiffened beams with artificial corrosion thickness reduction *(12)* and pitting holes *(13)*. They also proposed a method for residual shear strength evaluation of web-corroded panels *(14)*. Usukura et al. *(15)* conducted computational parametric analysis in order to investigate the capacity and the collapse mechanism of stiffened corroded girder ends. Yamaghuchi et al. *(16)* identified the significance of the corrosion pattern effect on the load-carrying capacity of deteriorated beams. The challenge of nonuniform local corrosion damage was the focus of the study by Khurram et al. *(17)*, who indicated that the minimum thickness within any damage height may be used to simulate the corrosion damage in a computational analysis.

There is also a wide choice of repair techniques in the literature. Ahn et al. *(18)* proposed CFRP usage, due to its low weight, high strength, and rapid and simple application. Miyashita et al. *(19)*, using the same repair method, conducted experimental and numerical shear buckling tests, reporting recovery of load-carrying capacity. Ogami et al. *(20)* attached

studs and rebar to the corroded girder before covering it with resin. With the proposed technique, buckling was prevented under axial compressive loading. Wu et al. *(21)* experimentally studied the influence of corrosion on I beam behavior, while in a second study *(22)*, specimens were strengthened by welding stiffeners on the two sides of the web and partially encasing it with high-strength grout.

Recent research efforts in neighboring states have focused on deteriorated beam ends, demonstrating the urgency of the problem. In Connecticut, another repair strategy was proposed by Zmetra et al. *(23)*, where shear studs were welded to the web and encased in ultra high-performance concrete (UHPC). One-third scale experiments revealed that the proposed technique managed to restore the capacity of the deteriorated girder by transferring shear forces from the web to the concrete through the stands. A series of push-out experiments was also performed to evaluate the capacity of studs embedded in UHPC *(24,25)*. Additionally, a finite element model was developed that was able to capture the behavior of the studs–UHPC configuration *(26)*. Finally, in order to check the durability of the proposed technique, push-out tests were performed on specimens subjected to accelerated electrochemical corrosion *(27)*. The mechanical performance was not affected; however, the followed procedure did not manage to assist the penetration of ions into the concrete.

In Massachusetts, MassDOT is the driving force for assessing the condition of steel bridges. In its efforts to ensure safety and maintain the infrastructure of the state, MassDOT engineers perform periodic bridge inspections that conform to the requirements of the *Code of Federal Regulations (28)*. MassDOT has introduced and is currently using a variety of standard inspection report forms *(29)* that fulfill the requirements of the National Bridge Inspection Standards. These reports provide extensive information for the overall condition of the structure (e.g., deck, superstructure, substructure, culvert) in the form of figures, text, photos, or sketches gathered by inspection engineers. The current procedure to estimate the remaining capacity of corroded unstiffened steel girder ends is included in the draft *MassDOT 2019 Bridge Manual (30*). The capacity is considered as the minimum of yielding and crippling resistance of a defined area of interest, which is calculated based on section loss reported in the corresponding inspection reports.

1.2 Research Goals

The goal of this research work is to investigate and ultimately improve the efficiency and accuracy of the current procedures for strength assessment of corroded beam ends. In detail, it is aimed at simple span and unstiffened above-bearing rolled girders, which are commonly found in the Commonwealth of Massachusetts. **This work is differentiated from all previous studies by its methodology, where every aspect emerges from real corrosion data.** The immediate research objectives of this study are:

- **The identification and quantification of the most common corrosion topologies.** During the first step of this work, the current deterioration condition of steel bridges was studied through MassDOT inspection reports of viaducts that have experienced beam end corrosion. Deterioration data on thickness loss, corroded area size, and

location were collected and analyzed for 808 corroded ends. The data were used to develop statistical information about the appearance of the phenomenon and ultimately identify common characteristics that would lead to the definition of the most prevalent geometries of the deterioration.

- **To investigate the failure mechanism of naturally corroded girders.** To the research team's knowledge, this project is the first to perform full-scale experimental testing of natural corroded beams. For all previous research efforts, corrosion was simulated with artificial thickness reduction, which insinuates results that are potentially not realistic. Six specimens were obtained from bridge rehabilitation projects around the Commonwealth of Massachusetts and loading rests were performed. Each specimen had some unique characteristics that allowed the team to study different aspects of the problem, such as section loss, initial imperfections, and web or flange areas with 100% thickness loss (holes). Reaction forces, vertical, lateral displacements, and strains were recorded to gain insight of the mechanism that leads to failure.
- **The calibration of a high-fidelity finite element model (FEM).** The experimentally obtained data were implemented to develop a FEM, which accounts for material and geometric nonlinearities, using the commercial software Abaqus. The exact experimental configuration of the first two specimens was simulated and the failure loads and modes were satisfactorily captured.
- **To define the parameters that significantly affect capacity reduction.** Combining the corrosion patterns identified in this project with numerical modeling, an extensive parametric analysis was performed, and thousands of combinations of corrosion topologies for several beam types and lengths were simulated and analyzed. The model generation under the validated assumption, as well as the post-processing, were automated by combining Python programming language and Abaqus software.
- **To provide new sets of equations for more accurate capacity assessment.** Combining the knowledge obtained from the conducted work on real corrosion data, the current procedures were modified to better reflect the actual capacity of deteriorated beam ends. The proposed modifications concern four main aspects: the initial imperfection, the area over which the remaining web thickness is determined, and equations for crippling capacity for $N/d > 0.2$ and $N/d \leq 0.2$.

2.0 Methodology for Categorization of Corrosion Topologies

This chapter includes the methodology for the first phase of the project. The goal of this phase is to identify the most common shapes and locations for steel beam end deterioration. To accomplish this, the research team reviewed inspection reports for various bridges and describe the data collection process, the tools built to process the data, and the preliminary filtering of the data. The post-processing of the data is included in Chapter 5.

2.1 Data Collection

The data collection process was based on the inspection report documents provided by the MassDOT Highway Districts. The conducted research focused on bridges with poor superstructure condition.

2.1.1 Format of Data Received from MassDOT Inspection Reports

General description of inspection reports

This research study focused on bridges with poor to critical superstructure condition. The data was collected using a form called "Structures Inspection Field Report." Fig. 2.1 includes the first page of a typical routine inspection report on which the general information about the bridges is mentioned. There are four different types of inspection field reports:

- Routine: provide information on the overall structure condition.
- Special member: provide information focused on specific bridge parts.
- Combination of routine and special member: provide information on the overall structure condition and specific bridge parts.
- Closed/Rehabilitation: mainly concern the traffic safety of the closed bridge.

As shown in Fig. 2.1, the front page includes basic information about the bridge identification such as the name, location, intersecting roads, structural system and deck type.

MASSACHUSETTS DEPARTMENT OF TRANSPORTATION PAGE 1 OF 29

STRUCTURES INSPECTION FIELD REPORT

ROUTINE INSPECTION

2-DIST	B.I.N.	BR. DEPT. NO.
05	AF0	K-01-010

CITY/TOWN	8.-STRUCTURE NO.	11-Kilo. POINT	41-STATUS	90-ROUTINE INSP. DATE
KINGSTON	K01010-AF0-DOT-NBI	028.871	A:OPEN	FEB 19, 2016

07-FACILITY CARRIED	MEMORIAL NAME/LOCAL NAME	27-YR BUILT	106-YR REBUILT	YR REHAB'D (NON 106)
ST 3 PILGRIM HWY	GRAND ARMY	1955	1979	0000

06-FEATURES INTERSECTED	26-FUNCTIONAL CLASS	DIST. BRIDGE INSPECTION ENGINEER	G. Simpson
HWY LANDING RD	Freeway/Expressway		

43-STRUCTURE TYPE	22-OWNER	21-MAINTAINER	TEAM LEADER W. Ferry
402 : Steel continuous Stringer/Girder	State Highway Agency	State Highway Agency	

107-DECK TYPE	WEATHER	TEMP. (air)	TEAM MEMBERS
1 : Concrete Cast-in-Place	SUNNY	4°C	M. SILVIA, M. MARSHALL

ITEM 58 — 6

DECK

		DEF
1.Wearing surface	7	-
2.Deck Condition	6	-
3.Stay in place forms	6	-
4.Curbs	N	-
5.Median	H	-
6.Sidewalks	N	-
7.Parapets	7	-
8.Railing	N	-
9.Anti Missile Fence	N	-
10.Drainage System	N	-
11.Lighting Standards	N	-
12.Utilities	N	-
13.Deck Joints	4	S-A
14.	N	-
15.	N	-
16.	N	-

CURB REVEAL (In millimeters)	E	W
	N	N

APPROACHES

		DEF
a. Appr. pavement condition	7	-
b. Appr. Roadway Settlement	7	-
c. Appr. Sidewalk Settlement	N	-
d.	N	-

OVERHEAD SIGNS (Attached to bridge) (Y/N) N

		DEF
a. Condition of Welds	N	-
b. Condition of Bolts	N	-
c. Condition of Signs	N	-

ITEM 59 — 5

SUPERSTRUCTURE

		DEF
1.Stringers	N	-
2.Floorbeams	N	-
3.Floor System Bracing	N	-
4.Girders or Beams	5	S-P
5.Trusses - General	N	-
a. Upper Chords	N	-
b. Lower Chords	N	-
c. Web Members	N	-
d. Lateral Bracing	N	-
e. Sway Bracings	N	-
f. Portals	N	-
g. End Posts	N	-
6.Pin & Hangers	N	-
7.Conn Plt's, Gussets & Angles	7	-
8.Cover Plates	N	-
9.Bearing Devices	6	M-P
10.Diaphragms/Cross Frames	7	-
11.Rivets & Bolts	7	-
12.Welds	7	-
13.Member Alignment	6	-
14.Paint/Coating	4	S-A
15.	N	-

Year Painted	1979

COLLISION DAMAGE: *Please explain*
None X) Minor ( ) Moderate ( ) Severe ( )

LOAD DEFLECTION: *Please explain*
None) Minor (X) Moderate ( ) Severe ( )

LOAD VIBRATION: *Please explain*
None) Minor (X) Moderate ( ) Severe ( )

Any Fracture Critical Member: (Y/N) N

Any Cracks: (Y/N) N

ITEM 60 — 7

SUBSTRUCTURE

	Dive	Cur		DEF
1. Abutments			7	
a. Pedestals	N	N		-
b. Bridge Seats	N	7		S-P
c. Backwalls	N	6		M-P
d. Breastwalls	N	7		-
e. Wingwalls	N	7		-
f. Slope Paving/Rip-Rap	N	6		M-P
g. Pointing	N	N		-
h. Footings	N	H		-
i. Piles	N	H		-
j. Scour	N	N		-
k. Settlement	N	7		-
l.	N	N		-
m.	N	N		-
2. Piers or Bents			7	
a. Pedestals	N	N		-
b. Caps	N	7		-
c. Columns	N	7		-
d. Stems/Webs/Pierwalls	N	N		-
e. Pointing	N	N		-
f. Footing	N	H		-
g. Piles	N	H		-
h. Scour	N	N		-
i. Settlement	N	7		-
j.	N	N		-
k.	N	N		-
3. Pile Bents			N	
a. Pile Caps	N	N		-
b. Piles	N	N		-
c. Diagonal Bracing	N	N		-
d. Horizontal Bracing	N	N		-
e. Fasteners	N	N		-

UNDERMINING (Y/N) If YES please explain N

COLLISION DAMAGE:
None X) Minor ( ) Moderate ( ) Severe ( )

SCOUR: *Please explain*
None X) Minor ( ) Moderate ( ) Severe ( )

I-60 (Dive Report): N *I-60 (This Report):* 7

93B-U/W (DIVE) Insp 00/00/0000

X=UNKNOWN N=NOT APPLICABLE H=HIDDEN/INACCESSIBLE R=REMOVED

RTN(1)7-96

Source: Adopted from K01010-AF0-DOT-NBI (District 5, Town of Kingston).

Figure 2.1: Front page from a typical routine inspection report.

In the routine reports, the overall structural condition of the bridge is summarized in the first two pages of the document. The condition of the deck (item 58), the superstructure (item 59), the substructure (item 60), the channel and channel protection (item 61), and the components of each of these items are evaluated using the same scale; a typical example of a routine report is shown in Fig. 2.2. The lowest condition number for a specific element does not necessarily define the overall condition number.

CONDITION RATING GUIDE (For Items 58, 59, 60 and 61)

	CODE	CONDITION	DEFECTS
	N	NOT APPLICABLE	
G	9	EXCELLENT	Excellent condition.
G	8	VERY GOOD	No problem noted.
G	7	GOOD	Some minor problems.
F	6	SATISFACTORY	Structural elements show some minor deterioration.
F	5	FAIR	All primary structural elements are sound but may have minor section loss, cracking, spalling or scour.
P	4	POOR	Advanced section loss, deterioration, spalling or scour.
P	3	SERIOUS	Loss of section, deterioration, spalling or scour have seriously affected primary structural components. Local failures are possible. Fatigue cracks in steel or shear cracks in concrete may be present.
C	2	CRITICAL	Advanced deterioration of primary structural elements. Fatigue cracks in steel or shear cracks in concrete may be present or scour may have removed substructure support. Unless closely monitored it may be necessary to close the bridge until corrective action is taken.
C	1	"IMMINENT" FAILURE	Major deterioration or section loss present in critical structural components or obvious vertical or horizontal movement affecting structure stablility. Bridge is closed to traffic but corrective action may put it back in light service.
	0	FAILED	Out of service - beyond corrective action.

Figure 2.2: Condition Rating Guide for items 58, 59, 60, and 61.

For both the routine and the special member reports, a detailed description of notable remarks follows the identification information. This description usually is combined with sketches (Fig. 2.3, left) or tables (Fig. 2.4), demonstrating the position and the geometry of the damage. In most cases, the reports also include drawings, sketches, or plans that describe the geometry of the structure (Fig. 2.7). Finally, if available, a series of photographs taken during the inspection are included at the end of the report, as shown in Fig. 2.3 (right).

Source: Adopted from W46010-3RY-DOT-NBI (District 5, Town of Wrentham).

Figure 2.3: The same beam, described by sketch (L) and by photograph (R).

Inspection report data variability

At this point, it is important to mention the variability of the data included in the inspection reports. The first source of variability can be found from different districts, as the reports between districts vary significantly. In particular, reports from District 3 generally do not include any sketches at all.

Beam	Beam Type	Abutment	Condition	Special Member?
B13	36WF230	South	13" x 5/8" steel web plate and L 4 x 6 x 5/8 bottom flange repairs installed. Bolts need to be tightened.	N
		North	See sketch 6	Y
B14	36WF230	South	13" x 5/8" steel web plate and L 4 x 6 x 5/8 bottom flange repairs installed. Bolts need to be tightened.	N
		North	0.452" remaining (3/16" section loss to east face; 1/8" section loss to west face) by up to 8" high to the lower portion of the web.	N
B15	36WF230	South	13" x 5/8" steel web plate and L 4 x 6 x 5/8 bottom flange repairs installed. Bolts need to be tightened.	N
		North	0.515" remaining (1/8" section loss to each face) by up to 10" high to the lower portion of the web.	N
B16	36WF230	South	13" x 5/8" steel web plate and L 4 x 6 x 5/8 bottom flange repairs installed. Bolts need to be tightened.	N
		North	0.452" remaining (3/16" section loss to east face; 1/8" section loss to west face) by up to 10" high to the lower portion of the web.	N
B17	36WF230	South	0.577" remaining (3/16" section loss to east face) by full height.	N
		North	0.515" remaining (1/8" section loss to each face) by up to 5" high to the lower portion of the web.	N
B18	36WF230	South	13" x 5/8" steel web plate and L 4 x 6 x 5/8 bottom flange repairs installed. Bolts need to be tightened.	N

Source: Adopted from S24017-14K-DOT-634 (District 2, City of Springfield).

Figure 2.4: Details of corrosion damage.

Secondly, within a specific district, the provided information usually differs by inspections performed by MassDOT or by consultants. In most cases, the sketches are not to scale, and as a result, it is not possible to extract conclusions about relative dimensions (Fig. 2.5).

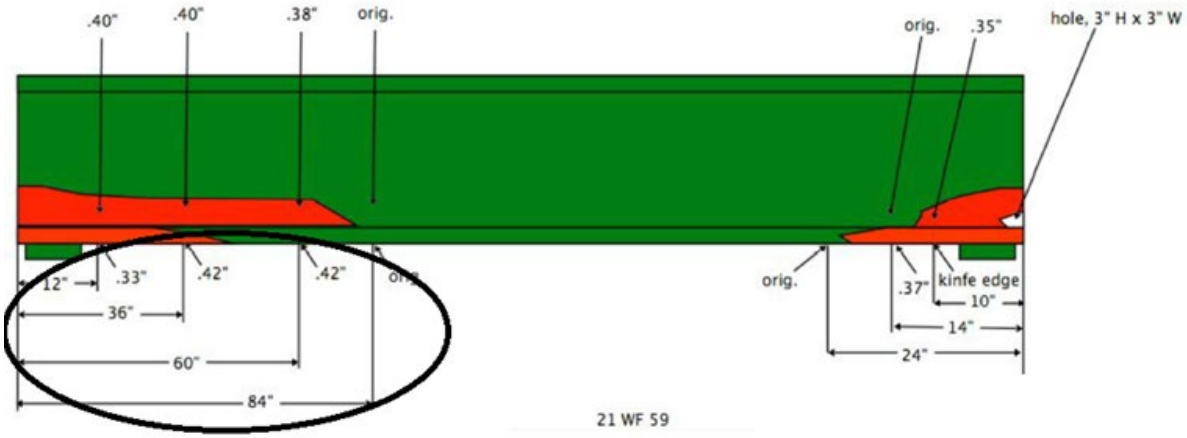

Source: Adopted from S10024-02H-MUN-NBI (District 1, Town of Sheffield).

Figure 2.5: Typical inspection report sketch, not to scale.

In some of the provided sketches, and in the narrative description, the loss of thickness for the corroded or damaged area is described providing multiple values in space, creating a very accurate representation of the damaged condition. However, in the majority of reports, only one measurement of loss of thickness or remaining thickness is reported (Fig. 2.6, right). For these cases, the team assumed that this value represents the maximum uniform thickness loss for the deteriorated area.

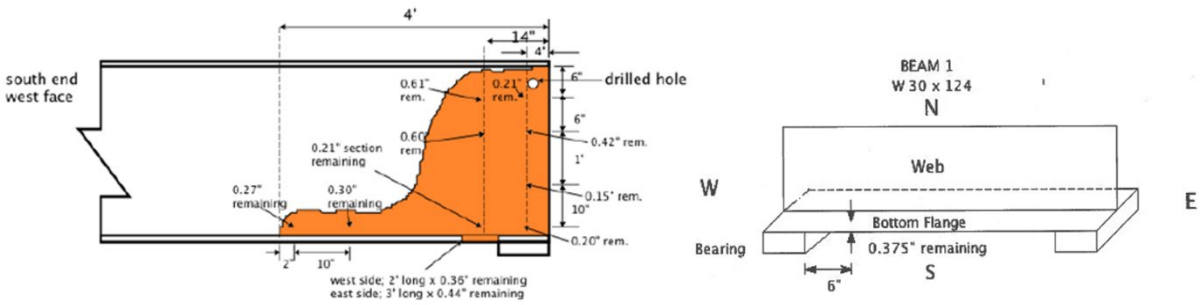

Source: Adopted from H08003-18J-MUN-NBI (District 2, Town of Hardwick) and W07029-4NA-DOT-NBI (District 2, Town of Warren) respectively.

Figure 2.6: Corroded area described by multiple thickness loss values (L) or by one (R).

In order to accurately describe a corroded beam end, usually the sketch is not enough; ideally, the authors were able to combine and crosscheck information from the narrative description, sketches, and photographs, but in some cases these were not available. In cases for which a photograph for a particular beam end is provided, it might not include the whole deteriorated area. There have been reports that there is occasionally disagreement between the different information sources (i.e. description vs. sketches). Very often for simplicity, the area of section loss is described as a rectangle (e.g., up to 3 in. high), and the same technique is used for 100% material loss, generally overestimating the phenomenon.

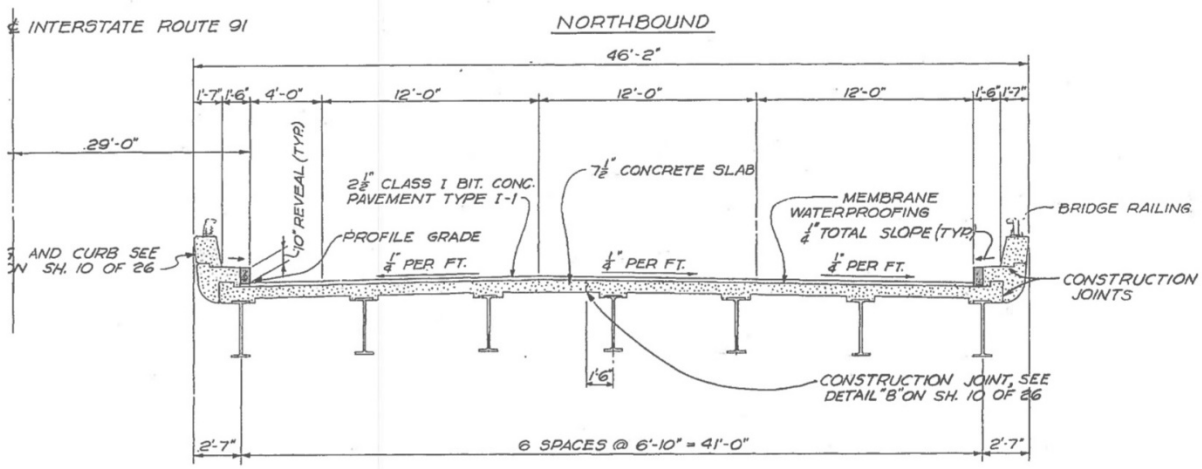

Source: Adopted from N19059-101-DOT-NBI (District 2, City of Northampton).

Figure 2.7: Construction drawings are usually included in the inspection reports.

2.1.2 Amount of Data

The authors were provided with 216 reports for 168 different bridges. The available reports per district varied from 2 to 118, as shown in Fig. 2.8.

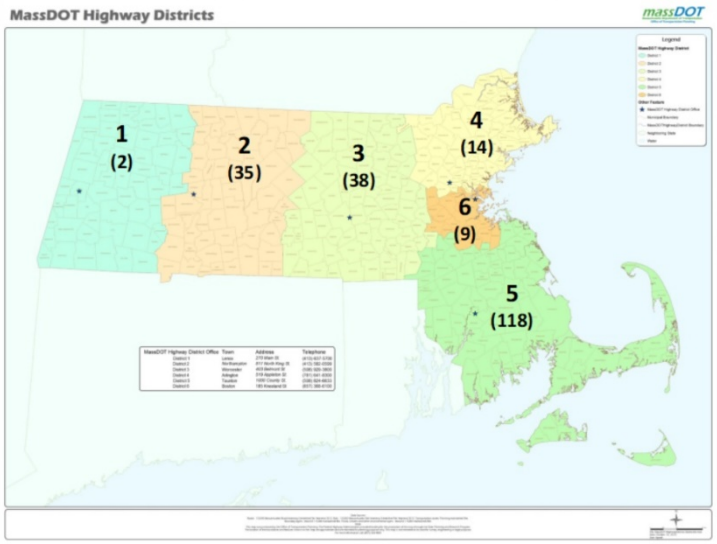

Figure 2.8: Distribution of inspection reports per district.

2.2 Definition and Quantification of the Phenomenon

2.2.1 Preliminary Filtering of Data

A preliminary look at the received data allowed for data filtering based on the general properties of the reports. The detailed numbers of that filtering process are shown in Table 2.1. The first column of Table 1 includes the different districts of the state, while the second column includes the total number of inspection reports received from each district. This information is the same as that shown in Fig. 2.8.

Table 2.1: Preliminary filtering of received data due to several reasons; last row depicts inspection reports that were post-processed.

District #	All	With Stiffeners	Reports showing deterioration over time	Corrosion data not provided	Other bridge type	Too corroded	Useful – Processed
District 1	2	0	0	0	0	0	2
District 2	35	1	0	6	5	0	23
District 3	38	4	12	4	2	1	15
District 4	14	0	8	2	0	0	4
District 5	118	24	13	24	8	0	49
District 6	9	1	0	0	8	0	0
Total	216	30	33	36	23	1	93
% of total		14%	15%	17%	11%	0%	43%

The third column of Table 2.1 identifies the number of reports provided for bridges with beam ends that had stiffeners. This particular type of beam end is out of the scope of the current project, and for that reason, these reports were removed from post-processing. The

fourth column of Table 2.1 identifies reports that describe the evolution of the corrosion phenomenon in time. For example, many of the reports describe the same bridge at different time intervals. Although this information is very important in order to observe the evolution of corrosion and possibly develop prediction tools, these reports were removed from post-processing and only the current (latest) condition of these bridges was accounted for. The fifth column of Table 2.1 counts inspection reports that did not provide corrosion data and therefore were not possible to be included in post-processing. Next, 11% of the provided inspection reports involved other types of bridges such as floor beam systems or concrete jack arches hidden by stay-in-plane (SIP) forms, which are outside of the current research scope. There were two reports that described bridges with extreme corrosion, and it was considered by the research team that these bridges should also be removed from further post-processing.

Based on all the above, the final column at the right of Table 2.1 includes all the inspection reports that were post-processed in detail. Bridges with stiffeners, as well as the inspection reports that documented losses in time, were considered as very interesting problems by the research team for potential future work on the topic. This preliminary filtering process involved a detailed processing of all 216 reports. However, 93 of these 216 (43% of the total received reports) were selected as the most suitable ones for further processing. The total number of beam ends included in the 93 reports, and that were post-processed in greater detail, was 808. This number of beam ends is considered a highly significant source of data, sufficient enough to allow the research team to reach meaningful conclusions for the phenomenon of steel beam end deterioration due to corrosion. To the best of the team's knowledge, this is the first time that such an extensive process has been followed.

2.2.2 General Categorization of Web Corrosion, Web Hole, and Flange Corrosion Patterns.

In order to manage such a large amount of data, the team developed a method to describe the phenomenon and to group similar cases with common characteristics. As a result, the first stage of post-processing involved the development of patterns for web corrosion and patterns of web holes based on the initial observations of all the data for the 808 beam ends. Following this categorization, all the beam ends went through a new way of processing the data from the respective inspection reports using an Excel spreadsheet, which constitutes the input of a Matrix Laboratory (MATLAB) script for the data valuation. This approach allowed the authors to extract conclusions quickly, efficiently, and accurately.

Web corrosion type/patterns

Based on the observations of the inspection reports, the research team developed six web corrosion patterns, which were the most common ones. These six patterns described almost all (95%) of the 808 deteriorated beam ends of the bridges (Tables 2.2 to 2.7).

Table 2.2: Web corrosion pattern W1.

Pattern Name	Pattern shape	Example from an inspection report
W1	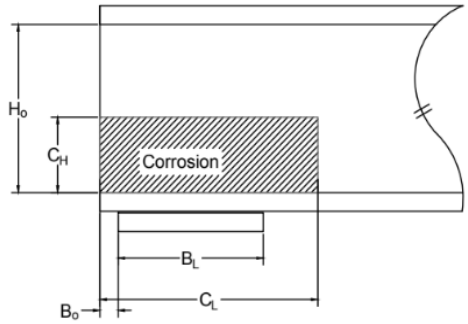	 Adopted from H-23-011-1UQ-DOT-NBI (District 3, Town of Hopkinton)
	Short description: W1 is a rectangular shape corrosion pattern that appears at the beam end above the bearing. The dimensions of the damaged area are C_H for the depth of the damaged area and C_L for the length. B_L is the bearing length and B_o is the length of the free end of the beam beyond the bearing. The photograph on the right shows a case of W1 for which the C_H is equal to the depth of the beam web H_o.	

Table 2.3: Web corrosion pattern W2.

Pattern name	Pattern shape	Indicative example from an inspection report
W2	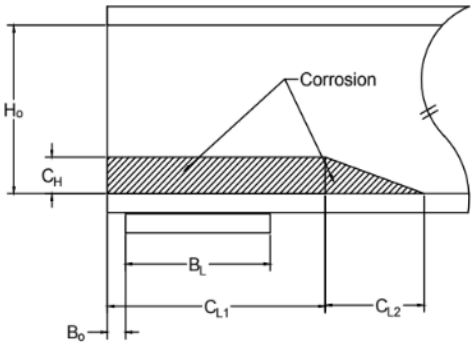	 Adopted from N-06-015-3WR-DOT-NBI (District 5, Town of New Bedford)
	Short description: W2 is similar to W1, with the addition of a triangular-shaped corrosion area at the end of the rectangular shape. For W2, C_H is the depth of the damaged area, while C_{L1} is the length of the rectangular part of the corrosion. C_{L2} is the length of the triangular damage. B_L is the bearing length, and B_o is the length of the free end of the beam beyond the bearing. The photograph on the right shows a typical case of W2.	

Table 2.4: Web corrosion pattern W3.

Pattern name	Pattern shape	Indicative example from an inspection report
W3	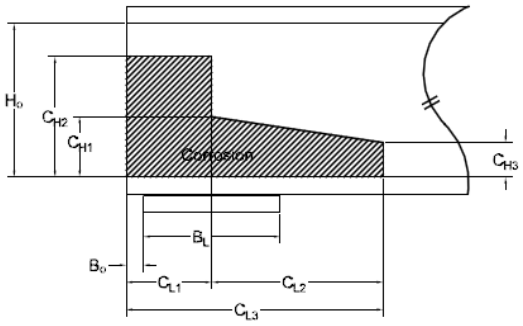	 Adapted from D-12-026-1XX-DOT-NBI (District 3, Town of Dudley)
	Short description: W3 is a more complicated shape than W1 and W3. It can be described by the three areas as shown in the sketch on the left. For W3, the depth of the corroded area is described using C_{H1}, C_{H2} and C_{H3}. Similarly, C_{L1} and C_{L2} are used to provide the length of the corroded area. B_L is the bearing length, and B_o is the length of the free end of the beam beyond the bearing. The photograph on the right shows a typical case of W3.	

Table 2.5: Web corrosion pattern W4.

Pattern name	Pattern shape	Indicative example from an inspection report
W4	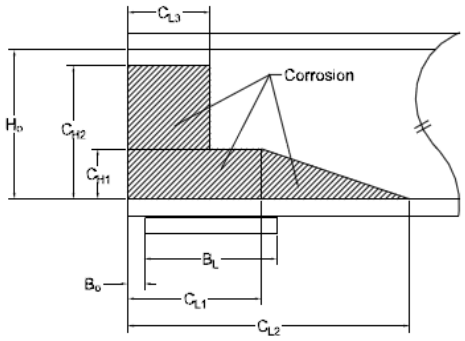	 Adapted from F-01-042-3X5-DOT-NBI (District 5, City of Fall River)
	Short description: W4 is a slight modification of W3 to include the complication of the shape of the bottom left rectangular shape. The depth of the corroded area is described using C_{H1} and C_{H2}. Similarly, C_{L1}, C_{L2} and C_{L3} are used to provide the length of the corroded area. B_L is the bearing length, and B_o is the length of the free end of the beam beyond the bearing. The photograph on the right shows a typical case of W4.	

Table 2.6: Web corrosion pattern W5.

Pattern name	Pattern shape	Indicative example from an inspection report
W5	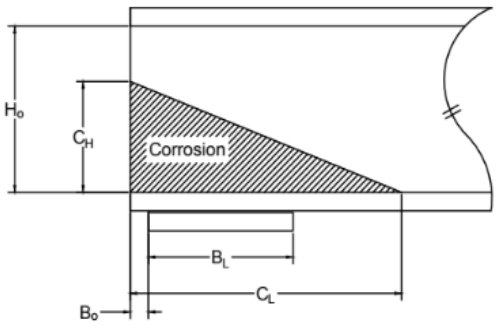	 Adapted from W-05-024-0T4-MUN-NBI (District 2, Town of Ware)
	Short description: W5 is a simple triangular shape corroded area described by C_H which is the height of the triangle, and C_L which is the length of the triangle. B_L is the bearing width, and B_o is the length of the free end of the beam beyond the bearing. The photograph on the right shows a typical case of W5.	

Table 2.7: Web corrosion pattern W6.

Pattern name	Pattern shape	Indicative example from an inspection report
W6	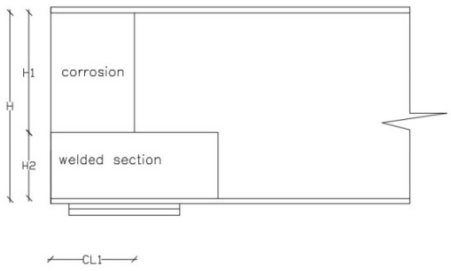	 Adapted from N-19-064-10C-DOT-NBI (District 2, City of Northampton)
	Short description: W6 is a rare case, but it is included here for the sake of completeness. It involves a welded plate at the bottom side of the web. The corrosion extends above the welded section as shown in the graph at the left. For this case H_1 is the height of the corroded area, C_{L1} is the length of the corroded area, and H_2 is the height of the welded plate. The photograph on the right shows a typical case of W6.	

Web hole type/patterns

Based on observations of the inspection reports, the authors developed four web hole patterns, which were the most common ones. These four patterns described almost all (95%) of the 808 deteriorated beam ends of the bridges (Tables 2.8 to 2.11).

Table 2.8: Web hole pattern M1.

Pattern name	Hole shape	Indicative example from an inspection report
M1	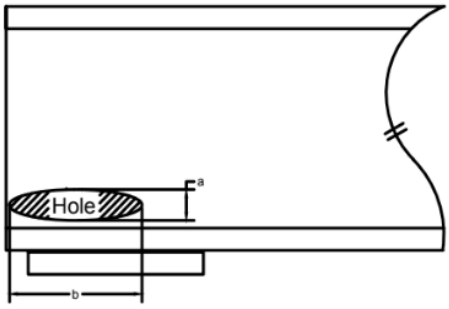	 Adapted from F-04-017-23N-DOT-634 (District 3, City of Fitchburg)
	Short description: M1 is a case where a hole appears at the lower part of the web and extends longitudinally over the bearing. For this case, a is the height of the hole and b is the length of the hole. The photograph on the right shows a typical case of M1.	

Table 2.9: Web hole pattern M2.

Pattern name	Hole shape	Indicative example from an inspection report
M2	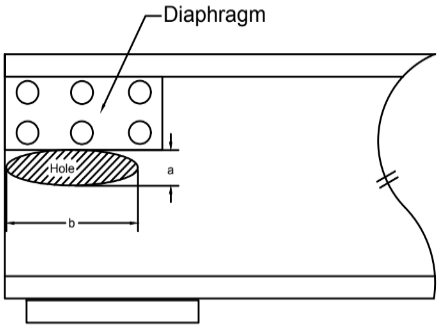	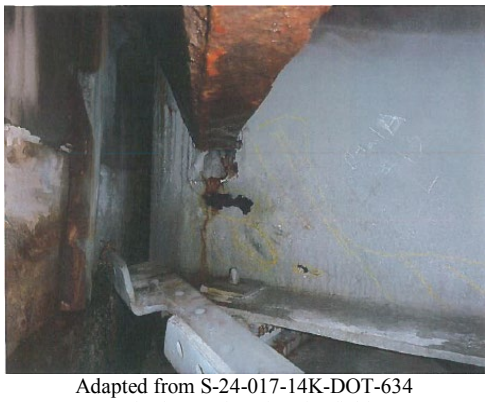 Adapted from S-24-017-14K-DOT-634 (District 2, City of Springfield)
	Short description: M2 is a case where the beams have a diaphragm, and the hole appears just below the diaphragm. For this case, a is the height of the hole and b is the length of the hole. The photograph on the right shows a typical case of M2.	

Table 2.10: Web hole pattern M3.

Pattern name	Hole shape	Indicative example from an inspection report
M3	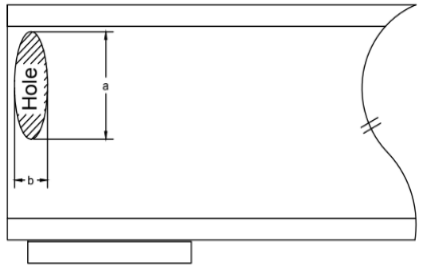	 Adapted from F-04-017-23N-DOT-634 (District 3, City of Fitchburg)
	Short description: M3 is a case where a hole appears at the top part of the beam. For this case, a is the height of the hole and b is the length of the hole. The photograph on the right shows a typical case of M3.	

Table 2.11: Web hole pattern M4.

Pattern name	Hole shape	Indicative example from an inspection report
M4	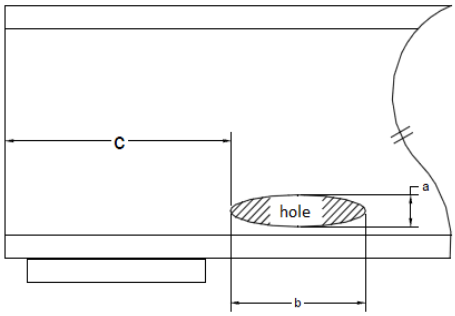	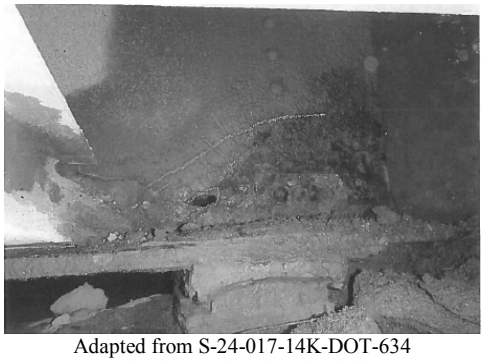 Adapted from S-24-017-14K-DOT-634 (District 2, City of Springfield)
	Short description: M4 is a case where a hole appears away from the bearing at the lower part of the beam. For this case, a is the height of the hole, b is the length of the hole and c is the distance of the end of the hole from the end of the beam. The photograph on the right shows a typical case of M4.	

Each web corrosion pattern can be combined with each of the hole patterns, as well as with three combinations of hole patterns: M1+M2, M1+M3, and M2+M4.

Flange patterns

For the flange corrosion, there was very limited information available in the inspection reports. For the purposes of the current work, the flange corrosion was based on the assumption that the deterioration extended to the full width of the flange for all the

deteriorated length. Similarly to the web corrosion, the thickness loss was considered uniform for the whole area. The length was taken from the inspection reports, and, in case no information was provided, the team considered no corrosion in the flange.

2.2.3 Summary Spreadsheet Implementation

Based on the categorization of the first stage of post-processing, the authors gathered the necessary data for all 808 beam ends. This process was performed by developing a new Excel spreadsheet, in order to summarize the important information for each bridge and beam end. The authors isolated data about the corrosion phenomenon and described it using a list of parameters.

	Identification		columns:	5	Item 59 Condition:	5		
	Bridge:	N-19-062-106 (n-s)	Area:	NORTHAMPTON	Construction:	1965	Location:	42°19'58.84"N 72°37'16.72"W
	Girders:	30WF99			Stringers:	concrete		Spans: 4
	No of corroded beams:		4	At both ends:	0	Type	composite	fy:
6	Beam type		30WF99	30WF99	30WF99	30WF99	same_end	
7	**Web cor. Type:**		W1	W3	W3	W1	0	
8	CL1 (%H):		127.16%	42.38%	42.38%	42.38%		

Figure 2.9: Bridge identification and general information at top of spreadsheet.

The top of the spreadsheet included general information for the bridge such as name, location, construction year, spans, etc. (Fig. 2.9). Below that, each corroded beam was described by a separate column (Fig. 2.10). By describing each corroded beam with a column, the authors accurately considered each unique beam end case. The new process is described in detail as follows. The main advantage of the new approach is that by using these spreadsheets, the post-processing became highly efficient and fast.

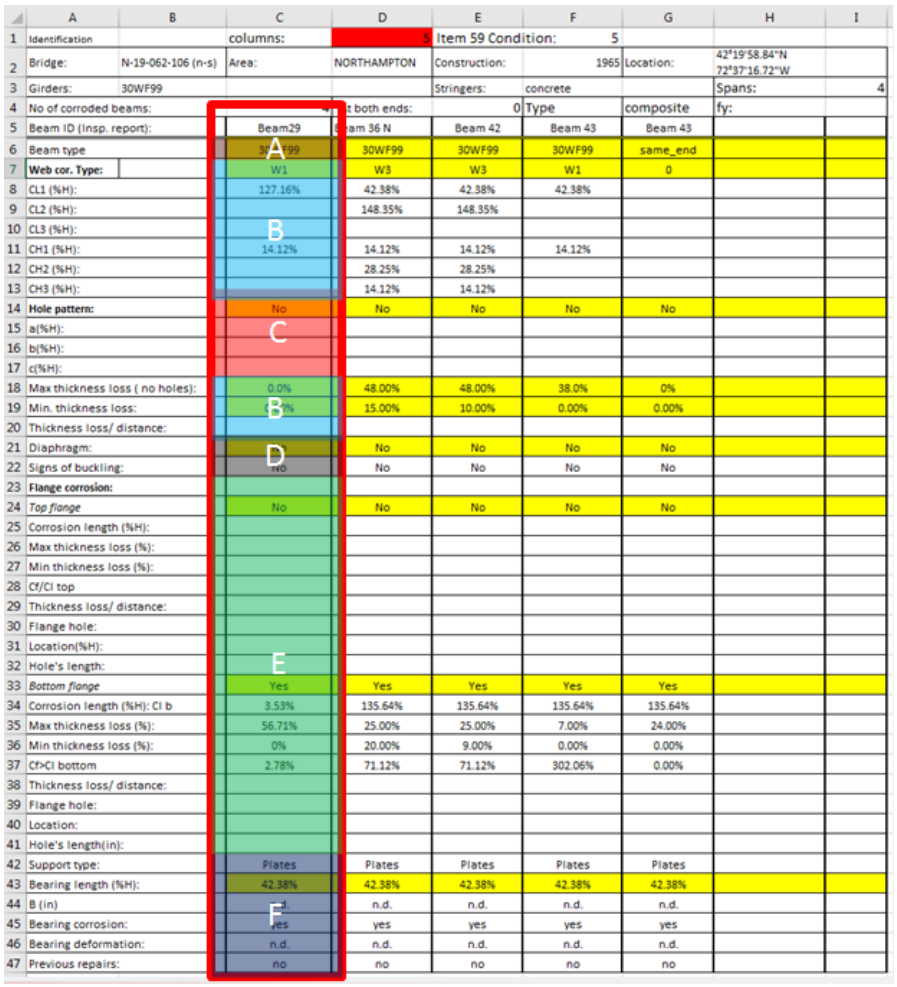

	A	B	C	D	E	F	G	H	I
1	Identification		columns:	5	Item 59 Condition:	5			
2	Bridge:	N-19-062-106 (n-s)	Area:	NORTHAMPTON	Construction:	1965	Location:	42°19'58.84"N 72°37'16.72"W	
3	Girders:	30WF99			Stringers:	concrete		Spans:	4
4	No of corroded beams:			t both ends:	0	Type	composite	fy:	
5	Beam ID (Insp. report):		Beam29	am 36 N	Beam 42	Beam 43	Beam 43		
6	Beam type		30WF99	30WF99	30WF99	30WF99	same_end		
7	**Web cor. Type:**		W1	W3	W3	W1	0		
8	CL1 (%H):		127.16%	42.38%	42.38%	42.38%			
9	CL2 (%H):			148.35%	148.35%				
10	CL3 (%H):								
11	CH1 (%H):		14.12%	14.12%	14.12%	14.12%			
12	CH2 (%H):			28.25%	28.25%				
13	CH3 (%H):			14.12%	14.12%				
14	**Hole pattern:**		No	No	No	No	No		
15	a(%H):								
16	b(%H):								
17	c(%H):								
18	Max thickness loss (no holes):		0.0%	48.00%	48.00%	38.0%	0%		
19	Min. thickness loss:		0%	15.00%	10.00%	0.00%	0.00%		
20	Thickness loss/ distance:								
21	Diaphragm:			No	No	No	No		
22	Signs of buckling:		No	No	No	No	No		
23	**Flange corrosion:**								
24	*Top flange*		No	No	No	No	No		
25	Corrosion length (%H):								
26	Max thickness loss (%):								
27	Min thickness loss (%):								
28	Cf/Cl top								
29	Thickness loss/ distance:								
30	Flange hole:								
31	Location(%H):								
32	Hole's length:								
33	*Bottom flange*		Yes	Yes	Yes	Yes	Yes		
34	Corrosion length (%H): Cl b		3.53%	135.64%	135.64%	135.64%	135.64%		
35	Max thickness loss (%):		56.71%	25.00%	25.00%	7.00%	24.00%		
36	Min thickness loss (%):		0%	20.00%	9.00%	0.00%	0.00%		
37	Cf>Cl bottom		2.78%	71.12%	71.12%	302.06%	0.00%		
38	Thickness loss/ distance:								
39	Flange hole:								
40	Location:								
41	Hole's length(in):								
42	Support type:		Plates	Plates	Plates	Plates	Plates		
43	Bearing length (%H):		42.38%	42.38%	42.38%	42.38%	42.38%		
44	B (in)			n.d.	n.d.	n.d.	n.d.		
45	Bearing corrosion:			yes	yes	yes	yes		
46	Bearing deformation:		n.d.	n.d.	n.d.	n.d.	n.d.		
47	Previous repairs:		no	no	no	no	no		

Figure 2.10: New spreadsheet with designated shadowed areas.

The first part of the spreadsheet described the web corrosion pattern (lines 7–13 in Fig. 2.10). The first field that had to be filled concerned the beam type (shadowed area A, in Fig. 2.10). Then, in Part B (lines 8–13 and 18–20), the corrosion shape was described using one of the six defined corrosion patterns; the corresponding dimensions were normalized with the height H_0, where $H_0 = H - 2\ t_f$ and the web thickness loss was reported as well, where H is the depth of the beam and t_f the flange thickness.

The second part of the spreadsheet involved the hole patterns. In Part C, if a web hole existed, it was classified according to the hole patterns. In case its dimensions were given, they were normalized the same way as web corrosion lengths. In Part D, the diaphragm and signs of buckling were reported with yes or no.

Part E was dedicated to flange corrosion. The corrosion length, the thickness loss, and, in the case of a hole, its position and length were reported. Finally, in Part F, the condition of the bearing was described, if any information was available.

3.0 Experimental Work Methodology

Over the years, a significant amount of research has been carried out in an attempt to determine experimentally the remaining capacity of corroded beam ends. However, to date, the research team found no study that looked specifically at beams with natural corrosion. In all cases, the corrosion was simulated with artificial thickness reduction, which renders results that are not verifiably realistic. **In the presented study, six naturally corroded girders were tested.** Due to the fact that these girders were removed from an in-service bridge, the need for artificial corrosion was precluded. An exact corrosion pattern from the field could be used instead.

The beam selection process, design, fabrication, and assembly of testing rig, as well as the instrumentation configuration, are described in this section. The mechanical model of each beam, in terms of geometry, corrosion topology, boundary, and loading conditions, is also included.

3.1 Experimental Preparation

3.1.1 Beam Selection and Shipment to UMass Testing Facilities

At the time this research began, a bridge rehabilitation project was in progress in Massachusetts. Specifically, a five-span bridge in Colrain, Massachusetts, was under demolition. The structure connects Route MA-112 over the East Branch of the North River. The Colrain bridge was built in 1933 as a three-span bridge consisting of five continuous riveted steel plate girders. Later on, the bridge was rebuilt with the addition of one span to each end. The bridge expansion design contains 33WF132 exterior and 33WF125 interior simply supported unstiffened rolled girders, spanning 50 feet.

By the initiation of this research, the west half of the structure had already been replaced. However, some of the remaining beams met the standards for the scope of the current research project. In total, eight beams were chosen to be shipped to the Brack Structural Testing Laboratory at the University of Massachusetts, Amherst (UMass). Before transporting the beams, it was decided the best practice would be to cut the beams in half (Fig. 3.1). The advantage of this was two-fold. First, it provided ease of transport. Second, it allowed both segments to be in compliance with laboratory length restrictions. Four beams cut in midspan, originally located in Span 5 of the Colrain bridge, were delivered to Brack Structural Testing Laboratory at UMass on Feb. 9, 2017.

Delivery 1

On Nov. 9, 2017, four of the beams (eight beam segments) removed from the fifth bridge span were delivered to the Brack Structural Testing Laboratory at UMass. The research team coordinated with UMass Construction Services to unload and place the beams into the backyard of the laboratory. Thick wood spacers were placed between the beams in order to avoid deformation of the corroded ends upon contact with one another.

Delivery 2

On Feb. 2, 2018, four additional beams (eight beam segments) from the Colrain bridge were delivered. These beams were procured from the first bridge span. It should be mentioned that wood spacers between the beams had not been used during the transport of the specimens. The beams were delivered heavily distorted. Their condition was such that these beams could not be tested for this project.

Figure 3.1: Delivery, unloading, and storage of first set of corroded beams from Colrain bridge.

In addition to the beams obtained from the Colrain bridge, six additional girders were recovered from a second rehabilitation project, taking place in the town of Charlemont. Six girders were retrieved from the simple span bridge that carries Maxwell Rd. over Maxwell Brook. According to the available drawings, the Charlemont bridge was built in 1939 and consists of six rolled 21WF59 beams spanning close to 23 feet. However, based on the measurements conducted prior to testing, the geometry of the section better matches the nominal dimensions of 21WF73.

Delivery 3

On Dec. 20, 2018, six girders delivered to the Brack Structural Testing Laboratory at the University of Massachusetts (Fig. 3.2). The research team coordinated with UMass Construction Services to unload and place the beams into the backyard of the laboratory.

Figure 3.2: Delivery and unloading of corroded beams from Charlemont bridge.

3.1.2 Final Beam Selection

Based on the conditions of the delivered beams, the evaluation of their testable quality was performed. Of the 22 acquired beams (eight girders cut in half from the Colrain bridge and six from the Charlemont bridge), only six (numbered as Specimens 1 to 6) were considered testable and promising of results that would be representative of load-carrying capacities. The discrepancy in the number of the acquired and the testable beams was attributed to the heavy distortion of the corroded ends caused during the demolition process (Fig. 3.3).

Figure 3.3: Distorted beams rejected for experimental testing due to condition.

3.1.3 Design of Experimental Configuration

An experimental rig was designed to mimic the boundary and loading conditions of in-service girders. By observation of inspection reports provided by MassDOT, it is noticed that the majority of the Commonwealth's structurally deficient bridges were built between 1940 and 1980. According to the construction drawings of these bridges, the steel beams were typically not composite. Shear studs were not implemented to promote interaction between the steel beam and the concrete deck, although in some cases the top flanges of the beams were encased in the deck. This encasement covered just the thickness of the top flange, and it is therefore controversial how much composite action can be developed. Based on the non-composite design assumption, a deck slab was not cast onto the girder prior to testing. However, its contribution was considered in the experiments by restraining the out-of-plane displacements of the top flange; cantilevered braces were placed every 5 ft. along the length of the specimen, with C channels bolted on the top in contact with specimen's top flange. This configuration prevented lateral torsional buckling while it ensured that web buckling occurred in the corroded region of interest. Specimens were simply supported by a pair of bearing plates.

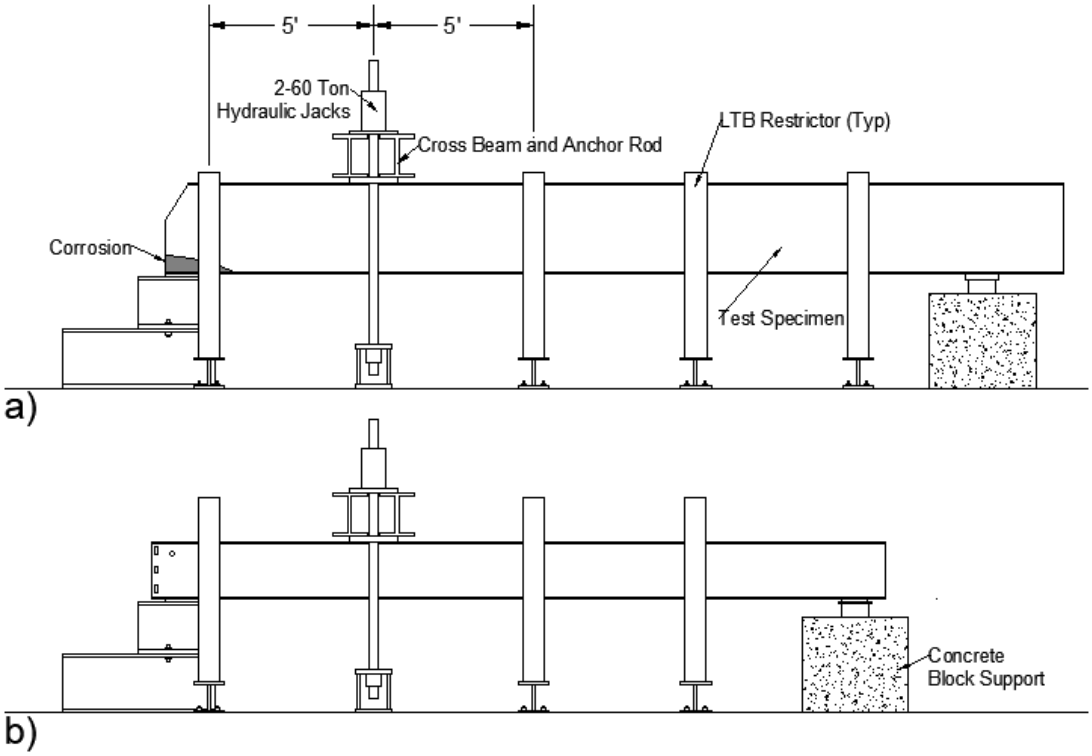

Figure 3.4: Experimental rig for (a) Specimens 1 to 3 and (b) 4 to 6.

The experimental test setup was initially designed for specimens with lengths of at least 25 ft. and web depth of 33 in., based on the Colrain Bridge specifications. The experimental test setup had to be modified slightly for the specimens taken from the Charlemont bridge, as these differed in depth and length (Fig. 3.4). Initially, the Lateral Torsional Buckling (LTB) restrain system was adjusted to the new beams' depth. The C channels, which restrict the top flange, were reduced in height. The experimental rig also had to be modified in order to be in

compliance with the reduced specimens' length. The LTB restriction device close to the intact end was removed and then replaced by a concrete block support where the bearing plate is placed. Both versions of the experimental configuration are presented in Fig. 3.5.

The loading configuration was designed to stay within the force limitations of the laboratory's strong floor. It consisted of two 60-ton through-hole jacks, placed in parallel, applying load to the specimen's top flange through a cross beam. The cross beam was designed to allow passage of a threaded rod that was anchored to the strong floor. In terms of this study, the beam end closer to the applied load is referred to as the corroded end, while the other end is the intact one. This configuration served two purposes: first, it ensured that the failure was shear dominated, and second, more than 70% of the load was distributed to the studied end. This loading configuration is distinguished from the one in *(8)* since it examines beam behavior and not column-like behavior of the beam end.

3.1.4 Instrumentation Configuration

All specimens were instrumented to record loads and deformations (Fig. 3.5). In order to measure the applied load, two 200-kip load cells, manufactured by Omega, were placed at the anchorage point of the threaded rods. A third compression load cell, with 100-kip capacity, was installed beneath the intact end to record the bearing reaction force. A TJE pressure transducer, by Honeywell, was installed to monitor pressure of the hydraulic fluid in the hose downstream of the hydraulic pump.

Nine displacement potentiometers were implemented to record vertical as well as lateral deflections. A spring-type potentiometer (LVDT) by Celesco was used to measure the maximum vertical beam deflection. This transducer has a 5-in. measuring capacity, and it was installed on the outer face of the bottom flange, beneath the point of load application. Eight Novotechnik rod-type potentiometers were used to measure the out-of-plane displacements at the corroded end. These potentiometers were installed on a frame, forming an arrangement of two columns and four rows. This configuration was chosen in order to record two different sets of out-of-plane displacements taken over the height of the web. The two columns of instruments were placed close to the inner and outer edges of the corroded end bearing, respectively. The rod-type potentiometers have a measuring capacity of 4 inches. Finally, at each specimen, six strain rosettes (SRs) by Tokyo Measuring Instruments Lab were attached to the corroded web and flange to measure the strains during the experimental procedure.

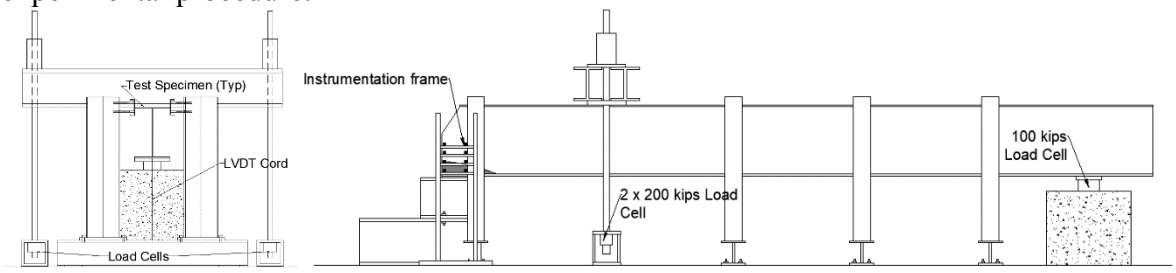

Figure 3.5: Side and front view of the instrumentation configuration.

A list of instrumentation equipment used in the experiment is as follows:

- Strains Gauges: 6 x FRA-5-11 by Tokyo Measuring Instruments Lab (per specimen)
- Potentiometers: 6 x TR-0100 by Novotechnik
- LVDT: 1 x PT-101-5A by Celesco
- Load cells: 2 x LC8400 by Omega Engineering Inc.
- Pressure Transducer: TJE by Honeywell

3.1.5 Assembly of Experimental and Instrumentation Configuration

Fabrication of the testing rig designed during the previous task was conducted. The testing apparatus was assembled and connected to the strong floor at the Brack Structural Testing Laboratory at UMass. This section includes a dated outline of all the performed tasks for the experimental configuration set-up.

May 14, 2018: Steel arrived at UMass Physical Plant from steel manufacturer. Space was not free in the lab, due to ongoing experiment, so beams were temporarily stored at Physical Plant until they could be transferred to the Brack Structural Testing Lab (Fig 3.6).

Figure 3.6: The steel for the experimental configuration.

June 19, 2018: Steel was moved to Brack Structural Testing Lab and painted with steel rust primer. Space in lab was still not available due to ongoing experiment. Painted beams were tarped and stored in the backyard of the Brack Structural Testing Lab (Fig. 3.7).

Figure 3.7: Beams painted with steel rust primer, and tarped and stored at the backyard of Brack lab.

July 26, 2018: Load cells ordered. One was delivered immediately; one had a four-week shipping time.

July 27, 2018: The ongoing experiment on concrete girders was completed, and the space was available. UMass fork truck was out of order, and it was not possible to remove the tested specimen from the lab.

Aug. 8, 2018: The specimen for the completed experiment on concrete girders was taken off the supports and laid on the right side of the lab (Fig. 3.8). The experimental configuration

from previous project was disassembled. All anchor spots for the steel setup were cleaned and removed.

Figure 3.8: Experimental configuration from completed test was disassembled, and anchor spots were cleaned and removed.

Aug. 10, 2018: Floor beams were moved into the Brack Structural Testing Laboratory. Floor beams were tied down using anchor rods and bolts (Fig.3.9).

Figure 3.9: Floor beams tied down at strong floor anchor spots of Brack testing facilities.

Aug. 24, 2018: Lateral bracing completely bolted together, anchor blocks, and cross beams moved into lab (Fig. 3.10).

Figure 3.10: Experimental configuration in Aug. 2018; anchor block, floor beams, and lateral bracing in position.

Sept. 6, 2018: Intact and corroded beam end supports were completed and aligned. LTB cantilevers were anchored only at one side of the specimen, in order to facilitate the moving and centering of the tested beam on its supports.

Sept. 27, 2018: First specimen moved into the lab and centered on its position (Fig. 3.11). The LTB cantilevers from the one side of the specimen beam were placed and anchored after centering the beam on its bearings.

Figure 3.11: First test specimen moving in position.

3.2 Specimens Geometry

3.2.1 Specimen 1

Specimen 1 is a 332 in. long 33WF125 with extensive end corrosion. The girder was identified in the Colrain bridge inspection reports as Beam 4 in Span 5 (Fig. 3.12).

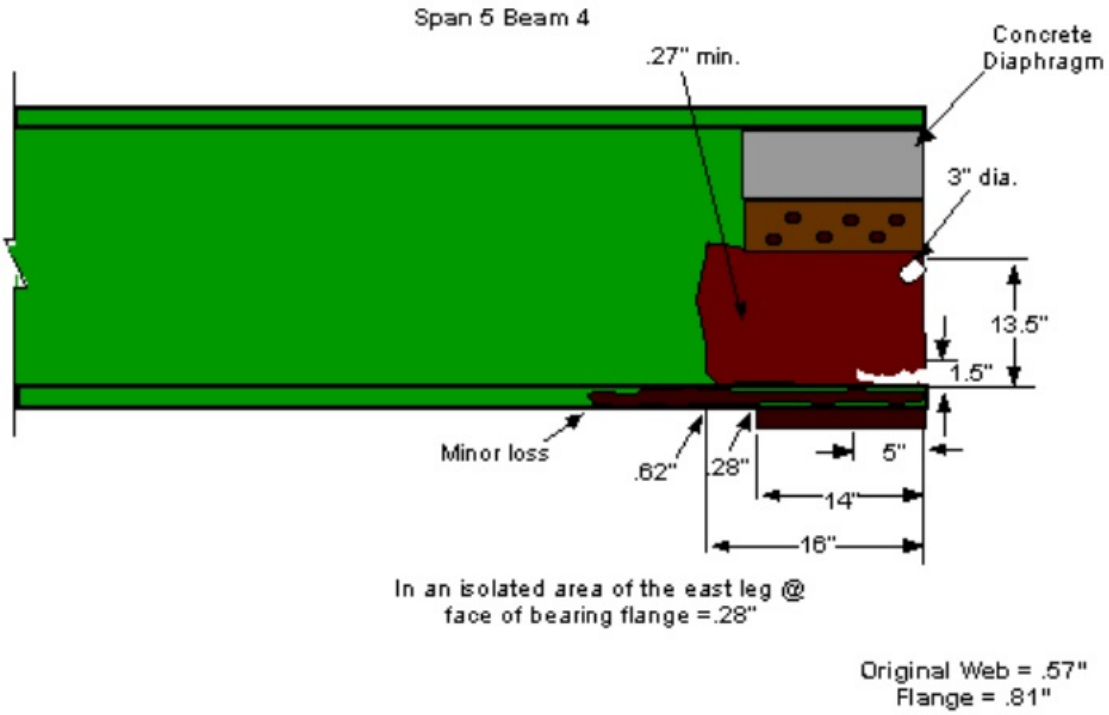

Figure 3.12: Specimen 1 as reported in MassDOT inspection report *(31)*.

While the bridge was in service, a concrete diaphragm was located above the support. During the bridge demolition, the concrete was removed, while the steel angle sections remained bolted to both sides of the web. The beam was delivered to the UMass testing facilities with the bearing plate still welded to the girder's end. The anchors protruding from the bottom of the bearing had to be sawn off. As previously mentioned, the flange was warped at the area of the support. In order to promote a uniform contact loading, grout was used to fill the gap between the flange and the support.

The most extensive section loss was observed in the lower half of the web (Fig. 3.13). Two holes could also be observed among the corrosion. The first one (6 in. long x 0.5 in. high) was located directly above the flange (Fig. 3.14). At the inner perimeter of the hole, the web had crippled in a distance of 3 in. along the longitudinal axis of the beam. The second area with 100% section loss was located below the steel section angles (Fig. 3.15).

Figure 3.13: Corroded end of Specimen 1.

Figure 3.14: Area with 100% section loss above the flange, shown from both web sides.

Figure 3.15: Area with 100% section loss below area where diaphragm was originally located.

Except for the areas with 100% thickness loss, it was necessary to define the thickness reduction profile along the corroded end. As already mentioned, the research team coordinated with MassDOT personnel to take advantage of specialized measurement devices

for taking such measurements. The data was gathered using a Pocket MIKE Compact Thickness Gauge manufactured by GE Inspection Technologies. This device provided display resolution of 0.001 in. for any material thickness up to 10 in. *(32)*. In total, 159 points were measured on the web, and 42 points at the bottom flange (Fig. 3.16). The measurement locations are shown in Fig. 3.16; the illustrated values are 10^{-2} in. Intact thicknesses are 0.57 in. for the web and 0.805 in. for the flange.

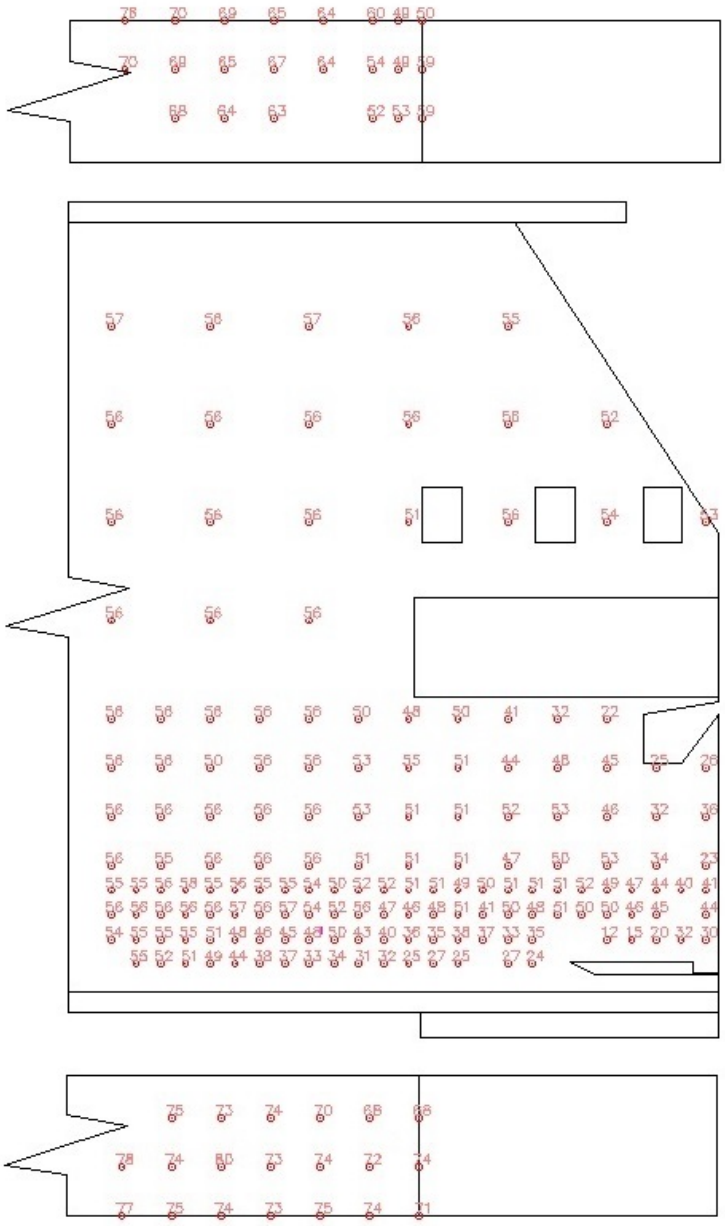

Figure 3.16: Measurement locations of web and flange thickness for Specimen 1.

The exact experimental configuration is illustrated in Fig. 3.17 and the instrumentation configuration in Fig. 3.18.

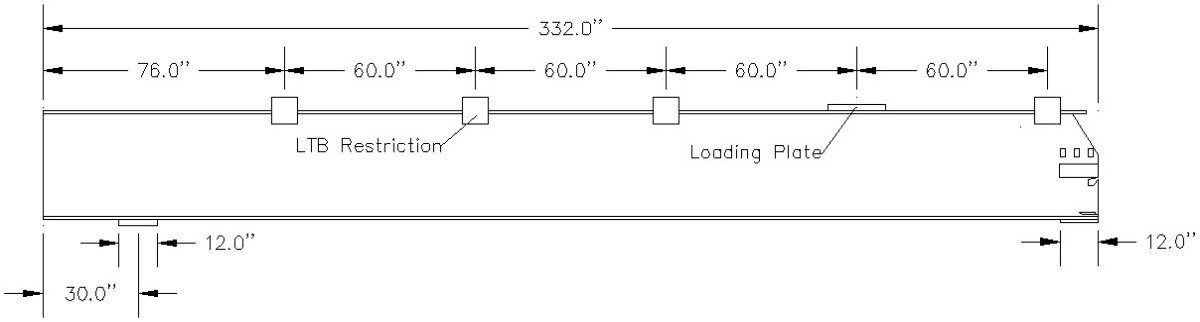

Figure 3.17: First specimen experimental configuration and dimensions.

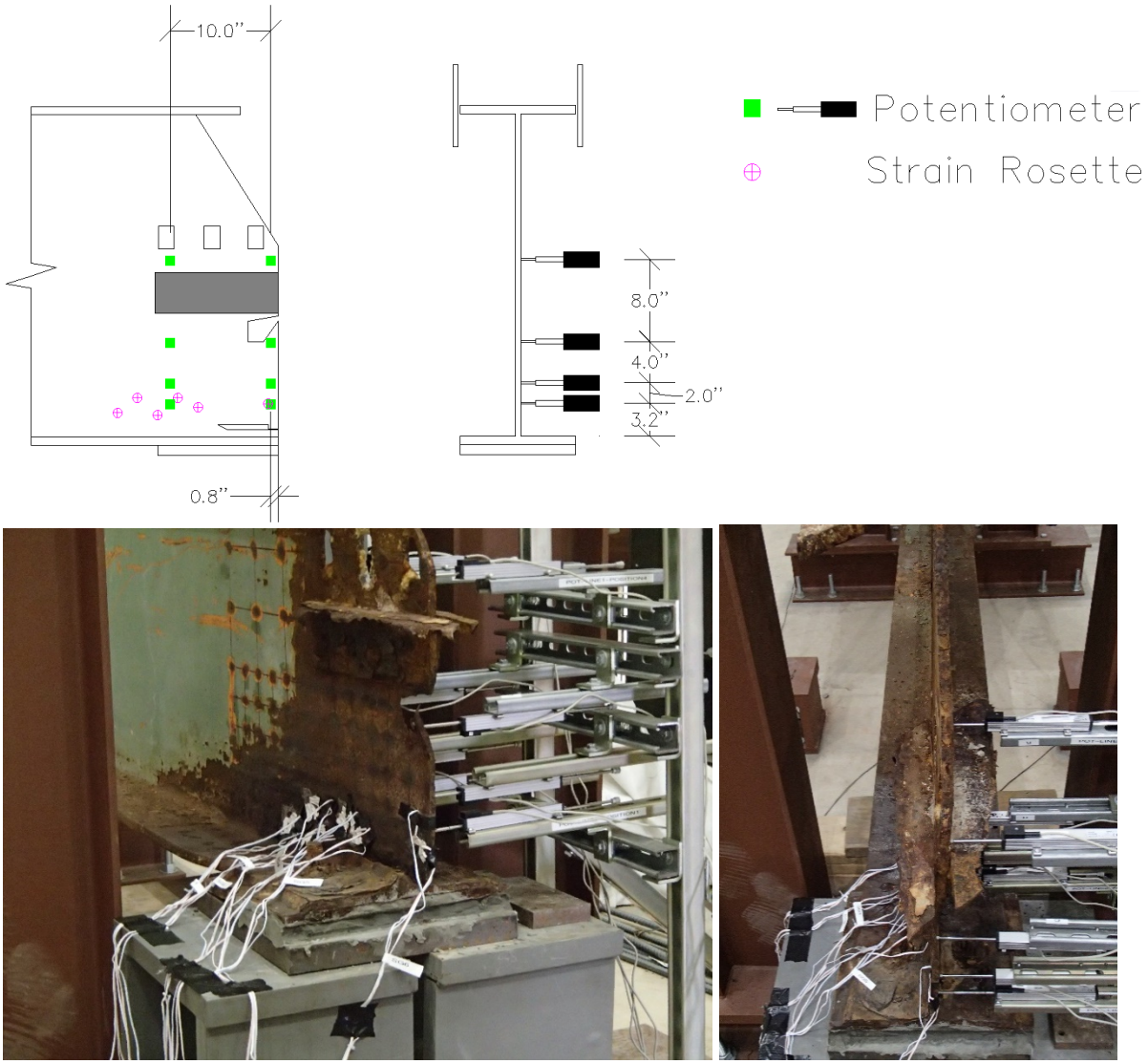

Figure 3.18: Instrumentation configuration at corroded end of Specimen 1.

3.2.2 Specimen 2

Specimen 2 is a 286.5 in. long 33WF132 with extensive end corrosion. The girder was identified in the Colrain bridge inspection reports as Beam 1 at Span 5 (Fig. 3.19).

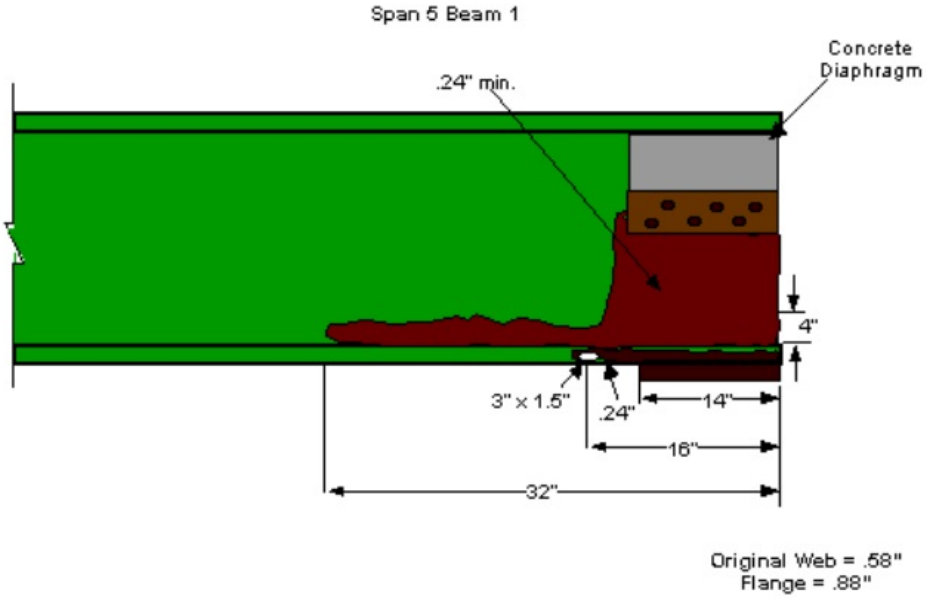

Figure 3.19: Specimen 2 as reported in MassDOT inspection report *(31)*.

While the bridge was in service, a concrete diaphragm was located above the support. During the bridge demolition, the concrete was removed, while the steel angle sections remained bolted to both sides of the web (Fig. 3.20). The beam was delivered to UMass testing facilities with the bearing plate still welded to the girder's end. The anchors protruding from the bottom of the bearing had to be sawn off. For this specimen, the condition of the flange over the bearing was better than that of the first beam. Significantly less warping of the flange was observed for this experiment. However, in order to promote a uniform loading, grout was again used to fill the gap between the flange and the support.

The most extensive section loss in the web was observed in three different areas above the support. The first distinct area was located parallel to the inner edge of the concrete diaphragm. This topology revealed a likelihood that water consistently flowed from the top of the beam to the bottom flange, following this path. The second area of distinct section loss proceeded diagonally across the web between the steel angle sections and the bottom flange. Finally, the last distinct area was a 5 in. x 1 in. area at the bottom of the web. It should be also mentioned that there is a small hole located below the steel angle sections. The defining feature of Specimen 2 was its extensive initial lateral web displacement, which reached 1.58 in. (Fig. 3.23).

It is worth mentioning that the flange hole (3 in. x 1.5 in.) at this specimen allowed the research team to investigate the effects of 100% flange section loss close to the bearing.

Figure 3.20: Corroded end of Specimen 2.

Figure 3.21: The two areas with extensive section loss at Specimen 2's web.

Figure 3.22: A ¼-in. diameter hole, located 4 in. below the steel angle sections.

Figure 3.23: Front view of Specimen 2; maximum initial lateral displacement is 1.58 in.

Similarly to the procedure followed for the first specimen, the research team coordinated with MassDOT personnel in order to conduct detailed thickness measurements to create the thickness reduction profile along the corroded end. The data was gathered again, using a Pocket MIKE Compact Thickness Gauge manufactured by GE Inspection Technologies. In total, 183 points were measured on the web and 10 points at the bottom flange (Fig. 3.24). The illustrated values are 10^{-2} inches. Intact thicknesses are 0.58 in. for the web and 0.88 in. for the flange.

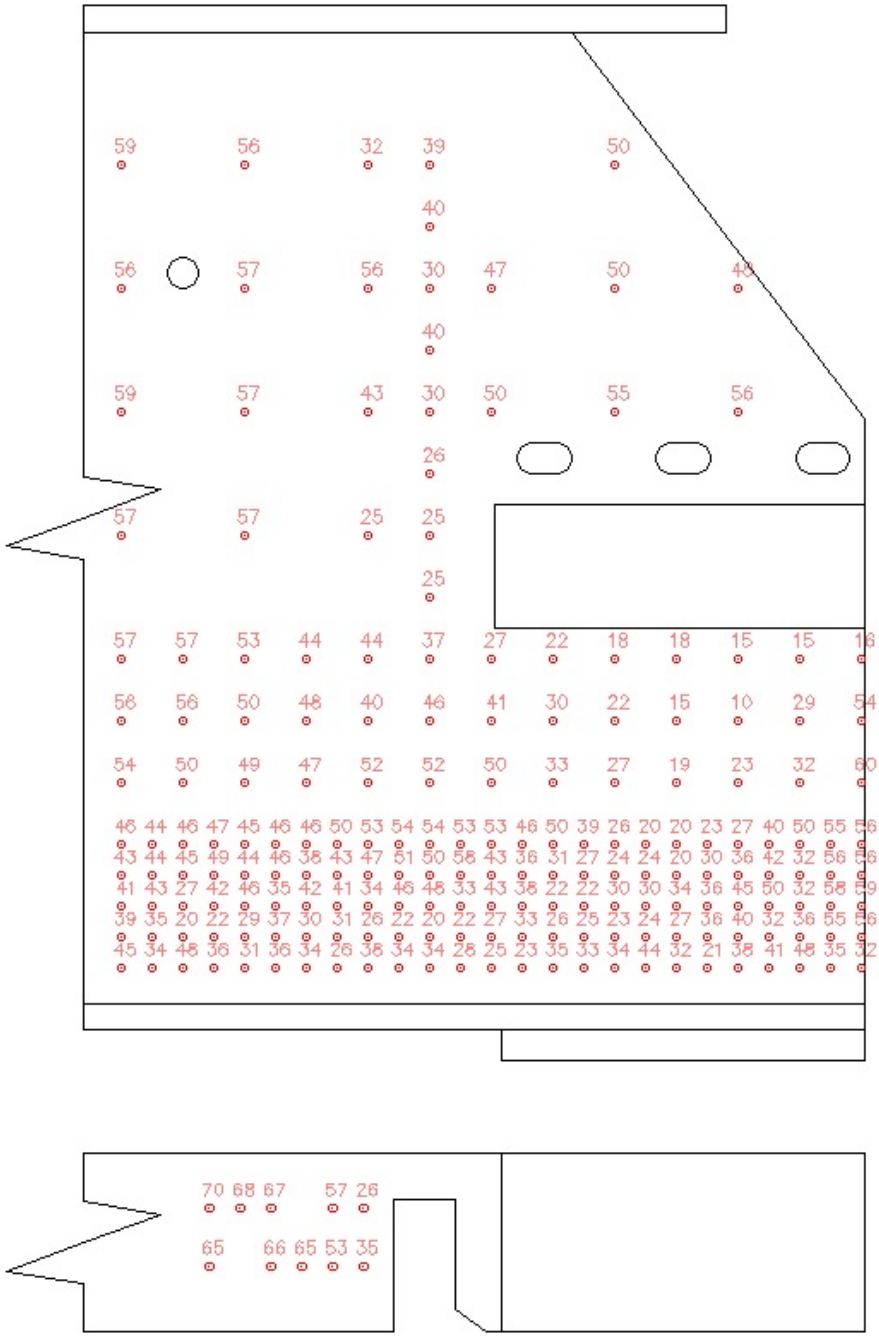

Figure 3.24: Measurement of web and flange thicknesses, Specimen 2.

The exact experimental configuration is illustrated in Fig. 3.25, and the instrumentation configuration in Fig. 3.26.

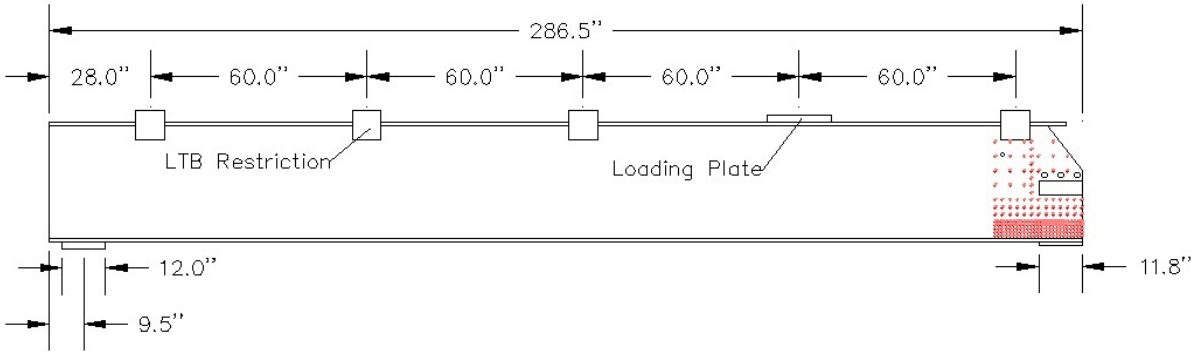

Figure 3.25: Specimen 2 experimental configuration and dimensions.

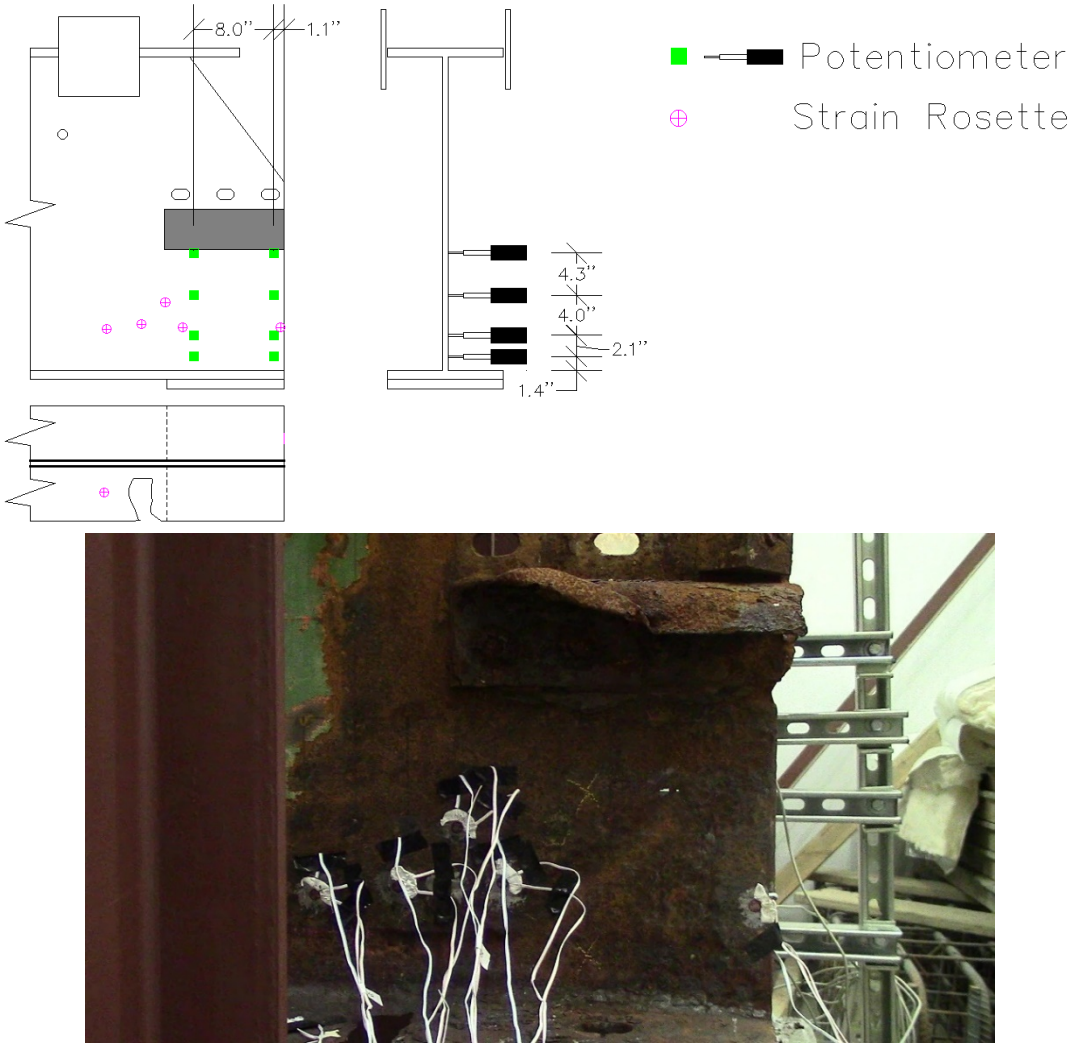

Figure 3.26: Instrumentation configuration at the end of Specimen 2.

3.2.3 Specimen 3

Specimen 3 is a 334.5 in. long 33WF125 with extensive end corrosion. The girder was identified in the Colrain bridge inspection reports as Beam 3 at Span 5 (Fig. 3.27).

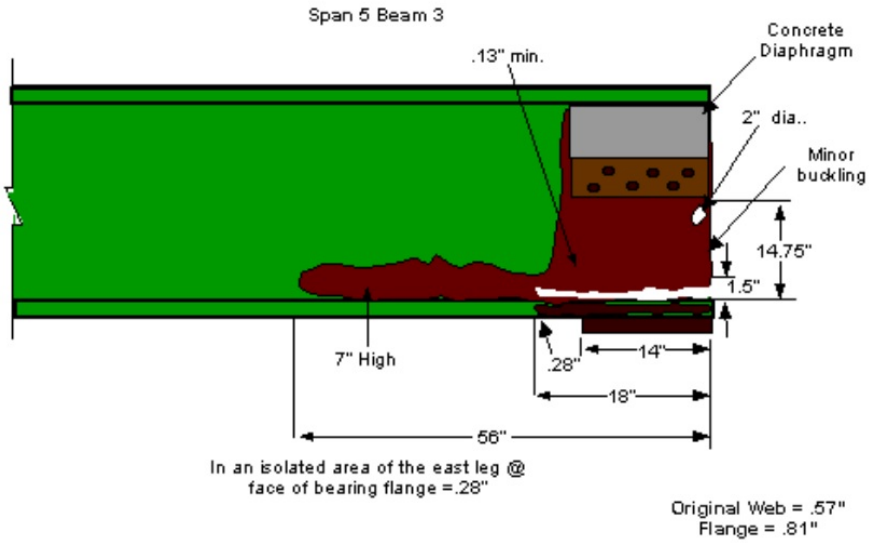

Figure 3.27: Specimen 3 as described in MassDOT inspection report (31).

While the bridge was in service, a concrete diaphragm was located above the support. During the bridge demolition, the concrete was removed, while the steel angle sections remained bolted to both sides of the web (Fig. 3.28). The beam was delivered to UMass testing facilities with the bearing plate still welded to the girder's end. The anchors protruding from the bottom of the bearing had to be sawn off. For this specimen, the condition of the flange over the bearing was worse than that of the two previous beams. The flange was warped at the area of the support. In order to promote a uniform contact loading, grout was used to fill the gap between the flange and the support that at the highest point was 1.75 in. thick.

The most extensive section loss was observed in the lower half of the web (Fig. 3.29). Two holes could also be observed among the corrosion. The first one (18 in. long) was located directly above the flange (Fig. 3.20). The area with the 100% section loss extends 6 in. beyond the end of the bearing. The second hole was located below the steel section angles, similar to Specimen 1.

The extensive material discontinuity above the bottom flange had allowed the web to deflect sideways while it was in service. The maximum initial lateral displacement is equal to 0.78 in. and is observed above the outer edge of the bearing.

Figure 3.28: Side and front view of Specimen 3.

Figure 3.29: Area with 100% section loss above flange.

Similarly to the procedure followed for the first two specimens, the research team coordinated with MassDOT personnel in order to conduct detailed thickness measurements

to create the thickness reduction profile along the corroded end. The data was gathered using a Pocket MIKE Compact Thickness Gauge, manufactured by GE Inspection Technologies. In total, 181 points were measured on the web and 30 points at the bottom flange (Figure 3.30). The illustrated values are 10^{-2} inches. Intact thicknesses are 0.57 in. for the web and 0.805 in. for the flange.

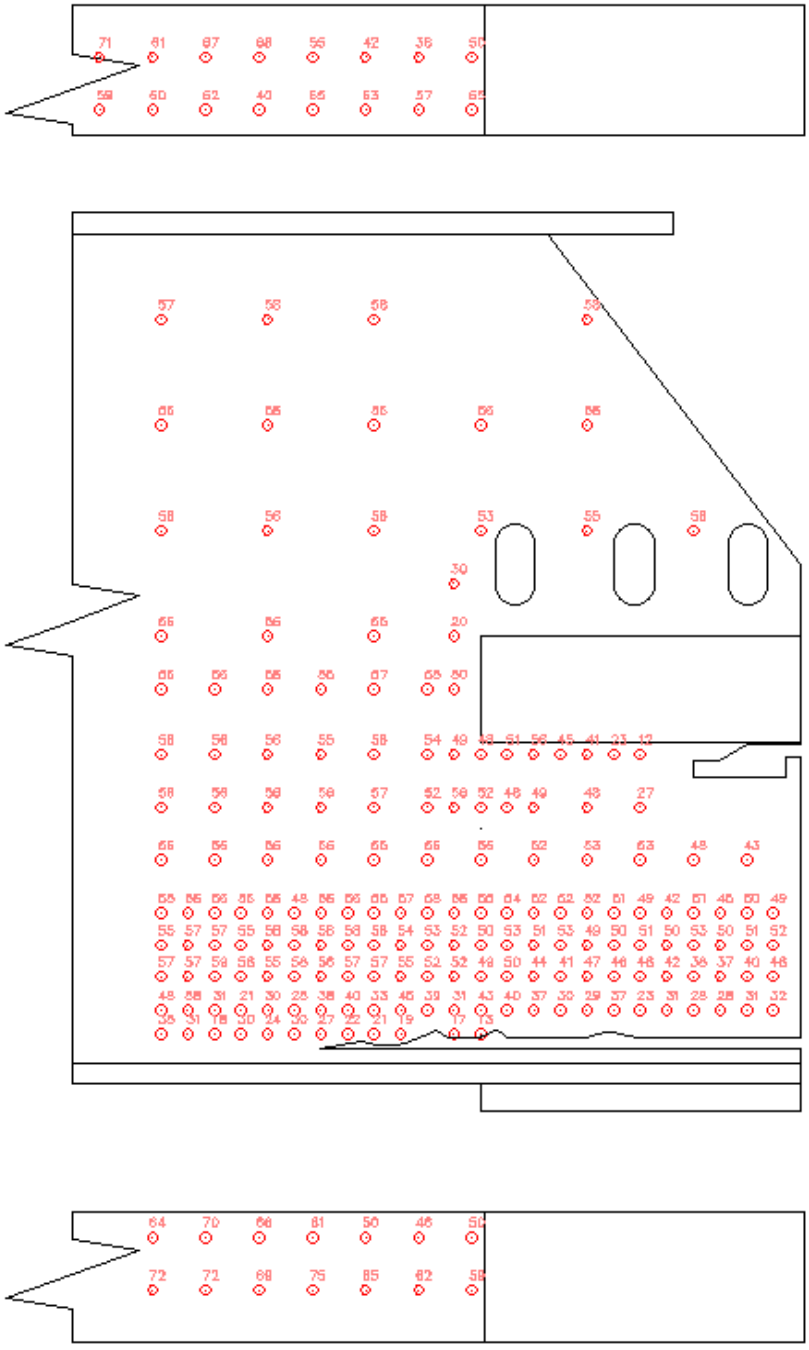

Figure 3.30: Web and flange thickness for Specimen 3.

The exact experimental configuration is illustrated in Fig. 3.31, and the instrumentation configuration in Fig. 3.32.

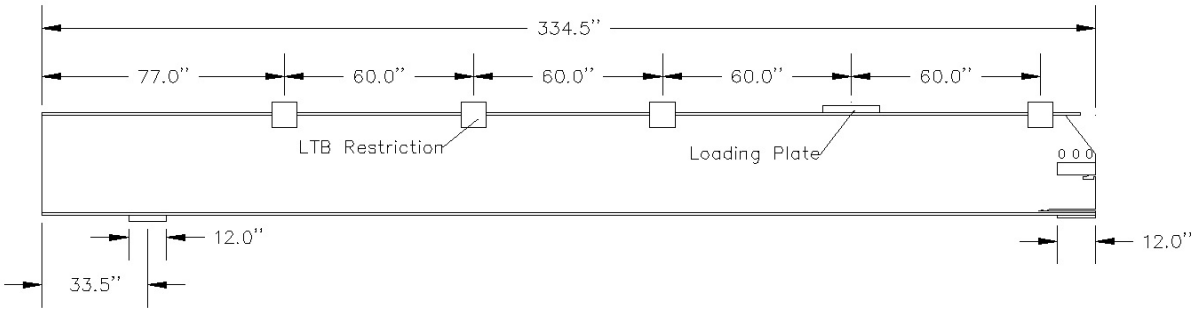

Figure 3.31: Specimen 3 experimental configuration and dimensions.

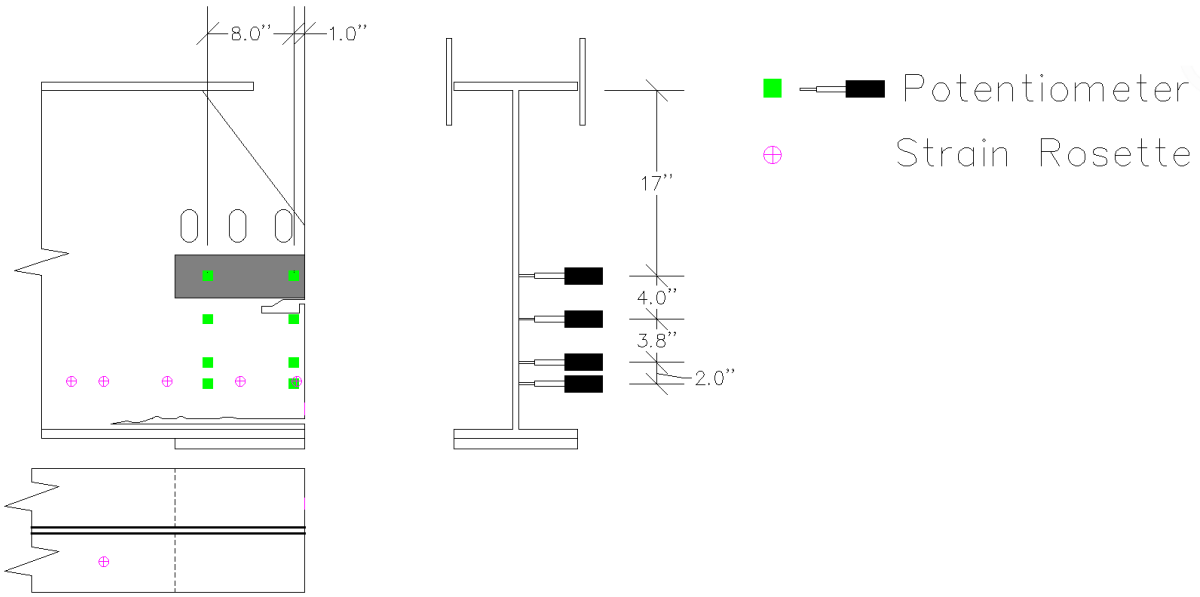

Figure 3.32: Instrumentation configuration for Specimen 3.

3.2.4 Specimen 4

Specimen 4 was the first beam extracted from Charlemont bridge, with length equal to 271.8 inches. According to the available construction drawings, the girder was a 21WF59. However, based on the measurements performed prior to testing, the geometry of the beam section better matched the nominal dimensions of a 21WF73. While the bridge was in service, the end of the beam was fully embedded in concrete, as shown in Fig. 3.33.

Figure 3.33: Bearing geometry of Charlemont bridge beams while in service.

During the bridge demolition, the concrete was removed, revealing three artificial holes in the web. The beam was delivered to UMass testing facilities with the bearing plate still welded to the girder's end. This specimen was the first and only one tested with the beam overhanging the bearing. Compared to the beams extracted from the Colrain bridge, despite the extensive thickness loss, the flange was not warped at the area of the support. The need for grout to ensure uniform contact loading was eliminated.

The most extensive section loss in the web was observed in two different areas above the support. The first distinct area was located parallel to the inner edge of the concrete diaphragm. This topology revealed a likelihood that water consistently flowed from the top of the beam to the bottom flange, following this path. The second area of distinct section loss proceeded across the longitudinal girder axis and vertical to the first section (Fig. 3.34). Probably the deterioration was initiated by the buildup of this runoff on the top face of the bottom flange. This claim is also justified by the extensive material loss at the bottom flange since the remaining thickness was limited to 0.17 in. (intact web thickness equaled 0.575 in.). At the inner edge of the bearing, the width of the flange was reduced at both sides of the web by 1 inch. Except from the bearing area, both flanges had experienced extensive section loss along the whole length.

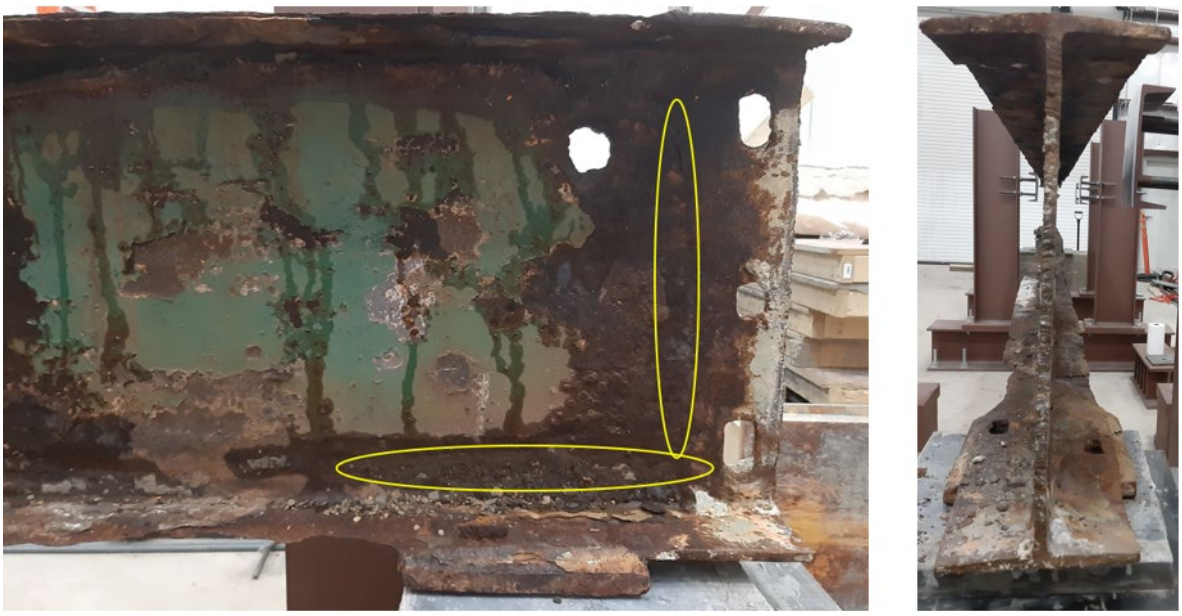

Figure 3.34: Side and front view of Specimen 4; yellow circles illustrate two areas with extensive section loss.

No initial web sideways deflection was observed at the bearing area. However, the specimen was heavily distorted and bent along the transverse axis of the web. The maximum deflection equaled 1.75 in. and was located 7 ft. away from the intact end. This deflection resulted in local buckling of the flange as is illustrated in Fig. 3.35. It is possible this deformation could be attributed to the demolition process.

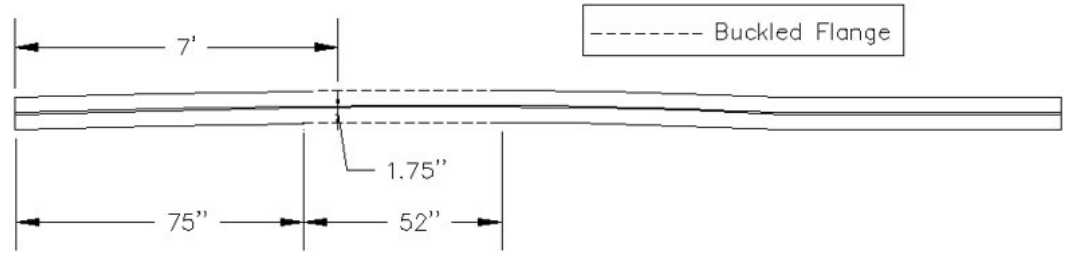

a)

b)

Figure 3.35: Top view of the specimen (a) and side view of the buckled web (b).

Similarly to the procedure followed for the first three specimens, the research team coordinated with MassDOT personnel in order to conduct detailed thickness measurements to create the thickness reduction profile along the corroded end. The data was gathered using a Pocket MIKE Compact Thickness Gauge manufactured by GE Inspection Technologies. In total, 183 points were measured on the web and 6 at the bottom flange (Fig. 3.36). The illustrated values are 10^{-2} inches. Intact thicknesses are 0.455 in. for the web and 0.74 in. for the flange.

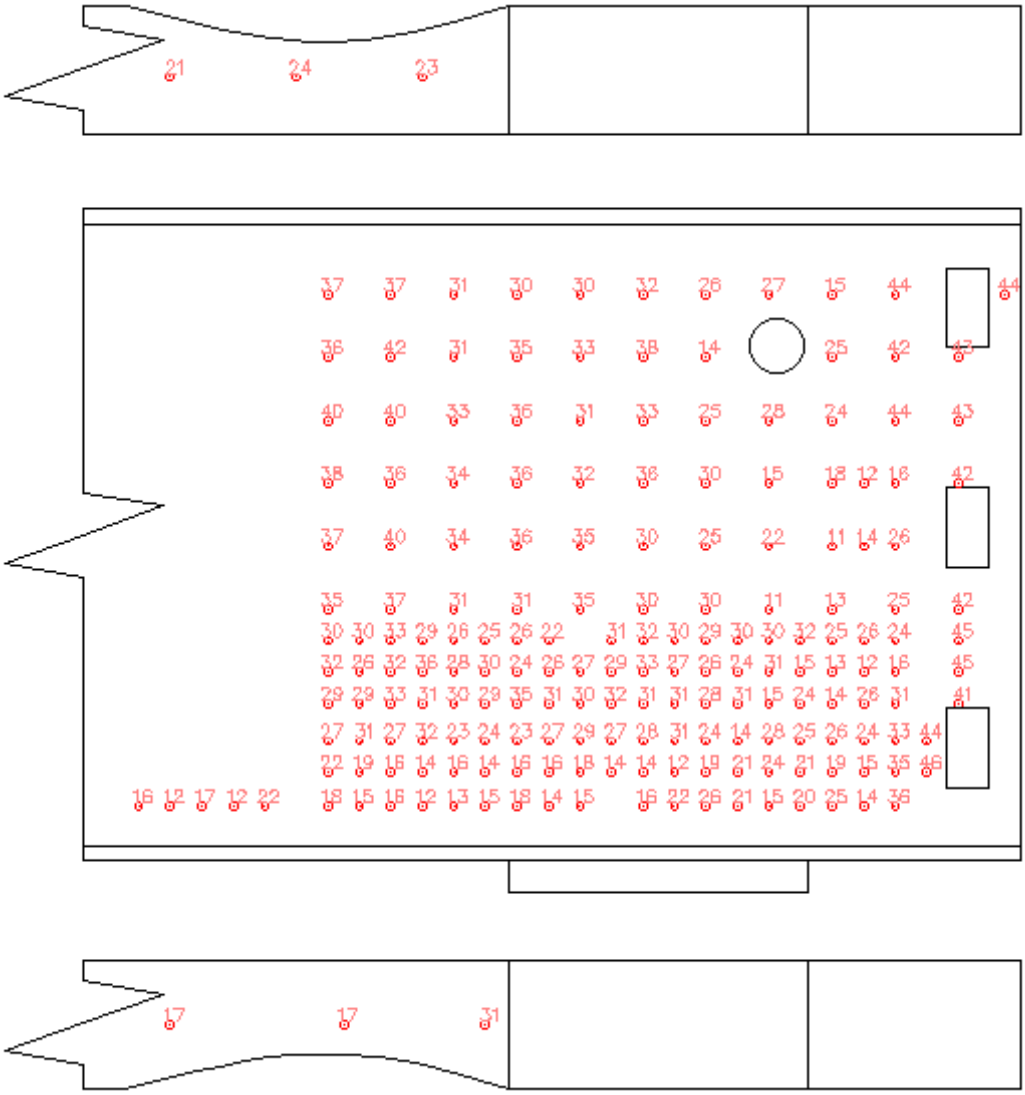

Figure 3.36: Web and flange thicknesses for Specimen 4.

The exact experimental configuration is illustrated in Figure 3.37, and the instrumentation configuration in Figure 3.38.

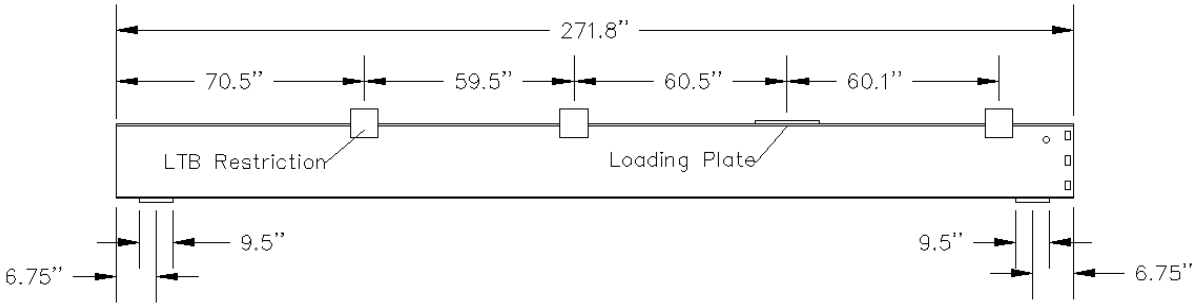

Figure 3.37: Specimen 4 experimental configuration and dimensions.

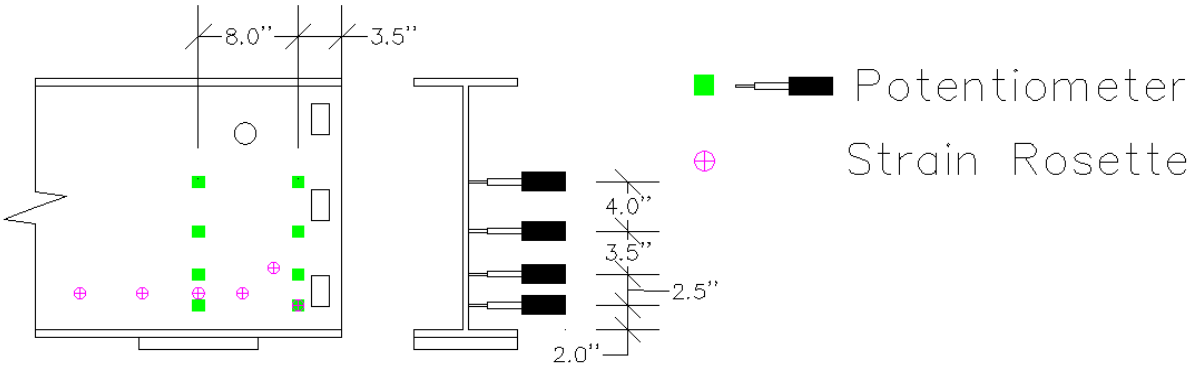

Figure 3.38: Instrumentation configuration for Specimen 4.

3.2.5 Specimen 5

Specimen 5 is a 241.5 in.long 21WF73 and was also retrieved from the Charlemont bridge. Similarly to Specimens 4 and 6, the end of the beam was fully embedded in concrete. At the embedded area, three artificial holes could be observed. The beam was delivered to the UMass testing facilities with the bearing plates removed. At the experimental configuration, the corroded end was resting on a 14 in. long plate initiating from the outer edge of the flange, which had not experienced severe distortion. However, grout was used to maximize the area of contact.

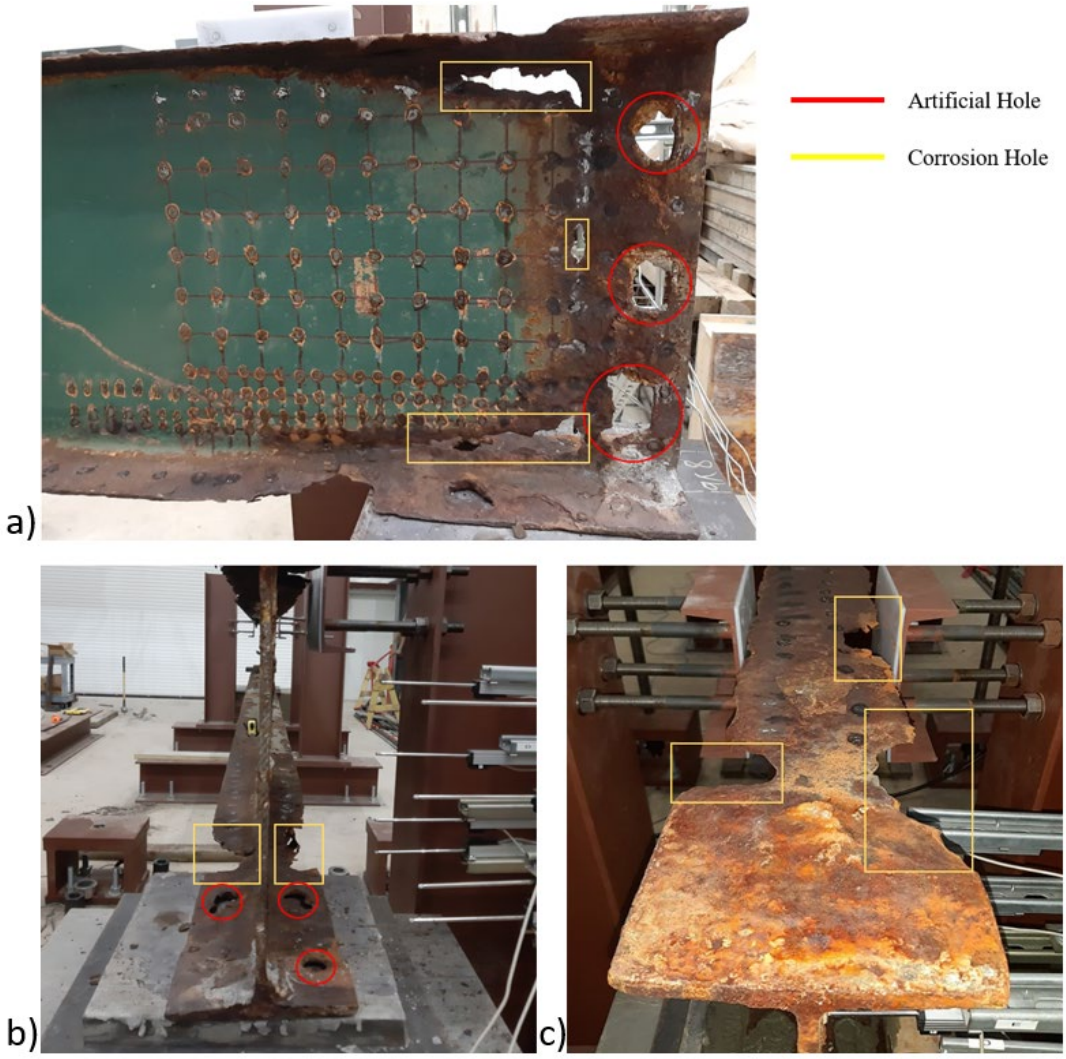

Figure 3.39: Artificial and corrosion holes of Specimen 5, photos (a), (b), and (c).

Regarding the corrosion topology, extensive section loss was observed at both web and flanges. Focusing at the support area, as with Specimen 4, an area with distinct thickness loss was located parallel to the inner edge of the concrete diaphragm. This topology revealed a likelihood that water consistently flowed from the top of the beam to the bottom flange, following this path. Three holes were spotted in the bounds of the previously described area. The first one was located mid-height of the web, while the last two were close to the top and

bottom flange, respectively. Both flanges had experienced extensive section loss along the whole length of the specimen. The phenomenon for both flanges was more intense close to the support area, where the flange widths trended to zero at both sides of the web.

Similarly to the procedure followed so far, detailed thickness measurements were performed. The data was gathered using a Pocket MIKE Compact Thickness Gauge manufactured by GE Inspection Technologies (Fig. 3.40); 178 measurements were taken at the web, 19 at the bottom flange, and 20 at the top flange. The illustrated values are 10^{-2} inches. Intact thicknesses are 0.455 in. for the web and 0.74 in. for the flange.

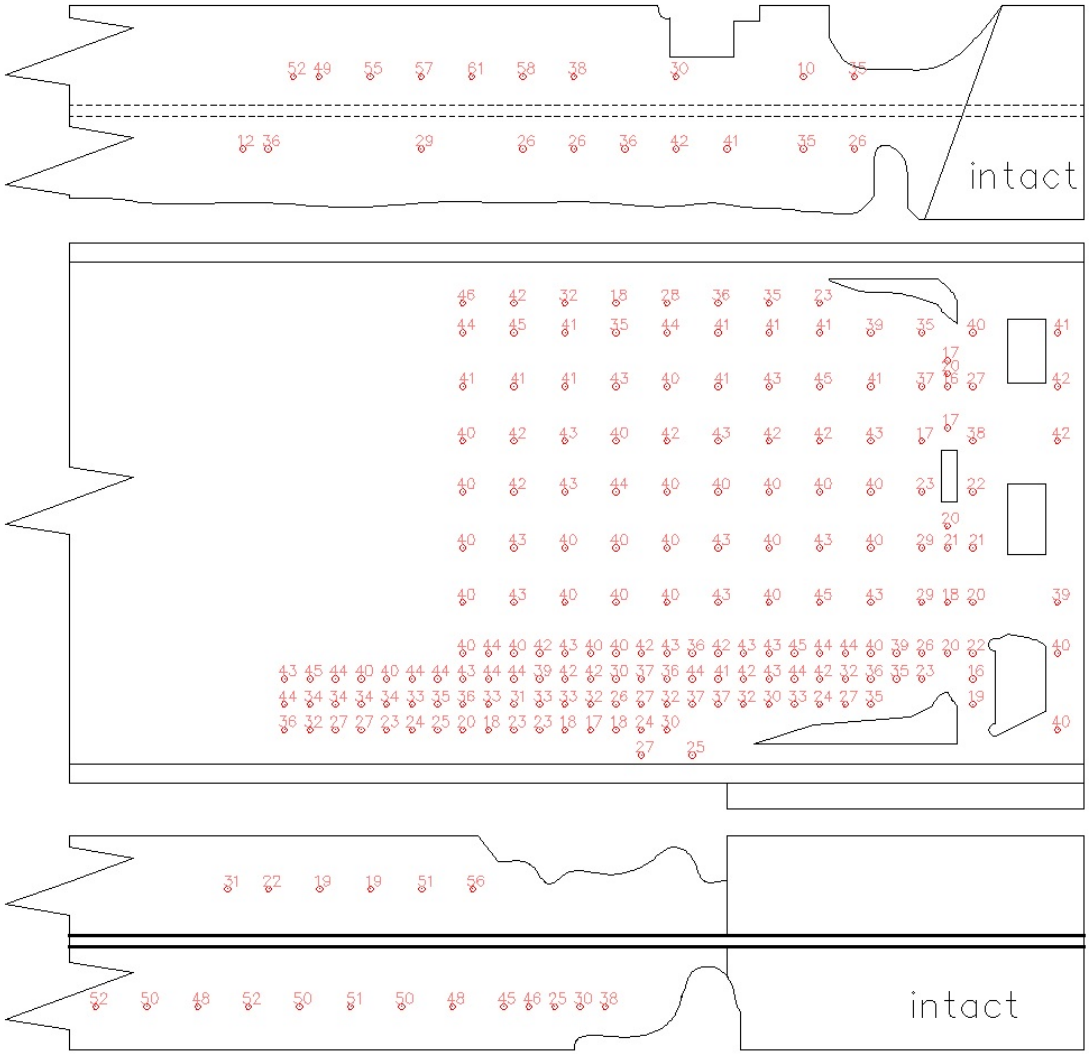

Figure 3.40: Web and flange thicknesses for Specimen 5.

The experimental configuration and the loading and boundary conditions are reported in Fig 3.41.

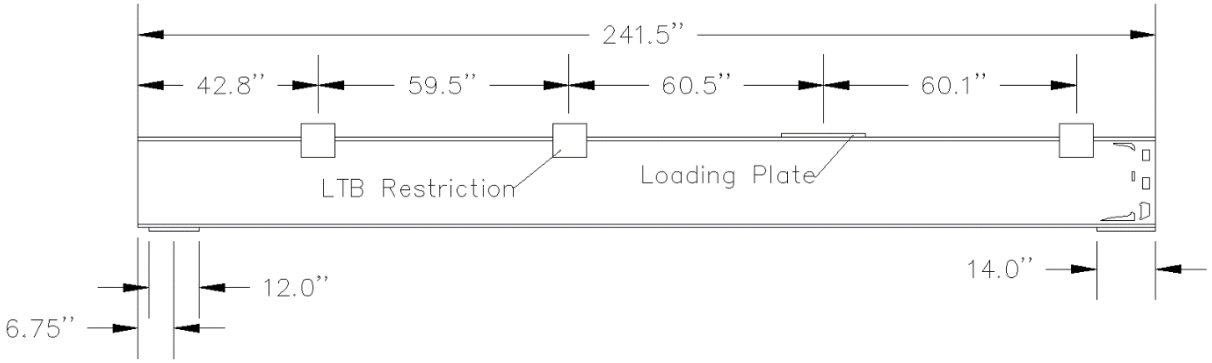

Figure 3.41: Specimen 5 experimental configuration and dimensions.

The first potentiometer column was placed close to the inner bearing edge, while the second one between the adjacent holes close to beam's end.

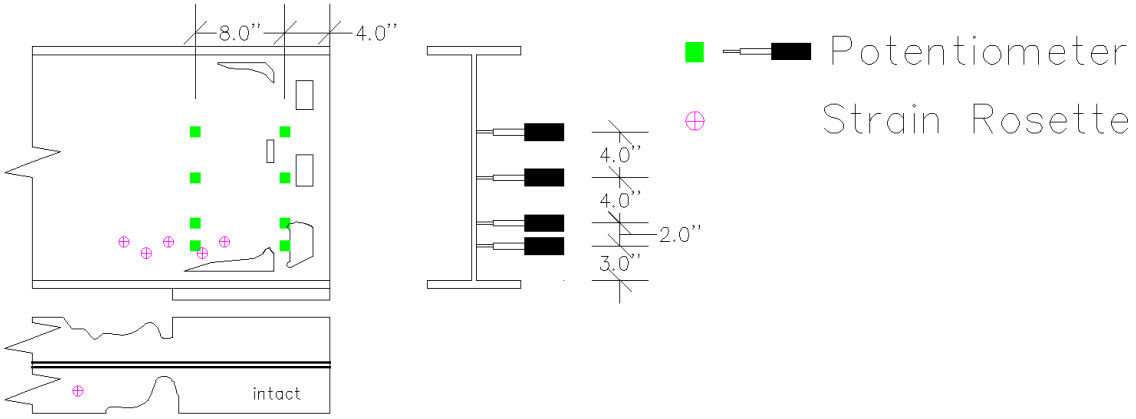

Figure 3.42: Instrumentation of Specimen 5.

3.2.6 Specimen 6

Specimen 6 is a 241 in. long 21WF59, and similarly to Specimen 5, the bearing plates had been removed during the demolition. For the experimental process, the corroded end was supported by a 14 in. long plate with 1.2 in. overhang length. The bottom flange, at the support area, had not experienced distortion; thus, grout was not used to ensure the contact between the two surfaces.

The corrosion topology was significantly biased by the in-service configuration, with one hole shaped as an angle section covering the whole depth. In detail, the hole expands 21 in. close to the bottom flange, 18 in. along the depth, and 16 in. close to the top flange. The hole configuration let part of the web loose along three edges and sideways deflected up to 0.4 in., while the outer web part, which was concrete embedded during the in-service period, remained unaffected. The concrete diaphragm removal also revealed three artificial holes along the depth (Fig. 3.43). In the figure, the yellow line illustrates the corrosion hole and the red line the artificial holes. The initial web lateral deflection is equal to 0.4 inch.

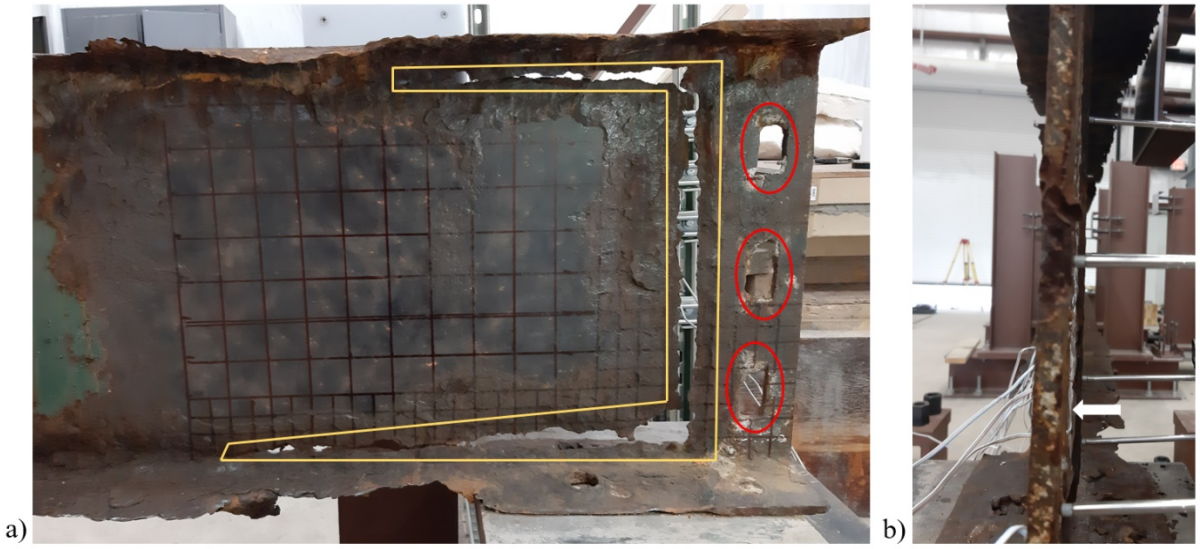

Figure 3.43: Side (a) and cross section (b) views of Specimen 5.

Regarding the section loss profile, similarly to all specimens extracted from Charlemont bridge, both flanges had experienced extensive section loss along the whole length. At the web, the section loss was limited only close to the hole edges (Fig 3.44). Once again, detailed thickness measurements were performed, using a Pocket MIKE Compact Thickness Gauge manufactured by GE Inspection Technologies. 165 measurements were taken at the web, 9 at the bottom flange, and 2 at the top flange. The illustrated values are 10^{-2} inches. Intact thicknesses are 0.39 in. for the web and 0.575 in. for the flange.

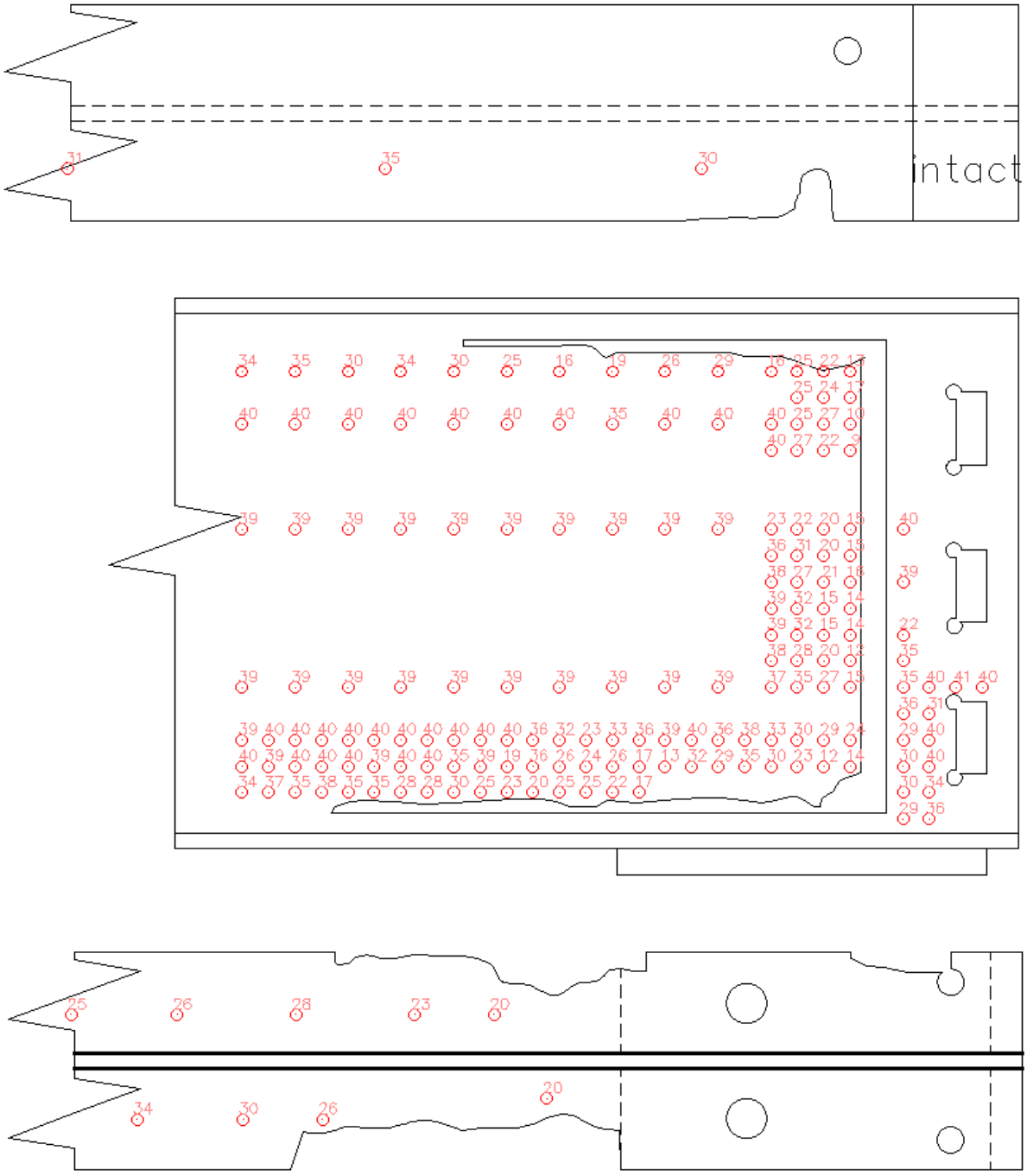

Figure 3.44: Web and flange thicknesses for Specimen 5.

The geometry and the loading and boundary configuration are reported in Fig. 3.45. The C-channels, placed at the top of the LTB restriction, expanded 8 in. each along the top flange, while the load was transferred to the beam through a 20 in. long plate.

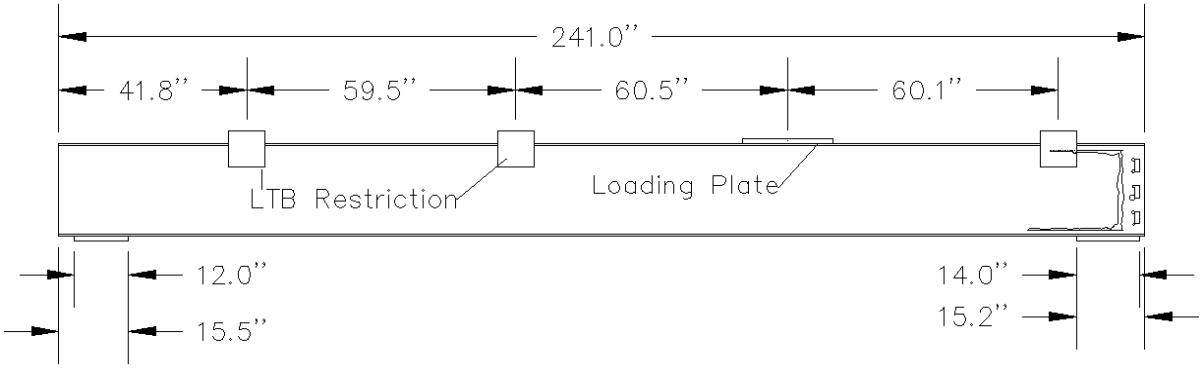

Figure 3.45: Specimen 6 experimental configuration and dimensions.

The first potentiometer column was placed at the stiff outer part of the web that used to be embedded in concrete while the Charlemont bridge was in service, while the second one was close to the inner bearing edge.

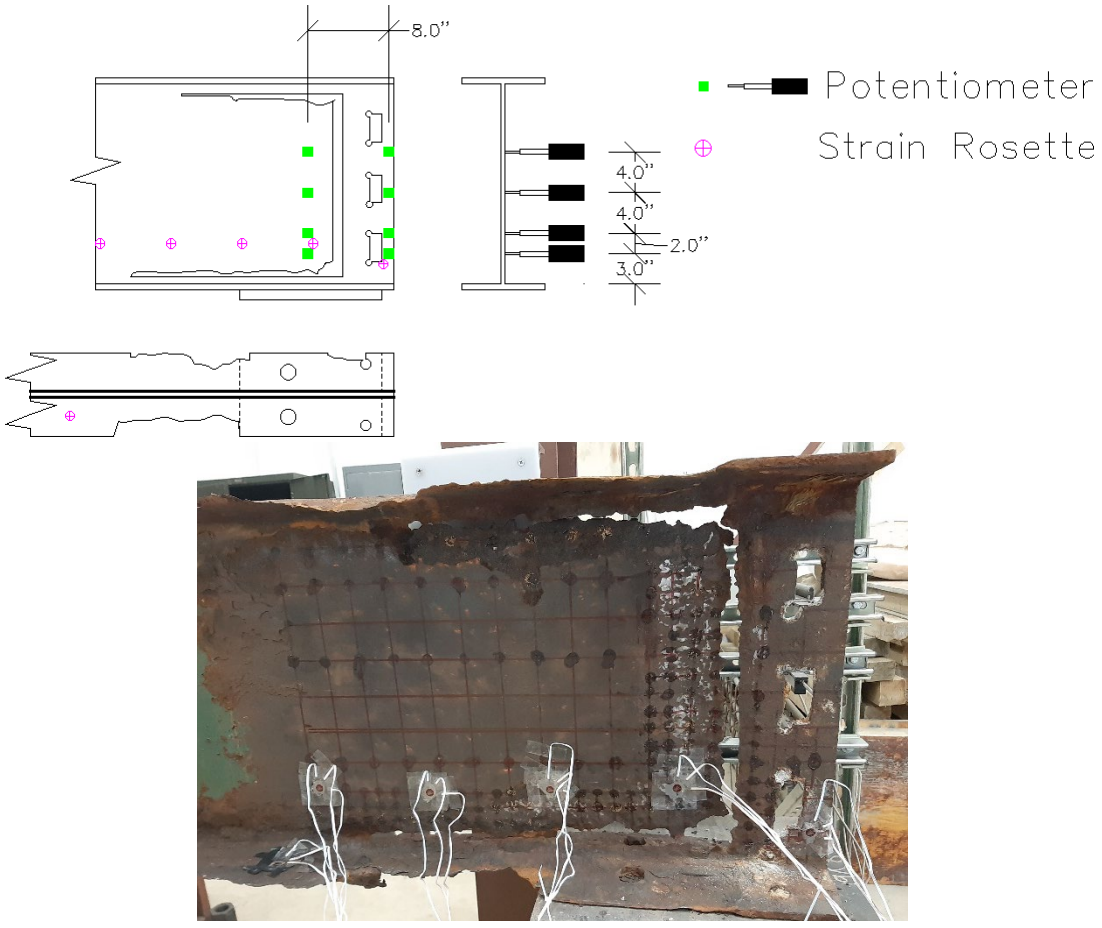

Figure 3.46: Instrumentation configuration of Specimen 6.

3.3 Material Properties

One very important aspect for the calibration of the computational modeling is the material properties. To determine the material properties of the steel girders, four 22 in. x 5 in. steel plates were cut out from Specimen 1. The plates were cut out at several different locations in order to check variability of the material properties throughout the specimen. The selected locations included a top flange, a bottom flange, and two different locations from the web. The number of coupon specimens, along with the preceding specifications, were derived from ASTM Standard E8 *(33)*. According to Section 6.2, for specimens with thickness less than 1.5 in., they shall be cut from the center of the parent material. This was satisfied by having the top flange coupon be cut at the center of the girder. The webs were then cut from the middle of the web at the quarter points of the girder. One web plate was cut with the 22 in. side in the longitudinal direction, whereas the second specimen was cut with the 22 in. side going vertically down the web. This was done to again further check variability; since steel is a homogenous material, the axis direction of the test coupon should be irrelevant. The final plate was cut from the bottom flange on the undamaged end of the girder. This was done to ensure nominal thickness in the flange. For a visual representation of the location of the coupons, see Fig. 3.47.

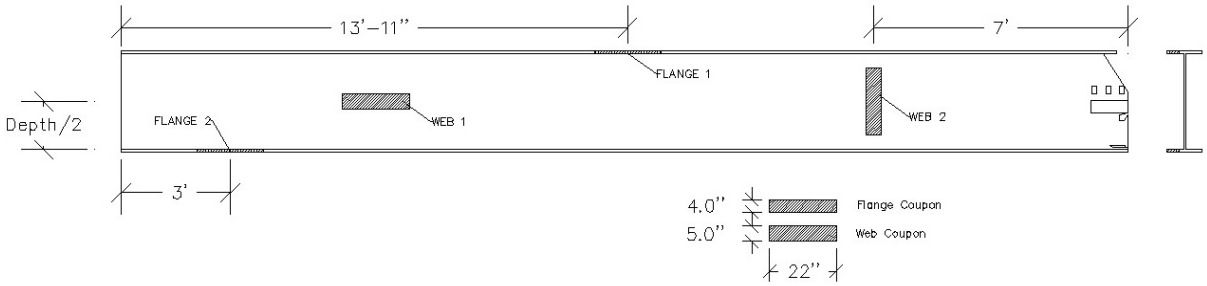

Figure 3.47: Location and nomenclature of the extracted coupons.

Using Section 6.2 from ASTM Standard E8 *(33)* a plate-type specimen was selected for an ideal measurement of the properties. This required a minimum thickness of 0.188 in. for a specimen. The web and flange of the tested girder had thickness values of 0.58 in. and 0.88 in., respectively. The plate-type specimen test calls for a *dogbone* shape to be cut. A dogbone is a steel coupon with a reduced central section to ensure that yielding and failure occur away from the grips. The specifications for the dogbone can be found in Fig. 3.48.

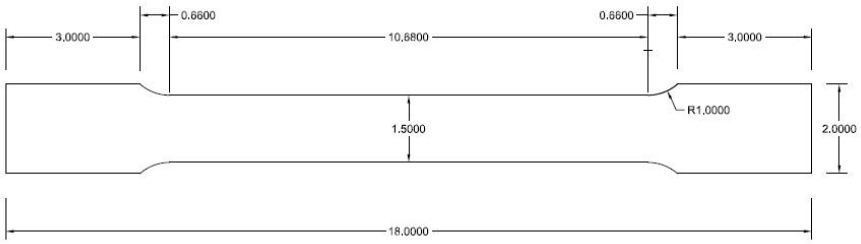

Figure 3.48: Specifications of dogbone specimen in inches.

4.0 Analytical Work Methodology

The goal of the methodology was to develop a high-fidelity numerical model capable of predicting the capacity of beam ends. Combining the corrosion patterns with numerical modeling, an extensive parametric analysis was performed and is described in this chapter.

4.1 Computational Model Validation

The presented numerical model was being developed simultaneously with the evolution of the experimental work. By comparison of the numerical and experimental output obtained by the first two specimens, the model was considered to fulfill the requirements for accuracy and efficiency, and the need to model the remaining beams was not followed. In this section, the modeling assumptions regarding the mechanical problem formulation in terms of its geometry, boundary, and loading conditions, material properties, and geometric imperfections are described in detail. Particular attention is paid to the procedure followed to replicate the initial beam imperfection and to represent the natural nonuniform thickness reduction profile.

4.1.1 Mechanical Model

Beam geometry

The first two specimens are simulated, and their geometry and defining features were explicitly described in Chapter 3.0.

Section loss

Except for the areas with 100% thickness loss, it is necessary to define the thickness reduction profile along the corroded end. Detailed thickness measurements were obtained. The data was gathered using a Pocket MIKE Compact Thickness Gauge manufactured by GE Inspection Technologies. The exact measurements performed at each specimen were presented in detail in Chapter 3.0. To summarize, the thickness was recorded at both web and flange. For ease of reference, a grid was drawn, covering the full depth of the web and 2 ft. along the length of the beam. Moving from top to bottom, the grid increased in resolution (from 16 sq. in. to 1 sq. in.), as visual inspection indicated the section loss to be most severe toward the bottom flange.

In order to replicate the thickness reduction distribution along the corroded end, points with common or similar thickness loss were grouped together, forming areas with uniform thickness reduction. The simulated section loss profile is presented in Figs. 4.1 and 4.2 for Specimens 1 and 2, respectively. For Specimen 1, a grid was drawn covering a full depth and 2 ft. of length (4.1a); 159 measurements were performed (4.1b); and points with common or similar thickness loss were grouped together, forming areas with uniform thickness reduction (4.1c). The intact web thickness is 0.57 in. For Specimen 2, 183 measurements were performed (4.2b); and points with common or similar thickness loss were grouped together, forming areas with uniform thickness reduction (4.2c). The intact web thickness is 0.58 in.

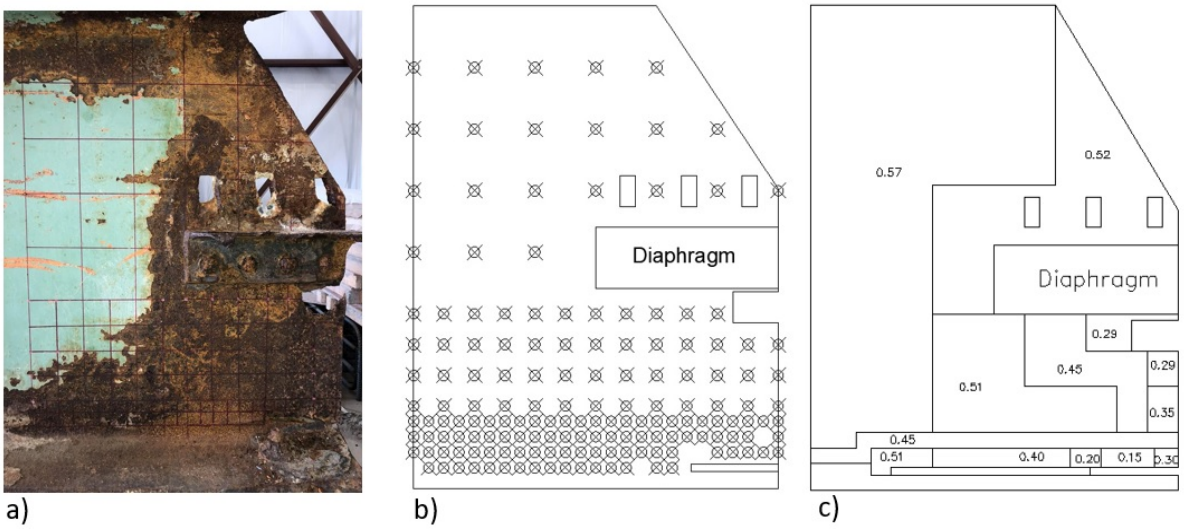

Figure 4.1a-c: Definition of material loss at the corroded end of Specimen 1.

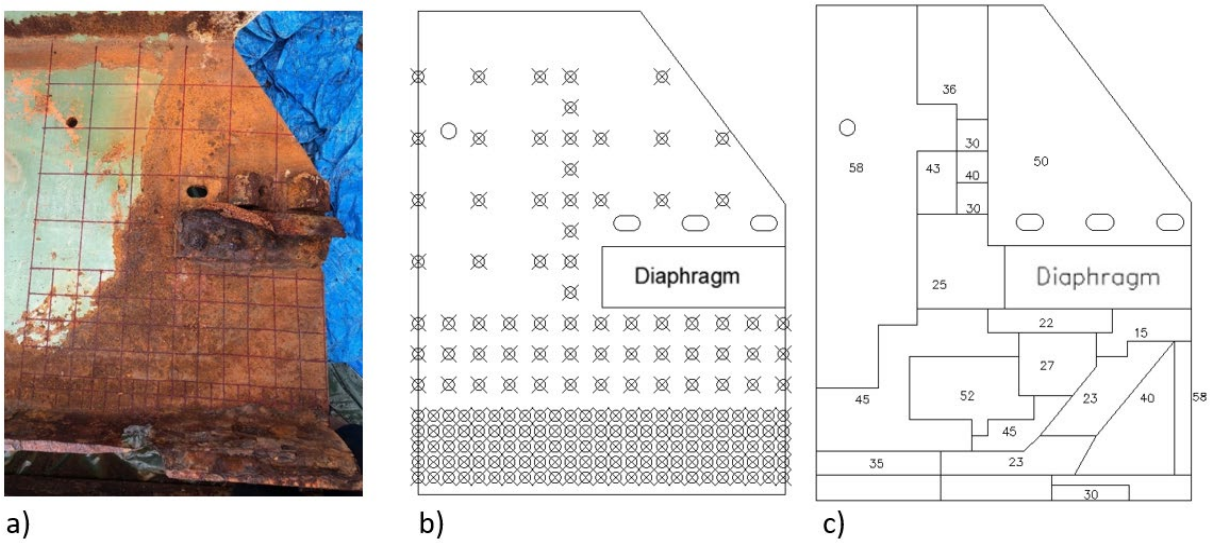

Figure 4.2a-c: Definition of material loss at corroded end of Specimen 2.

Material properties

The two modeled specimens were obtained from the Colrain bridge. While the viaduct was in service, both specimens were part of a unique span, constructed at the same period of time. Thus, material properties from one beam were considered representative for all the beams belonging to the same group. Based on this assumption, common material properties were used for both modeled specimens. Four plates were cut out from Specimen 1, and a dogbone shape coupon was extracted and tested from each plate.

The stress-strain curves obtained by the tensile tests are presented in Section 6.7. Fig. 4.3 presents the simplified backbone curves formulated by seven linear branches each, which were imported in the FEM software. Web stress-strain relationship was formed according to "Web 1" coupon results. For top and bottom flanges, the team used data extracted from coupons "Flange 1" and "Flange 2," respectively. Experiments revealed discrepancy in yield

and ultimate stress of the steel at web and flange, which can be attributed to the manufacturing procedures at that time. However, the curves for the top and bottom flange are similar, so the results were considered valid. The material was modeled as isotropic with Young's Modulus equal to 29,000 ksi and Poisson's ratio equal to 0.27.

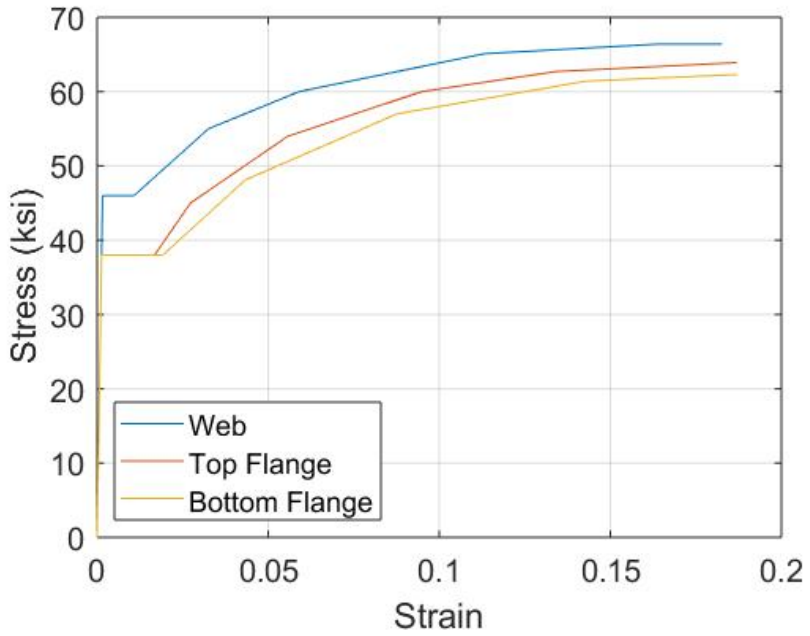

Figure 4.3: Stress strain curves of tested coupon as imported in the finite element software.

Boundary and loading conditions

Both boundary and loading conditions simulate the exact experimental configuration. The load is applied as uniform pressure in the location of the loading plate (Fig. 4.4). The loading plate covers the full flange width, and its length equals 18 inches. The out-of-plane displacement is not allowed at the locations of the LTB restrictions. The bottom flange of the girder is resting on two steel bearing plates, which are considered fixed.

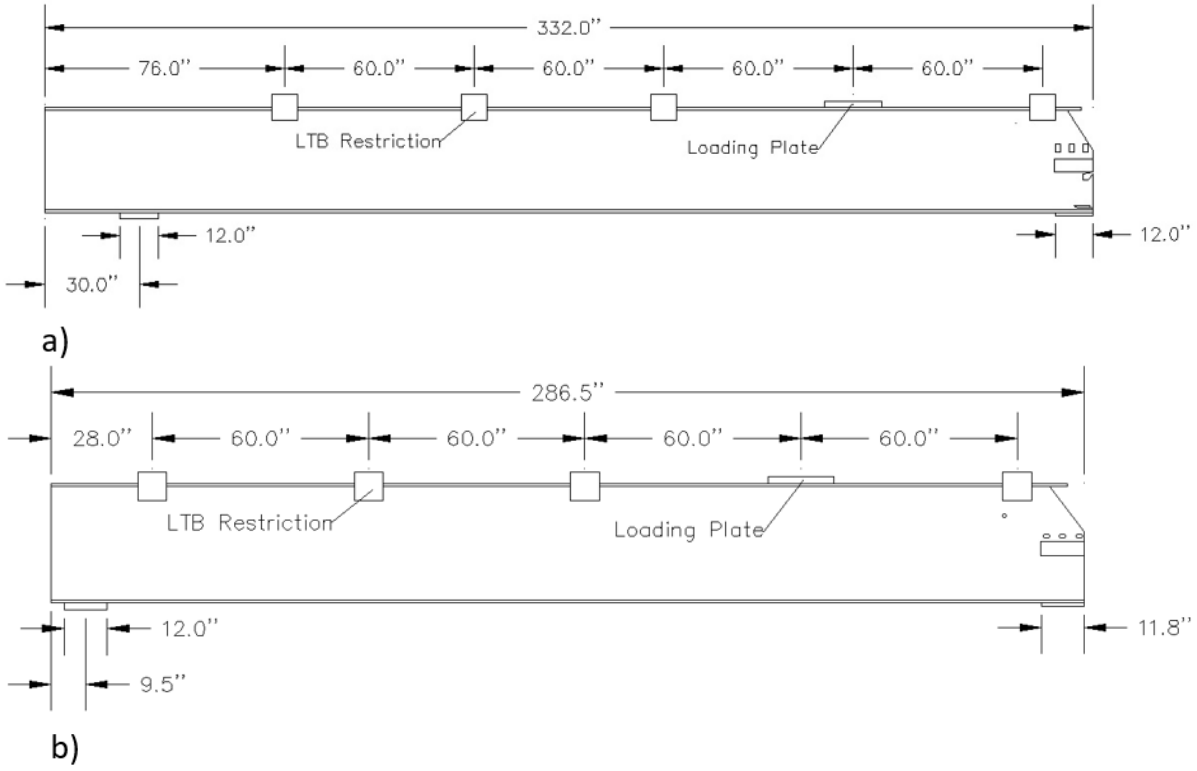

Figure 4.4: Exact experimental configuration and dimensions for (a) Specimen 1 and (b) Specimen 2

Geometric imperfection

Having described the exact dimensions, thickness reduction, material properties, boundary, and loading conditions, the last aspect of the mechanical problem formulation is the applied geometric imperfection.

For any plate or shell buckling problem, it is well known that the structure will suffer from geometric imperfections. Overlooking imperfections can be catastrophic when predicting the capacity of a structure. For the mechanical problem of the deteriorated steel beam ends, initial geometric imperfections are needed for the proper formulation of the problem. In many similar problems, scaled eigenmode shapes are commonly used as the initial geometric shapes of the shell or plate.

For intact beams, initial imperfections obtained during the rolled steel manufacturing process are negligible. However, corrosion does not symmetrically reduce the thickness along web sides, resulting in geometric nonlinearities that are able to trigger an instability. Thus, extreme thickness reduction usually results in instability phenomena, making deteriorated webs slender buckling-prone members.

Imperfections were introduced in the model, based on the eigenmodes' shapes. Each model was initially solved using an eigenvalue buckling analysis algorithm. Then, the eigenmode that better matched the web shape of the actual beam was introduced as an initial geometric

imperfection for the quasi-static analysis, scaled to the measured maximum lateral displacement of the web.

For Specimen 1, the part of the web that extended beyond the dashed line (Fig. 4.5a) was free at the three edges. The web was not supported at the top due to the skewed cut, and at the bottom a hole was located parallel to the flange. The maximum initial lateral web displacement reached 0.57 inches. However, the lateral displacement profile was characterized by a uniform displacement along the web's depth. This behavior can be attributed to lack of restrictions, as it was previously described. On the other hand, the chosen eigenmode did not manage to represent satisfactorily the presented lateral displacement profile. It was characterized by a half buckling wave formulated along the whole depth, contrary to the actual uniform displacement (the eigenmode in Fig. 4.5c is scaled to 1 in. for illustrative purposes).

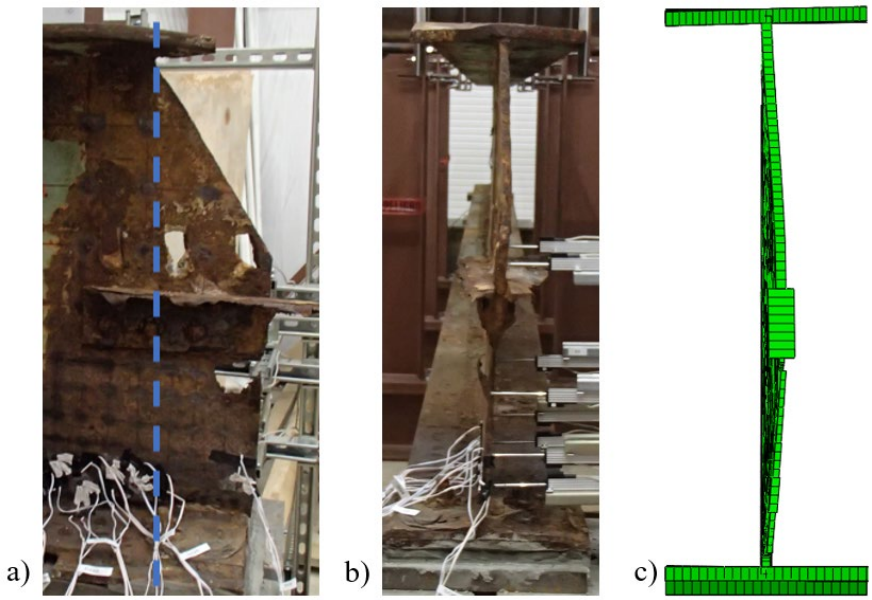

Figure 4.5: Lateral displacement of Specimen 1, from (a) side view and (b) front view; (c) imported eigenmode as imperfection to the FEM.

For Specimen 2, the maximum initial web lateral displacement was observed at mid-height and equaled 1.58 in. (Figure 4.6a). In contrast to Specimen 1, the selected eigenmode managed to represent accurately the initial out-of-plane web displacement, as shown in Fig. 4.6b. In both Figs. 4.5c and 4.6b, the increased thickness area at mid-height web represented the combined thickness of the web and the remaining steel section angles.

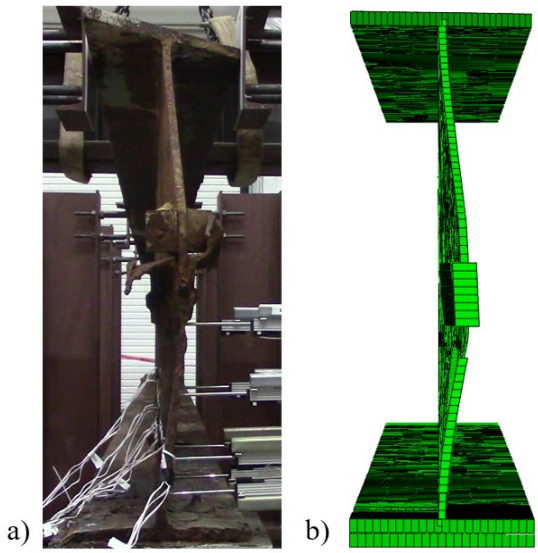

Figure 4.6: (a) Front view of Specimen 2; and (b) initial geometric imperfection as was imported to the FEM.

4.1.2 Finite Element Procedures

Quasi-static analysis was performed to simulate the applied load of the experimental configuration. This type of analysis is terminated once instability phenomena occur; however, it is preferred, as post buckling is currently out of the scope of this study. The simulations of the mechanical problem described in the previous section were performed using the software Abaqus *(34),* a general-purpose finite element program that engages powerful nonlinear analysis routines that are necessary for the failure/instability analysis of the corroded beam ends.

The first step for a finite element model is to accurately describe the mechanical model in terms of its geometry. This includes the type and size of the beam, its length as well as the topology of the corroded area. All these parameters were described in the previous section. After the tested geometries were imported, the beams had to be simulated using the appropriate element types.

The Abaqus library contains a wide range of beam, plate, shell, and solid structural elements. Beam elements are one-dimensional line elements, in plane or three-dimensional space. The one-dimensional simulation is based on slenderness assumption, as well as small cross-section deformation compared to dimension along the beam axis. Plate or shell elements approximate a three-dimensional continuous body with a surface, for cases where the thickness is significantly smaller than the other two dimensions. Thickness is assigned as a parameter to an element. Finally, solid elements are defined in the three-dimensional space, and thickness is described from the nodal geometry.

For the presented research, the beam element was considered insufficient for simulating the deterioration at the end of the beam, as it was inadequate to capture stability failures across the beam's depth or to provide an extensive view of the girder's stress-strain state. On the other hand, the loading and boundary conditions were not expected to cause deformation and

stress development normal to the thickness; thus, solid elements were considered too computationally costly and without significant advantages for this problem compared to shell elements.

Finite Element Model

The girder was simulated with a mid-surface shell model. Both the web and flange thicknesses were assigned to the corresponding shell elements. The remaining thickness was simulated by assigning a uniform reduced thickness at the elements located in the deteriorated area. Holes were simulated by removing elements.

The interaction between the bottom flange and the bearing plate was simulated with a stiff but *softened contact*. The contact interaction was defined using a linear contact pressure-overclosure relationship. The contact algorithm in Abaqus does not take into account material, section, or other properties to automatically calculate the contact pressure-overclosure, but the user needs to define the slope of the linear relationship, "k" (Fig. 4.7a). The "k" value was defined using the experimental data (Fig. 4.7b).

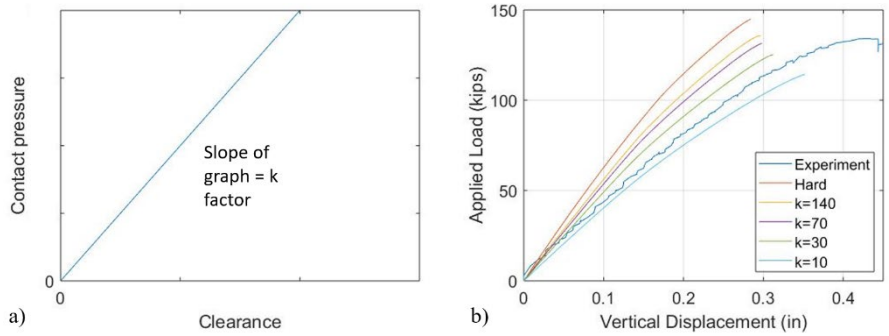

Figure 4.7: (a) For softened contact, the pressure-overclosure relationship is defined by assigning value to k factor; (b) comparison between numerical and experimental results for variety of k factors.

Furthermore, a *hard contact* constraint was used for the normal contact behavior between web and flange, in the case of hole existence. This formulation eliminates the penetration of the slave nodes (web) into the master one (flange), Fig. 4.8.

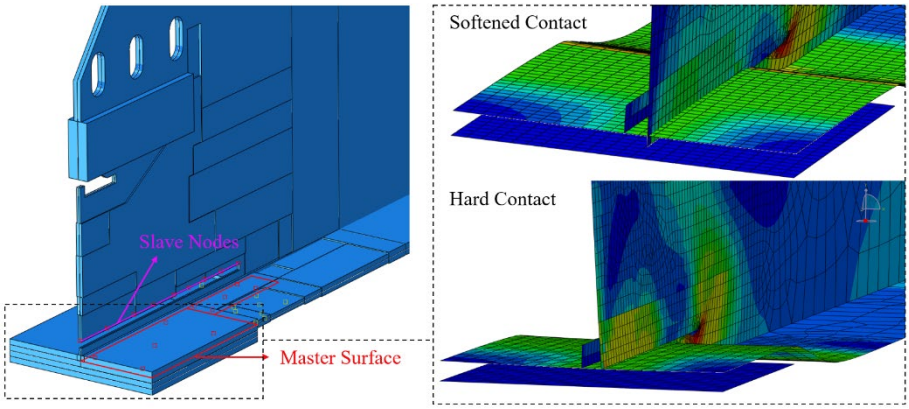

Figure 4.8: Model of interaction between web nodes and flange surface.

Except for contact properties defined in the normal direction between the bottom flange and the bearing plate, friction was also defined to simulate the interaction between the bottom flange and the bearing plate in the tangential direction. In order to define a correct friction coefficient value, a sensitivity analysis was performed. The analysis was consecutively performed for friction coefficients in the range of {0.5, 0.55, 0.6, 0.65, 0.7, 0.75, 0.8, 0.85, 0.9}. The beam capacity seemed to be only slightly affected by the contact coefficient variation. The maximum divergence among the results was 1.2%. A contact coefficient equal to 0.74 was selected for the rest of the work.

Computational time was an important aspect of this research, because thousands of analyses would be performed. To limit the computational time while ensuring the accuracy of the results and the ability of the model to capture all failure modes, a mesh convergence study was performed. At midspan, equal-sized S4R elements were used, and the element size was 2 inches. At the beam ends, where stress concentration and the failure were expected to occur, a denser mesh area was defined. This area covered the full height of the web, and its length exceeded the corrosion length by 5 inches. For this area, the element size was 0.5 inch.

Contact interaction can potentially be sensitive also to the load increment used in a quasi-static analysis. In order to validate analysis against this kind of sensitivity, an increment convergence was also performed. In conclusion, analyses were performed using the following loading-increment sizes: Initial 0.001, Minimum $1x10^{-15}$, and Maximum 0.01.

4.2 Parametric Analysis Setup

The researchers aimed to conduct computational parametric analyses to investigate the capacity and the collapse mechanism of unstiffened corroded girder ends. Different combinations of beams, corrosion topologies, and loading conditions were used to develop an extensive series of computational models, which in turn were analyzed to provide the failure mode of the deteriorated beam ends, along with the failure load.

4.2.1 Corrosion Scenarios

During the first part of this research project, the most common beam end corrosion topologies were identified and quantified. Initially, based on inspection reports of bridges that had experienced this phenomenon, six general corrosion cases were created. A total of 808 unique deteriorated beams ends were accurately described, making use of these preliminary defined patterns. An extensive statistical analysis of these records was conducted, and the final most common corrosion scenarios were quantified (see Sections 1 and 5). The exact metrics of the analyzed scenarios, including a hole pattern, are presented in Table 4.1 and the corresponding nomenclature in Fig. 4.9. The rectangular corrosion scenario was chosen for two reasons. First, it was the most common deterioration topology (Fig. 5.1). Second, according to the final corrosion shapes presented in Section 5, all other scenarios were subsets of the extreme geometrical bounds of the analyzed rectangular scenarios. Parametric analysis was initiated to study the effect of corrosion length and height type to capacity, under the assumption of uniform thickness reduction along the corroded area. The advantage of this assumption is two-fold. First, it follows the current procedures for strength evaluation of corroded girders. Second, it correlates to the usually low-density thickness measurements performed by state inspection engineers.

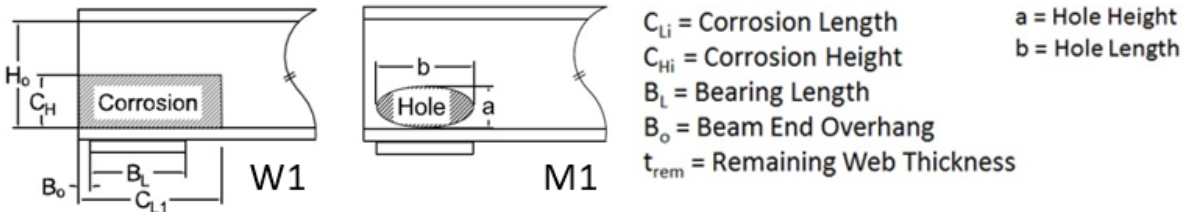

Figure 4.9: Shape and location of the examined deterioration topologies.

Table 4.1: The metrics of the examined scenarios; nomenclature is given in Fig. 4.9.

	Web						
No	Patt.	C_{H1}	C_{H2}	C_{H3}	C_{L1}	C_{L2}	t_{loss}/t_{web}
1	W1	(0.0.3]	na	na	(0,1.5]	na	[0.2, 0.8]
2	W1	1	na	na	(0,1.5]	na	[0.2,0.8]
3	W1	1	na	na	(0,0.5]	na	[0.2,0.8]
	Hole extreme scenarios						
	Patt.	a (Ho)	B (B_L)	Web case			
6	M1	(0,0.15]	(0,2]	W1			

4.2.2 Beam Geometries

Having defined the corrosion scenarios, the associated beam types needed to be identified and correlated to the different scenarios. This task was achieved by using the MATLAB script that was created during the first part of this project. In this way, it was possible to identify the correlation between corrosion patterns and beam types (Tables 4.2 and 4.3). This approach allowed the team to simulate beam geometries and corrosion scenarios that MassDOT inspection engineers found in the field. Parametric analysis was initiated to study the effect of beam type and length on the residual capacity of corroded ends. In this

framework, a variety of different corrosion scenarios were projected on 36WF150 and 30WF108 girders.

Table 4.2: Correlation between corrosion scenarios W1 to W3 and beam types.

W1	# of occurrences	W2	# of occurrences	W3	# of occurrences
36WF150	32	36WF135	9	33WF118	23
36WF230	26	27WF94	5	36WF135	21
30WF108	25	27WF102	3	36WF160	15
36WF160	24	33WF118	3	18W114	11
33W141	22	21WF59	3	30WF124	11
36WF135	21	24WF100	3	36WF170	11
33WF118	20	27WF114	2	18W96	9
30WF99	16	33W130	2	36WF150	9

Table 4.3: Correlation between corrosion scenarios W5 to W6 and beam types.

W4	# of occurrences	W5	# of occurrences
36WF135	13	36WF170	5
33WF118	6	21WF55	4
27WF84	4	36WF194	2
30WF99	4	36WF150	2
36WF194	3	21WF59	1
36WF150	2	21WF63	1
30WF124	2	33W118	1
18W50	1	30W108	1

Whether or not the beam's length should be included as a parameter in the proposed methodology was studied. Three different deterioration scenarios in terms of corrosion height and length were chosen, and each one of them was projected on 36WF150 girders spanning 40 ft., 60 ft., and 80 ft. Analyses were run for section loss in the range of 20% to 80% of intact web thickness, in order to examine if the beam length had an influence on the failure load. The lengths were chosen based on their frequency distribution in the Commonwealth of Massachusetts (Fig. 4.10).

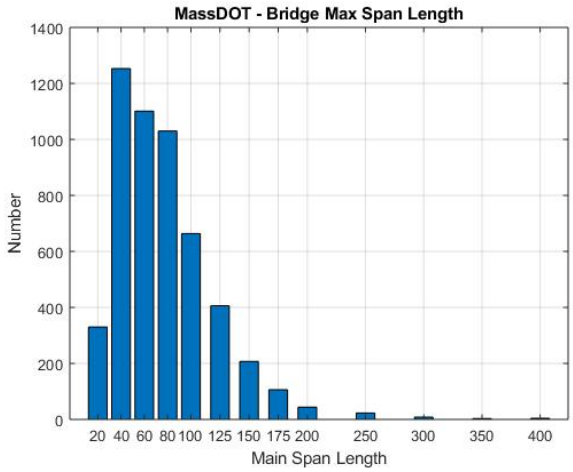

Figure 4.10: Bridge max span length in Massachusetts.

4.2.3 Material Properties

The phenomenon of beam end corrosion is observed on structures that have been designed and constructed typically between 1900 and 1980 (Fig. 4.11). According to the available inspection reports and drawings, 36 ksi steel was mainly reported. A bilinear elastoplastic constitutive model with hardening was used, with 36 and 58 ksi yield and ultimate stress, respectively. The material was modeled as isotropic, with Young Modulus equal to 29,000 ksi and Poisson ratio equal to 0.27.

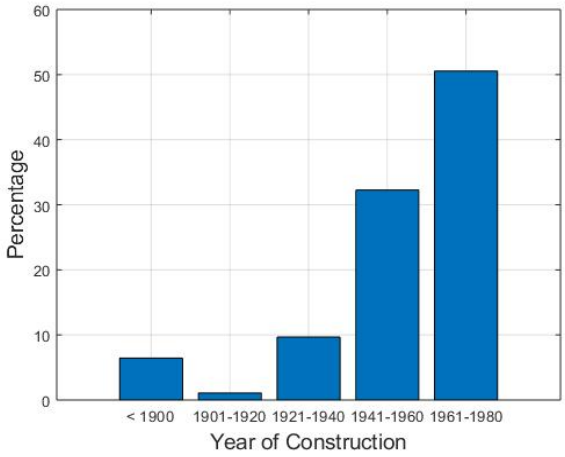

Figure 4.11: Year of construction distribution for 93 bridges in study.

4.2.4 Boundary Conditions

The research group aimed to study in detail all the aspects of the computational framework that were needed to capture the complicated phenomenon of failure of deteriorated steel beam ends. This model has to describe the actual behavior of single span beams without stiffeners above the bearings. Thus, the boundary conditions must reflect the transitional and rotational restriction applied to the girder due to the slab and the supports.

By careful observation of the construction drawings provided by MassDOT, it was noted that most of the examined bridges were built between 1940 and 1980. According to the established technique at that time, the steel beams were not typically composite. Shear studs didn't exist to promote interaction between the steel beam and the concrete deck, although in some cases the top flanges of the beams were encased in the deck. This encasement covered just the thickness of the top flange, and it was therefore controversial how much composite action could be developed. Based on the non-composite design assumption, the deck was not explicitly considered in the mechanical model of the deteriorated beam end, but its contribution was considered by restraining the out-of-plane displacements of the top flange (perpendicular to the beam web and parallel to the width of the flange). In addition, the rotation of the top flange along the beam's longitudinal axis was also constrained.

The most important part of the boundary conditions in the mechanical model studied concerned the support conditions of the bottom flange of the beam on the bearing plate. It should be noted that for the support condition of the bottom flange, several different techniques were observed in the construction drawings, such as pin bearing, bearing plates, or curved-type supports. It was noticed that bearing plates were the most common technique for bridges that were built between 1940 and 1980, which included most of the bridges studied in the project. For that reason, the mechanical model included a bearing plate support condition.

Two typical examples of this type of support condition are shown in Figs 4.12 and 4.13. The bottom flange of the girder was resting on two steel bearing plates. The bottom plate was resting on the concrete abutment. The system was anchored with anchor bolts. The anchor bolts went through the bottom flange and the bearing plates, and they were anchored in the concrete. For the expansion bearing condition, the slots on the top bearing plate were oval in shape, to allow longitudinal translations of the girder, while for the fixed bearing condition, the slots were circular.

Based on the preceding, the mechanical description of the bearing support is straightforward. The support would have to include a bearing plate below the bottom flange, which is in contact with the bottom flange. This contact should allow for any uplift (separation of the two surfaces) but not any penetration between the two surfaces. The anchor bolts constrain the bottom flange and the bearing plate vertically at their location. The longitudinal translation of the bottom flange for an expansion support should be allowed, while for the case of a fixed support, the same translation should be constrained.

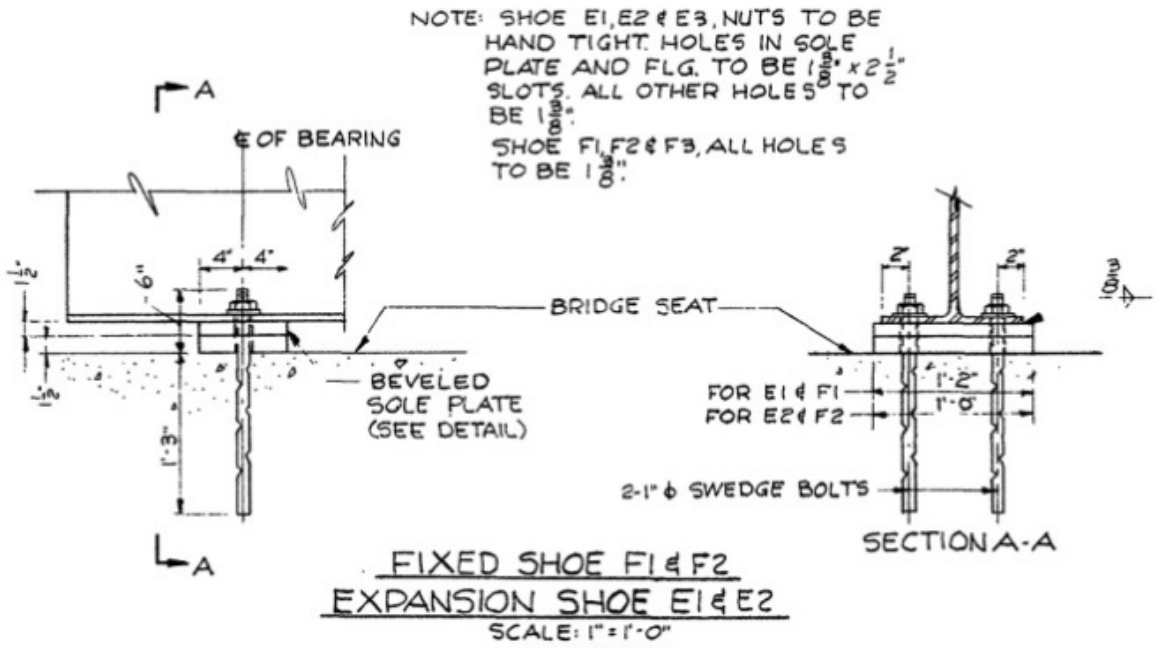

Figure 4.12: Bearing drawing details from B-10-18, showing bottom flange of girder, the two bearing plates, and anchor bolts. Note describes the holes, which allow the longitudinal translation.

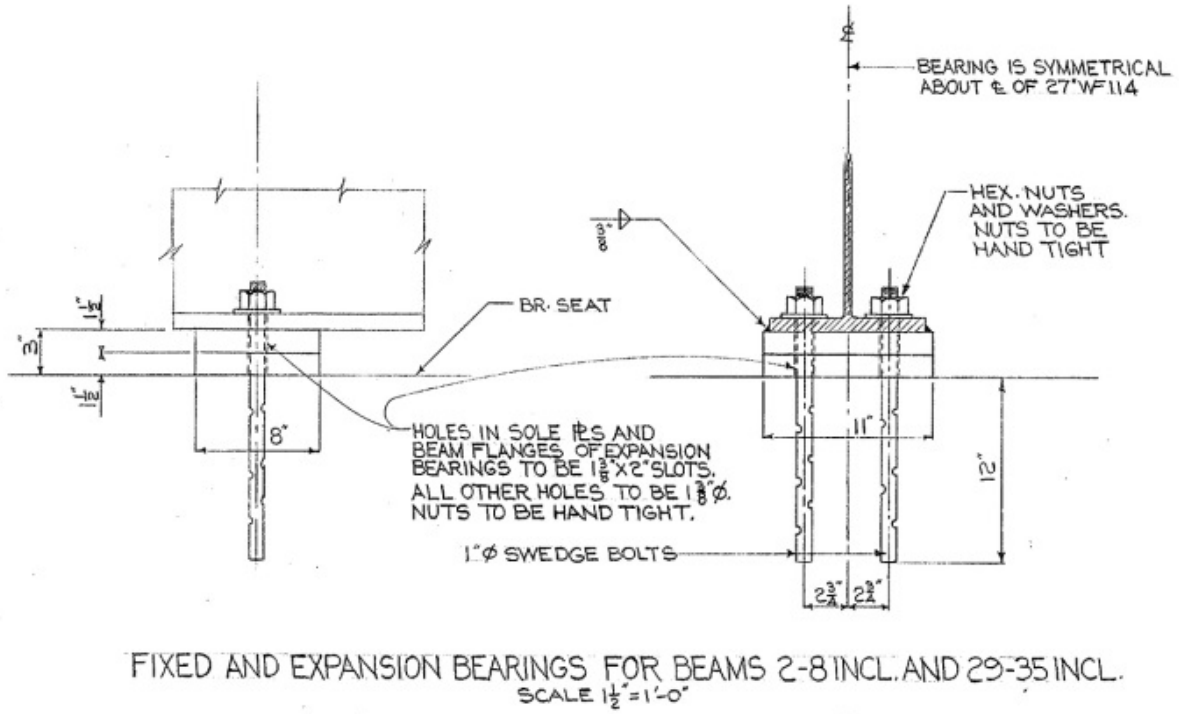

Figure 4.13: Bearing drawing details from F-2-42, showing bottom flange of girder, the two bearing plates, and anchor bolts. Note describes holes, which allow the longitudinal translation.

All the preceding are based on the design of the bridges. However, the reality of the field and the work done by the inspectors documented in their inspection reports showed a different situation. Fig. 4.14 shows examples of cases where the anchor bolts were either completely missing or severely corroded or bent, as noted by inspectors. These examples are just some of the many cases of similar condition. To conclude, it was decided that the set of boundary conditions would not include the anchor bolts. This meant that the vertical constraint coming from these bolts would not be included in the model. This condition can be described as the most damaged condition.

Photo 30: Typical bearing, over extended without anchor bolts.

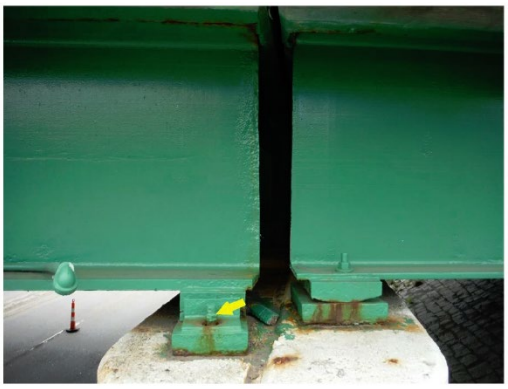

Photo 11: Heavy section loss to the anchor bolt nut of the Beam 37 bearing at Pier 2 in Span 5.

Photo 9: Beam #6 at the South end.

Photo 21: Span 4, Beam 31, West Abutment: Missing south anchor bolt and rotated bearing

Figure 4.14: Examples of deteriorated beams with missing or damaged anchor bolts.

4.2.5 Loading Conditions

The type of loading was defined based on the load rating procedures that are in use by MassDOT. According to the 2019 ed. *LRFD Bridge Manual (30)*, the rating factor is calculated based on equation 4.1:

$$LRFR\ Rating\ Factor = \frac{Corroded\ Web\ Factored\ Resistance - Dead\ Load_{shear}}{(Live\ load + I)_{shear}} \quad (4.1)$$

Where *I* is the dynamic load allowance that is applied in addition to the static vehicle load, to account for its dynamic effects. The corroded web resistance is calculated as the minimum of the yielding ($R_{n,yield}$) and crippling ($R_{n,crip}$) capacity. The equations for the computations of

each one of these capacities are also included in the draft *MassDOT 2019 Bridge Manual,* Chap. 7 *(30)*.

Besides the dead load of the beam, the applied dead load takes into account the contribution of the deck that the beam is carrying, using tributary areas. Live loads are applied based on the HL-93 load check. The HL-93 consists of a three-axle truck (HS20), or a design tandem plus the design lane load that is equal to 0.64 kip/ft. The shear loads of the beam in equation (4.1) are calculated using beam theory formulas. According to *(30)*, substituting the corroded web factored resistance, equation (4.1) becomes:

$$R.F.=\frac{\mathrm{Min}\left[(\Phi_b{=}1.0)\left(R_{n,yield}\right),(\Phi_w{=}0.8)\left(R_{n,crip}\right)\right]-(1.25\ \mathrm{x}\ V_{dead\ load}+1.5\ \mathrm{x}\ V_{wear.\ surf.})}{1.75\ \mathrm{x}\ g_s x\ (V_{Lane\ Load}+(1+0.33)\ \mathrm{x}\ \max(V_{HS20},V_{Tandem}))} \quad (4.2)$$

The computation of the shear live load distribution factor (g_s) depends on whether the girder is interior or exterior in the bridge. For the current work, it was decided to follow the process for an interior girder in order to limit the dependence from the bridge geometry.

The magnitude of the rating factor (R. F.) denotes how much live load the beam is able to withstand in addition to the factored dead load. Based on that, the applied loads of the mechanical model and, later on, of the computational model were in accordance with the load rating procedures and were applied in multiple steps.

During Step 1, the unfactored dead load is applied as a uniform downwards pressure on the top flange. At Step 2, the factored live loads are applied. The lane load is applied as a uniform downwards pressure on the top flange. The truck load tire contact areas cover the full flange width and 20 in. longitudinally. If the second step is completed without failure, the corroded girder has managed to withstand the whole live load but the loading–carrying capacity is not obtained. In order to force the corroded beam to failure, additional steps with additional live load were applied.

The capacity of the beam end is measured by the reaction force at the bearing, when failure occurs.

4.2.6 Geometric Imperfection

For intact beams, rolled according to modern manufacturing techniques, initial imperfections are negligible. However, the researchers had to account for two factors. First, the majority of examined beams were manufactured between 1900 and 1980. Second, geometric nonlinearities may come from the non-symmetric thickness reduction along the web sides. Thus, extreme section loss usually results in instability phenomena, making deteriorated webs slender buckling-prone members.

For the problem studied here, geometric imperfections were accounted in the form of scaled eigenmode shapes. The effect of the pre-loading imperfection amplitude was extensively examined by analysis performed in the range of 10% up to 200% of the intact web thickness.

4.2.7 Programming Implementation

As extensively explained in previous sections of this report, each model was run initially using an eigenvalue buckling analysis solver, and the scaled eigenmode of the first positive eigenvalue was imported as a geometric imperfection for the quasi-static analysis. Based on this approach, the number of different models to be analysed was substantially high. Each model described a different combination of beam type, load conditions, and corrosion topology.

Creating an Abaqus model from scratch, based on the procedure described in this report, could require more than one hour of work by an experienced user. Of course, some models can be produced by slightly modifying existing configurations, such as adjusting remaining corrosion thickness parameter. However, the productivity can be remarkably increased with programming implementation. For this purpose, an Excel sheet that described one tested scenario in each row was introduced (Fig. 4.15). The scenario parameters described in the Excel sheet concerned only the configuration of the geometry.

Beam Geometry						Bearing		Web Corrosion								Flange Corrosion	
Beam	Depth(total)	tflange	tweb	Bflange	Length	Bearing Length	Lo	Pattern	t web loss	CL1	CL2	CL3	CH1	CH2	CH3	t flange loss	Cf/Cl
33W130	33.13	0.855	0.58	11.51	780	11	0	W1	0.2	0.25	0	0	0.1	0	0	0	0
33W130	33.13	0.855	0.58	11.51	780	11	0	W1	0.4	0.25	0	0	0.1	0	0	0	0
33W130	33.13	0.855	0.58	11.51	780	11	0	W1	0.6	1.5	0	0	0.1	0	0	0	0

Figure 4.15: Description of geometry of tested scenarios.

This Excel sheet constituted the input for the new developed python script. The script operated through Abaqus and resulted in two files for each row (one for eigenvalue buckling analysis and one for quasi-static) that could be executed by the available Abaqus solvers. The loading conditions were described in the script. The dead load was user defined, in contrast with live loads. The selection between HS20 and design tandem was done automatically, based on the beam's length. The most sensitive procedure during building the model was the mesh generation. Considerable effort was put into creating a reliable combination of edge partition settings, which resulted in a high-quality mesh independently of beam geometry and corrosion topology (Fig. 4.16). To validate the outcome of the script, a mesh check was always performed.

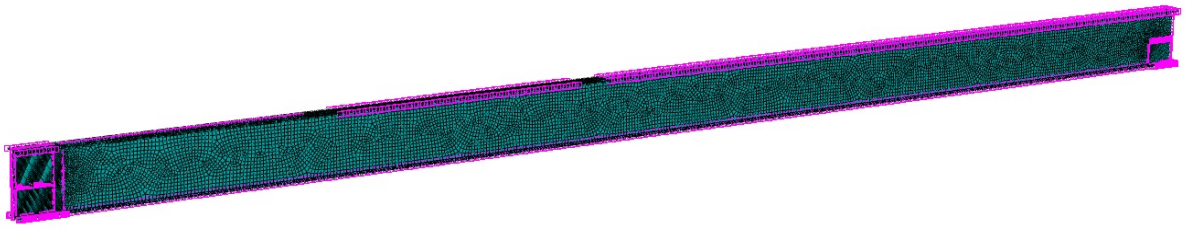

Figure 4.16: Mesh partition for quality mesh.

4.2.8 Definition of Failure

One of the main concerns was the establishment of a criterion in order to define the failure bearing load. Initially, a variety of indexes (e.g., maximum lateral displacement between sequential computational time steps) were defined and implemented. However, the

displacement controlled experiments revealed that there is actually a peak load beyond which the post buckling behavior is characterized by a reduction of load. As is presented in Section 7.1, the developed numerical model was able to accurately capture this maximum load before the termination of the analysis. Thus, for the parametric analysis, the bearing load at the last computational step was considered as the peak load and, consequently, the capacity of the corroded end.

In order to ensure the smooth operation of the developed methodology as well as that every analysis was terminated due to instability phenomena, supplementary scripts that read the Abaqus output files were also developed, and in addition to bearing load, data relevant with the maximum out-of-plane displacement and Von Mises stresses were automatically extracted. An example is given is Fig. 4.17a-d, where multiple conclusions can be drawn for a 36WF150 beam with full height corrosion and section loss in the range of 20% to 80% of intact web thickness. The beams with 80% and 75% material loss are not able to undertake the full dead load, and they fail prior to the completion of Step 1. The failure mode is characterized by a buckling wave formulated along the same direction for all specimens (following the initial imported eigenmode). For cases with extensive section loss, buckling occurs shortly after the fest element yields. Finally, the obtained capacities are smoothly reducing for increasing section loss.

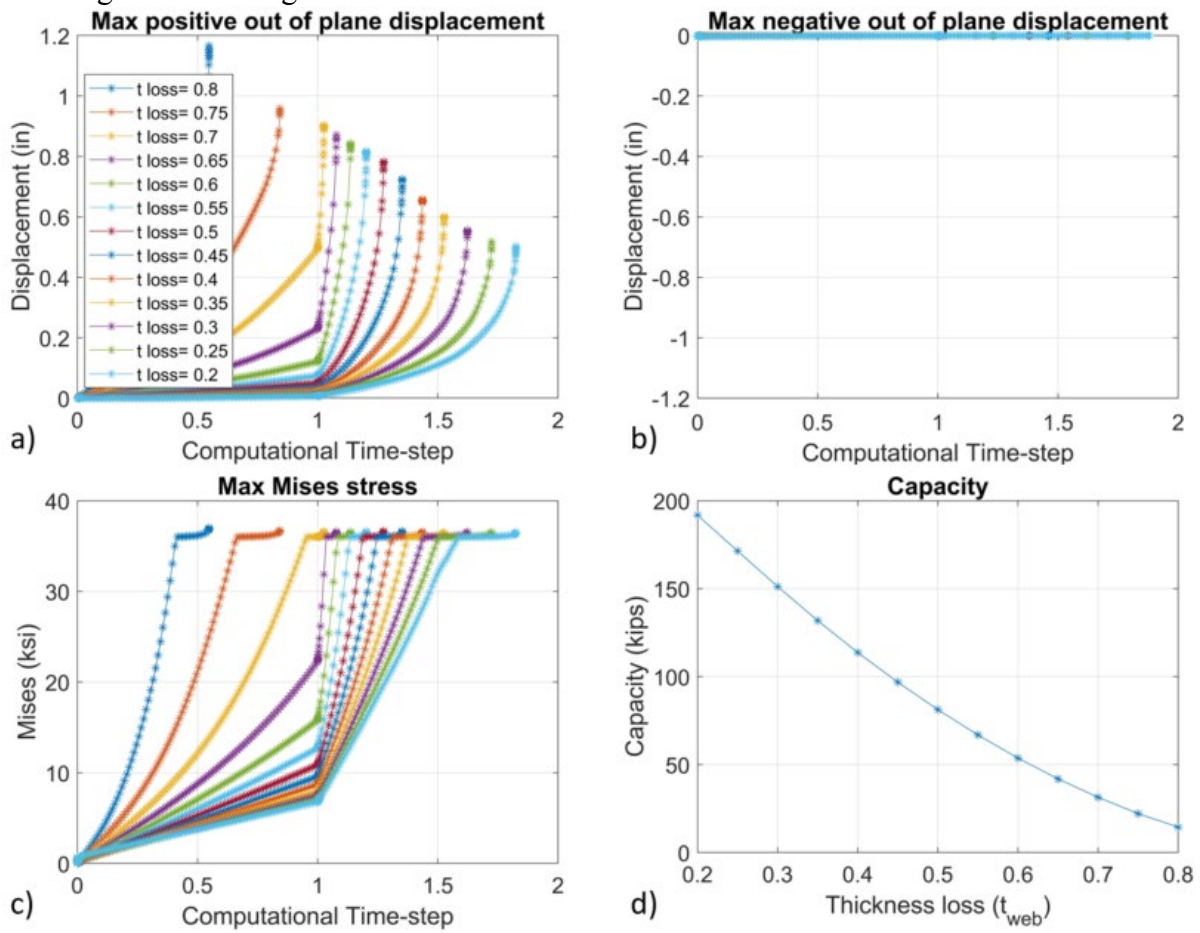

Figure 4.17a-d: Data extracted and plotted from every set of analyses, for a 36WF150 beam with full section loss in the range of 20% to 80% intact web thickness.

This page left blank intentionally.

5.0 Statistical Analysis of Corrosion Data

5.1 Post-Processing of the Data

The new spreadsheet format described in Chapter 2 was the basis on which the post-processing was performed. A MATLAB script was developed to extract, manage, and process the data from the reports. The script saved all the summary sheets in an array and cell format, and each beam end was defined as a unique entry calculating the frequency of each parameter. This way, max, min, average, and distribution data were calculated. The new data were used to develop statistical information about the appearance of the phenomenon and ultimately identify common characteristics which would lead to the definition of the most prevalent geometries of the deterioration. These geometries would then be used for the computational part of the project. The script was designed to satisfy all the different cases, such as web hole combinations, information for both side's flanges of the same end, or beams with both ends corroded. As expected, this process provided a variety of output data that are presented in entirety in Appendix 1 (for deteriorated beam ends without a diaphragm) and Appendix 2 (for deteriorated beam ends with a diaphragm).

Initially, it was possible to observe the frequency of each web corrosion and hole pattern. Fig. 5.1a demonstrates the frequency of the raw-based patterns for beams with or without a diaphragm above the bearing. A first conclusion is that the diaphragm affects the general shape of the corroded area significantly. The web corrosion patterns W1 and W3 were the most dominant ones for the cases of beams with diaphragm, consisting of 84% of all beams. For the cases without diaphragm, which were the focus of the current research, W1 and W3 consisted of 76% of all beams. The frequency of W4 and W5 patterns was lower by a measurable margin.

The post-processing also unveiled important distributions of geometric corrosion parameters within a specific corrosion pattern. For example, Fig. 5.1.b shows the corrosion height distribution for the W1 pattern (rectangular-shaped web corrosion) for beams without diaphragm above the bearing. The corrosion height was normalized with respect to web height. Two main trends were identified: one group of beams, for which the corrosion extended up to 20% of their web height, and a second group of beams, for which the corrosion covered their full height. These two trends were recorded and examined separately.

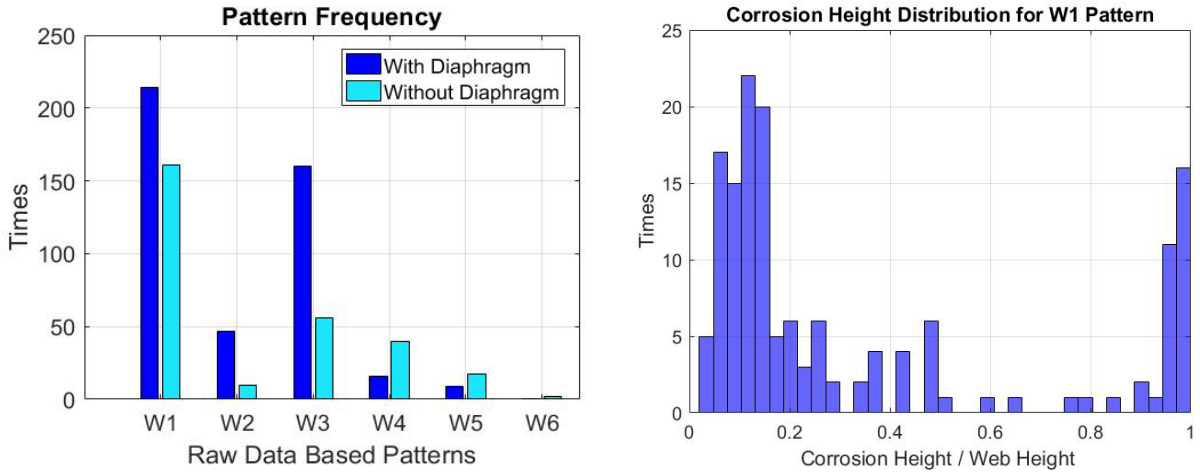

(a) (b)

Figure 5.1: (a) Visualization of corroded area of beam end showing extreme W1 case on top of extreme W2 scenario, as produced by new MATLAB code; (b) correlation between beam type and W3 corrosion pattern.

Another interesting finding was related to the correlation of corrosion patterns and beam type or structure age. Fig. 5.2b illustrates the four beam types for which the W3 corrosion pattern was observed more frequently.

In addition to the previously mentioned features, the MATLAB script developed within this part of the research work was also be used to visualize the corrosion patterns along with the extreme scenarios. Fig. 5.2a illustrates the side view of a corroded beam with dimensions normalized with respect to web height. The blue shaded area indicates the extreme W1 case, on top of the red extreme W2 scenario. Since all the W2 cases fit within the blue shaded area, and the thickness reduction distributions were similar, W1 for corrosion height up 30% (Table 5.1, No. 1) was eventually merged with W2.

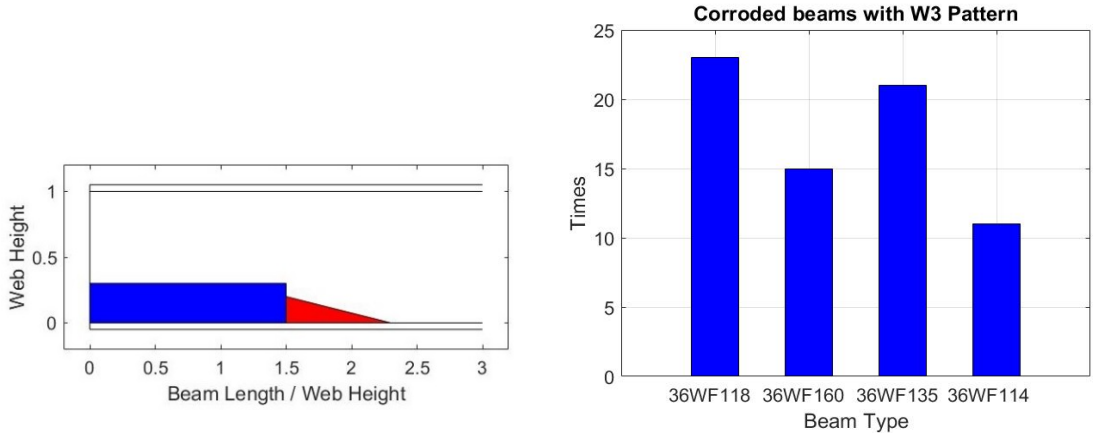

(a) (b)

Figure 5.2: (a) Visualization of corroded area of a beam end showing extreme W1 case on top of extreme W2 scenario as produced by new MATLAB code; (b) correlation between beam type and W3 corrosion pattern.

5.2 Final Corrosion Patterns

Following the procedure described previously, the characteristics of all 808 beam ends were recorded and statistically analyzed. Out of the 808, only 76 beam ends included flange corrosion without any web corrosion, and they were taken out of the study, leaving a total population of 732 beam ends. The final deterioration scenarios do not include any corrosion on the top flange of the beams, since only 19 out of 808 beam ends had reported top flange deterioration. Figs. 5.3 and 5.4 include all the most commonly found final corrosion cases that were selected to be analyzed further. Table 5.1 presents the detailed ranges of all the parameters involved in describing the patterns for the cases without a diaphragm, while Table 5.2 includes the same information for the cases with a diaphragm.

The observation of the thickness ratio reduction in Table 5.1 (t_{loss}/t_{web} and t_{loss}/t_{flange}) considering that in intact condition the flange is thicker than the web, results in concluding that the flange absolute thickness loss is higher. This can be explained by observing the final corrosion patterns shapes in Fig. 5.3. The water from the leaking deck joints was initially concentrated on the upper side of the bottom flange, starting the deterioration, which then uniformly extended to the web. In addition, the common thickness loss range for Cases 1 and 2 indicated that Case 2 may be the evolution in time of Case 1. Case 4 could reveal the water flow from the top of the beam to the bottom flange. Hole patterns 6 and 7 were located at the bottom of the web, where the water was concentrated, resulting in extensive material loss. These hole patterns were projected on corrosion topologies that more frequently correlated.

Fig. 5.4 includes the final 11 corrosion patterns with a diaphragm. The diaphragm is illustrated with a black box located at the most common position for each one of the patterns. Cases 8–13 reveal that the diaphragm did not have a substantial effect on the appearance of corrosion. In some cases, the corrosion went around the diaphragm, and in some others, it did not. The last four Cases 15–18 included holes at the base of the web, right above the bottom flange.

Following the notation of Tables 2.2 to 2.9, the analytical description of the final corrosion patterns is presented in Tables 5.1 and 5.2. C_f and C_l represent the flange and web corrosion length, respectively.

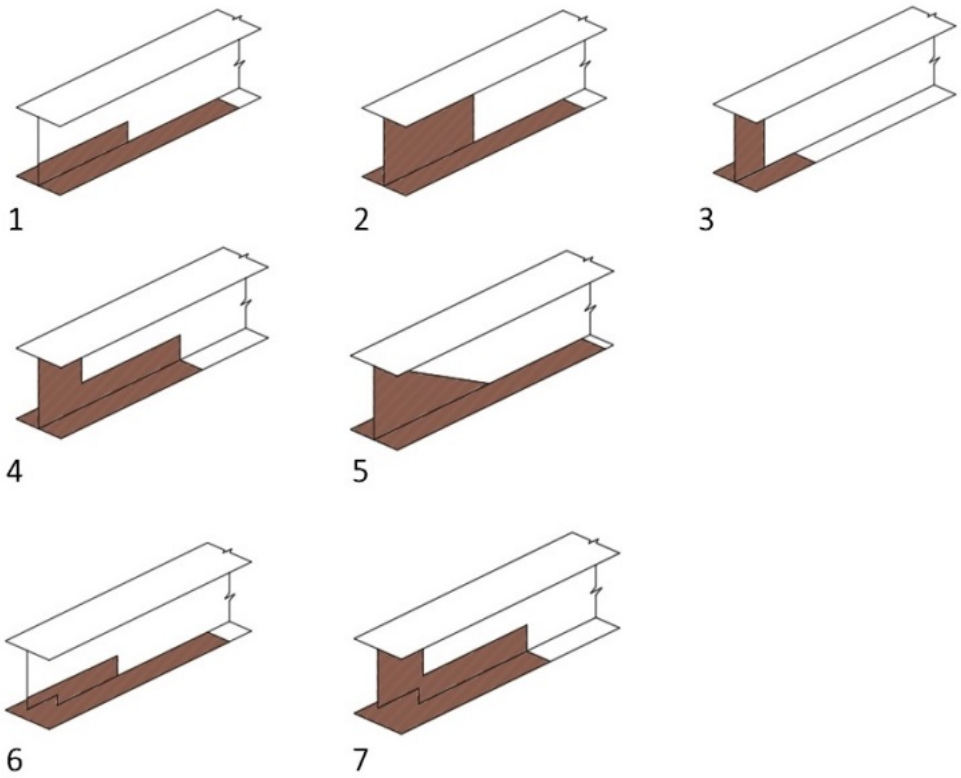

Figure 5.3: The seven final corrosion patterns for beam ends without a diaphragm.

Table 5.1: Analysis of final corrosion topologies for cases without a diaphragm. Parentheses denote that endpoint of interval is excluded.

	Web							**Flange**	
No	Patt.	C_{H1}	C_{H2}	C_{H3}	C_{L1}	C_{L2}	t_{loss}/t_{web}	C_f/C_l	t_{loss}/t_{flange}
1	W1	(0.0.3]	na	na	(0,1.5]	na	[0.2, 0.8]	[1,2]	[0.2,0.8]
2	W1	1	na	na	(0,1.5]	na	[0.2,0.8]	[1,2]	[0.45,0.65]
3	W1	1	na	na	(0,0.5]	na	[0.2,0.8]	[1,2]	[0.45,0.65]
4	W3	(0,0.35]	1	(0,0.35]	[0.05,0.7]	[0.5,2.3]	[0.1,0.8]	1	[0.4,0.6,0.8]
5	W5	[0.15,1]	na	na	[0.5,1.8]	na	[0.2,0.5]	[1,1.8]	[0.1,0.8]
	Hole extreme scenarios								
	Patt.	a	b	Web case					
6	M1	(0,0.15]	(0,0.5]	W1					
7	M1	0.21	(0,0.63]	W3					

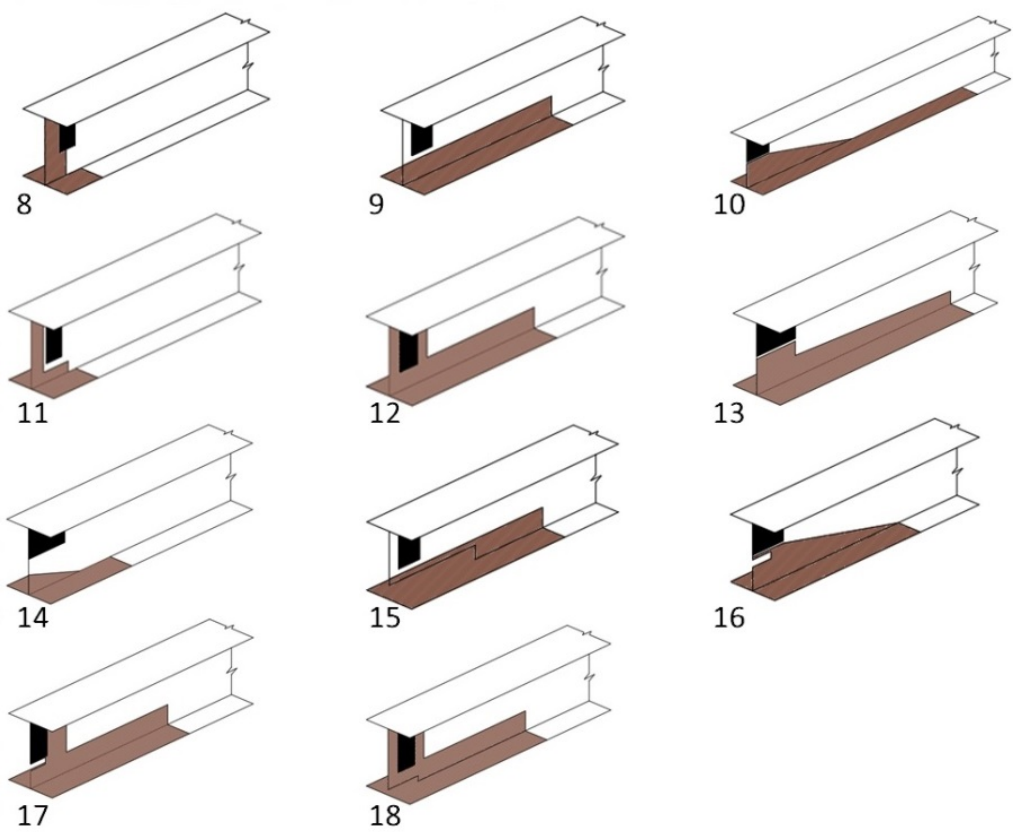

Figure 5.4: Eleven final corrosion patterns for beam ends with a diaphragm. Diaphragm is indicated as a black box located at the top part of the web.

Table 5.2: Analysis of final corrosion topologies for cases with a diaphragm. Parentheses denote that endpoint of interval is excluded.

	Web							**Flange**	
No	Patt.	C_{H1}	C_{H2}	C_{H3}	C_{L1}	C_{L2}	t_{loss}/t_{web}	C_f/C_l	t_{loss}/t_{flange}
8	W1	1	na	na	(0,0.35]	na	0.2,0.4,0.6	[1,1.7]	[0.1,0.45]
9	W1	(0,0.3]	na	na	(0,2.5]	na	0.2,0.4,0.6	[0,1]	[0.2,0.8]
10	W2	(0,0.5]	na	na	[0.5,0.6]	(0,1.8]	[0.2,0.8]	[1,2]	0.25,0.5,0.65
11	W3	(0.1,0.16]	1	[0.1,0.16]	[0.1,0.2]	(0.25,0.6]	[0.4,0.6]	1.2	[0.3,0.6]
12	W3	(0.0,0.3]	1	(0.0,0.3]	[0.2,0.6]	[1,2.3]	[0.2,0.8]	1	0.65
13	W3	[0.05,0.25]	0.5	[0.05,0.18]	[0.2,0.75]	[0.5,3]	0.4,0.6,0.8	1	0.3,0.6,0.8
14	W5	[0.15,0.3]	na	na	[0.3,0.85]	na	[0.2,0.35]	[1,1.6]	0.3,0.6,0.8
	Hole extreme scenarios								
	Patt.	a	b	Web case					
15	M1	(0,0.21]	(0,1.4]	W1					
16	M2	(0,0.11]	(0,0.3]	W2					
17	M2	(0,0.1]	(0,0.25]	W3					
18	M1	(0,0.08]	(0,0.5]	W3					

This page left blank intentionally.

6.0 Experimental Results

This chapter includes the results obtained from the experimental testing of six naturally corroded girders, numbered as Specimens 1 to 6. Except for Specimen 4, a common characteristic of the corroded ends was the web holes located above the support. This section includes some introductory observations and then a detailed description of the failure mechanisms, along with several graphs on each test. At the end of the chapter, the team presents the results of the material coupon testing.

Table 6.1 summarizes the maximum experimentally obtained applied load at failure, as well as the corresponding reaction force developed at the corroded end. Predicted failure loads according to the current procedures were also included for comparison purposes. The highest values between predictions and experimental obtained strengths are displayed in the shaded cells. A detailed evaluation of the current strength assessment methodology is found in Chapter 8. The data presented in Table 6.1 provided the first piece of evidence that the current methodology overestimated in some cases the capacities of the beam ends and underestimated the capacities in other cases.

Table 6.1: Beam identification data, experimentally obtained capacities, and failure loads calculated according to current procedures.

Specimen	Bridge	Beam type	Max Applied Load (kips)	Bearing Failure Load (kips)	Prediction (kips)
1	Colrain	33WF125	134.1	99.1	38.3
2	Colrain	33WF132	91.3	67.6	102.2
3	Colrain	33WF125	112.5	84.3	0
4	Charlemont	21WF73	53.3	42.8	91.5
5	Charlemont	21WF73	45.1	30.9	17.6
6	Charlemont	21WF59	58.8	40.9	6.1

Some interesting general observations about the experimental tests:

- The failure mechanism of Specimens 1 and 5 was characterized by a buckling wave appearing in the web.
- One of the most important findings of the project came out of the test of Specimen 2. The failure mode of Specimen 2 was strongly affected by the initial lateral web imperfection, revealing that this type of imperfection, which is not currently considered in the manual procedures, severely affected the capacity of corroded beam ends.
- Specimens 3 and 6 had holes at the bottom of the web expanding beyond the bearing length, for both cases. After the initiation of loading, the top edge of the hole made contact with the beam bottom flange, and the beam end started bearing load, revealing an alternative loading path that was not known before the test.
- For Specimen 4, a long wave instability mode governed the failure. Local web buckling was captured at the narrow strip with limited remaining thickness above bearing. However, it is not clear if the observed local buckling initiated the long-wave

failure or if it was the result of a second-order phenomenon from the extensive midspan lateral and torsional deflection.

- The peak load of all specimens (except Specimen 4) was combined with lateral deflection of the web, indicating buckling-related failure mechanism.
- It is worth mentioning that at previously conducted experimental efforts on deteriorated ends with artificial thickness reduction, an abrupt failure was reported. On the other hand, the post-buckling behavior of Specimens 1, 2, and 3 was characterized by a progressive loss of stiffness with rapidly increasing deformations.

6.1 Specimen 1

Specimen 1 was successfully tested on Oct. 4, 2018. According to the summation of the reaction forces measured in the two load cells installed at the bottom end of each rod (Fig. 3.4), the total applied load at failure was equal to 134.08 kips (Fig. 6.1a). As previously noted, the maximum beam deflection was measured using a linear variable displacement transducer (LVDT) installed on the outer face of the bottom flange beneath the point of load application.

The loading protocol was displacement controlled. From Fig. 6.1b, an increasing discrepancy is seen between the load applied by each jack during the experimental process. This differential loading resulted in a slight inclination of the loading beam. This can be attributed to a non-symmetrical shape of the beam, which originated from the demolition process.

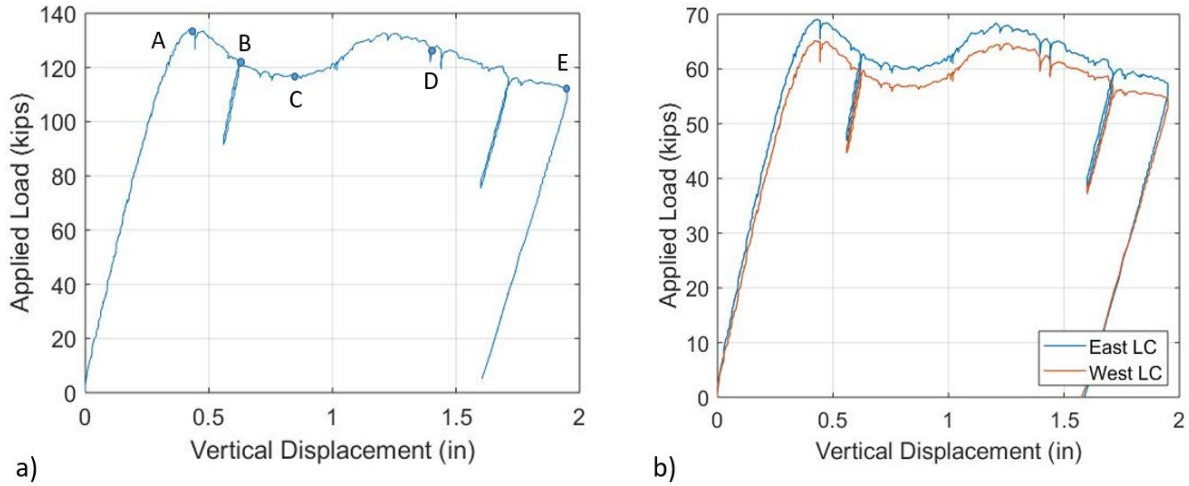

Figure 6.1: (a) Total applied load—vertical displacement plot for the first specimen; (b) Total applied load was calculated from summation of two load cells installed at bottom of each rod (west and east side of Specimen 1).

Based on statics and the geometry of the configuration, the distribution of reaction forces dictates that 25% of the load should travel to the intact end, while 75% should travel to the corroded end. Fig. 6.2 presents the ratio of the reaction force developed at the intact end to the total applied load, as it was recorded by the load cells during the experimental process.

The initial value of the experimental ratio was 0.23 and began to increase with loading. This rise may occur because of the uplift observed at the bearings while the applied load was increasing. This uplift did not evolve in the same way at both supports. It is possible this could then affect the ratio of the distances between the supports and the loading area for both ends. Based on applied load contribution to supports, the reaction force at the corroded end was equal to **99 kips**.

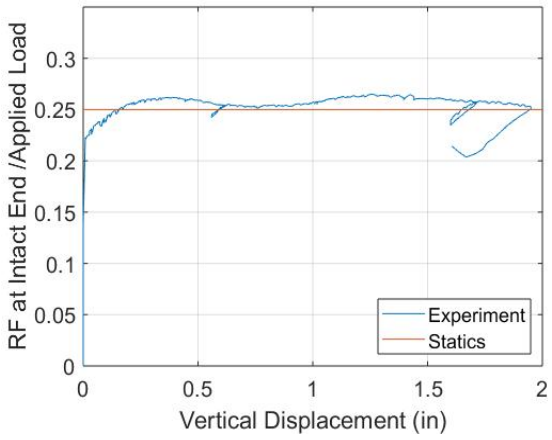

Figure 6.2: Ratio of reaction force developed at intact end to total applied load, as recorded by load cells during experimental process.

In Fig. 6.3, the deformation of the corroded end is presented, using images captured from two cameras that recorded the experimental process. The first camera recorded the plane of the web (side view of the beam), while the second camera recorded the beam profile. These pictures illustrate the girder's deformation at the initial condition before loading, followed by deformations observed at different steps of the experimental procedure (Points A to E, at Fig. 6.1a).

From the initial condition pictures, two holes were observed in the web. For the bottom one, the web above the hole was not bearing at the flange. At Point A, 130 kips were applied to the specimen. A slight uplift of the bearing was observed, while extensive crippling took place at the inner perimeter of the bottom hole. The flange had warped while the vertical displacement was limited to 0.44 in. and the lateral displacement was plainly visible.

After the peak load was reached, the vertical displacement was increasing while the load was dropping. Point B captured the deformation at 120 kips. The web's rapidly increasing out-of -lane displacement allowed for the top edge of the bottom hole to move downwards without touching the hole's bottom edge.

At Point C, the deformed web began bearing at flange. The uplift reduced, and the system gained stiffness and began retaining additional load. The out-of-plane displacements were further increasing, while the vertical displacement reached 0.9 inch.

At Point D, due to the extensive out-of-plane displacement, the web had begun bearing at the top of the anchor protruding from the flange. The system lost stiffness, and the flange bent

significantly as the vertical displacement reached 1.4 inch. At Point E, the experiment was terminated because the top flanges reached the boundary of the lateral support.

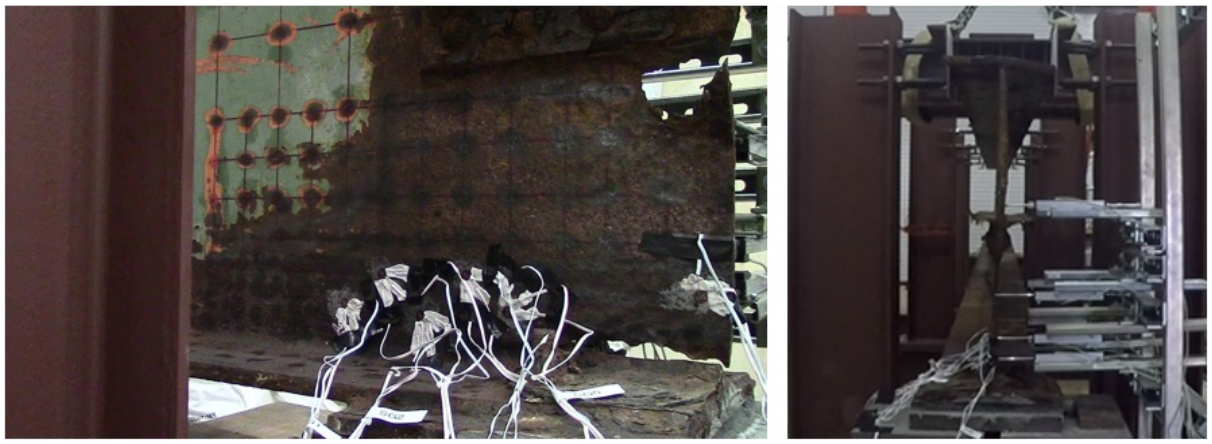

Initial

A

B

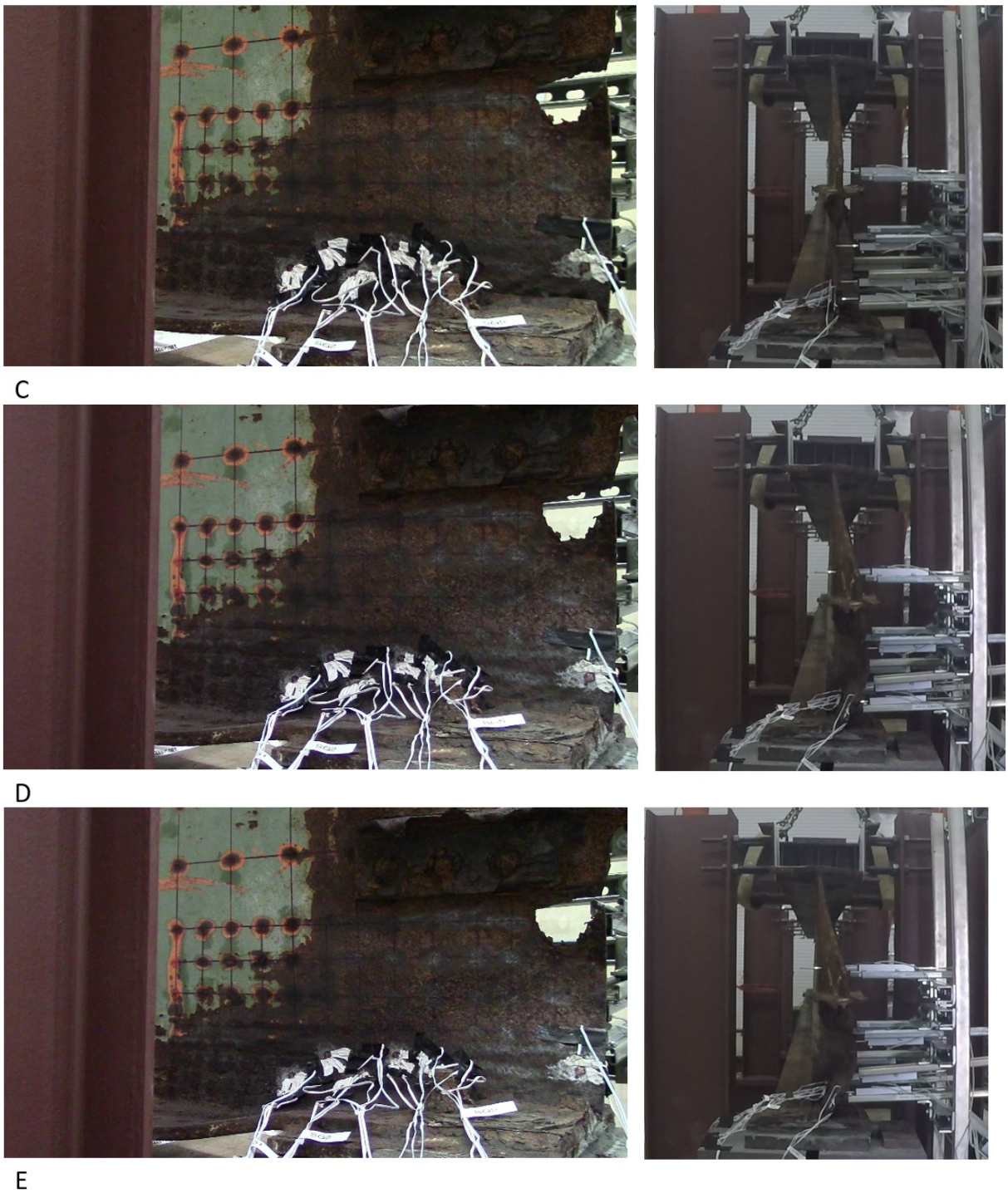

Figure 6.3: Side-by-side images showing side view of web and profile view of beam during experiment. Letters A-E correspond to Fig. 6.1a.

Fig. 6.4 presents the out-of-plane displacement profile as it was recorded from the two potentiometer columns; the exact configuration is presented in Fig. 3.18. The instruments were positioned over the height of the web above the outer (blue) and inner (red) edges of the bearing. Results are presented for three different loads: at a half, three quarters, and the maximum applied load (F_u). The used potentiometers have a 4 in. capacity and were placed

close to half of the stroke in order to capture possible sideways deflection along both directions. The instruments were recording relative displacements from the moment of loading initiation; thus, the initial imperfection of the beam was not captured. As a result, the vertical black line illustrates the ideal web condition. Between adjacent potentiometers in the same instrumentation column, the web section was considered linear. The section between the fillet and the closest to the fillet instrument was also assumed as linear. The blue line was terminated at the location of the bottom potentiometer, in order to mimic the web profile discontinuity due to the area with 100% section loss.

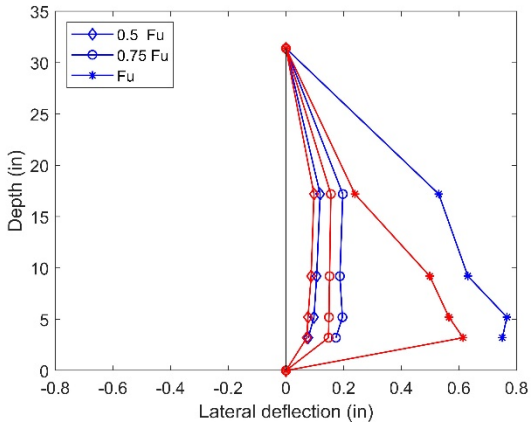

Figure 6.4: Beam's end lateral displacement profile as recorded from outer (blue) and inner (red) column of potentiometers, for three different loads: 0.5, 0.75, and 1 F_u.

Interpreting Fig. 6.4, potentiometers at the same height along the beam's length followed the same pattern, revealing a buckling wave created at the bottom of the web with maximum magnitude at the outer edge of the web of the beam above bearing. The failure mode is presented in Fig. 6.5.

Figure 6.5: The residual deformation after unloading Specimen 1.

Fig. 6.6 presents the principal strains and directions for each one of the strain rosettes (SRs) that were installed on Specimen 1. For peak load, Fig. 6.6c visualizes the direction of compressive (solid line) and tensile (dashed line) strains and the magnitude of each strain normalized to the maximum recording. According to this figure, the part of the web beyond the bearing was subjected to shear deformation, while SR3 and SR5 captured direct compression. SR6 revealed that the area above the hole did not experience plane deformations.

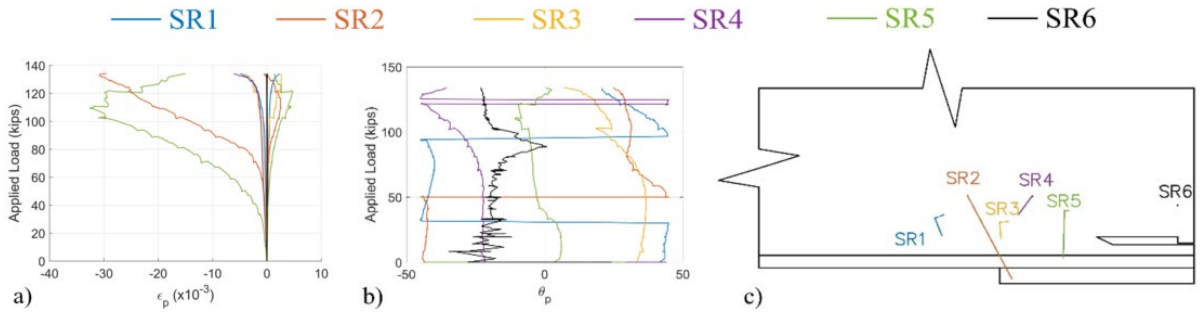

Figure 6.6: (a) Principal strains and (b) directions up to peak load from SRs installed at Specimen 1; (c) direction and normalized magnitude in respect to the maximum strain at peak load for each SR; compressive strains illustrated with solid lines and tensile strains with dashed lines.

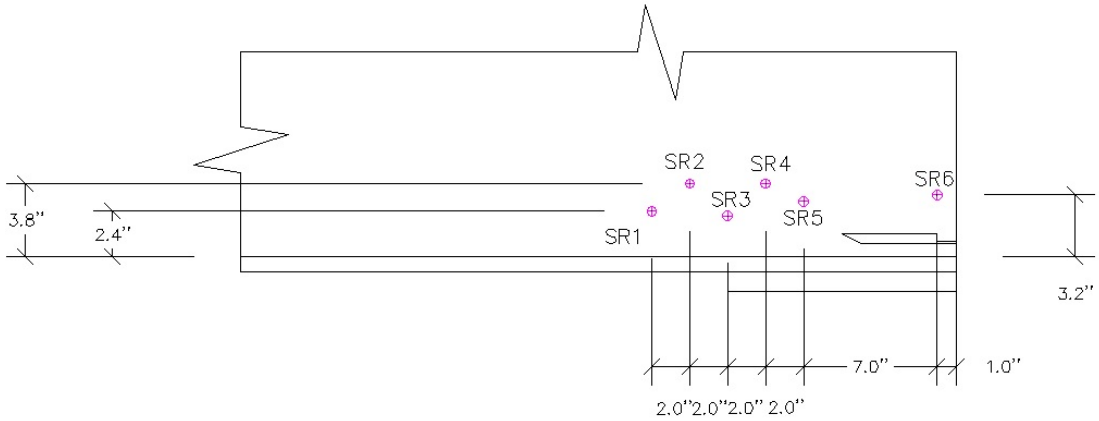

Figure 6.7: Exact location and SR nomenclature for Specimen 1.

6.2 Specimen 2

Specimen 2 was successfully tested on Oct. 24, 2018. According to the summation of the reaction forces measured in the two load cells installed at the bottom end of each rod, the total applied load at failure was equal to 91.3 kips (Fig. 6.8a). As previously noted, the maximum beam deflection was measured using an LVDT installed on the outer face of the bottom flange, beneath the point of load application. Fig. 6.8b confirms the consistency of the load applied by each jack during the experimental process. This load was applied equally

between the two jacks until buckling. The discrepancy that was observed in the post-buckling region can be attributed to disturbance of the initial beam's geometry.

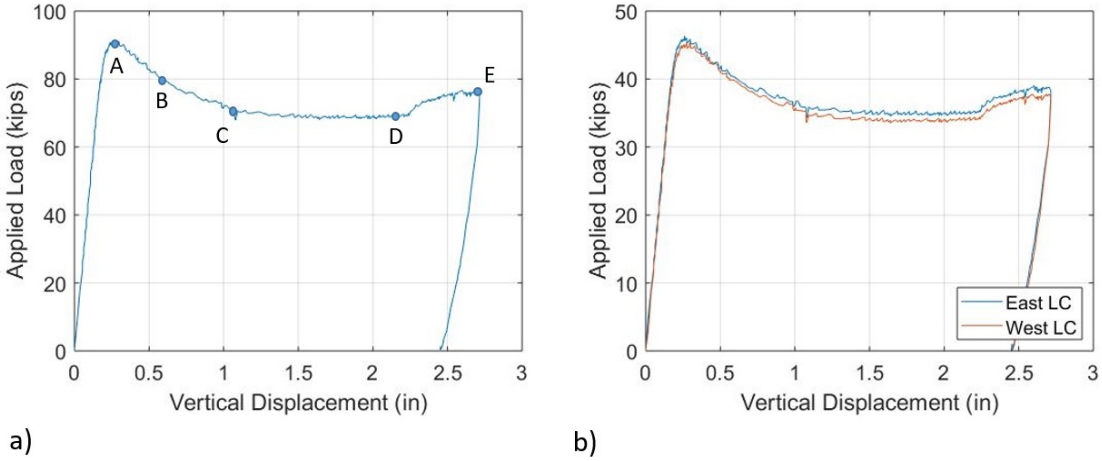

Figure 6.8: (a) Applied load vs. vertical displacement plot for Specimen 2; (b) total applied load was calculated from summation of two load cells installed at bottom of each rod (west and east side of specimen).

Based on statics and the geometry of the configuration, the distribution of reaction forces dictated that 26% of the load should travel to the intact end, while 74% should travel to the corroded end. Fig. 6.9 presents the ratio of the intact end as it was recorded by the load cells during the experimental process. The observed variation may have occurred because of the uplift observed at the bearings while the applied load was increasing. This uplift did not evolve in the same way at both supports. It is possible this could then affect the ratio of the distances between the supports and the loading area for both ends. Based on the applied load assumed to be reaching the supports, the reaction force at the corroded end was equal to **67.6 kips**.

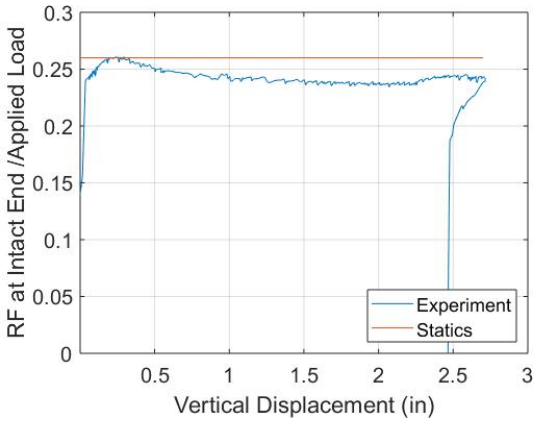

Figure 6.9: Ratio of reaction force of intact end to total applied load; based on statics, ratio should be equal to 0.26.

In Fig. 6.10, the deformation of the corroded end is presented, using images captured from two cameras that recorded the experimental process. The first camera recorded the plane of

the web (side view of the beam), while the second camera recorded the beam profile. These pictures illustrate the girder's deformation at the initial condition before loading, followed by deformations observed at different steps of the experimental procedure (Points A to E, at Fig. 6.8a).

From the initial condition pictures, two holes were observed in the corroded end. One small area with 100% section loss was located on the web below the steel angle section, and another in front of the inner bearing edge. Point A captured the deformation at peak load. Initiation of lateral displacement was observed when the vertical displacement reached 0.27 inches.

At Point B, the undertaken load was dropped to 80 kips, while both vertical and lateral displacements doubled in magnitude. At Point C, the applied load plateaued at 70 kips. Due to flange uplift, the grout was cracked, while displacements were rapidly increasing. At Point D, the applied load remained constant, while the vertical displacement approached 2.2 in., a 100% increase over the response observed at Point C under the same loading.

Similar to the first specimen, the system gained stiffness and began retaining additional load. This behavior can be attributed to the web bearing on the top of the anchor protruding from the flange. Point D captured this geometrical configuration.

At Point D, the deformed web began bearing on the flange. The uplift reduced, and the system gained stiffness and began retaining additional load. The out-of-plane displacements continued to increase, while the vertical displacement reached an additional 0.6 inch. At Point E, the experiment was terminated because the top flange reached the boundary of the lateral support.

Intact

A

B

C

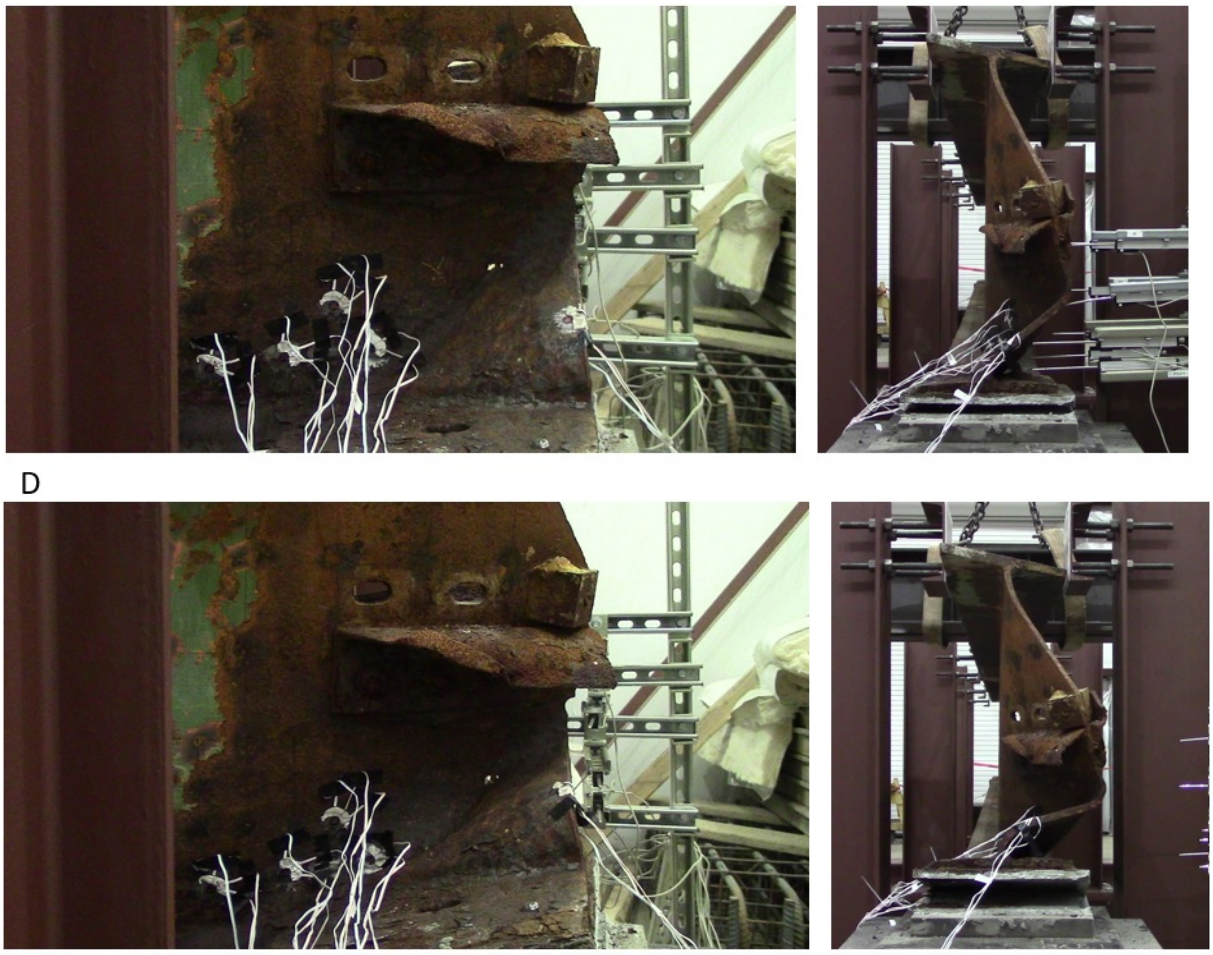

Figure 6.10: Side-by-side images showing side view of web and profile view of beam during experiment. Letters A-E correspond to Figure 6.8a.

Fig. 6.11 presents the lateral displacements as they were measured by the eight potentiometers for three different loads: 45.65, 68.48, and 91.3 kips (0.5, 0.75, and 1 F_u, where F_u equals the failure load). Two columns of instruments were installed, with four potentiometers each. The first column was placed to record the sideways deflection profile over the height of the web above the outer bearing edge (blue), while the second one above inner bearing edge (red).

Potentiometer data revealed that the area with extensive section loss presented in Fig. 6.11b defined the lateral displacement profile and consequently the failure mode. In detail, for the inner potentiometer column (red line), the maximum displacement amplitude for the total of the three examined loads (0.5, 0.75, and 1 F_u) was observed at bottom of the web, at the same depth where the lower section of the corroded area was located (illustrated with chalk lines in Fig 6.11b).

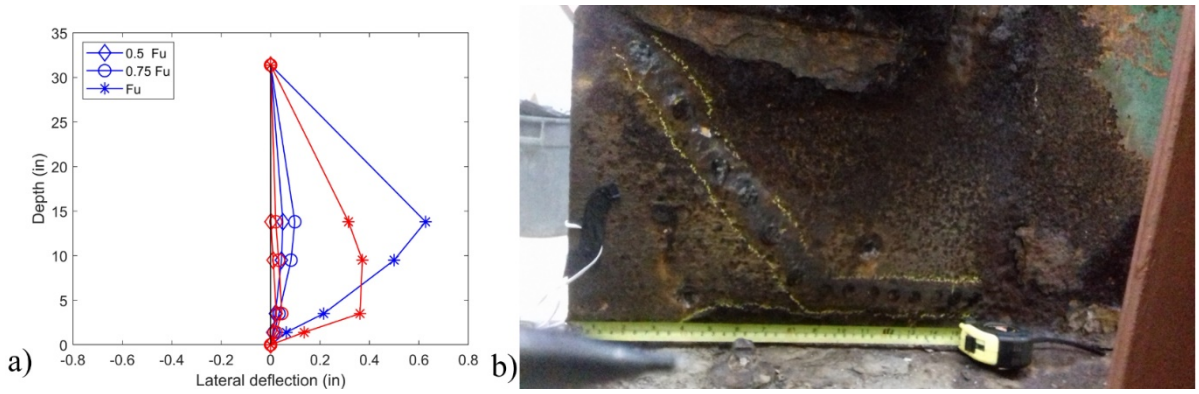

Figure 6.11: (a) Measured web lateral deflections recorded above outer web edge (blue) and above inner one (red) for 0.5, 0.75, and 1 F_u, where F_u denotes maximum applied load; (b) Area with extensive section loss at web of Specimen 2.

The same behavior was observed at the outer web edge, but in this case the maximum amplitude was noticed mid-height, where the web folded around the domain with considerable material loss. The residual deformation is presented in Fig. 6.12, and the exact potentiometer configuration in Fig. 3.26.

Figure 6.12: Residual deformation after unloading Specimen 2.

Fig. 6.13 presents the principal strains and directions for each of the SRs that were installed at Specimen 2. Their exact location is illustrated in Fig. 6.14. Five gauges were installed at the web, and one at the flange close to the hole. Fig. 6.13c visualizes the direction of the principal strains at 30 kips applied load. Compressive strains are illustrated with solid lines, and tensile strains with dashed lines. Based on these figures, the SR installed at the flange recorded almost zero strain up to peak load. The web beyond both bearing edges was subjected to shear strain deformation. In addition, it is worth noticing how a sudden stress redistribution, attributed to bending strains, was captured at failure from the total of the gauges.

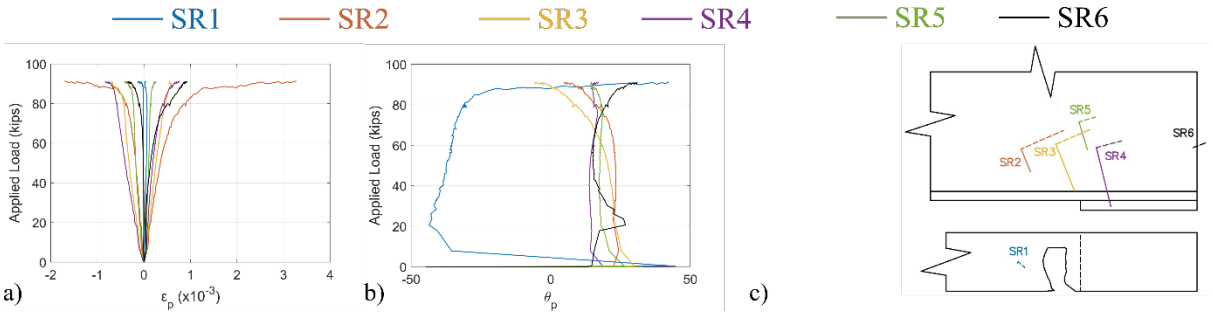

Figure 6.13: (a) Principal strains and (b) directions up to peak load from SRs installed on Specimen 2. (c) Direction and normalized magnitude at 30 kips applied load for each SR.

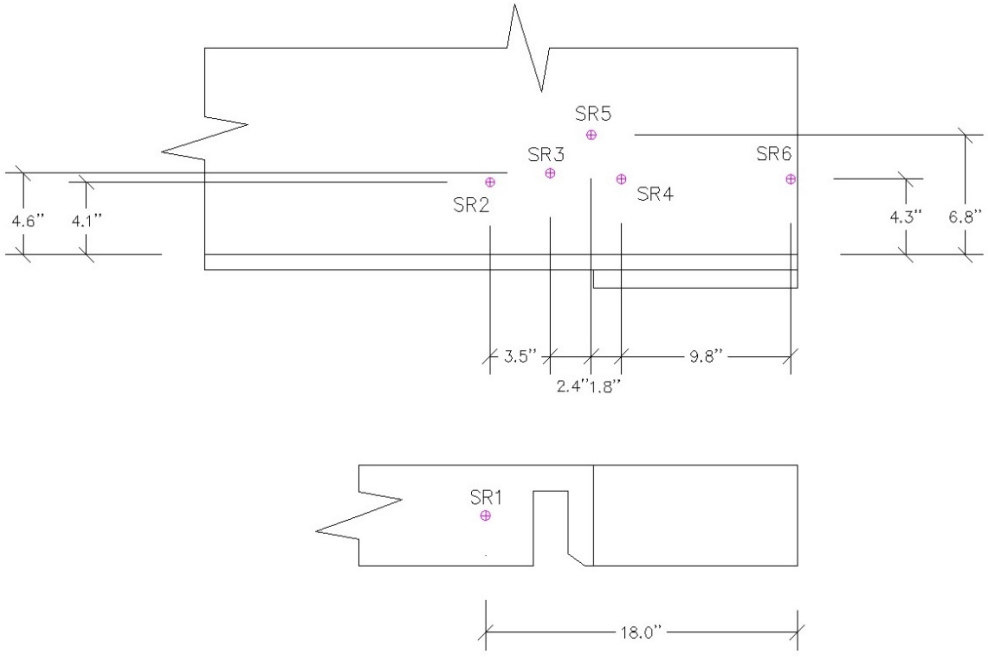

Figure 6.14: Exact location and SR nomenclature for Specimen 2.

6.3 Specimen 3

Specimen 3 was successfully tested on Nov. 28, 2018. According to the summation of the reaction forces measured in the two load cells installed at the bottom end of each rod, the total applied load at failure was equal to 112.45 kips (Fig. 6.15a). As previously noted, the maximum beam deflection was measured using a linear variable displacement transducer (LVDT) installed on the outer face of the bottom flange beneath the point of load application. Fig. 6.15b confirms the consistency of the load applied by each jack during the experimental process. This load was applied equally between the two jacks during the whole process.

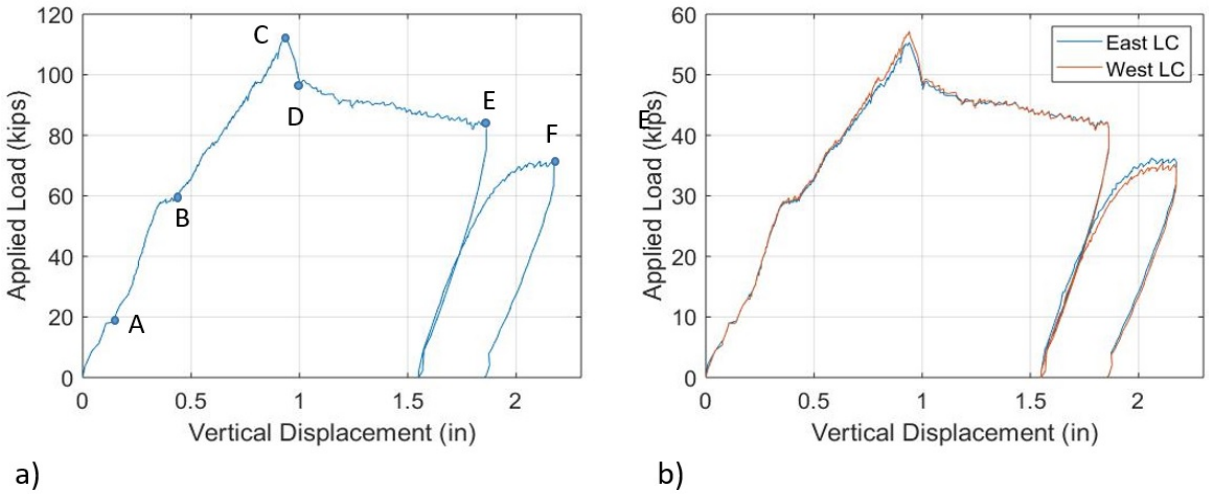

Figure 6.15: (a) Applied load vs. vertical displacement plot for Specimen 3; (b) total applied load was calculated from summation of two load cells installed at bottom of each rod (west and east side of specimen).

Based on statics and the geometry of the configuration, the distribution of reaction forces dictated that 24% of the load should travel to the intact end, while 76% should travel to the corroded end. Fig. 6.16 presents the ratio of the intact end as it was recorded by the load cells during the experimental process. The observed variation may have occurred because of the uplift observed at the bearings while the applied load was increasing. This uplift did not evolve in the same way at both supports. It is possible this could then affect the ratio of the distances between the supports and the loading area for both ends. Based on the applied load assumed to be reaching the supports, the reaction force at the corroded end was equal to **84.25 kips**.

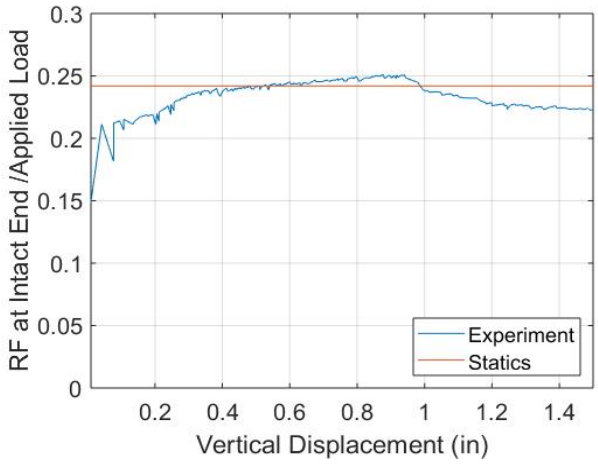

Figure 6.16: Ratio of reaction force of intact end to total applied load. Based on statics, ratio should be equal to 0.24.

In Fig. 6.17, the deformation of the corroded end is presented, using images captured from two cameras that recorded the experimental process. The first camera recorded the plane of the web (side view of the beam), while the second camera recorded the beam profile. These pictures illustrate the girder's deformation at the initial condition before loading, followed by

deformations observed at different steps of the experimental procedure (Points A to E, at Fig. 6.15a).

From the initial condition pictures, two holes were observed in the corroded end. One small area with 100% section loss was located on the web below the steel angle section, and another at the base of the web. The bottom hole expanded 6 in. beyond the inner edge of the bearing. However, due to extensive bearing uplift, the web started bearing on the flange prior to loading.

After the loading procedure initiated, the applied load temporarily plateaued at Points A and B (Fig. 6.15a). This behavior was attributed to the sliding of the web on the upper face of the flange. At Point A, the translation occurred instantly and is captured by a short straight line. At Point B, sliding evolved progressively and is illustrated by a wavy line, almost parallel to the x axis.

Point C captured the failure mode and load of the specimen. From the initial condition up to Point C, the web deformation was described by a progressive sideways deflection. The bottom of the web was folding as a result of the bearing to the flange under loading.

Compared to the results of the first two specimens, this was the first time that a sudden stiffness loss was observed after peak load was reached (leading to Point D). Beyond that point, the load was reducing under a constant rate up to Point E, where unloading took place. In order to further investigate the behavior of the specimen, the research team reloaded the specimen. The girder initially had the same stiffness, following the unloading path of the plot. Close to 50 kips applied load, the stiffness began reducing. At Point F, the experiment was terminated because the top flange reached the boundary of the lateral support.

Initial

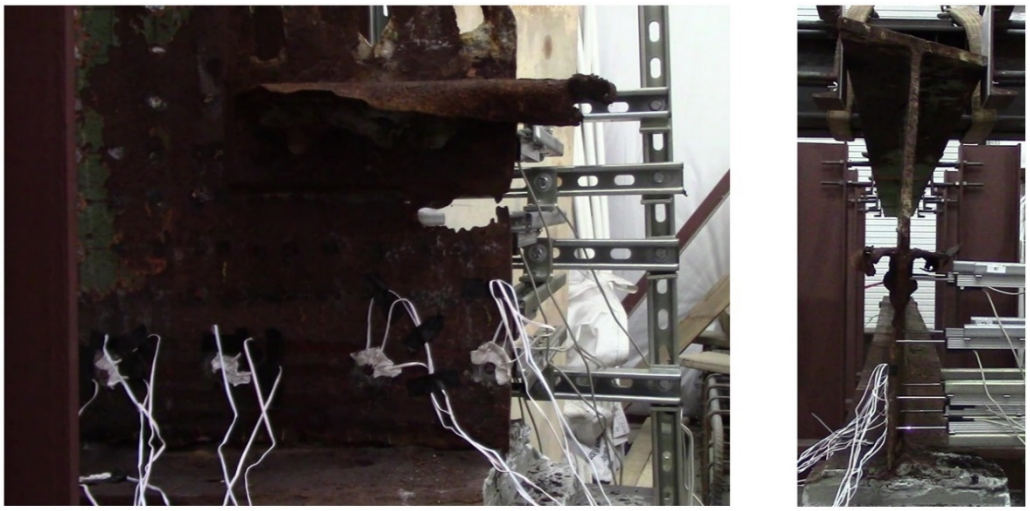

A

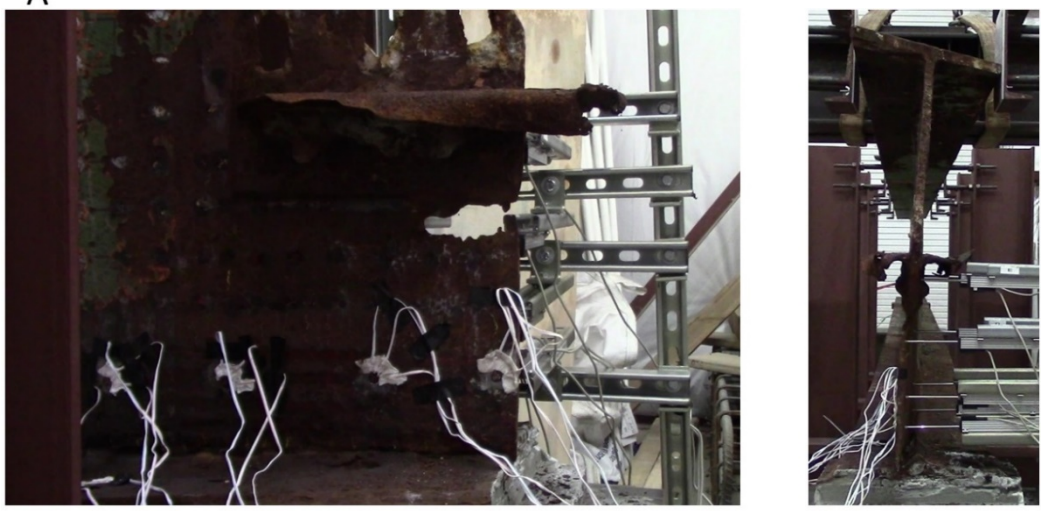

B

C

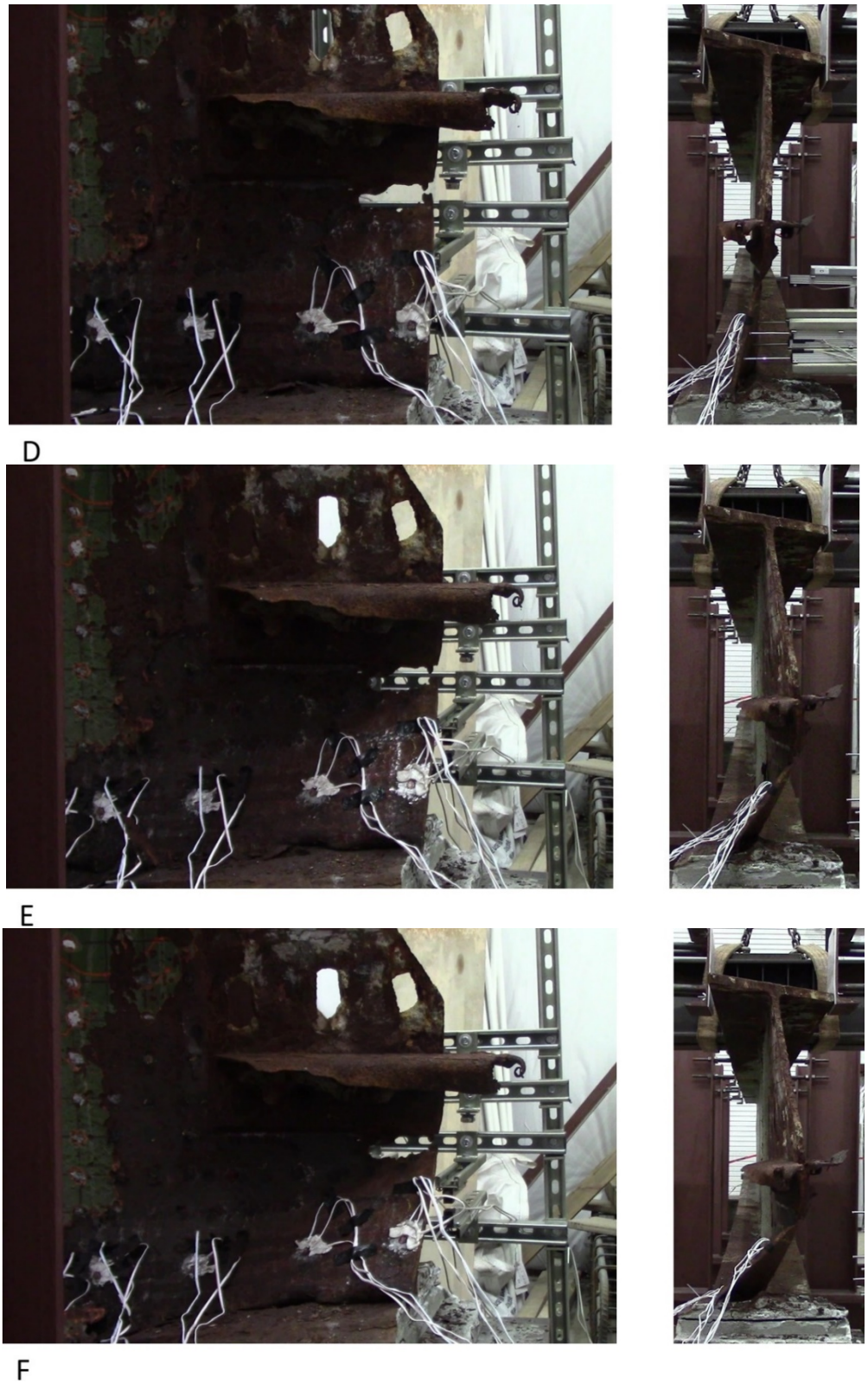

Figure 6.17: Side-by-side images showing side view of web and profile view of beam during experiment. Letters A-F correspond to Fig. 6.15a.

Fig. 6.18 presents the lateral displacement profiles as they were recorded by the eight potentiometers formulating two columns with four instruments each for 0.5 and 0.75 F_u, where F_u equals the maximum applied load. The failure mode was not captured, because the top potentiometer at each column was removed to be protected from the remaining steel angle section, which was approaching the instrumentation frame while the load was increasing (Fig. 6.17b). The first potentiometer column was placed above the outer edge of the bearing (blue), and the second one above the inner edge of the bearing (red). The exact potentiometer configuration is presented in Fig. 3.32. The lines were not connected to the bottom of the web in order to mimic the discontinuous web profile due to the 18 in. long hole existence.

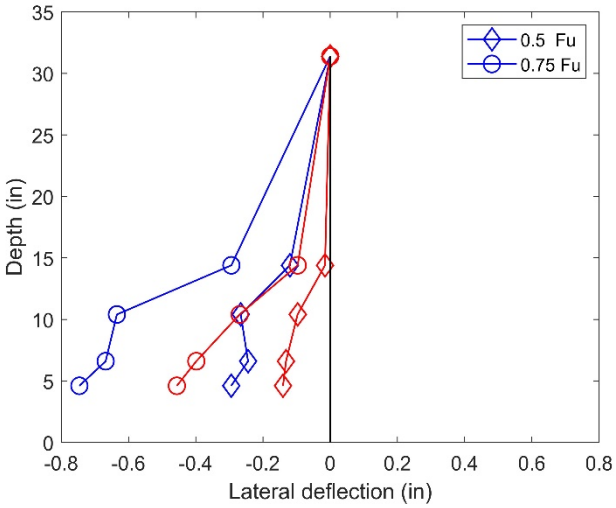

Figure 6.18: Measured web lateral deflection recorded above outer web edge (blue) and above inner one (red) for 0.5 and 0.75 F_u, where F_u denotes maximum applied load.

Interpreting these figures, potentiometers at the same height along the beam's length followed a similar pattern, capturing the web sliding on the flange, across the same direction. The residual displacement is presented in Fig. 6.19.

Figure 6.19: Residual deformation after unloading Specimen 3.

Fig. 6.20 presents the principal strains and directions for each one of the SRs that were installed on Specimen 3. Their exact location is illustrated in Fig. 6.21.

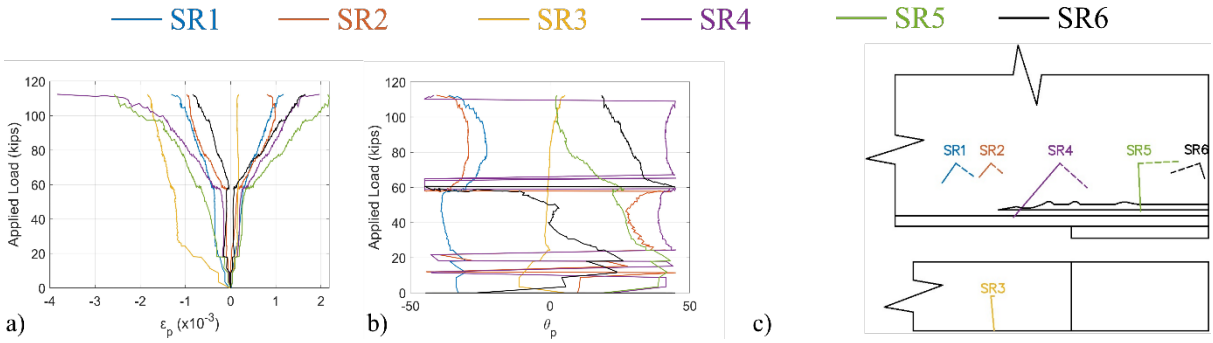

Figure 6.20: (a) Principal strains and (b) directions up to peak load from SRs installed in Specimen 3; (c) direction and normalized magnitude in respect to maximum strain at peak load for each SR.

During the largest part of the loading process, the principal strain direction at SR3 was approaching zero, revealing that flange was subjected to direct tension. On the other hand, SR5 with the initiation of the loading process recorded shear deformation (θ approaching 45 degrees), which was progressively reduced to 2 degrees at peak load, reflecting pure compression. This behavior can be attributed to the contact with the flange. However, compared to the rest of the gauges installed on the web, it experienced the most intense compressive strains. One can assume that the decomposition of these strains to membrane and bending strains would include increased bending strains due to its position. In particular, SR5 is located very close to the imaginary line around which the web folds (Fig. 6.17f).

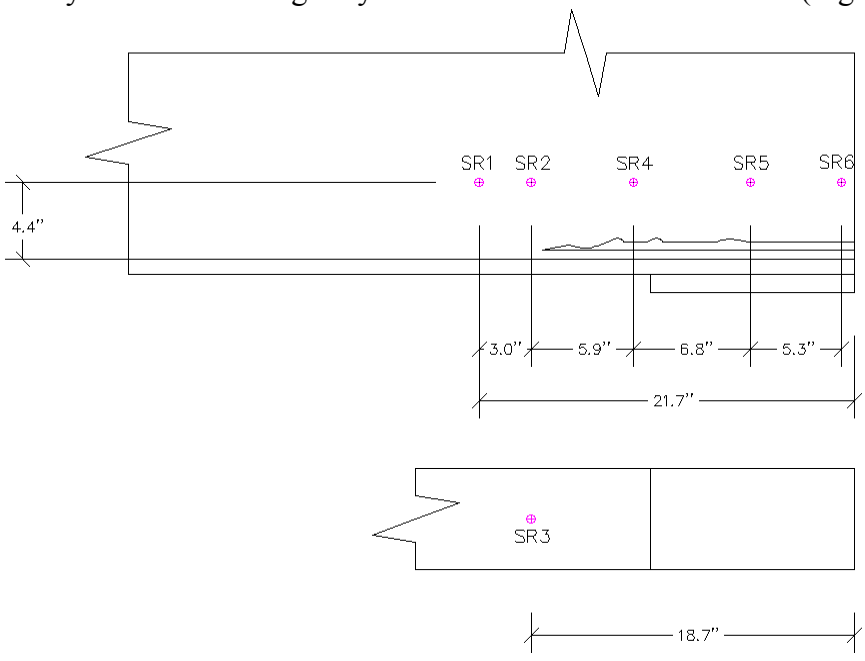

Figure 6.21: Exact location and SR nomenclature for Specimen 3.

6.4 Specimen 4

Specimen 4 was tested on Feb. 20, 2019. According to the summation of the reaction forces measured in the two load cells installed at the bottom end of each rod, the total applied load at failure was equal to 53.33 kips (Fig. 6.22a). However, instead of web buckling, a long wave instability mode was observed along the longitudinal axis of the specimen.

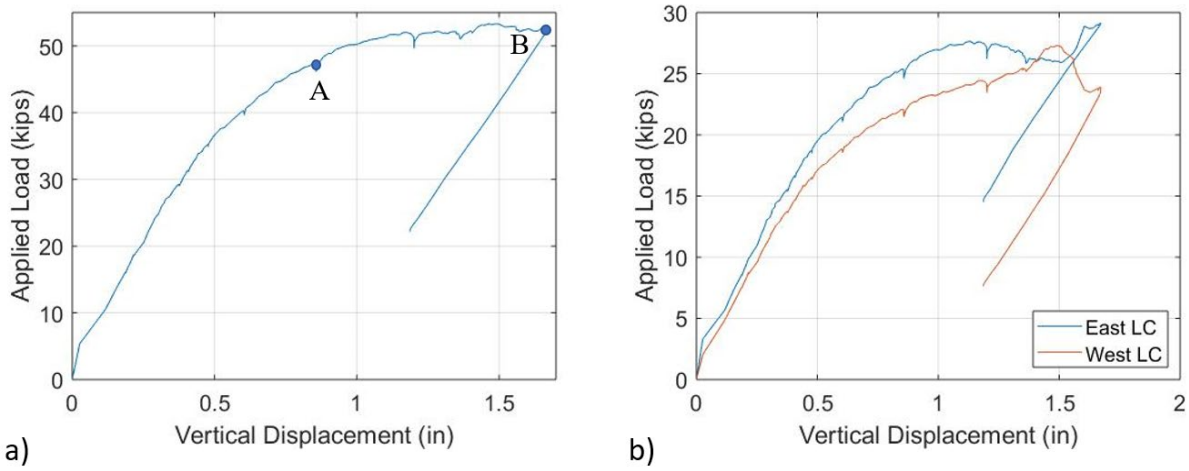

Figure 6.22: Applied load vs. vertical displacement plot for Specimen 4; b) total applied load was calculated from summation of two load cells installed at bottom of each rod (west and east side of specimen).

Based on statics and the reduced length of the specimen compared to the previous cases, the distribution of reaction forces dictated that 28% of the load should travel to the intact end, while 72% should travel to the corroded end. Fig. 6.23 presents the ratio of the intact end as it was recorded by the load cells during the experimental process. As already mentioned, no beam end failure was observed; thus, the capacity of the corroded end was not attained. However, it is worth noticing the loading redistribution that took place for vertical displacement equal to 1.28 in., due to the instability mode initiation.

In Fig. 6.24, the deformation of the corroded end is presented using images captured from two cameras that recorded the experimental process. The first camera recorded the plane of the web (side view of the beam), while the second camera recorded the beam profile. These pictures illustrate the girder's deformation at the initial condition before loading, followed by deformations observed at different steps of the experimental procedure (Points A and B, Fig. 6.22a).

At Point A, the specimen has already experienced maximum vertical displacement equal to 0.86 inch. However, the initial imperfection of the beam governed the deformation profile, with lateral displacements initiated at midspan. In particular, as illustrated with the red arrow in Fig. 6.24, the bottom flange exhibited extensive in-plane translation. Between Points A and B, the applied load tended to plateau with rapidly increasing deformations. The deformation profile indicated torsional buckling. In detail, both flanges were deflecting along the longitudinal axis, mainly in the domain defined by the two LTB restrictions located closer to the studied end.

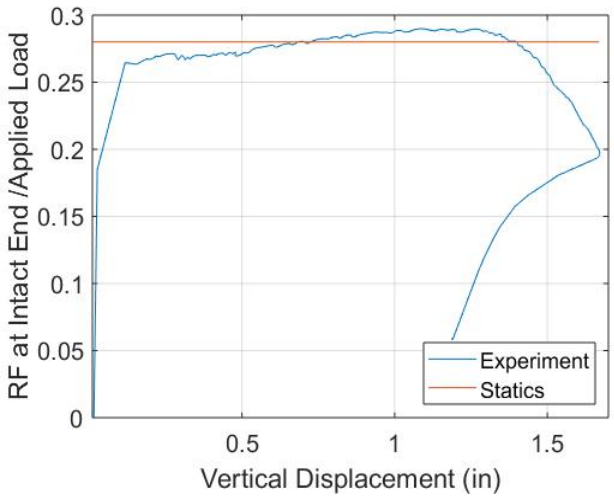

Figure 6.23: Ratio of reaction force developed at intact end to total applied load, as recorded by load cells during experimental process.

Fig. 6.25 presents the lateral displacements as they were measured by the eight potentiometers for three different loads, 26.7, 40, and 53.3 kips (0.5, 0.75, and 1 F_u, where F_u equals the failure load). Two columns of instruments were installed, with four potentiometers each. The first column was located to record the sideways deflection profile along the overhang length (blue), while the second one above the middle of the bearing. The exact configuration is presented in Fig. 3.38.

With a macroscopic look at the residual deformation, a long wave failure mode dominated and no instability phenomena relative to the corroded end were observed. However, for applied load equal to 40 kips (Fig. 6.25), the inner potentiometer configuration captured extensive sideways deflection (red line with circular marker) developed at the opposite direction of the initial leftwards deflection pattern (pyramid marker). The displacement profile was observed at the lower half of the web, with the maximum amplitude observed 2 in. from the bottom.

Additionally, SR recordings, Fig. 6.27, revealed stress redistribution taking place between SRs 2, 4, and 5 for applied load equal to 35 kips. In particular, the strain magnitude was reducing at the location of the first two sensors, while it was rapidly increasing at the location of SR5. These clues denoted that local instability phenomenon potentially occurred at this area. Indeed, the videos, along with a close look at the residual deformation, revealed that local buckling took place at the narrow strip with limited remaining thickness, expanding along the longitudinal axis between the strain gauges and the bearing plate. The buckling area is highlighted with a yellow line in Fig. 6.24. It is unclear if the observed local buckling came before the long wave instability, or if it was a second-order phenomenon resulting from the extensive midspan lateral and torsional deflection.

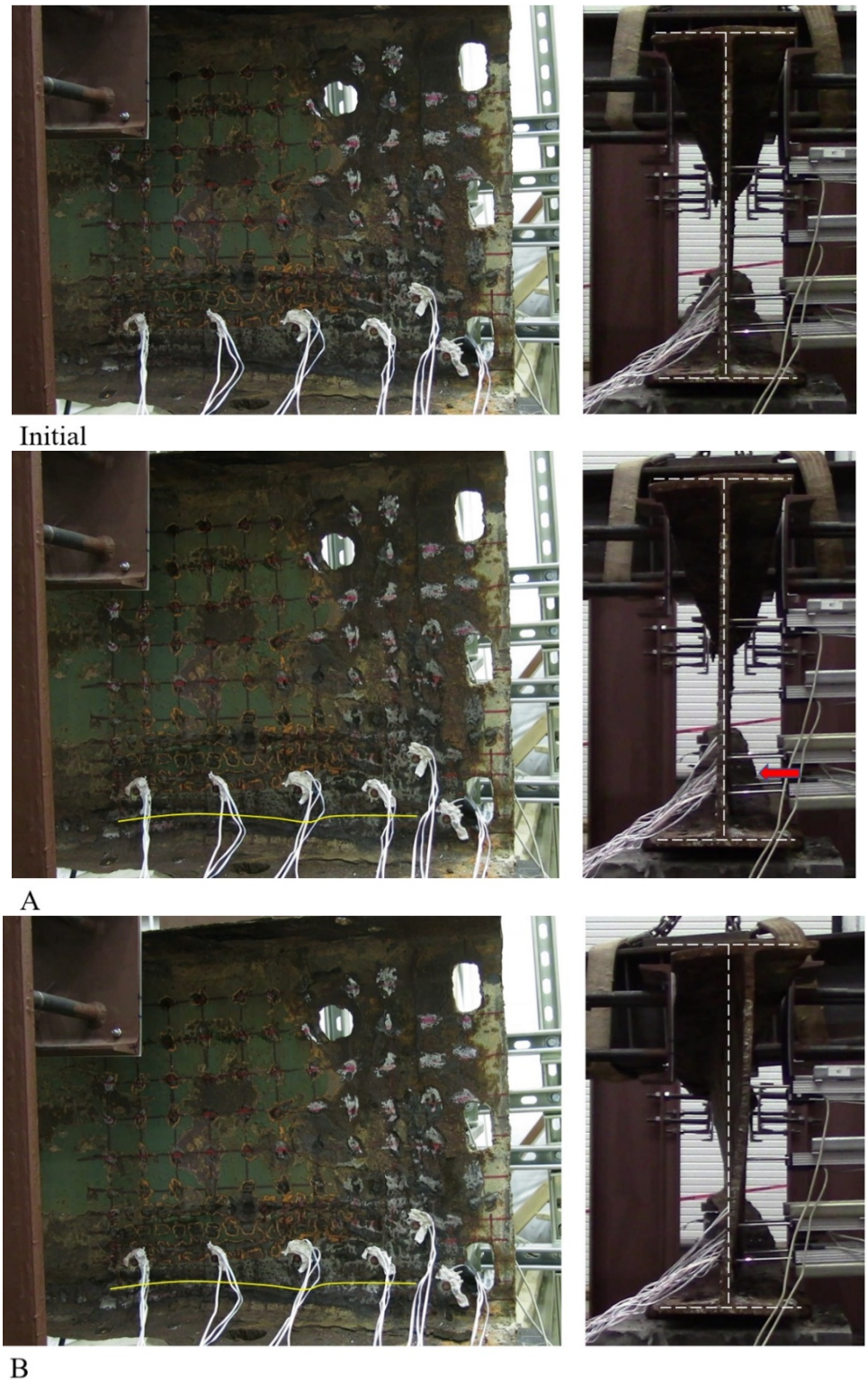

Figure 6.24: Side-by-side images showing side view of web and profile view of beam during experiment. Letters A-B correspond to Fig. 6.22a. The yellow line denotes local buckling domain, while dashed white line denotes mid surfaces of Specimen 4.

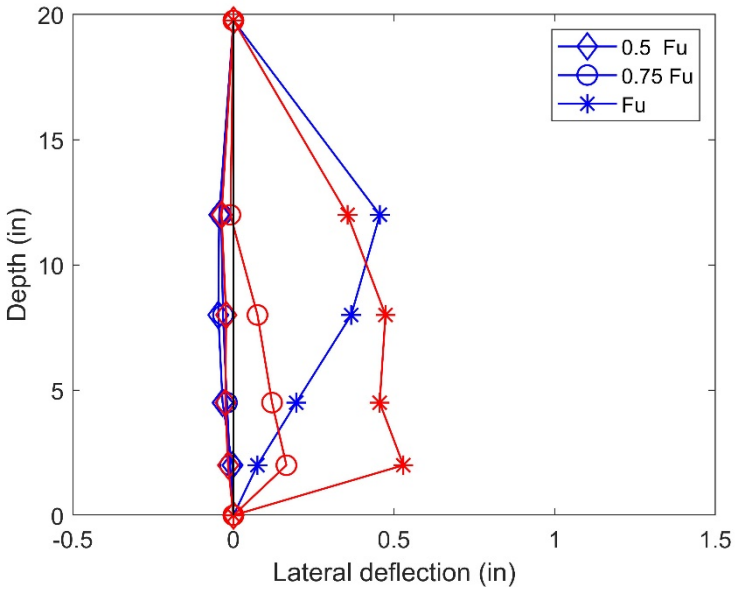

Figure 6.25: Measured web lateral deflection recorded at overhang length (blue) and above center of bearing (red) for 0.5, 0.75, and 1 F_u, where F_u denotes maximum applied load.

The residual deformation of the corroded end is presented in Fig. 6.26. Considering the long wave failure mode, the only observation worth noting at the studied end is the 17 in. long buckling zone above the support.

Figure 6.26: Residual deformation of studied end.

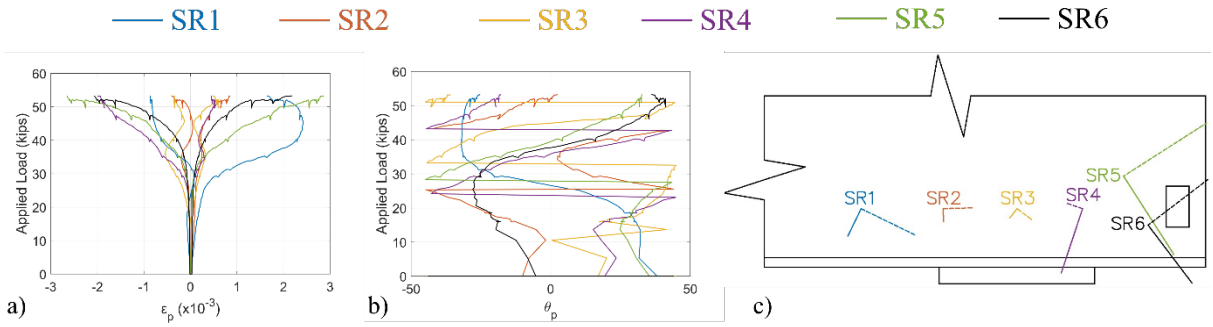

Figure 6.27: (a) Principal strains and (b) directions up to peak load from SRs installed in Specimen 4. (c) Visualization of direction and magnitude at peak load for each SR.

Regarding bearing behavior, the web beyond both bearing edges was subjected to shear strain deformation, while the reaction force development resulted in compression above bearing. It is worth mentioning that SRs 1 and 5, which captured shear deformations, were in the plastic regime at peak load. However, no safe conclusion can be drawn from this observation, for three reasons. First, a local instability phenomenon had already occured, so reaction force redristribution had taken place. Second, due to extensive sideways deflection, the contribution of bending strains along the web thickness could not be neglected. Finally, the nattural corrosion pattern resulted in nonuniform thickness reduction; thus, the strain recordings depended on the remaining thickness of the installation point.

The SR nomenclature and the exact configuration are illustrated in Fig. 6.28.

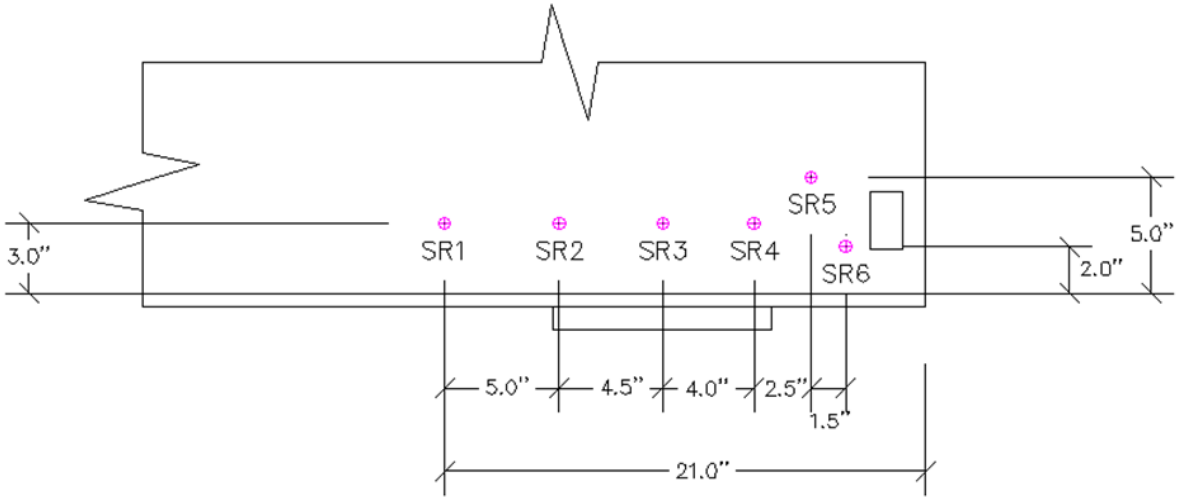

Figure 6.28: Exact location and SR nomenclature for Specimen 4.

6.5 Specimen 5

Specimen 5 was successfully tested on March 20, 2019. According to the summation of the reaction forces measured in the two load cells installed at the bottom end of each rod, two peak loads were observed, the first one at 45.14 kips and the second one at 88.28 kips. Fig. 6.29b confirms the consistency of the load applied by each jack during the experimental process.

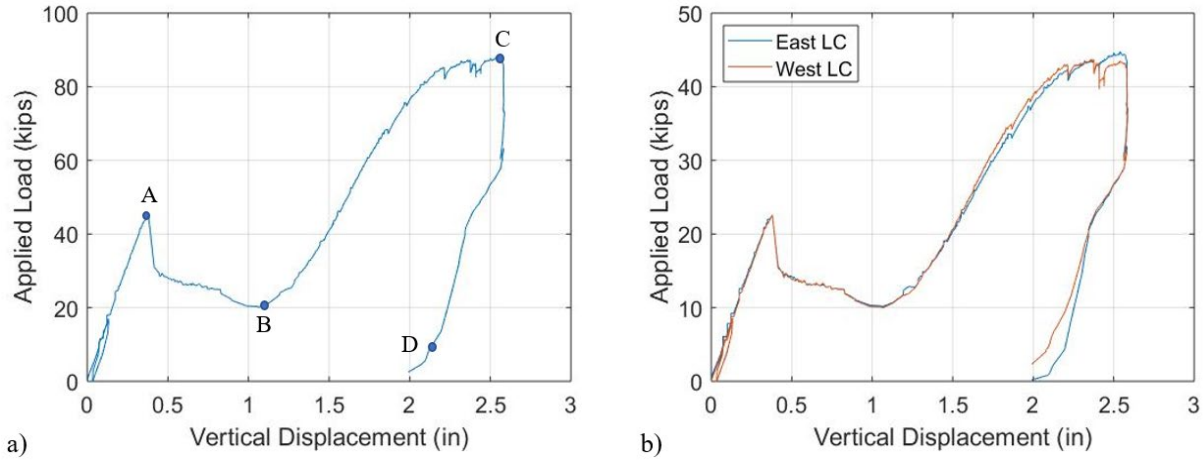

Figure 6.29: (a) Applied load vs. vertical displacement plot for Specimen 5; (b) total applied load was calculated from summation of two load cells installed at bottom of each rod (west and east side of specimen).

Based on statics and in particular on the nominal distance of bearings center lines and the midpoint of the cross beam, 32% of the applied load should travel to the intact end, while 68% should travel to the corroded one. However, the initial condition of the beam affected this ratio. In detail, the bottom flange was warped at bearings, as well as the top one at the point of load application. While the applied load was increasing, the deformation of the flange allowed a more uniform contact between the cross beam and the specimen, improving the load distribution ratio. In addition, this variation could be attributed to the uplift that did not evolve in the same way at both supports. Based on the applied load assumed to be reaching the supports, the reaction force at the corroded end was equal to **30.94** and **65.7 kips** for the first and the second peak, respectively.

In Fig. 6.31, the deformation of the corroded end is presented, using images captured from two cameras that recorded the experimental process. The first camera recorded the plane of the web (side view of the beam), while the second camera recorded the beam profile. These pictures illustrate the girder's deformation at the initial condition before loading, followed by deformations observed at different steps of the experimental procedure (Points A to D, Fig. 6.29a). Fig. 6.32 presents the lateral displacement profiles as they were measured by the eight potentiometers for three different loads, 0.5, 0.75, and 1 F_u, where F_u is the corresponding load at Point A. Two columns of instruments had been installed. The first one was placed close to the inner bearing edge, while the second one (Fig. 3.42) between the adjacent holes

close to beam's end. The red lines were not connected to bottom of the web bounds in order to mimic the discontinuous web profile due to holes existence.

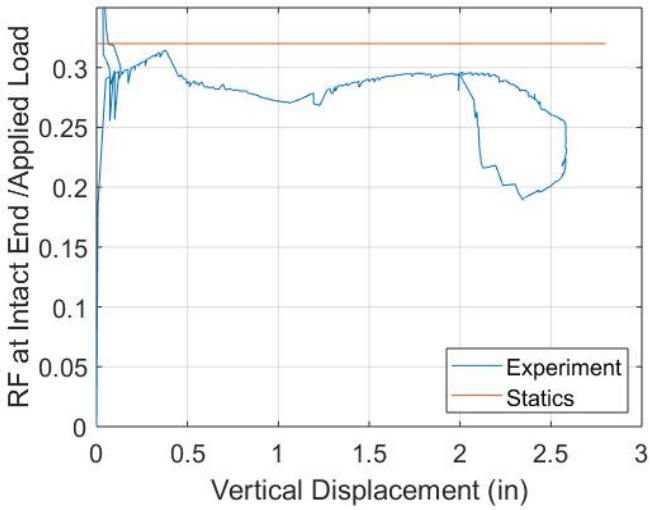

Figure 6.30: Ratio of reaction force of intact end to total applied load. Based on statics, ratio is equal to 0.32.

The preloading conditions of the corroded end, which was mainly characterized by the combination of artificial and corrosion holes expanding along the largest part of the bottom of the web, defined the failure. In detail, at Point A (Fig. 6.29), a brittle failure was observed at the narrow material strips located at the outer web part. The buckling area was limited at the strips area, potentially due to the corrosion holes, which prevented the buckling wave propagation to the rest of the web. The web uniformly translated out of plane. This behavior can be observed both at cameras (Fig. 6.31a) as well as at potentiometer recordings. The blue line (Fig. 6.32) at peak load described a buckling wave formulated at the outer web part, while the red one an almost linear displacement profile.

The brittle failure was combined with instant 30% load loss. This was the first time that a sudden load drop followed the peak load. This first peak can be considered as the capacity of specimen.

The continuously reducing specimen's stiffness continued up to Point B, where the protruding web part started bearing on the bottom flange. The system gained stiffness and began retaining additional load, up to the total load of 88.28 kips at Point C, where a global system failure mode initiated. The extensive lateral displacements at the corroded end distorted the member's center line for its straightness. This condition could have triggered the long wave instability mode that resulted in the lateral translation of the corroded end. The experiment was terminated due to the distortion of the experimental support configuration under the corroded end at Point D.

Initial

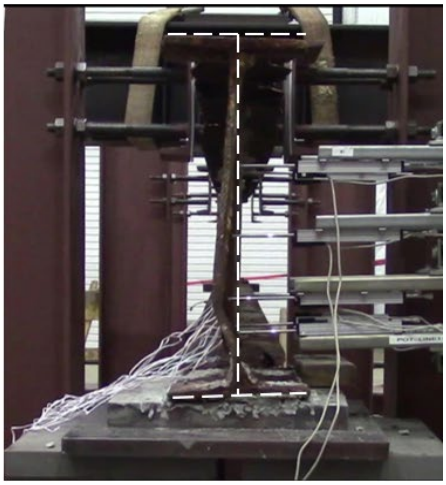

A

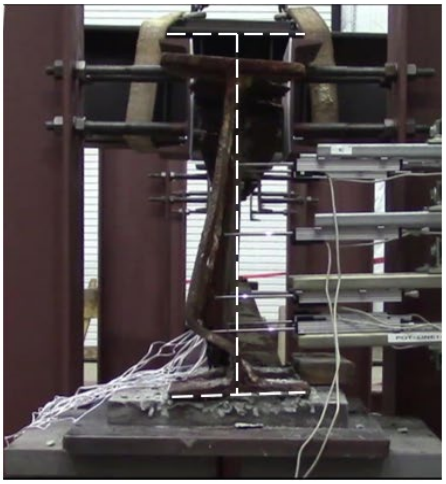

B

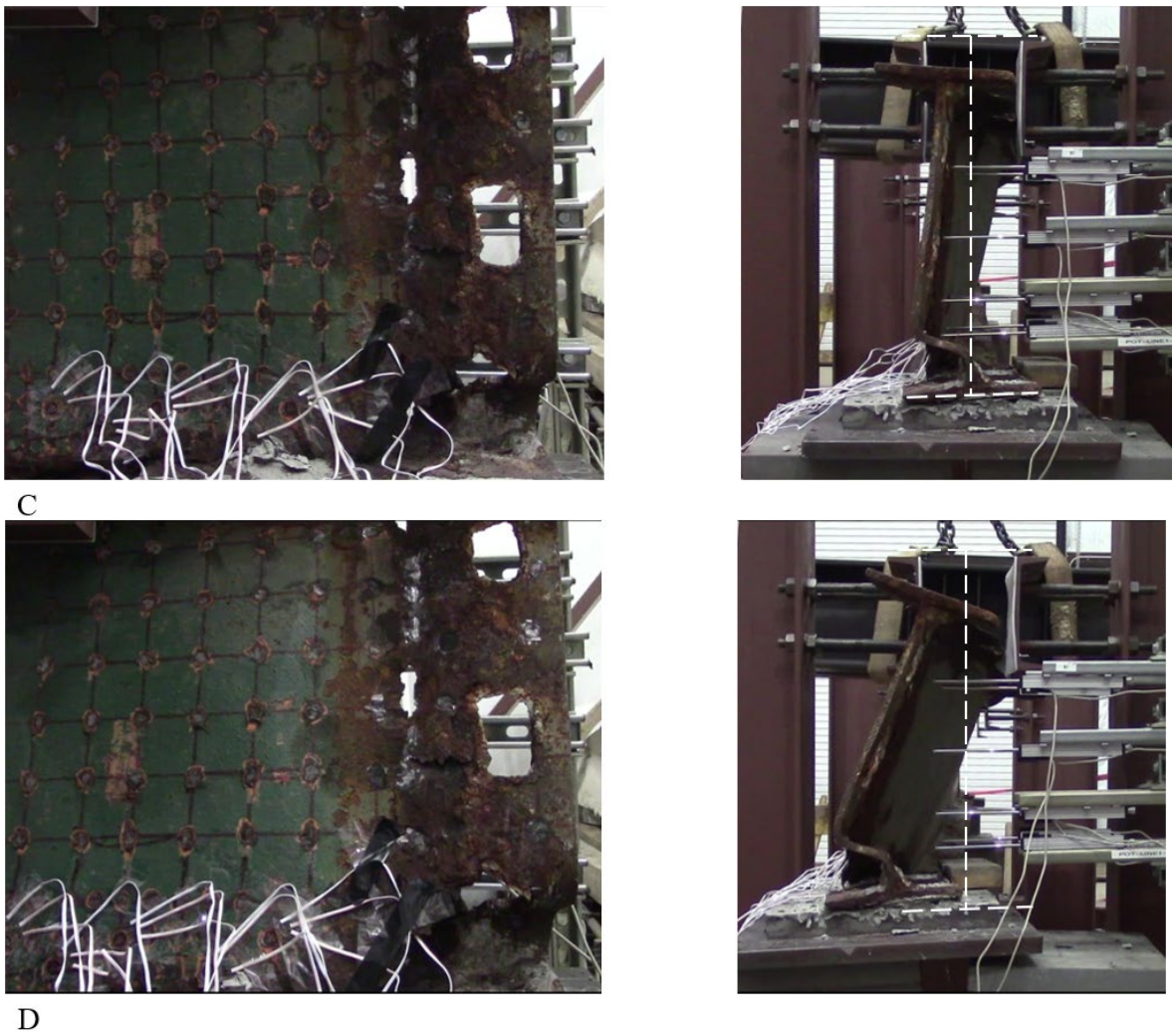

Figure 6.31: Side-by-side images showing side view of web and profile view of beam during experiment. Letters A-D correspond to Fig. 6.29a.

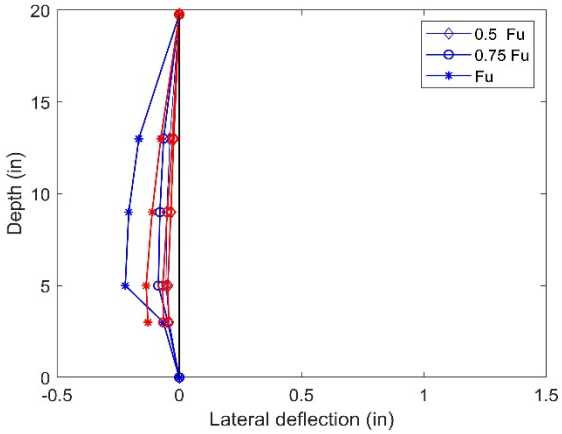

Figure 6.32: Measured web lateral deflection recorded above outer bearing edge (blue) and above inner one (red).

The residual deformation of the corroded end is presented in Fig. 6.33. Note that crippling was observed underneath the load application area, Fig. 6.34.

Figure 6.33: Residual deformation of corroded end after unloading.

Figure 6.34: Web crippling observed underneath area of loading.

Fig. 6.35 presents the principal strains and directions for each one of the SRs that were installed on Specimen 5. Their exact location is illustrated in Fig. 6.34. When failure occurred, the total of SRs were in the elastic regime; however, the SR configuration did not allow to explore the strain conditions at the narrow material strips where the buckling wave was formulated.

Regarding bearing behavior, the part of the web located above bearing was subjected to direct compression, while beyond the bearing web shear deformation governed.

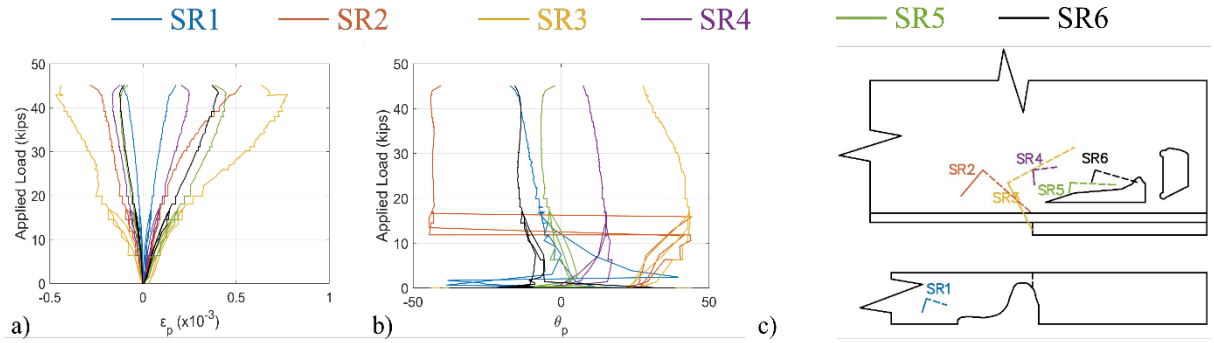

Figure 6.35: (a) Principal strains and (b) directions up to 45.14 applied kips. (c) Direction and normalized magnitude in respect to maximum strain at peak load; the dashed line illustrates the compressive direction, and the solid line the tensile one.

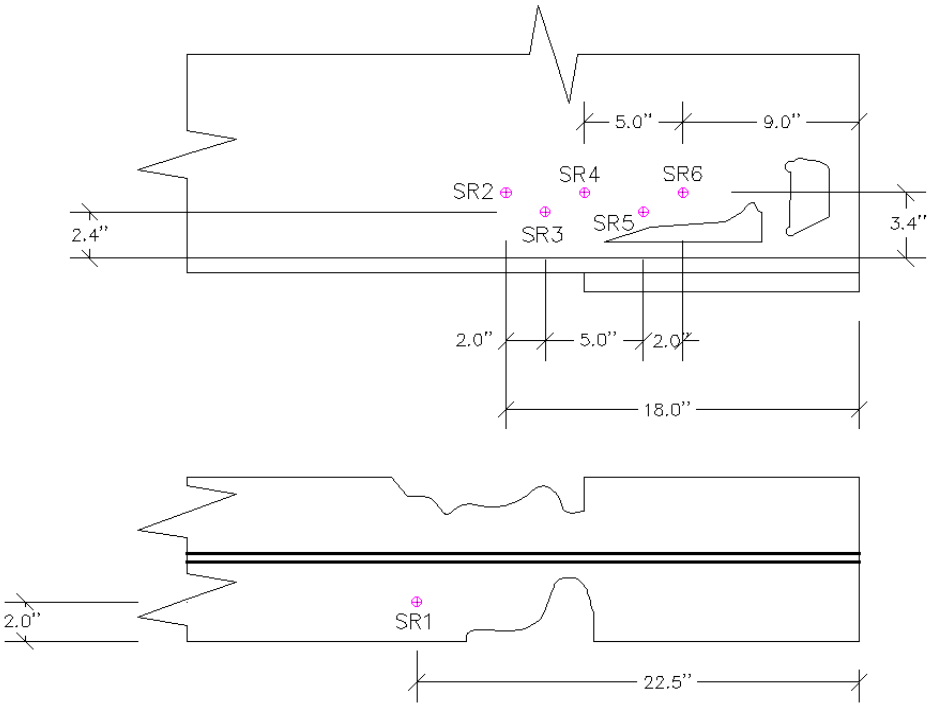

Figure 6.36: SR configuration for Specimen 5.

6.6 Specimen 6

Specimen 6 was successfully tested on June 5, 2019. According to the summation of the reaction forces measured in the two load cells installed at the bottom end of each rod, the total applied load at failure was equal to 58.8 kips (Fig. 6.37a). As previously noted, the maximum beam deflection was measured using a linear variable displacement transducer (LVDT) installed on the outer face of the bottom flange beneath the point of load application.

Fig. 6.37b confirmed the consistency of the load applied by each jack during the experimental process. This load was seen to be applied equally between the two jacks until

the buckling point. The discrepancy that was observed in the post-buckling region could be attributed to disturbance of the initial beam's geometry.

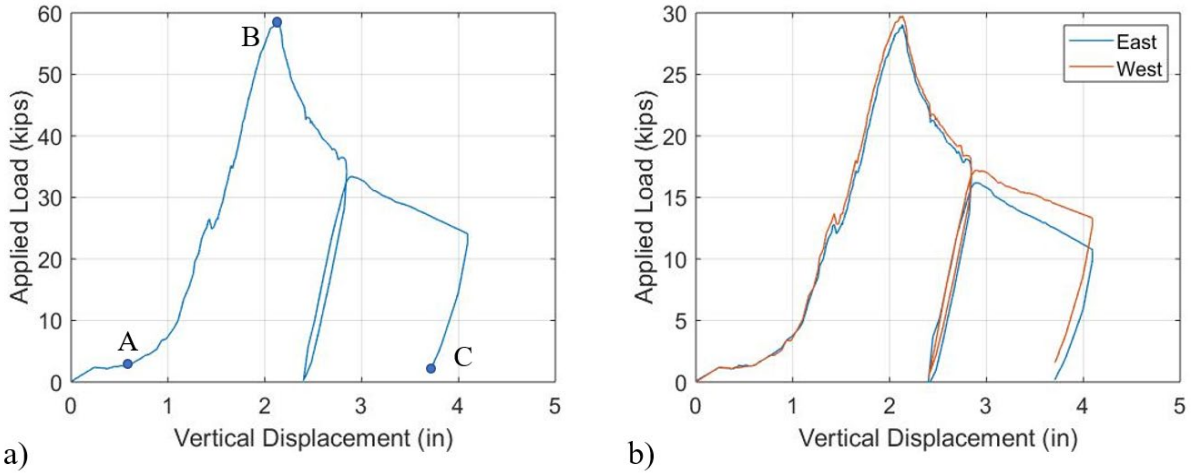

Figure 6.37: (a) Applied load vs. vertical displacement plot for Specimen 6; (b) total applied load was calculated from summation of two load cells installed at bottom of each rod (west and east side of specimen).

Based on statics and the geometry of the configuration, the distribution of reaction forces dictated that 32% of the load should travel to the intact end, while 68% should travel to the corroded end. Fig. 6.38 presents the ratio of the intact end as it was recorded by the load cells during the experimental process. During the first loading steps, the experimental ratio perfectly matched the statics, validating the decision not to grout the interface between the support and the bottom flange. The observed variation after the loading initiation may have occurred due to the uplift observed at the bearings while the load was increasing. This uplift did not evolve in the same way at both supports, having an impact on the effective length as well as the distances between the supports and the loading area for both ends. Based on the applied load assumed to be reaching the supports, the reaction force at the corroded end was equal to **40.86 kips**.

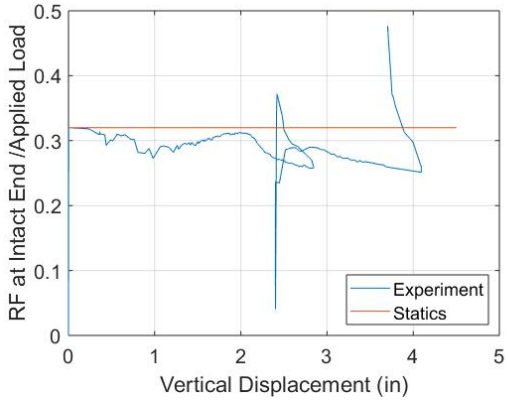

Figure 6.38: Ratio of reaction force of intact end to total applied load. Based on statics, ratio is equal to 0.32.

The failure mechanism of Specimen 6 is explained through Figs. 6.39 to 6.41. In Fig. 6.39, the deformation of the corroded end is presented, using images captured from two cameras that were recording the web plane and the cross-section view of the beam during the experimental process. Fig. 6.40 presents the lateral displacements as they were measured by the eight potentiometers for three different loads, 0.5, 0.75, and 1 F_u, where F_u is the bearing failure load. Two columns of instruments were installed. The first one (blue) was placed above the outer edge of the bearing measuring the deflection of the stiff outer part of the web, while the second one above the inner edge of the bearing (red) recording the displacement of the nonsupported web. Red lines were not connected to web bounds, in order to mimic the discontinuous web profile due to holes existence. Finally, Fig. 6.42 presents the principal strain and its directions at six locations on web and flange, and the exact strain rosettes configuration is presented in Fig. 6.43.

After the loading initiation, due to the hole's extension, the web had limited contribution to the specimen's stiffness. The initial plateau observed at the load displacement curve captured mainly the flange action and was characterized by rapidly increasing deformations. This situation alternated for deflection equal to 0.6 in. (Fig 6.39a); where the unrestricted web began bearing the flange, the system gained stiffness and started retaining additional load. Principal stains development revealed that contact was initiated at the domain close to SR6, and the area below SR4 followed. The nonrestricted web continued experiencing large deformations, following the initial imperfection profile (Fig. 6.40), while the stiff part of the web (blue) was deflecting along the opposite direction. Finally, at 58.8 kips applied, the bearing on flange web buckled (Fig. 6.40b); its bottom, which was in contact with the flange, remained almost at constant position compared to 0.75 F_u, while the top part translated 0.8 in. to the left (Fig. 6.40). The post-peak regime was characterized by rapidly reducing stiffness and extensive uplift (Fig. 6.37).

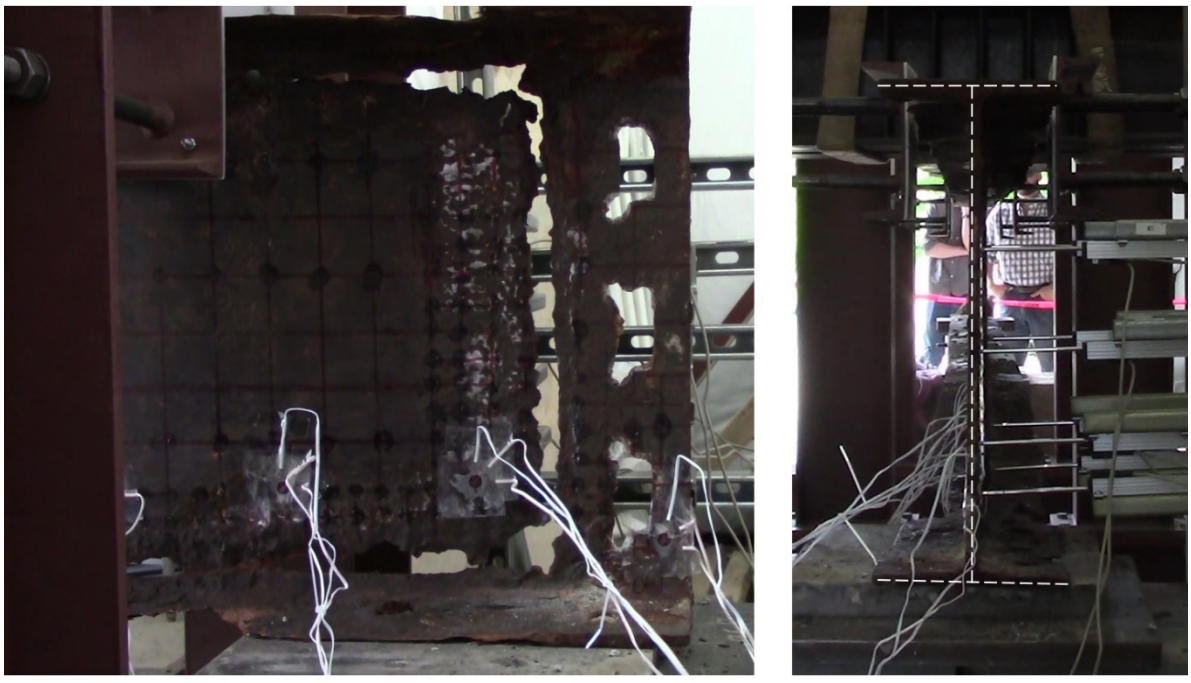

Initial

A

B

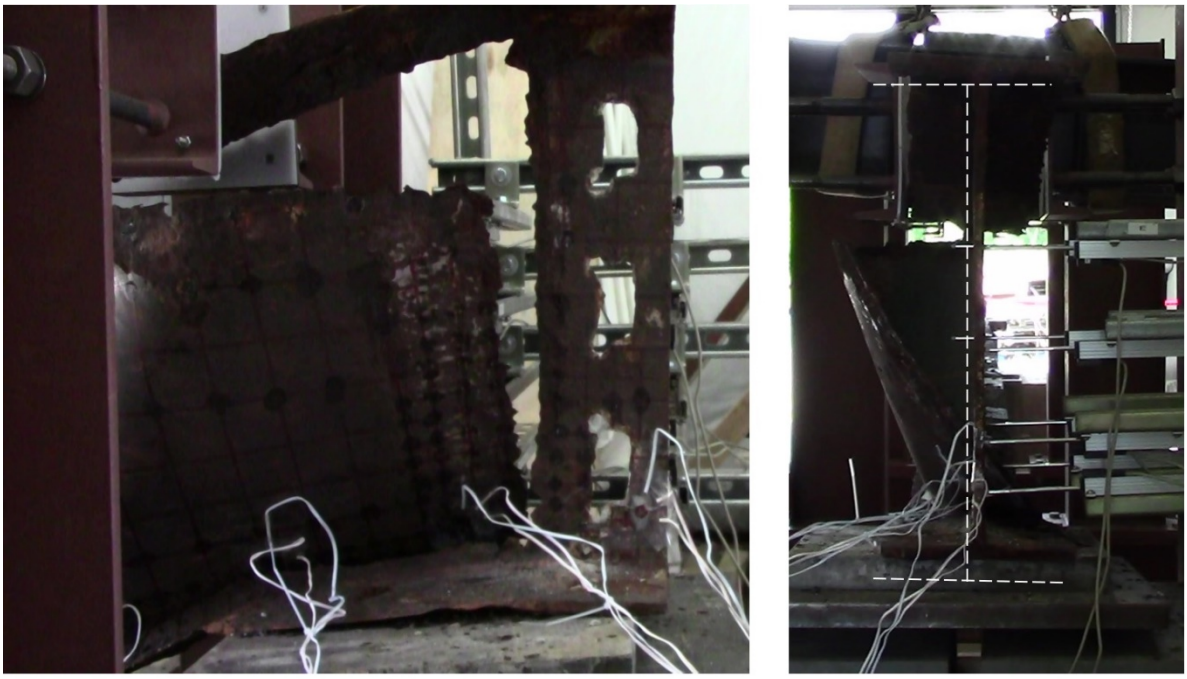

C

Figure 6.39: Side-by-side images showing side view of web and profile view of beam during experiment. Letters A-C correspond to Fig. 6.37a. White dashed lines illustrate cross-section location at loading initiation.

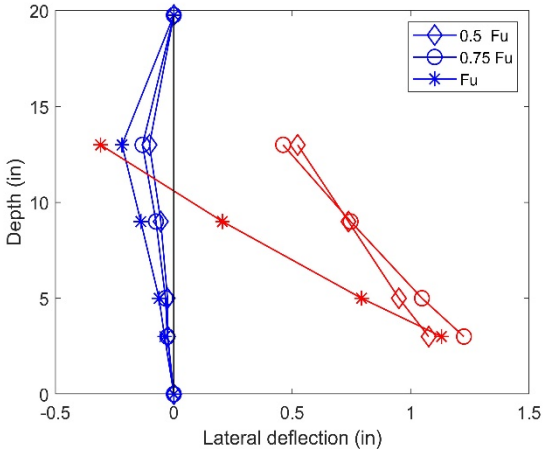

Figure 6.40: Measured web lateral deflection profiles recorded above outer bearing edge (blue) and inner one (red).

The residual deformation after unloading of the corroded end is presented in Fig. 6.41.

Figure 6.41: Residual deformation of Specimen 6.

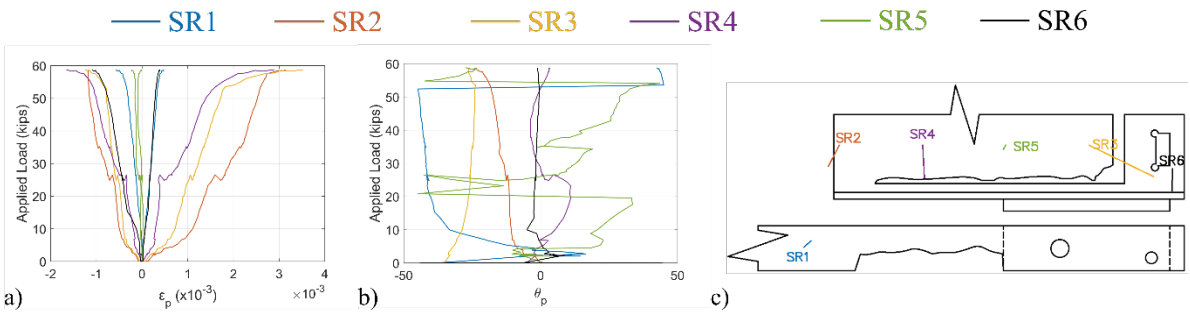

Figure 6.42: (a) Principal strains and (b) directions up to peak load. (c) Direction and normalized magnitude in respect to maximum strain at peak load; dashed line illustrates compressive direction; solid line illustrates tensile direction.

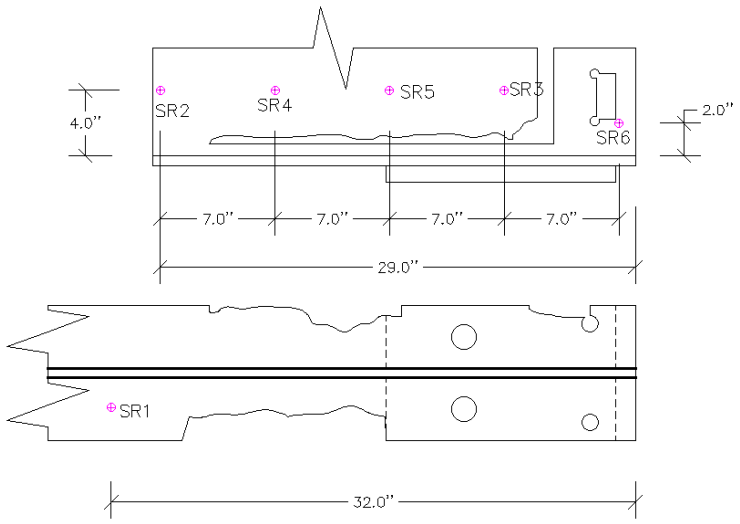

Figure 6.43: SR configuration of Specimen 6.

6.7 Material Properties

Results obtained by the tensile test of the four coupons obtained from Specimen 1 are illustrated in Fig. 6.44. Tests revealed a discrepancy in yield and ultimate stress of the steel along the rolling and transverse direction. Variation was also observed between the web and flange coupons. However, the curves for the top and bottom flange were similar, thus the results were considered valid.

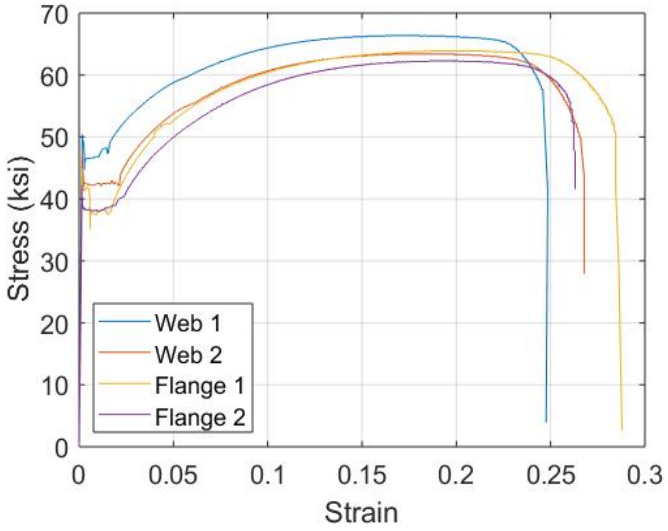

Figure 6.44: Stress strain curves for four coupons extracted from Specimen 1. Nomenclature of specimens is according to Figure 3.47.

Table 6.2 summarizes the material properties of the used steel obtained from Specimen 1.

Table 6.2: Material properties.

Position	Direction	Young Modulus (ksi)	Yield Stress (ksi)	Tensile Strength (ksi)
Web	Longitudinal	29,000	46	66.4
Web	Transverse	29,000	43	63.4
Top Flange	Longitudinal	29,000	38	63.9
Bottom Flange	Longitudinal	29,000	38	62.3

7.0 Analytical Results

This section includes the results of the computational modelling. A high-fidelity computational model, capable of accurately predicting the capacity of corroded beam ends, was validated based on the experimental data of the first two specimens. Making use of the finite element model (FEM), more than 2,000 combinations of corrosion topologies, beam types, and lengths were analyzed to gain better understanding of the mechanics of the corroded beam end. First, the effect of the initial imperfection on the beam capacity was examined. Second, the corrosion topology effect on the strength of deteriorated beam was investigated. Finally, the contribution of the support configuration in the beam capacity, in terms of beam type, length, and bearing, was studied.

Some interesting general observations from the parametric analysis:

- The numerically obtained capacities proved to be extremely sensitive to the initial geometric imperfection of the web.
- The effect of a hole to the capacity of the corroded end was highly related to the configuration at the bearing.
- The length of the specimen did not have an influencing effect on numerically obtained capacities.
- A deterioration scenario with relatively accounted dimensions (corrosion length and height expressed as a percentage of the depth) had a similar harming effect on all beam types with the same depth-to-bearing length ratio. However, the harming effect of corrosion length reduced for increasing bearing length ratio (BL/d).

7.1 Computational Model Validation

Following the procedure described in Chapter 4 and using contact stiffness “k” equal to 12, the applied load–vertical displacement curve was plotted to compare the finite element with the experimental results for the first two specimens.

Quasi-static analysis was performed up to failure, as post buckling is currently out of the scope of this study. Comparison of load–vertical displacement curves for numerical and experimental models is presented in Figs. 7.1 (a) and (b) for the first two specimens, indicating that the computational model successfully captured the failure load as well as the stiffness of the specimen. For Specimen 1, the difference between the numerically acquired peak load and the experimental value was -3.6% (Experimental: 134.1 kips; FEM: 129.3 kips), while for Specimen 2, the computational model overestimated the peak load by 1.1% (Experimental: 91.3 kips; FEM: 92.3 kips).

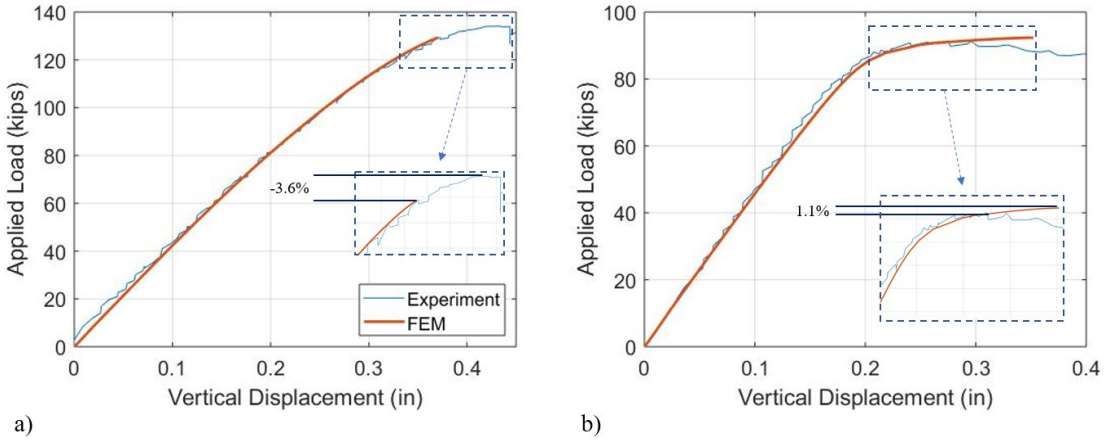

Figure 7.1: Comparison of experimental and numerical results for (a) Specimen 1 and (b) Specimen 2.

A detailed comparison of the lateral displacements recorded from the potentiometers and the associated nodal out-of-plane translations from the FEM model is presented in Figs. 7.2 and 7.3, for Specimens 1 and 2, respectively. The location of the potentiometer for each graph is illustrated with a green rectangle. Note that there was a small source of error, considering that a potentiometer measures the lateral displacement at a constant location in space as the experiment is developed through time, while the corresponding nodal value (FEA) refers to the node that initially (before loading) was located at the same location with the potentiometer (this node in the FE model is translated during the loading).

The general picture emerging from these plots was that the model can capture the failure mode. However, the accuracy varied among different potentiometers. A possible interpretation of this discrepancy is the initial applied geometric imperfection. In detail, for Specimen 1, at mid-height locations where the imported imperfection managed to satisfactorily represent the actual web shape, the numerical data were consistent with the experimental data. An increasing discrepancy was observed for potentiometers placed lower in height, where the initial uniform deflection was not captured by the eigenmode.

For Specimen 2, a reduced stiffness for numerical results compared to the experimental ones was observed for potentiometers placed mid-height. This behavior can be attributed to the existence of the steel section angles from the diaphragm. Regarding the numerical model, these sections were taken into account by increasing the applied thickness at the corresponding area. However, the results indicated that the model underestimates the stiffness of the web's portion where the steel sections are bolted.

To conclude, based on the presented results for Specimens 1 and 2, the model is considered valid and capable of capturing the stiffness, the failure load, and the mode of the corroded specimens. The reason behind validating the FE model with just two specimens and not with all six was that the validation needed to occur while the project was underway. Just after the testing of the first specimens, the team validated the model. The research team used that model to validate the second test and concluded that it is capable of capturing the behavior.

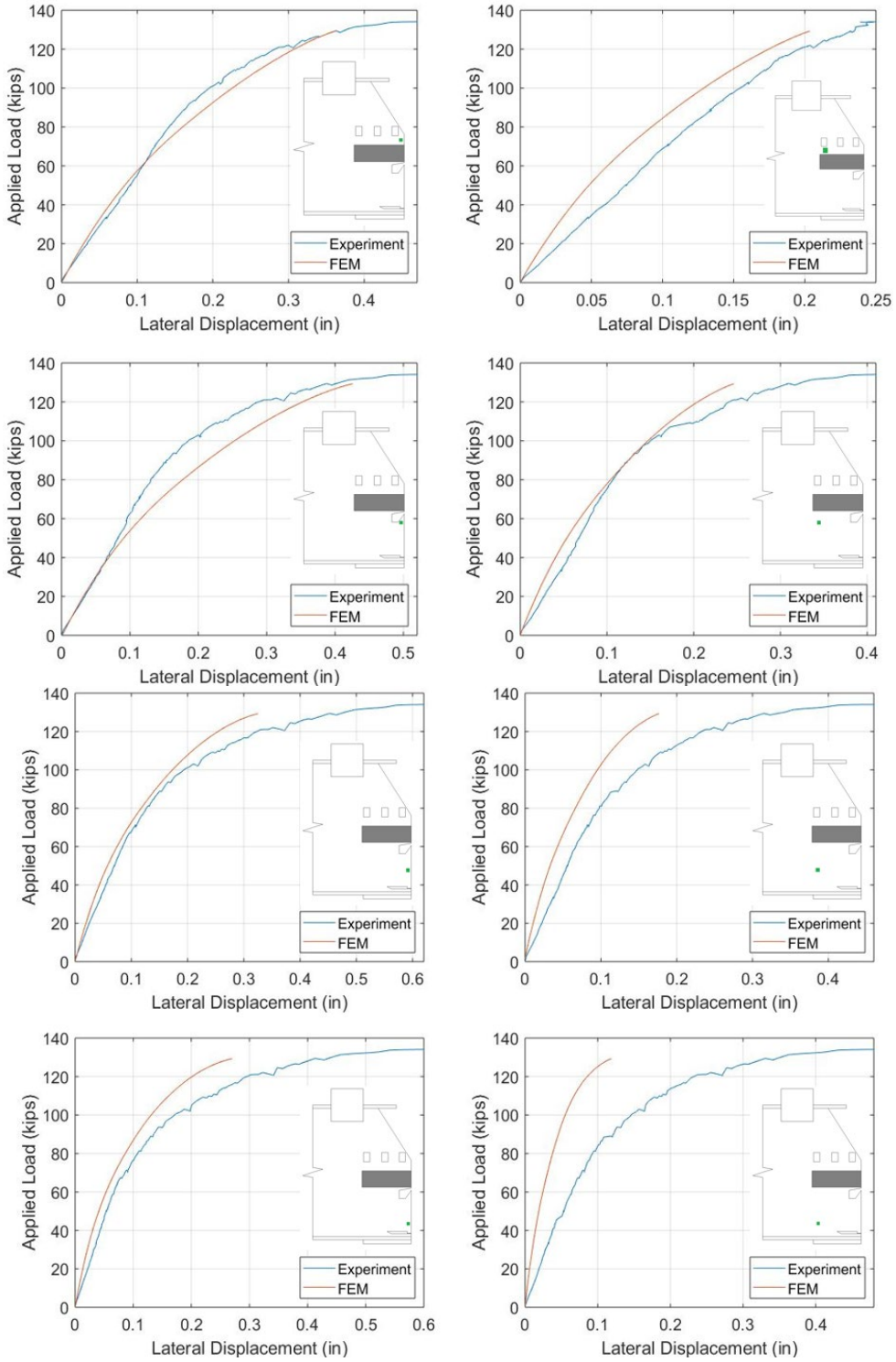

Figure 7.2: Comparison of experimentally and computationally obtained later displacements for Specimen 1. Potentiometer locations are illustrated with a green rectangle.

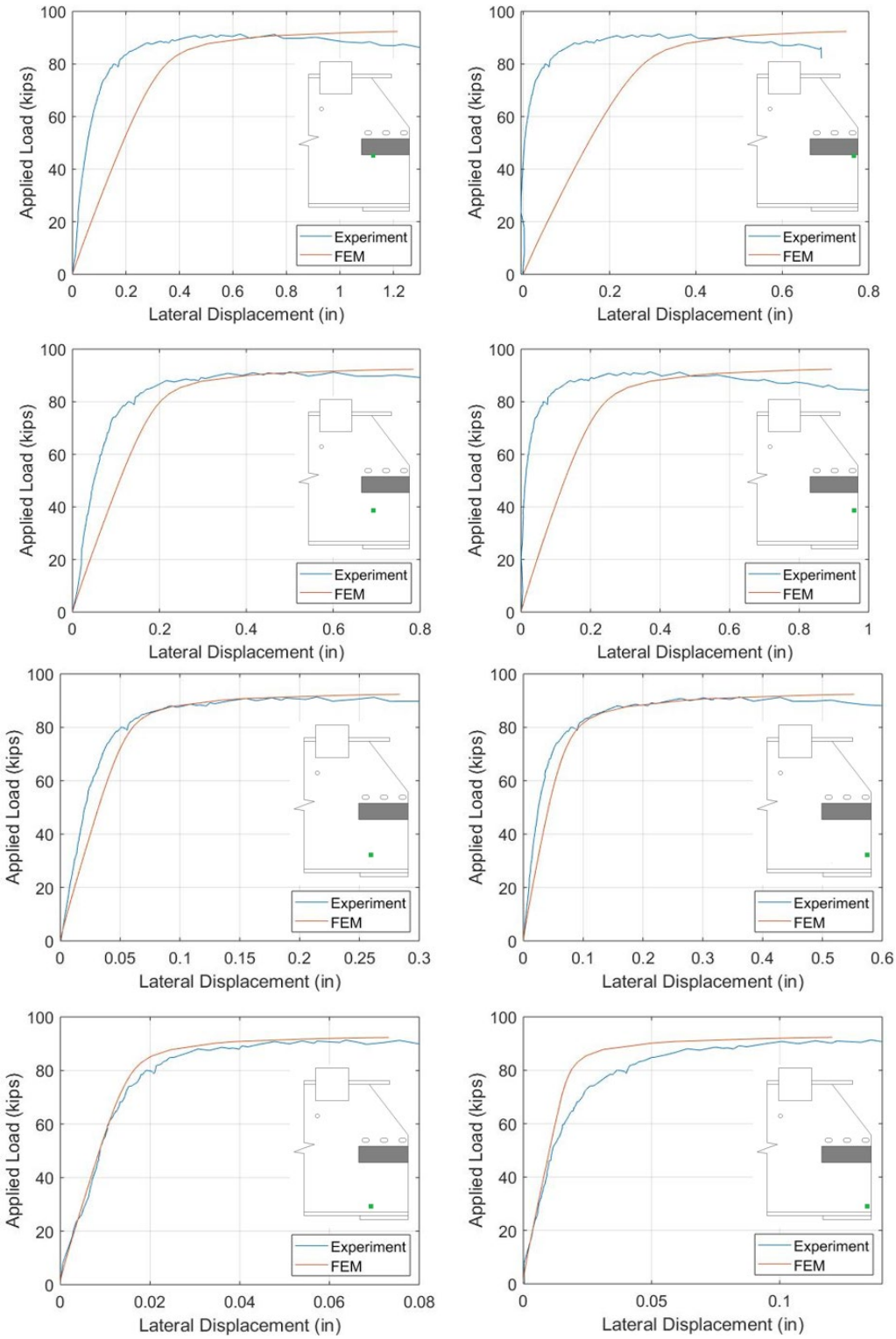

Figure 7.3: Comparison of experimentally and computationally obtained later displacements for Specimen 2. Potentiometers location is illustrated with a green rectangle.

7.2 From Experimental Length to Full-Length Models

The computational model presented in the previous section is an effort to simulate the experimental configuration. However, the research group aimed to conduct the parametric analysis simulating the geometry, boundary, and loading conditions of in-service girders. The mechanical problem formulation was slightly differentiated, to be consistent with the current load rating procedures. The girders obtained from the Colrain bridge were used as a benchmark for this modification.

Specimens extracted from the Colrain bridge were cut in half for testing, due to size restriction and a focus on just the corroded girder end. For the purpose of the parametric analysis, full beam lengths were considered. To validate this change, the length of Specimens 1 and 2 was increased to 50 ft., based on available construction drawings. The interaction properties defined in the previous section remained the same, while the modifications were limited to the expansion of the top flange restrictions domain from the LTB locations to full length, mimicking the effect of the deck. Regarding the loading conditions, the configuration described in Chapter 4 was assigned for maximum shear.

According to experimental configuration simulation, corroded end capacities equaled 97.75 kips and 69.49 kips, while for the in-service configuration, they were increased to 103 kips and 73.24 kips for Specimens 1 and 2, respectively. This capacity increase for both specimens was less than 5% and can be attributed to the stiffer boundary conditions applied to the top flange, as previously described. Based on the results, the full-length model was considered validated and was used for the parametric analysis conducted.

7.3 Imperfection Amplitude

As previously mentioned, girders are not perfectly straight. The cross-section may deviate from the ideal shape as well as the member's center line for its straightness. Additionally, based on the imperfection amplitude, both the behavior and the strength of beams can be severely affected. For the mechanical model formulation of the deteriorated steel beams problem, imperfections were an essential aspect that had to be considered; otherwise, their absence could result in overestimating capacity predictions. In general, plate and shell structures suffer greatly from geometric imperfections, and therefore, for the problem at hand, this aspect needed to be carefully approached. This was also supported by the experimental results of Specimen 2; the beam had an initial out-of-plane web imperfection with a magnitude of around $2t_w$, which had a dramatic result on the capacity. This result triggered the following work and the team's detailed approach to the problem of geometric imperfections.

For the parametric analysis of all the beam ends, imperfections were introduced into the model based on the eigenmodes' shapes. This was consistent with the stability theory, as imperfection mode shapes are considered the most deleterious of all imperfection shapes. Each model was initially solved using the eigenvalue buckling analysis algorithm. Then, the

eigenmode that appeared at the deteriorated end (the zone of interest) was introduced as an initial geometric imperfection for the quasi-static analysis.

One key parameter of geometric imperfections is the magnitude of the imperfection shape. To explore the effect of the magnitude, the research team performed another parametric analysis which focused on a specific beam type. A 36WF150 beam was used with two different corrosion topologies projected on the corroded end. For corrosion length 1.4 times the bearing length, two different corrosion heights, 10% and 30% of the beam depth, were investigated for imperfection amplitude between 10% and 200% of the intact web thickness. Furthermore, to get a first look on the comparison between the numerical results and the current procedures, the nominal capacity based on the draft *MassDOT 2019 Bridge Manual* was also included. It should be mentioned that all captured failures were crippling related, according to the current procedures.

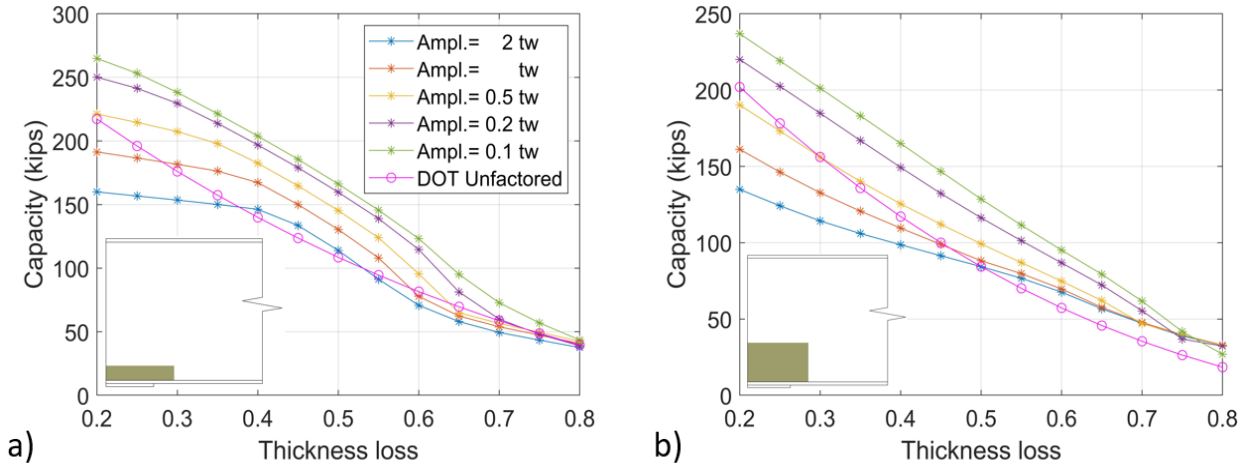

Figure 7.4: Imperfection amplitude effect on a 36WF150 beam with rectangular corrosion topology initiated at bottom of web for corrosion height (a) 10% and (b) 30% of depth.

The general picture emerging from these analyses was that there are cases for which, even with imperfection amplitude equal to $0.5t_w$, the current procedures are overestimating the capacity. In order to gain better understanding on the phenomenon for both examined deterioration topologies, the results for thickness loss 25%, 45%, and 60% were isolated (see Fig. 7.5).

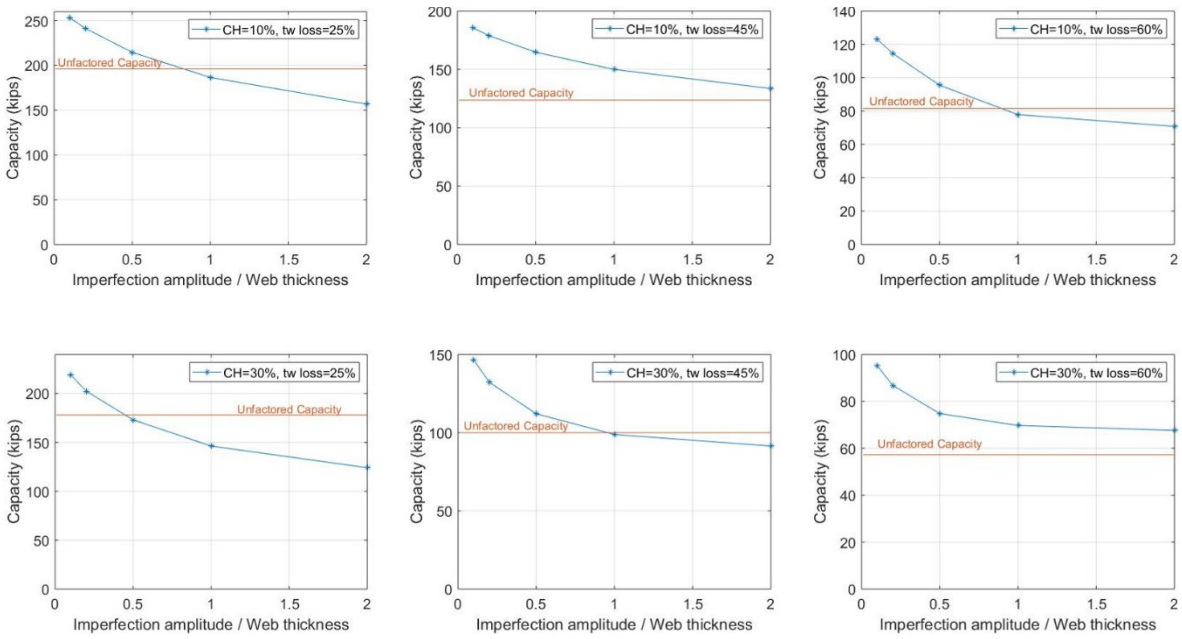

Figure 7.5: Comparison of numerically obtained with nominal capacities.

For both corrosion scenarios (CH= 10% and CH=30%), the team observed that for extensive thickness reduction, the capacity tended to plateau for imperfection amplitude equal to 1 t_{web}. For higher remaining material, the imperfection governed the failure load. An interesting finding was that the cases that were overestimated by the current procedures were dependent both on section loss and corrosion topology dimensions. Based on these inconclusive findings, the parametric analysis was performed for three different amplitudes: 0.1, 0.5, and $1t_{web}$. In this way, the team covered a significant range of imperfection amplitudes, enriching the parametric analysis. The unit value was chosen based on the presented results and reflected beams with corrosion related imperfection.

7.4 Corrosion Topology Effect

For the purpose of this work, the case of a rectangular deteriorated area was examined. This corrosion scenario was defined as pattern W1 (Table 2.2) and the upper and lower bounds of its geometric dimensions are shown in Table 5.1. To study the effect of web corrosion to girder capacity and to gain better understanding of the mechanics at the bearing area, the flange corrosion was provisionally excluded from the simulations. The deterioration scenario was initially projected on a 36WF150 beam (and later for all the rest of the scenarios and beam types), which, according to the conducted statistical analysis, was the most commonly related beam type to the examined corrosion topology. Regarding the initial imperfection, the eigenmode of the first positive eigenvalue was imported for the quasi-static analysis, scaled to one time the intact web thickness. Parametric analysis was initiated to study the effect of corrosion length, height, and beam type to capacity, under the assumption of uniform thickness reduction along the corroded area.

7.4.1 Corrosion Length Effect

To investigate the effect of corrosion length, two series of analyses, for imperfection amplitude 1 and 0.1 t_{web}, in the range of 0.25 to 1.5 times the depth, were performed for three different corrosion heights (10%, 20%, and 30% of depth), according to the examined corrosion scenario bounds. The results are presented in Fig. 7.6, where corrosion lengths are expressed in respect of bearing length (B_L), which equals 12 inches. For each examined corrosion height, analyses were performed for corrosion lengths of 0.7 up to 4.3 times the bearing length and thickness loss, in the range of 20% to 80% of the intact web thickness.

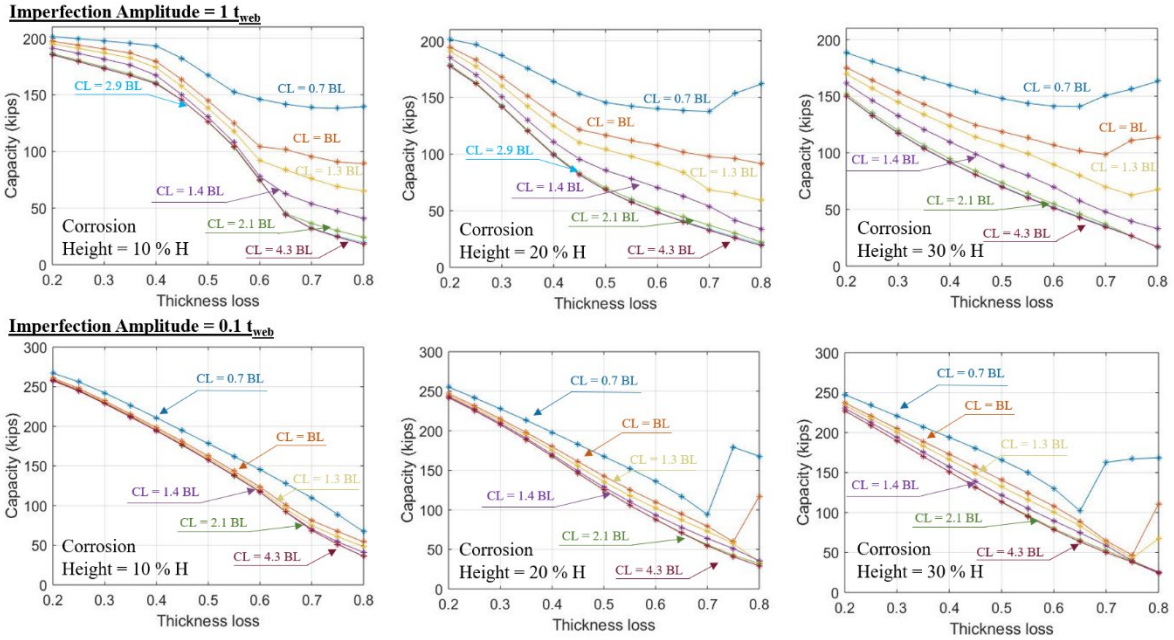

Figure 7.6: Capacity of beam ends with rectangular corrosion topology and imperfection amplitude 1 and 0.1 t_{web}, for corrosion height 10%, 20%, and 30% of depth.

For imperfection amplitude equal to 1 t_{web}, in case the corrosion length exceeded the bearing length more than 1.1 times its length, it has no further effect on beam strength. However, for imperfection amplitude 0.1 t_{web}, the corresponding effective deterioration length was reduced to 0.4 times beyond the bearing length. An interesting side finding from Fig. 7.6 was the paradox of increasing capacity for growing material losses. This behavior was limited to cases where the corrosion length did not expand beyond the bearing length. The investigation revealed a different failure mechanism for increasing section loss.

Fig. 7.7a presents the failure modes obtained from the analysis. For reduced remaining material, the buckling zone was limited to the corrosion area, and the half buckling wave was formulated only along the corrosion height. This trend was also combined with increasing uplift at the outer edge of the flange (Fig. 7.7b).

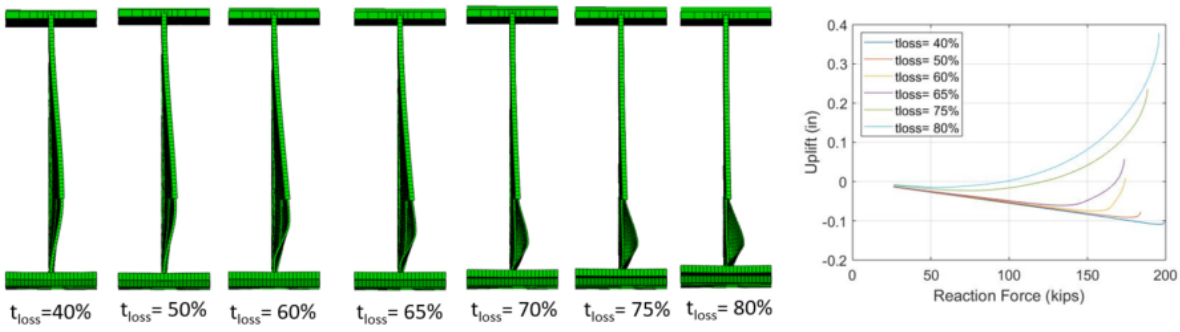

Figure 7.7: (a) Failure modes for corrosion height 30% and corrosion length 0.7 of bearing length; (b) measured uplifts at outer flange edge.

The uplift resulted in reaction force concentration at the inner bearing edge (Fig. 7.8a), where the web had experienced no loss, providing additional strength to resist load. Finally, even if the corroded part experienced extensive lateral deflection, buckling occurred only when the intact part failed (Fig. 7.8b).

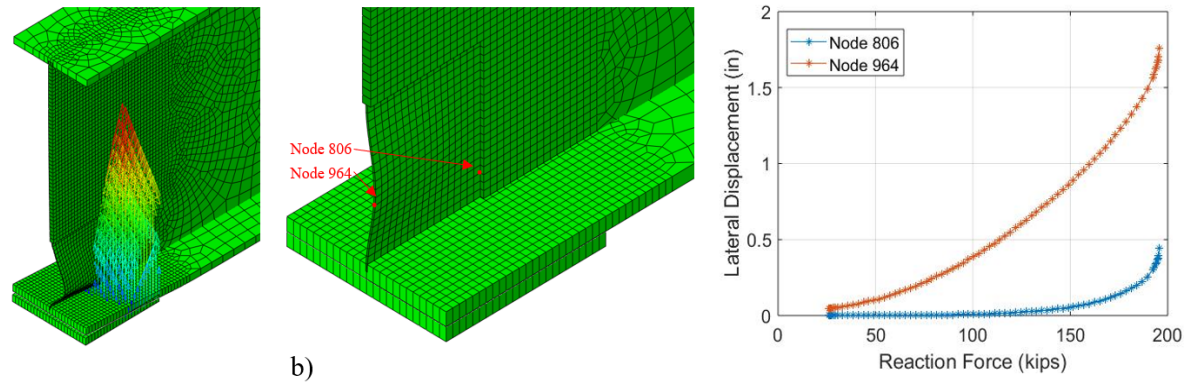

Figure 7.8: (a) Reaction forces profile, developed at beam's end where web corrosion length does not exceed bearing length; (b) web lateral displacements for node 806 located at edge between corroded and intact geometry.

7.4.2 Corrosion Height Effect

A similar procedure was followed to study the effect of corrosion height (Fig. 7.9). The length was fixed to three different values (25%, 50%, 150% of depth or 75%, 140%, 430% of bearing length), and corrosion heights of 10% to 30% of depth were simulated. Beyond 30% of corrosion height, there was no significant impact on the capacity, and it is safe to conclude that for increasing corrosion height, its impact on the capacity decreased and thickness loss dominated.

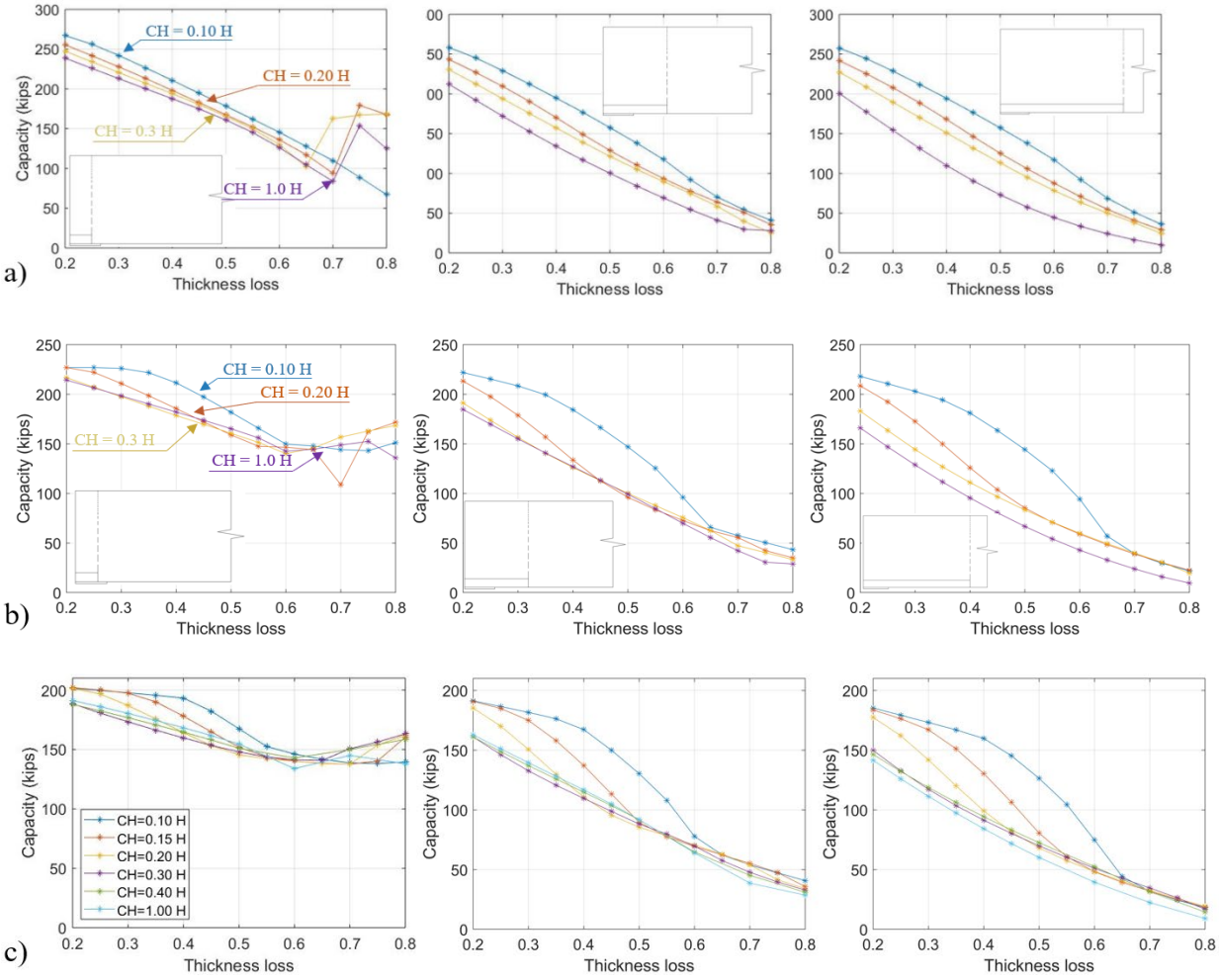

Figure 7.9: Corrosion height effect for corrosion length equal to 75-140-430% of bearing length. Analyses performed for imperfection amplitude (a) 0.1, (b) 0.5, and (c) 1 t_{web}.

7.4.3 Hole Effect

To investigate the effect of hole's existence at the corroded end, a parametric analysis was conducted for varying hole length (HL) and height (HH). To realistically simulate the bearing area of a deteriorated beam, additional to the hole, 20% material reduction was considered for an area with corrosion height 30% of depth and corrosion length 2.1 times the bearing length. Bearing length was equal to 12 inches. The corrosion scenario was projected on a 36WF150 girder, with the first positive eigenmode imported as imperfection and scaled to 1 t_{web}.

Initially, the hole height was set constant to 3% of depth, while the hole length initiated from 28% up to 200% of B_L. The obtained results are presented in Fig. 7.10. It might seem counterintuitive that for a hole expanding beyond bearing, increasing capacity was noticed, but this behavior was attributed on the web bearing on flange. The hole gap was eliminated, and the specimen was able to undertake additional load. Fig. 7.11 displays the failure modes with lateral displacement contours plotted on web surface.

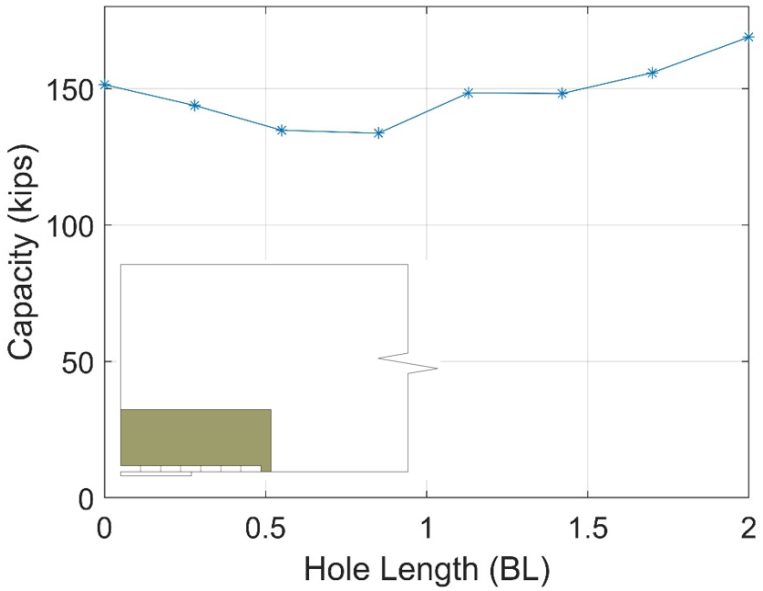

Figure 7.10: Effect of hole length on corroded 36WF150 end (20% section loss with CH=30%, CL= 2.1 B_L), for constant hole height equal to 3% of depth.

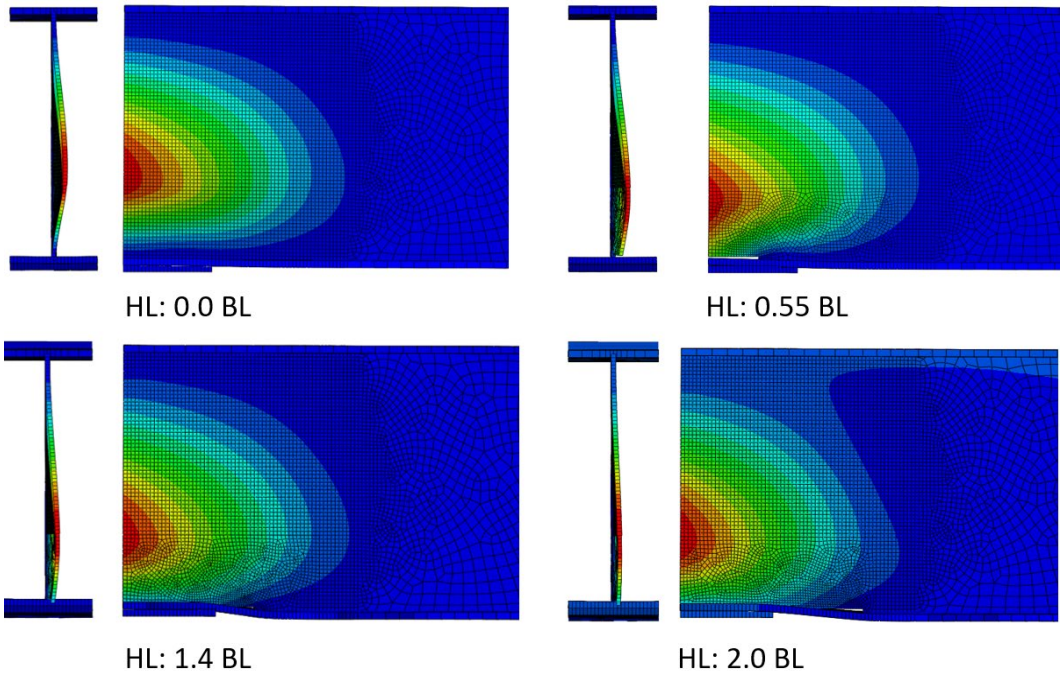

Figure 7.11: Failure modes for hole scenarios presented in Fig. 7.10

A similar procedure was followed to study the effect of corrosion height. For three different hole lengths (28%, 70%, 140% of B_L), hole heights up to 15% of the depth were simulated. Based on the presented results, there was a strong association between the hole height effect on the capacity and the hole length. In detail, if the area with 100% section loss was limited above the outer edge of the bearing, it had no significant effect on the capacity, regardless of its height (Fig. 7.12a). For hole length equal to 70% of B_L (Fig. 7.12b), capacity tended to plateau for hole height equal to 10% of depth and resulted in a capacity reduction of 30%. An

interesting behavior is observed for the case where the hole expanded beyond bearing length. The increasing capacity trend was already identified in Fig. 7.7; however, in Fig. 7.12c, a sudden capacity drop was observed for hole height greater than 7% of depth.

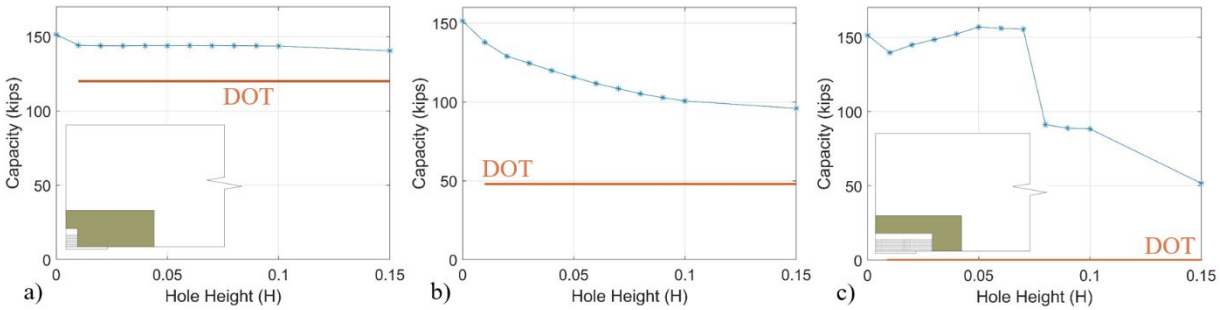

Figure 7.12: Effect of hole height on a corroded 36WF150 end (20% section loss with CH=30%, CL= 2.1 B_L), for hole length equal to a)28% b)70% and c) 140% of depth. The capacity according to the current procedures is also included.

As shown in Fig. 7.13, the capacity drop was correlated with the failure mode differentiation. The drop occurred when the buckling wave was formulated above the inner edge of the bearing instead of the outer edge.

It is worth noting that, according to the current procedures, all of the scenarios presented in Fig. 7.12c have zero nominal capacity, while the current work revealed that even in the worst-case scenario, bearing load up to 50 kips could be developed (around a third of the capacity corresponding to the non-hole geometry). However, this failure mechanism could be observed under the condition of extensive downwards translation of the top flange. This condition is controversial as to whether it is realistic or not on in-service girders due to the additional stiffness emerging from the deck, as well as potential diaphragm existence. Moreover, even if it is realistic, the likelihood is that serviceability issues would result in the extensive deformation.

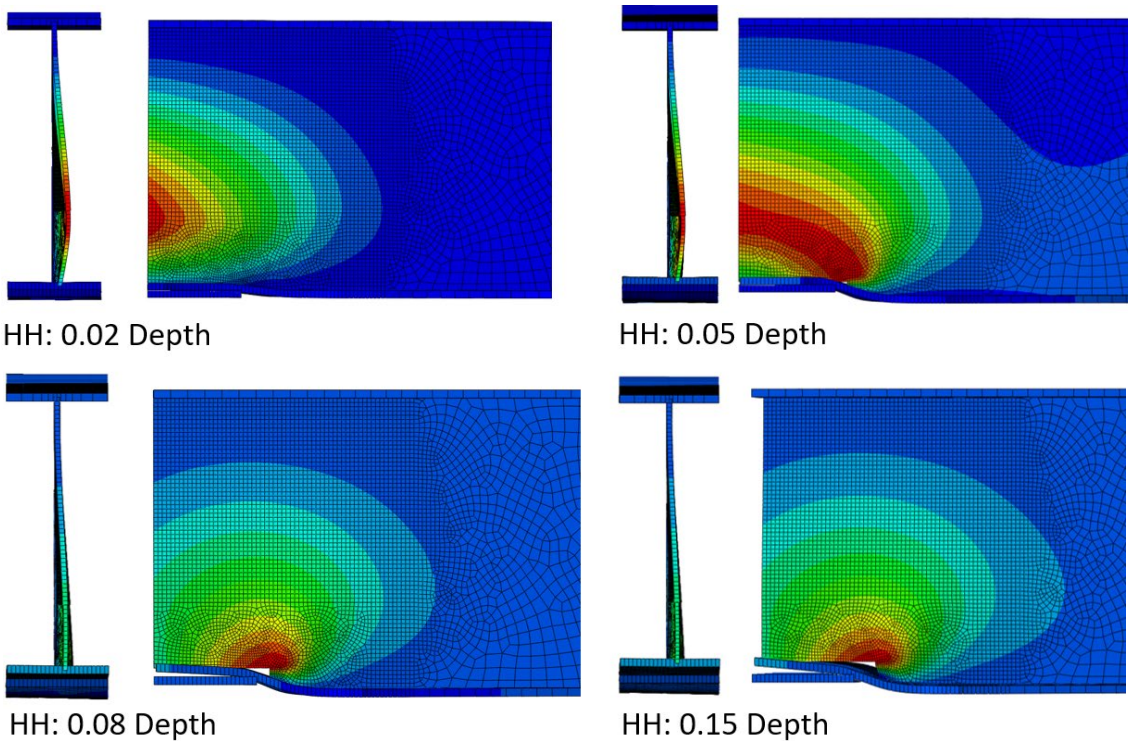

Figure 7.13: Failure modes for hole scenarios presented in Fig. 7.12. Lateral displacement contours are plotted on web surface.

7.5 Effect of Beam Type

To investigate the effect of beam type to corroded girder's capacity, the research team repeated part of the analyses, projecting the corrosion cases on a 30WF108 beam for imperfection amplitude 1 t_{web}. Three different corrosion lengths (25%, 50% and 150% of depth or 70%, 140%, and 430% of B_L) were simulated for corrosion heights 10% to 30% of web depth. The bearing length was reduced to 10 in. to maintain the ratio of bearing length to depth as constant. The obtained failure loads for each beam type were normalized in respect to the corresponding capacity for section loss equal to 20%. The curves for both beams in Fig. 7.14 followed an almost identical path, providing strong evidence that the relevant capacity reduction for increasing section loss was beam-type insensitive.

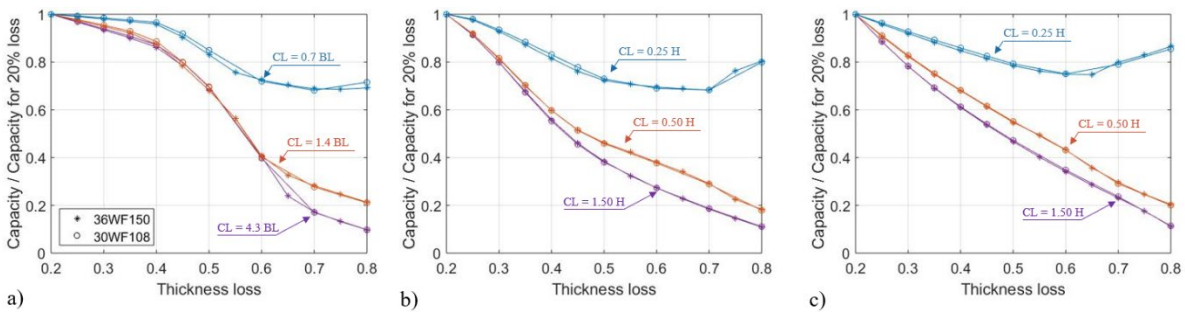

Figure 7.14: Beam effect for corrosion height (a) 10%, (b) 20%, and (c) 30% of depth.

7.6 Effect of Beam Length

In order to investigate whether a beam's length should be included as a parameter in the proposed methodology or not, a set of analyses were performed. Three different corrosion scenarios with section loss in the range of 20% to 80% of intact web thickness were projected on beams spanning 40 ft., 60 ft., and 80 ft. The applied imperfection was scaled to 1 t_{web}. In Fig. 7.15, curves with equivalent color denote common corrosion length, while the marker (pyramid, circle, or asterisk) denotes the length of the specimen. The corrosion height varied from 30% of depth in Fig. 8.16a, to 10% of depth in Fig. 7.15c.

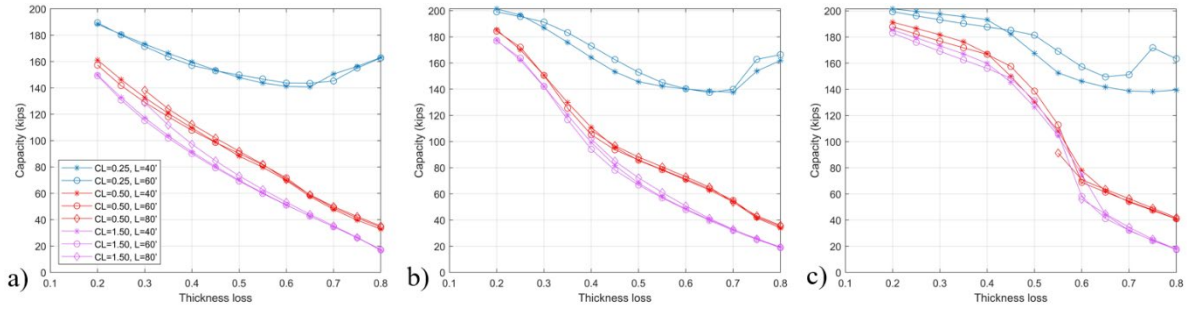

Figure 7.15: Effect of beam length on capacity of deteriorated beams. Corrosion height equals a) 30%, b) 20%, and c) 10% of depth.

Based on these figures, no significant correlations were obtained between corroded beam capacities and beam length, thus excluding this parameter from the upcoming analytical expression.

7.7 Effect of Bearing Length

In Section 7.5, it was demonstrated that a deterioration scenario with relatively accounted dimensions (corrosion length and height expressed as a percentage of the depth) had a similar harming effect on all beam types with the same depth-to-bearing length ratio (BL/d). Supplementary to that work, the goal of this subsection was to investigate how the bearing length affected the capacity of the corroded end for a given beam type (varying B_L for constant d). A 21WF59 girder with imperfection amplitude 0.1 t_{web}, and four different bearing lengths, 5.2 in., 6.9 in., 9.4 in., and 14 in. (or 0.25, 0.33, 0.45, and 0.66 BL/d), were examined. In order to investigate the bearing contribution to the beam's capacity, deterioration scenarios were also introduced. In these scenarios, the corrosion height equaled 20% of web depth, and the corrosion lengths are expressed as a percentage of bearing length (75%, 120%, 230% of B_L).

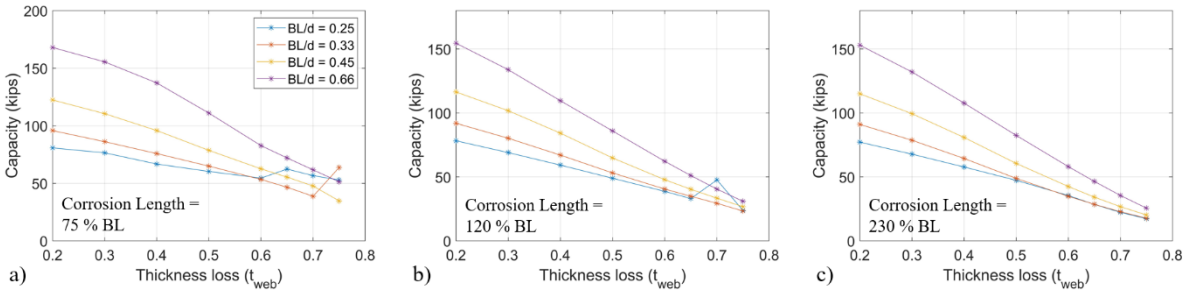

Figure 7.16: Effect of bearing length (B_L) on capacity of deteriorated beams. Corrosion length equals (a) 75%, (b) 120%, and (c) 230% of bearing length.

In Section 7.4.1, the team identified the harming effect of corrosion length relatively expressed as a percentage of the bearing length. However, based on Fig. 7.16, the harming effect of corrosion length reduced for increasing BL/d ratio.

This page left blank intentionally.

8.0 Implementation and Technology Transfer

This chapter describes the new proposed procedures that were the outcome of the research project. The structure is as follows: The current procedures are presented and evaluated through a comparison to the experimentally and numerically obtained capacities. The new procedures are presented in detail and the new equations are described, along with the necessary information on how they should be applied for different deteriorations. At the end of the Chapter 8.0, the new procedures are evaluated, following the same comparison to experimental and numerical results. The efficiency of the new results is demonstrated at the end of the section, when the numerically obtained capacities from the extensive parametric analysis are compared to the predictions coming from the new procedures.

8.1 Evaluation of Current Procedures

Before proceeding with the development of new procedures for deteriorated beam capacity, it was critical to evaluate the current MassDOT procedures. This evaluation first included the following two steps for the six specimens that were tested during this research project:

I. Follow the current MassDOT procedures and calculate the remaining capacity.
II. Compare the values from (I) with the experimentally obtained capacities.

In addition, the predictions from the current MassDOT procedures were compared with the results coming from the high-fidelity numerical model that was built based on the experimental observations. In Section 8.1.3., the authors present indicative results from this comparison, highlighting the effect of imperfection amplitude and the effect of bearing length over depth (N/d).

8.1.1 Brief Description of Current MassDOT Procedures

After gathering the data from inspection reports on a deteriorated end section loss, it is possible to calculate the remaining capacity following the recommendations of Section 7.2.9 of the draft *MassDOT 2019 Bridge Manual (30)*.

The factored corroded web resistance at both the inventory and operating level is calculated as the minimum of the yielding ($R_{n,yield}$) and crippling ($R_{n,crip}$) capacity, based on the equation:

$$\text{Corroded Web Factored Resistance} = \min [\Phi R_{n,yield}, \Phi R_{n,crip}] \quad (8.1)$$

Where:
$\Phi R_{n,yield} = (\Phi_b = 1.0\ ) (R_{n,yield})$
$\Phi R_{n,yield} = (\Phi_b = 0.8\ ) (R_{n,crip})$

Based on the geometric configuration of the specimens that fall under the scope of the current research work (with overhang length < 5k), the nominal yielding capacity is calculated as follows:

$$R_{n,yield} = F_y t_{ave}(2.5k + N) \quad (8.2)$$

Where:
F_y = minimum yield strength (ksi)
t_{ave} = the average remaining thickness within the bottom 4 in. of the web height (inches)
k = distance from outer face of flange to web toe fillet (inches)

And the web local crippling capacity in kips ($R_{n,crip}$) is calculated as follows:

At interior-pier reactions and for beam end reactions applied at a distance from the end of the member that is greater than or equal to d/2:

$$R_{n,crip} = 0.8t_{ave}^2 \left[1 + 3\left(\frac{(N-H)}{d}\right)\left(\frac{t_{ave}}{t_f}\right)^{1.5}\right]\sqrt{\frac{EF_y t_f}{t_{ave}}} \quad (8.3)$$

Otherwise,

$$R_{n,crip} = 0.4t_{ave}^2 \left[1 + \left(\frac{4(N-H)}{d} - 0.2\right)\left(\frac{t_{ave}}{t_f}\right)^{1.5}\right]\sqrt{\frac{EF_y t_f}{t_{ave}}}, \text{ when } N/d > 0.2 \quad (8.4)$$

$$R_{n,crip} = 0.4t_{ave}^2 \left[1 + 3\left(\frac{(N-H)}{d}\right)\left(\frac{t_{ave}}{t_f}\right)^{1.5}\right]\sqrt{\frac{EF_y t_f}{t_{ave}}}, \text{ when } N/d \leq 0.2 \quad (8.5)$$

Where:
d = entire depth of steel section (inches), without deductions for encased diaphragms, if any
t_f = thickness of the flange resisting the concentrated load or bearing reaction (inches)
E = modulus of elasticity of steel (ksi)

The average web thickness, for the beams that fall under the scope of the current research (with overhang length <5k), is calculated as follows:

$$t_{ave} = \frac{(N + 2.5\,k - H) * t_w}{(N + 2.5\,k)} \quad (8.6)$$

Where:
t_w = remaining web thickness (inches)
H = length of hole along length used for capacity (here: N + 2.5k) (inches)
N = bearing length (inches)
k = distance from outer face of flange to web toe fillet (inches)

Both capacities (crippling and yielding) are dependent on t_{ave} (the average remaining thickness within the bottom 4 in. of the web). The value for t_{ave} is calculated using equation (8.6), where the remaining web thickness needs to be introduced. Given the fact that section loss is not uniform along this area, the calculated capacity is heavily dependent on engineering judgement regarding the remaining thickness estimation.

8.1.2 Comparison between Experimental and Current Predicted Capacities

In order to calculate the failure load of the tested specimens according to the current procedures, the average of the conducted thickness measurements was used to estimate the remaining thickness (t_w) within the area of interest. In addition, the safety factors in equation (8.1) were temporarily neglected in order to evaluate the efficiency of yielding and crippling related equations.

Specimen 1

Specimen 1 is a 33WF125 with a defining feature of a 6 in. long hole at the bottom of the web, initiating from the outer web edge. The exact parameters used to calculate the unfactored nominal capacity according to the current procedures are given in Table 8.1.

Table 8.1: Parameters used for capacity calculation of Specimen 1.

	E (ksi)	**F_y (ksi)**					
Material Properties	29.000	36					
	d (in)	**t_w (in)**	**b_f (in)**	**t_f (in)**	**k (in)**	**N (in)**	**L_0 (in)**
Beam Geometry	33	0.57	11.5	0.805	1.505	11.8	0
	t_{rem} (t_{web})	**H (in)**					
Corrosion	40%	6					

Following the procedure presented in 8.1.1, the nominal crippling capacity of Specimen 1 was 38.3 kips and underestimated the experimental capacity, which was equal to 99 kips, by 2.6 times (Table 8.2). For this specimen, the experimental peak load was not achieved with the web bearing onto the flange. The observed discrepancy could be attributed to a strong association between the hole effect and its length, which was highlighted in Section 7.4.3 and the for which the current procedures do not account. According to the draft *MassDOT 2019 Bridge Manual*, any holes, regardless of their position and height, are considered ineffective for the full 4 in. height. They linearly reduce the t_{ave} based on the ratio of the hole length over the length of the area for which the remaining web thickness is determined (eq. 8.6).

Table 8.2: Comparison between experimental and predicted capacity for Specimen 1.

Specimen 1	
Current MassDOT prediction (kips)	38.3
Experimental peak load (kips)	99

Specimen 2

Specimen 2 is a 33WF132 with the defining feature of the extensive initial web displacement, which equals two times the intact web thickness, as well as a bottom flange hole (Table 8.3).

Table 8.3: Parameters used for capacity calculation of Specimen 2.

	E (ksi)	**F_y (ksi)**					
Material Properties	29.000	36					
	d (in)	**t_w (in)**	**b_f (in)**	**t_f (in)**	**k (in)**	**N (in)**	**L_0 (in)**
Beam Geometry	33.15	0.58	11.51	0.855	1.555	11.8	0
	t_{rem} (t_{web})	**H (in)**					
Corrosion	60%	0					

The nominal crippling capacity of Specimen 2 is 102.2 kips and overestimates the experimental capacity, which is equal to 67.6 kips, by 51% (Table 8.4). This variation is contrary to the discrepancy observed for Specimen 1. However, there is strong evidence for the role of the initial web imperfection in the beam's strength, as it was extensively reported in Section 7.3, and the current procedure does not include this aspect. Furthermore, the flange hole could act as an additional source of discrepancy, due to the fact that only web corrosion is considered from the code.

Table 8.4: Comparison between experimental and predicted capacity for Specimen 2.

Specimen 2	
Current MassDOT prediction (kips)	102.2
Experimental peak load (kips)	67.6

Specimen 3

Similarly to Specimen 1, Specimen 3 is a 33WF125 girder and its characterizing feature is a thin hole at the bottom of the web initiating from the outer web edge, extending 6 in. beyond the bearing (Table 8.5).

Table 8.5: Parameters used for capacity calculation of Specimen 3.

	E (ksi)	**F_y (ksi)**					
Material Properties	29.000	36					
	d (in)	**t_w (in)**	**b_f (in)**	**t_f (in)**	**k (in)**	**N (in)**	**L_0 (in)**
Beam Geometry	33	0.57	11.5	0.805	1.505	12	0
	H (in)						
Corrosion	18						

Due to the hole length, the nominal capacity of Specimen 3 is 0 kips, while the experimental capacity equals 84.3 kips (Table 8.6). The web, as it has been previously presented, due to the bottom flange distortion, was bearing on the flange from the initiation of the experimental process. This behavior validates the claim resulting from the parametric analysis on holes, that as soon as the web starts bearing on the flange, the specimen is able to undertake significant load.

Table 8.6: Comparison between experimental and predicted capacity for Specimen 3.

Specimen 3	
Current MassDOT prediction (kips)	0
Experimental peak load (kips)	84.3

Specimen 4

Specimen 4 is a 21WF73 beam that experiences a long wave instability mode. SR recordings revealed a local buckling limited to a narrow material strip with extensive thickness loss above part of the bearing, expanding along the longitudinal axis between the strain gauges and the bearing plate (Fig. 6.26). However, it is not clear if the observed local buckling is a result of the bearing load or if it is a second-order phenomenon resulting from the extensive midspan lateral and torsional deflection.

Nevertheless, for the sake of completeness, the nominal capacity (Table 8.8) was calculated equal to 91.5 kips, based on the metrics presented in Table 8.7.

Table 8.7: Parameters used for capacity calculation of Specimen 4.

	E (ksi)	**F_y (ksi)**					
Material Properties	29.000	36					
	d (in)	**t_w (in)**	**b_f (in)**	**t_f (in)**	**k (in)**	**N (in)**	**L_0 (in)**
Beam Geometry	21.24	0.455	8.295	0.75	1.24	9.5	6.75
	t_{rem} (t_{web})	**H (in)**					
Corrosion	55%	1.4					

Table 8.8: Comparison between experimental and predicted capacity for Specimen 4.

Specimen 4	
Current MassDOT prediction (kips)	42.8
Experimental peak load (kips)	91.5

Specimen 5

Specimen 5 is a 21WF73 beam, with an artificial (during construction) and a corrosion hole located at the bottom of the web above bearing (Table 8.9).

Table 8.9: Parameters used for capacity calculation of Specimen 5.

	E (ksi)	**F_y (ksi)**					
Material Properties	29.000	36					
	d (in)	**t_w (in)**	**b_f (in)**	**t_f (in)**	**k (in)**	**N (in)**	**L_0 (in)**
Beam Geometry	21.24	0.455	8.295	0.75	1.24	14	0
	t_{rem} (t_{web})	**H (in)**					
Corrosion	70%	10					

The failure mode, which was governed by the buckling of the material strips between the holes, was observed for bearing load equal to 30.9 kips (Table 8.10). The prediction according to the current procedures equals 17.6 kips, highlighting once again the effect of holes.

Table 8.10: Comparison between experimental and predicted capacity for Specimen 5.

Specimen 5	
Current MassDOT prediction (kips)	17.6
Experimental peak load (kips)	30.9

Specimen 6

Specimen 6 is a 21WF59 beam with the defining feature of one web hole, shaped as an angle section, covering the whole depth and leaving the web loose along three edges. For the capacity calculation, only the section loss measured at the web that used to be fully embedded in concrete was considered, due to the hole extending along the remaining length of the domain where the t_{ave} was calculated (Table 8.11).

Table 8.11: Parameters used for capacity calculation of Specimen 6.

	E (ksi)	F_y (ksi)					
Material Properties	29.000	36					
	d (in)	**t_w (in)**	**b_f (in)**	**t_f (in)**	**k (in)**	**N (in)**	**L_0 (in)**
Beam Geometry	20.91	0.39	8.23	0.575	1.075	14	1.2
	t_{rem} (t_{web})	**H (in)**					
Corrosion	90%	13.25					

Based on the metrics presented in Table 8.11, the nominal bearing failure load equals 6.1 kips, which predicts the crippling capacity of the web above the outer bearing edge that used to be embedded in concrete. However, after loading initiation, the web above the hole started bearing on the flange, defining a different loading path. Ultimately, failure occurred at 40.95 kips reaction load, due to buckling of the web bearing on flange (Table 8.12).

Table 8.12: Comparison between experimental and predicted capacity for Specimen 6.

Specimen 6	
Current MassDOT prediction (kips)	6.1
Experimental peak load (kips)	40.95

Taken altogether, the current procedures significantly overestimate the capacity of specimens with web imperfections and do not satisfactorily assess the strength of girders with holes at their beam ends.

8.1.3 Comparison between Numerically Obtained and Current Predicted Capacities

In order to gain better understanding of the efficiency of the current procedures, the predictions obtained according to the 2019 draft *MassDOT Bridge Manual (30)* were compared with selected results coming from the high-fidelity numerical model, under the assumption of uniform section loss. In cases where the examined corrosion scenario did not exceed the area over which the remaining web thickness (t_w) was calculated, the weighted average over the entire area was calculated. An indicative example is given in Fig. 8.1, where a deterioration scenario with section loss 50 % of the intact web thickness is presented. Its length equaled half of the area of interest; thus, the remaining thickness t_w in equation (8.6) was 75% of the intact web thickness.

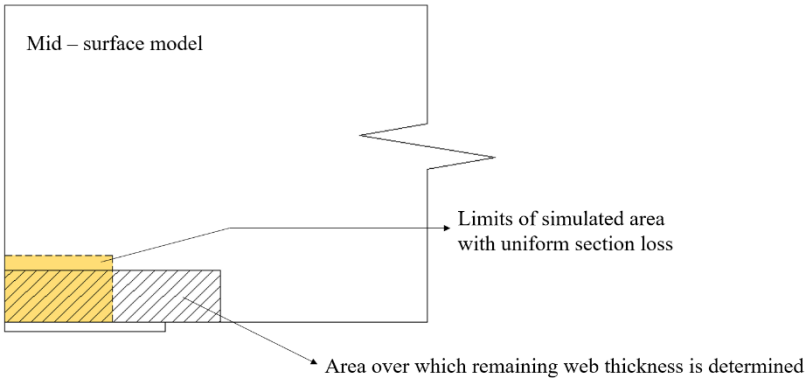

Figure 8.1: Beam end with corrosion scenario projected on bottom of web.

In Fig. 8.2, the magenta line denotes the unfactored predicted load according to the 2019 draft *MassDOT Bridge Manual (30)* for the corrosion scenario represented in each figure. Analyses were run for three different imperfection amplitudes, 1, 0.5, and 1 t_{web}.

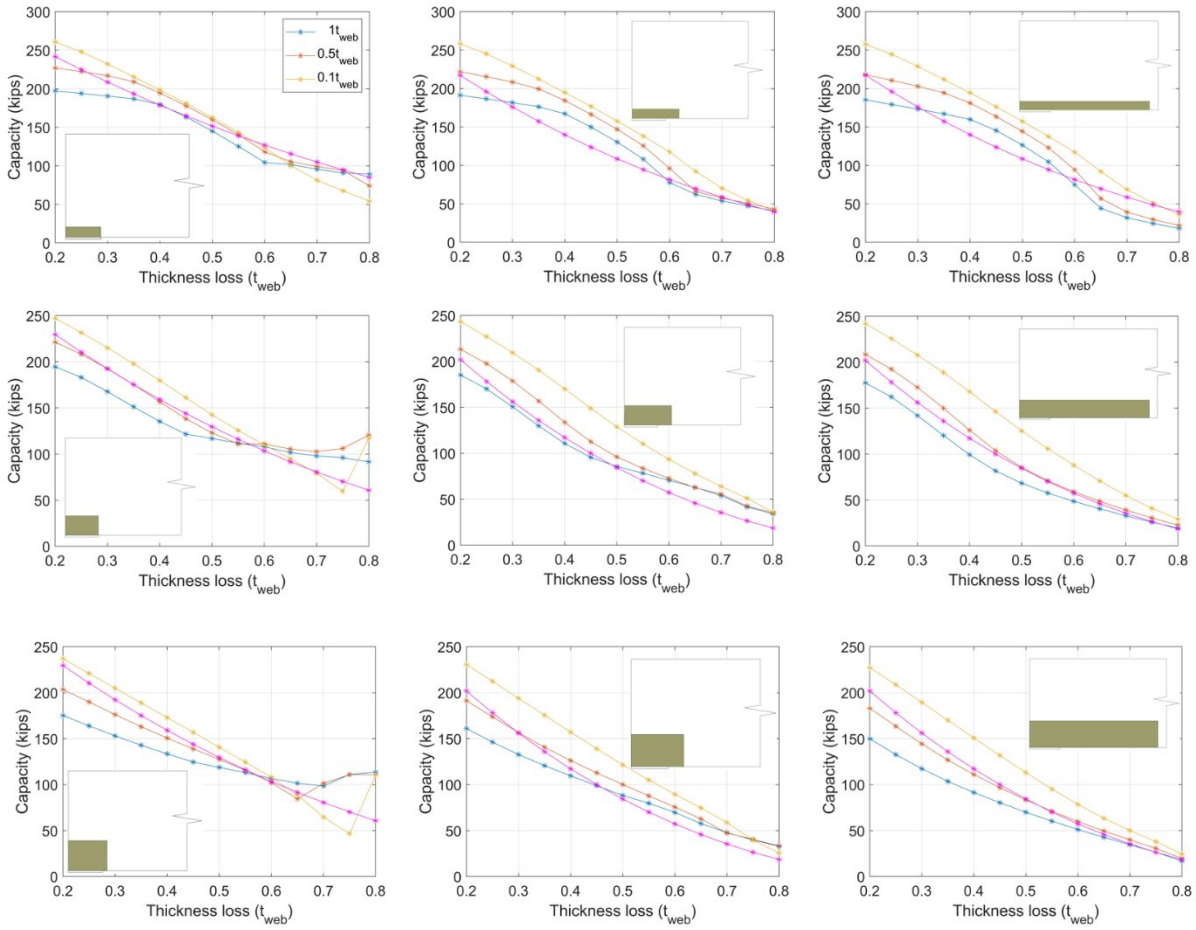

Figure 8.2: Comparison between numerically obtained capacities and failure load predictions based on current procedures for 36WF150 beam with N/d = 0.33 and imperfection amplitude 1, 0.5, and 1 t_{web}. Corrosion height equals 10%, 20%, or 30% of depth, and corrosion length 1.1, 1.4, or 4.25 times bearing length.

The presented corrosion scenarios cover a wide range of corrosion topology dimensions as well as thickness losses. The general picture emerging from these plots is that, for imperfection amplitude equal to $1t_{web}$, the current procedures underestimate in some cases the actual capacity and overestimate it in others. However, for reducing imperfection amplitude, the predictions tend to underestimate the numerically obtained capacities.

8.2 Proposed Procedures for Web Crippling

The crippling capacity prediction governed all the numerically simulated scenarios as well as the conducted experiments. In detail, regarding the experimentally obtained failure modes at

each specimen, there was at least one SR recording plastic strains at peak load. Regarding the numerical models, the failure modes were always combined with a web portion in the plastic regime. However, for both cases, due to the imperfect geometry, it was not possible to justify whether the local yielding (occasionally only along a unique web surface) had triggered instability or not. Ultimately, the failures from both the experimental and computational work could be considered as buckling and crippling phenomena; thus, the effort was focused on the crippling related equations.

The capacity should be estimated as the minimum between the proposed crippling and yielding capacity as currently is, according to equation (8.1), while engineering judgement shall be used in situations where section loss exceeds 65% of intact web thickness.

The researchers expanded the investigation on equations (8.4) and (8.5), which assess the capacity for beam end reactions, similarly to the conducted experiments (overhang length less than 5k). The modifications, which aim to create an envelope for both types of failure, crippling and buckling, focus on **four** main aspects:

The initial imperfection amplitude

The proposed procedures are developed for three different imperfection amplitudes (0.1, 0.5, and 1 t_{web}), according to findings described in Section 7.3.

The area over which the average web thickness (t_{ave}) is determined

The height of 4 in. remained unchanged in order to maintain the physical behavior of crippling that these equations capture. However, t_{ave} is calculated as follows:

$$t_{ave} = \frac{(N + m\,d - H) * t_w}{(N\ + m\,d)} \tag{8.7}$$

Where:
t_w = remaining web thickness (in.)
H = length of hole along length used for capacity (here: N + m d) (in.)
N = bearing length (in.)
d = beam depth (in.)
m = factor specified in Table 8.13

Table 8.13: Proposed values of factor m, for average web thickness calculation.

	Imperfection Amplitude		
	1 t_{web}	**0.5 t_{web}**	**0.1 t_{web}**
N/d > 0.2	0.2	0.2	0.1
N/d ≤ 0.2	0.1	0.1	0

Crippling capacity equation (8.4) for N/d > 0.2

Initially, equation (8.4) was rewritten as the summation of two terms that both include the average thickness t_{ave}, which is the only corrosion input.

$$R_{n,crip} = \mathbf{0.4}\sqrt{EF_y t_f}\, t_{ave}^{1.5} + \mathbf{0.4}\left(\frac{4(N-H)}{d} - 0.2\right)\frac{\sqrt{E\,F_y t_f}}{t_f^{1.5}}(t_{ave})^3 \quad (8.8)$$

By comparison of the predicted capacities and the numerically obtained failure loads, it was decided to increase the significance of corrosion length by multiplying equation (8.8) by the factor $(CL/(N + m\ d))^h$.

Where:
CL = Corrosion length along length used for capacity estimation (in).
h = Constant specified in Table 8.14.

Hence, equation (8.8) becomes:

$$R_{n,crip} = \mathbf{0.4}\sqrt{EF_y t_f}\left(\frac{CL}{N + m\ d}\right)^h t_{ave}^{1.5} + \mathbf{0.4}\left(\frac{4(N-H)}{d} - 0.2\right)\frac{\sqrt{E\,F_y t_f}}{t_f^{1.5}}\left(\frac{CL}{N + m\ d}\right)^h (t_{ave})^3 \quad (8.9)$$

Linear regression was performed to model the relationship between the average remaining thickness (which is the corrosion input) and the crippling capacity. Linear regression implies, by definition, a linear relationship between the explanatory variable (X) and the dependent variable (Y), in the form of:

$$Y = a + b\ X \quad (8.10)$$

The goal of this part was to recalculate the coefficients of each term (denoted with bold text in eq. 8.9), which from now on will be referred to as the unknowns **a** and **b**. In this framework, FEA results will be implemented. The numerically obtained capacity of the examined beam end will be imported as $R_{n,crip}$, while the corresponding t_{ave} will be calculated for every corrosion scenario. For a given beam geometry, corrosion topology as well as material properties are constants. Thus, equation (8.9) can be expressed as:

$$Y = \mathbf{a} * \text{constant} * X1 + \mathbf{b} * \text{constant} * X2 + \mathbf{e} \quad (8.11)$$

Where:
$Y = R_{n,crip}$
$X1 = (t_{ave})^{1.5}$
$X2 = (t_{ave})^3$
e is requested to be zero.

For the calculation of **a** and **b** coefficients, linear regression was performed, based on at least 312 simulations per imperfection amplitude. To statistically evaluate the fitness of the model, the P-value for each coefficient was used. The P-value for each term tests the null hypothesis that the coefficient is equal to zero (no effect). A low P-value (< 0.05) indicates that the null hypothesis can be rejected. Table 8.14 summarizes the proposed constant values as well the corresponding P-values. For each imperfection amplitude, the values of factor h are also included.

Table 8.14: Linear regression results for coefficients a and b for N/d>0.2.

Imperfection Amplitude	1 t_{web}	0.5 t_{web}	0.1 t_{web}
Scenarios	381	312	312
a	0.41	0.36	0.6
b	0.19	0.59	0.24
P-value for ***a***	3e-112	2e-55	9e-89
P-value for ***b***	2e-9	4e-29	1e-7
h	0.1	0.4	0.4

The statistically obtained coefficents for **a** and **b** were uniformly factored by 10% for imperfection amplitude 1 and 0.5 tweb and 5% for 0.1 t_{web} to limit capacity overestimation, based on comparison with numerically obtained capacities. The final coefficients for the equation (8.12) are presented in Table 8.15.

The presented values of **a**, **b,** and h were calibrated based on at least 312 corrosion scenarios per imperfection amplitude, projected on a 36WF150 beam with 12 in. bearing length (N/d = 0.33). In order to capture the effect of N/d ratio presented in subsection 7.6, **b** is raised to the power of (0.33d/N). With this approach, the significance of the second term in equation (8.12) increases for higher values of N/d in order to capture the increased capacity observed for higher N/d ratios.

$$R_{n,crip} = \left(\boldsymbol{a}\sqrt{EF_y t_f}\, t_{ave}^{1.5} + \boldsymbol{b}^{\left(\frac{0.33d}{N}\right)}\left(\frac{4(N-H)}{d} - 0.2\right)\frac{\sqrt{E\,F_y t_f}}{t_f^{1.5}}(t_{ave})^3\right)\left(\frac{CL}{N+m\,d}\right)^h \quad (8.12)$$

Table 8.15: Proposed coefficients for equation 8.12.

Imperfection Amplitude	1 t_{web}	0.5 t_{web}	0.1 t_{web}
a	0.37	0.32	0.57
b	0.17	0.5	0.23
h	0.1	0.4	0.4
m	0.2	0.2	0.1

Crippling capacity equation (8.5), for N/d ≤ 0.2

Similarly to the procedure previously described, equation (8.5) is rewritten as the summation of two terms, that both include the average thickness t_{ave}:

$$R_{n,crip} = \mathbf{0.4}\sqrt{EF_y t_f}\, t_{ave}^{1.5} + \mathbf{1.2}\left(\frac{(N-H)}{d}\right)\frac{\sqrt{E\,F_y t_f}}{t_f^{1.5}}(t_{ave})^3 \quad (8.13)$$

In order to limit failure load overestimation observed for section loss above 60% of intact web thickness, equation (8.13) is multiplied by $(t_{ave}/(t_{web}))^h$.

Where,
t_{web} = nominal web thickness of the intact section
h = constant specified in Table 8.16.

Hence, equation (8.13) becomes:

$$R_{n,crip} = \mathbf{0.4}\sqrt{EF_y t_f}\left(\frac{t_{ave}}{t_{web}}\right)^h t_{ave}^{1.5} + \mathbf{1.2}\left(\frac{(N-H)}{d}\right)\frac{\sqrt{E\,F_y t_f}}{t_f^{1.5}}\left(\frac{t_{ave}}{t_{web}}\right)^h (t_{ave})^3 \quad (8.14)$$

Similarly, to the case for N/d>0.2, linear regression is performed based on 312 computational simulations for each imperfection amplitude. It should be also noticed, that the exponent of t_{ave} at the first term of equation (8.14) is reduced from 1.5 to 1.2 to better fit the numerical results. Equation (8.14) is rewritten as:

$$R_{n,crip} = \boldsymbol{c}\sqrt{EF_y t_f}\left(\frac{t_{ave}}{t_{web}}\right)^h t_{ave}^{1.2} + \boldsymbol{d}\left(\frac{(N-H)}{d}\right)\frac{\sqrt{E\,F_y t_f}}{t_f^{1.5}}\left(\frac{t_{ave}}{t_{web}}\right)^h (t_{ave})^3 \quad (8.15)$$

Where **c** and **d** are calculated, as shown in Table 8.16.

Table 8.16: Linear regression results for coefficients a and b for N/d ≤ 0.2.

Imperfection Amplitude	**1 t_{web}**	**0.5 t_{web}**	**0.1 t_{web}**
Scenarios	312	312	312
c	0.37	0.35	0.4
d	0.04	0.19	0.04
P-value for ***c***	2e-170	3e-175	5e-163
P-value for ***d***	0.95	0.05	0.77
h	0.4	0.2	0.15

For imperfection amplitude 0.5 t_{web} the P-value for coefficient **d** is slightly higher than the study's standards (< 0.05), yet close to them. Both the sign and magnidute are realistic, thus ultimately, the coefficient is accepted and factored by 10% to create an envelope below the FEM results. On the other hand, for imperfection amplitude equal to 1 and 0.1 t_{web}, the P-values for coefficient **d** are out of the acceptance limits (<0.05); thus, the respective second term in equation (8.15) is removed as statistically insignificant and linear regression is repeated, considering only the contribution of the first term as:

$$Y = \mathbf{c} * \text{constant} * X1 + \mathbf{f} \quad (8.16)$$

Where:
$Y = R_{n,crip}$
$X1 = (t_{ave})^{1.2}$
f is requested to be zero.

The statistically obtained values for coefficient **c** remained unaffected for both imperfection amplitudes, and similarly with the procedure so far, they were scaled to limit overestimation of the numericallly obtained capacities. The final form of the equation for crippling capacity equation for N≤ 0.2, as well the corresponding coefficients, is summarized as follows:

$$R_{n,crip} = \left(\boldsymbol{c} \sqrt{EF_y t_f}\, t_{ave}^{1.2} + \boldsymbol{d} \left(\frac{(N-H)}{d} \right) \frac{\sqrt{E\, F_y t_f}}{t_f^{1.5}} (t_{ave})^3 \right) \left(\frac{t_{ave}}{t_{web}} \right)^h \quad (8.17)$$

Where, as shown in Table 8.17:

Table 8.17: Proposed coefficients a and b for N/d ≤ 0.2.

Imperfection Amplitude	1 t_{web}	0.5 t_{web}	0.1 t_{web}
c	0.33	0.32	0.38
d	0	0.17	0
h	0.4	0.2	0.15

8.3 Evaluation of Proposed Procedures

8.3.1 Comparison between Experimental and New Predicted Capacities

The beams tested in this research study had a variety of deterioration at their ends. Out of the six specimens tested in this project, five of them had holes in their deteriorated end. The new procedures proposed as a result of this research project have not focused on alternating the way of hole inclusion in the methodology for the prediction of the capacity of deteriorated ends, and therefore, the impact of the new procedures for these specific cases is estimated to be minimal. However, the experimental program has been instrumental in validating the finite element model (FEM) which constituted the basis for the extensive parametric analysis presented in 8.3.2. The only specimen that did not have a hole was Specimen 2, and for that reason only, this specimen is presented in this section.

Specimen 2

The initial web imperfection amplitude of Specimen 2 equaled two times the nominal intact web thickness, which is outside the maximum imperfection amplitude considered in this study. The closest values for the new proposed parameters are the ones for 1 t_{web} : (Table 8.15) for equation (8.12), N/d > 0.2. Using these values, Table 8.18 summarizes the predicted bearing loads calculated according to current and proposed methodologies, as well as the experimentally obtained capacity.

Table 8.18: Comparison between experimental and predicted capacities for Specimen 2.

	Experimental (kips)	Current Procedure (kips)	Proposed Procedure (kips)	Difference
Capacity (kips)	67.6	102.2	81.2	-21%

The proposed methodology reduces the discrepancy between the experimental and the estimated capacity that emerges from the flange hole as well as the extensive initial web displacement. The efficiency of the new prediction is demonstrated in this example, due to the fact that there is no hole in this specimen. However, the new procedures still overestimate the capacity. This is attributed to the extensive imperfection that cannot be accounted for, even with the new procedures (2 t_{web}).

This issue of the imperfection amplitude is still an open problem of the proposed method, mainly because there are no real data on web imperfections. The proposed procedures should be used for imperfection amplitudes less than 1 t_{web}. If higher imperfection amplitudes are observed, the proposed procedures do not predict the capacity accurately. Either a finite element model should be built and run, or future research should cover a higher range of imperfection amplitudes.

8.3.2 Comparison between Numerically Obtained and New Predicted Capacities

In order to evaluate the efficiency of the proposed equations, the failure loads of a large number of scenarios coming from the numerical models were compared to the new procedures. Due to the size of the data (more than 2,000 models were used), indicative examples of this comparisons will be presented here. In addition to that comparison, the predictions of the current procedures are also included in the graphs. In this way, the increased efficiency of the new procedures can be observed when compared to the limited accuracy of the current procedures.

Imperfection amplitude $1 \cdot t_{web}$

For demonstration purposes, the corrosion scenarios for three different corrosion heights (10%, 20%, and 30 % of the beam depth) are projected on a 36WF150 girder with 12 in. long bearing plate. The N/d ratio (N/d=0.33) implies that the coefficients presented in Table 8.15 are used, and the obtained results are presented in Fig. 8.3.

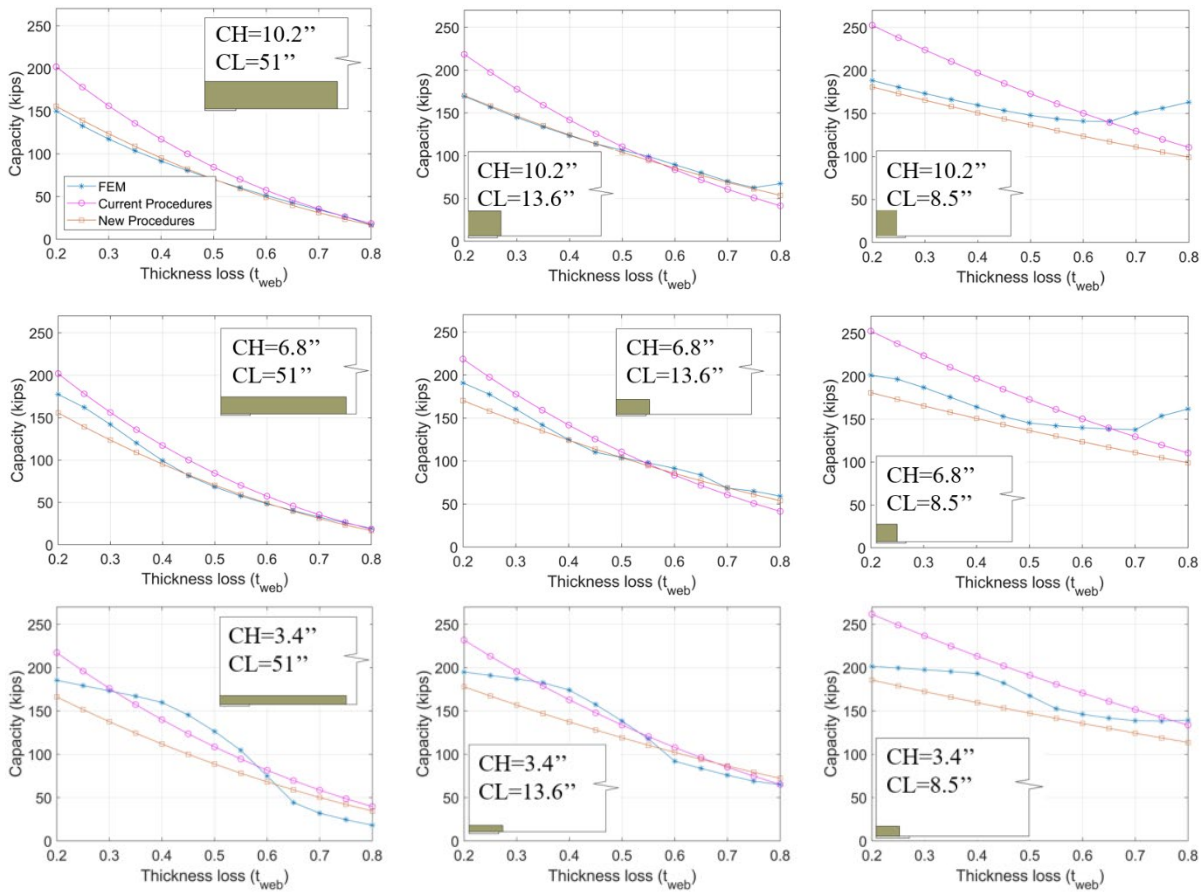

Figure 8.3: Comparison between numerically obtained capacities and failure load predictions based on current and proposed procedures, for N/d=0.33 and imperfection amplitude t_{web}.

Imperfection amplitude $0.5 \cdot t_{web}$.

For demonstration purposes, the corrosion scenarios for three different corrosion heights (10%, 20%, and 30% of the beam depth) are projected on a 36WF150 girder with 7 in. long bearing plate. The N/d ratio (N/d = 0.2) implies that the coefficients presented in Table 8.17 are used, and the obtained results are presented in Fig. 8.4.

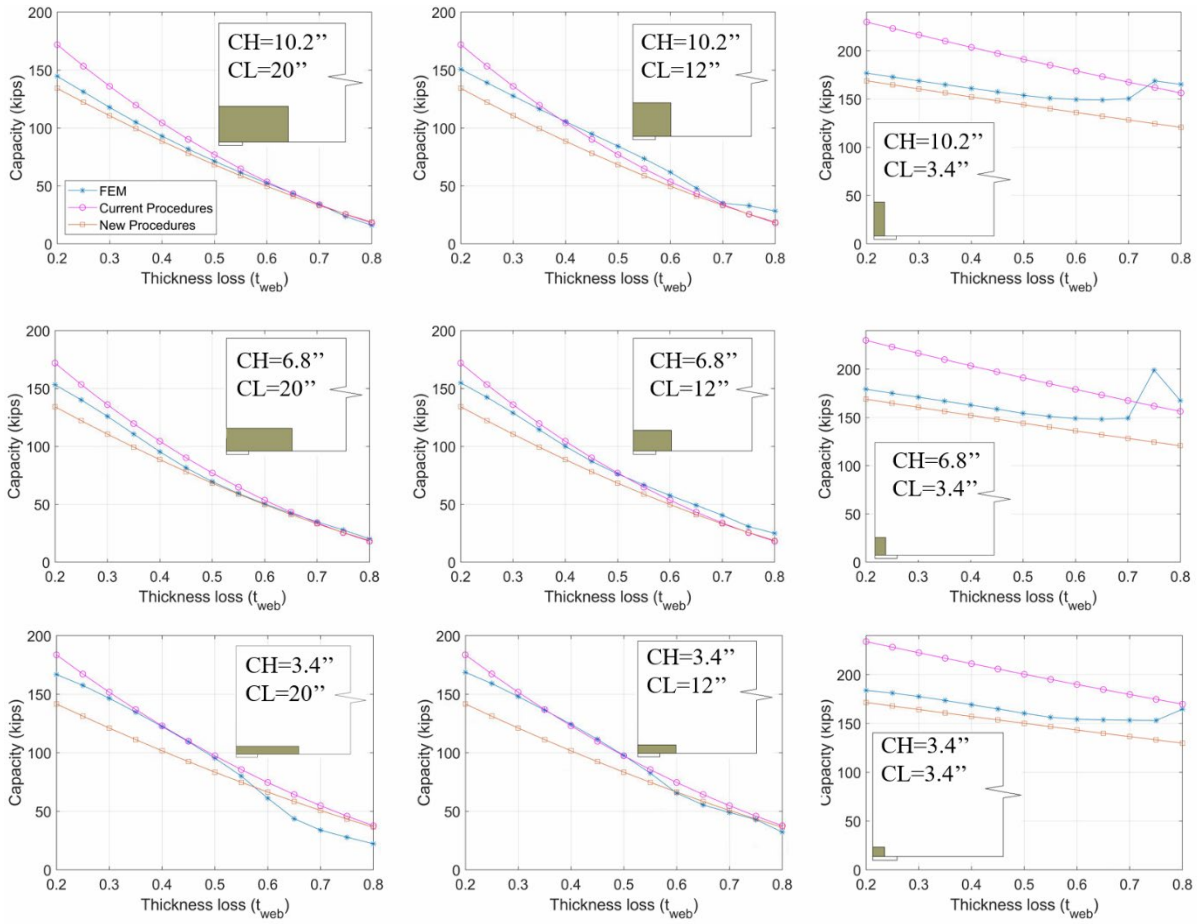

Figure 8.4: Comparison between numerically obtained capacities and failure load predictions based on current and proposed procedures, for N/d ≤ 0.2 and imperfection amplitude 0.5 t_{web}.

Imperfection amplitude 0.1·tweb.

For demonstration purposes, a deterioration scenario with corrosion height 20% of web depth and corrosion lengths expressed as a percentage of bearing length (210%, 110%, and 75% of N) were projected on a 21WF59 girder with imperfection amplitude 0.1 t_{web}, for four different bearing lengths, 14 in., 9.5 in., 6.9 in., and 5.2 in. (or 0.66, 0.45, 0.33, and 0.25 BL/d). The N/d ratios imply that the coefficients presented in Table 8.15 are used, and the obtained results are presented in Fig. 8.5.

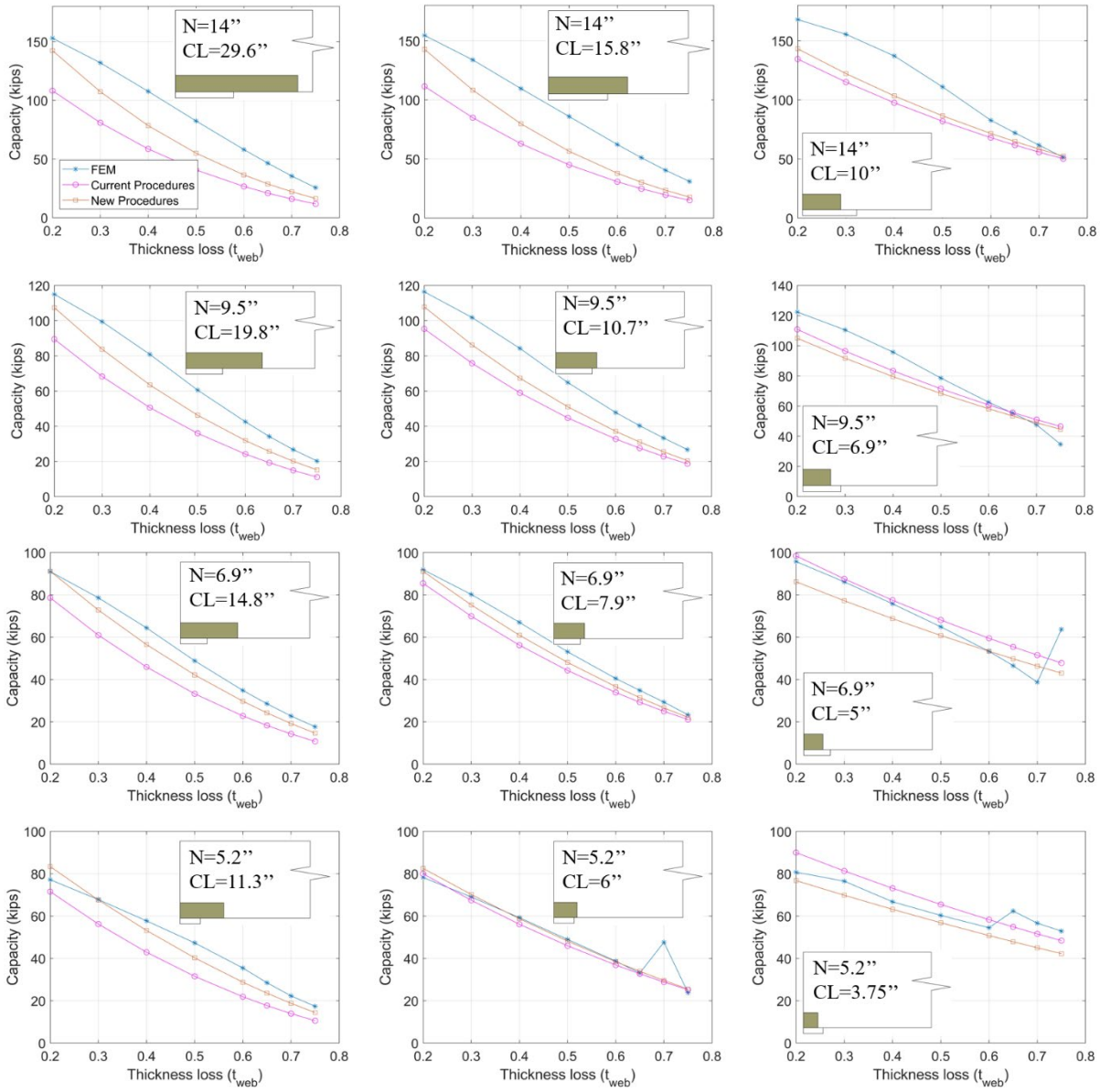

Figure 8.5: Comparison between numerically obtained capacities and failure load predictions based on current and proposed procedures, for a variety of N/d ratios and imperfection amplitude 0.1 t_{web}.

Taken altogether, the results presented in this chapter offer strong evidence that the proposed procedures provide a more accurate estimation of the actual capacity of corroded beam ends.

9.0 Conclusions

This research project focused on corroded steel beam ends, which are commonly found in the Commonwealth of Massachusetts as a result of aging and deterioration. The goal of the study was to investigate the efficiency and accuracy of the current procedures for the evaluation of the remaining capacity of the beam ends. The most important outcome of this work is the new set of equations provided in Chapter 8. Several interesting findings from all the phases of the work are presented in this chapter.

9.1 Phase I: Most Common Corrosion Topologies—Data Collection

More than 200 inspection reports of bridges with beam end deterioration, and 808 corroded beam ends, were examined in detail. Based on this real data, numerous parameters were defined and quantified through an extensive statistical analysis. Thickness loss, corrosion dimensions and locations, and hole dimensions and locations were studied in detail. Eighteen corrosion patterns were proposed for further detailed computational analysis. The main findings from Phase I are:

- Corrosion topologies
    - 18 corrosion patterns are provided, which describe the examined deteriorated beam ends.
    - The majority of the examined beam ends can be described by two patterns (W1 and W3), which are a rectangular shape with or without reducing corrosion depth along the longitudinal beam axis (84% of the examined beam ends).
    - A strong correlation between the diaphragm existence and corrosion topologies was noticed.
    - There is a significant population of beam ends with holes (15% of the examined beam ends).
- Inspection Methods
    - There is currently a lack of a comprehensive and unified inspection protocol among the MassDOT districts, as well as among inspection engineers.
    - The quality of measurements taken by the inspectors is highly susceptible to accessibility, weather conditions, and available equipment (e.g., different d-meter types with varying accuracy).
    - Usually, there are no more than one or two thickness measurements reported per corroded end.
    - To the authors' knowledge, there is a need for a set of criteria for the condition of beam ends that would decide whether a beam end should be further examined for load rating.

9.2 Phase II: Experimental Testing

This project was the first that tested naturally corroded specimens obtained from two different bridge rehabilitation projects in the Commonwealth of Massachusetts. The research team tested six beams and reported the peak failure load as well as the failure mechanism. The six beams tested spanned at least 20 ft., with 33 in. and 22 in. depth. Each specimen had some unique characteristics that allowed the research team to study different aspects of the problem, such as section loss, initial imperfections, and web or flange areas with 100% thickness loss (holes). The experimental configuration was designed to restrict the top flange, mimicking in-service conditions and ensuring that failure occurs at the corroded end. The load was applied to the top flange 5 ft. from the studied end. This configuration served two purposes: It ensured that the failure was shear dominated, and that more than 70% of the load was distributed to the studied end. This loading configuration is distinguished from the existing literature and the one in *(8)*, since it examines beam behavior and not column-like behavior of the beam end. The main findings of Phase II as follows:

- Regarding the experimental failure loads comparison to the manual predictions, out of the six experiments, one was found 51% lower than the prediction, four were significantly underestimated by the current procedures, while for Specimen 4, the failure of the corroded end was not reached due to a beam long-wave instability mode. From these results, a first conclusion is that **the current manual procedures underestimate in some cases the actual capacity and overestimate it in others**. It is impossible to overwhelmingly conclude between the two, as there is evidence for both conditions; however, the authors have gained a better understanding on several factors that affect the capacity.
- Specimens 1, 3, 5, and 6 were all underestimated by current procedures. These specimens had web holes as a common characteristic. This observation provides evidence that **the current procedures do not satisfactorily assess the strength of girders with holes at their beam ends**. This conclusion is further supported by the experimental observation that if a hole is present, the top edge of the hole will make contact with the bottom beam flange, and the beam end will start bearing load. This is a mechanism that was previously unknown. It is still unclear if this mechanism can be considered as a reliable load path at the beam end, mainly because the activation of this load path is associated usually with large vertical deflections that could pose a serviceability problem.
- The failure mechanism of Specimen 2 revealed one of the most important findings of the experimental program. The failure mode was strongly affected by the initial lateral web imperfection. This type of imperfection is not currently considered in the manual procedures, and that is the reason that the procedures significantly overestimated the capacity of this beam. This test was particularly important, since it showed that this **initial lateral web imperfection severely affects the capacity of the beam end**. Although this finding is consistent with basic plates or shells theory, it was not part of the existing procedures or the current inspection protocol. Based on this result and on oral correspondence with inspectors, it was found that this type of

imperfection is more common than previously thought, and therefore it is a highly important parameter to be measured. That is the reason the final proposed procedures provided in Chapter 8 are given for a set of different imperfection amplitudes, since there was no data to the research team about the initial imperfection.

- All experimental observed failures had a common characteristic, **the lateral deflection of the web at peak load,** which indicated a buckling-related failure mechanism.
- The experiments revealed that the **post buckling behavior is characterised by a progressive loss of stiffness** with rapidly increasing vertical and lateral deformations, contrary to previous studies conducted on specimens with artificial thickness reduction, where an instant failure was reported.

9.3 Phase III: Computational Results—Parametric Analysis

The experimentally obtained data was used to calibrate a high-fidelity numerical model capable of predicting the capacity of beam ends. The numerous aspects of the calibration for the numerical modeling are not provided here and are included in Chapter 4. The model generation, under the validated assumption, as well as the post-processing, were automated by combining Python programming language and Abaqus FEA software. This technique remarkably increased the efficiency of the available computational capacity, allowing the researchers to conduct an extensive parametric analysis simulating and analyzing thousands of combinations of corrosion topologies for several beam types and lengths. The scenarios computationally analyzed came from the corrosion topologies identified in Phase I of this work, under the assumption of uniform thickness loss. This assumption does not reflect the actual condition of in-service beams; however, its advantage is two-fold. First, it is in compliance with the current manual procedures for strength evaluation of corroded girders. Second, it serves the usually limited thickness measurements performed by state inspection engineers. The main findings of Phase III are as follows:

- **The research team analyzed more than 2,000 models,** accounting for a plethora of corrosion scenarios. The results were processed, and the peak loads of the beam ends were recorded.
- The computational model assumptions are based on experimental observations. **The team has built a high-fidelity computational model that is capable of predicting accurately the capacity of corroded beam ends.**
- The numerically obtained capacities proved to be **extremely sensitive to the initial geometric imperfection of the web**. Based on this sensitivity, analyses were performed for three different amplitudes: 0.1, 0.5, and 1 times t_{web}.
- The length of the specimen does not have an influencing effect on numerically obtained capacities.
- A deterioration scenario with relatively accounted dimensions (corrosion length and height expressed as a percentage of the depth) has a similar harming effect on all

beam types with the same N/d ratio, where d denotes the depth of the beam and N its bearing length.

- **The effect of a hole to the capacity of the corroded end is highly related to the configuration at the bearing**. If the hole is limited above the outer edge of the bearing, it has no significant effect on the capacity, regardless of its height. However, its harming effect escalates when the hole expands close to the inner bearing edge and beyond.
- The numerically obtained findings are in good compliance with the experimental findings. The failure mechanism related to the existence of holes observed from the FEA results justifies the outcome of the experimental work.

9.4 New Procedures—Final Outcome

Taken altogether, the current procedures, which are based on two different failure mechanisms (yielding and crippling), are able to capture the general trend of reduced capacity for increasing section loss along the corroded end, but they lack accuracy. It is worth mentioning that the crippling capacity governed all the numerically simulated scenarios as well as the conducted experiments; thus, the effort was focused on the crippling related equations. The proposed modifications regard three main aspects:

1. **The initial imperfection amplitude.**
2. **The area over which the remaining web thickness is determined.**
3. **The values of the constant factors of the current procedures.**

A set of equations, based on the N/d ratio, is proposed for three different imperfection amplitudes (0.1, 0.5, and 1 t_{web}).

The current procedures do not include an equation for buckling. It was accounted for in previous versions of the manual, but to the authors' knowledge, this was removed because of overly conservative predictions. This study's observations from experiments and computations can be considered both as buckling and crippling phenomena. The current equations were modified to create an envelope for both of these types of failure, crippling and buckling, while future research could distinguish them further with separate prediction tools for each case.

10.0 Limitations and Future Work

Every aspect of this work emerges from real corrosion data. Nevertheless, there are still some limitations as well as some open problems. The investigation efforts were focused on the girder, while the deck contribution was simulated by the applied boundary conditions. Good understanding was gained for the corroded beams' behavior. However, the physical absence of both deck and diaphragm from the experimental configuration have potentially affected the findings regarding stiffness, uplift, and reaction force distribution along the bearing. Finally, the tested specimens were naturally corroded with a continuously varying section loss profile along the affected area. This probably has affected the strain magnitudes recorded by the instrumentation, which capture the localized deformation, partially reflecting the material thickness of the web or the flange that were attached on. Thus, relative magnitude differences may include a source of uncertainty.

For some specimens, the web holes were located at the bottom of the web above bearing. After the initiation of the loading process, the upper web hole edge began bearing at flanges, and the specimens were able to retain significant additional loads. However, this failure mechanism can be observed under the condition of extensive downwards translation of the top flange. This condition is considered controversial for in-service girders, due to the additional stiffness emerging from the deck as well as potential diaphragm behavior. This is an area for future study.

Future studies will have to examine the behavior of the corroded beams as part of the whole bridge and the potential redistribution of forces after the failure (or even the loading) of one beam end. The system behavior of the bridge is hugely important, and it is expected to provide more capacity, although this remains to be validated.

Considering the accessibility difficulties that engineers face during inspections, the initial web imperfection assessment in the field is considered not accurate but hugely important. To resolve this problem and to improve the efficiency of the state inspections, organized measurements have to be performed, following the same methodology to ensure qualitative results and to gain better understanding on the actual beam condition. This issue should be examined as part of a larger effort to unify and update the inspection protocol for beam ends. Related to this, new technologies for taking measurements should be explored that will make the inspection process easier and more accurate.

There are other types of beam ends that were not examined in detail in this project. The two main examples are beam ends with stiffeners and beam ends with diaphragms. These types of beam ends will most probably behave differently to what is included in the current report.

This page left blank intentionally.

11.0 References

1. U.S. Federal Highway Administration. *National Bridge Inventory Database*. https://www.fhwa.dot.gov/bridge/nbi/no10/defbr17.cfm. Accessed July 21, 2018.
2. American Society of Civil Engineers (ASCE). *Infrastructure Report Card.* https://www.infrastructurereportcard.org/
3. Roberts, T. M. Slender Plate Girders Subjected to Edge Loading. *Proceedings of the Institution of Civil Engineers Part B,* 1981. 71: 805-819.
4. Johansson, B., and O. Lagerqvist. Resistance of Plate Edges to Concentrated Forces. *Journal of Constructional Steel Research*, 1995. 32: 69-105.
5. Kayser, J. R., and A. S. Nowak. Capacity Loss Due to Corrosion in Steel-Girder Bridges. *Journal of Structural Engineering*, 1989. 115: 1525-1537.
6. Tohidi, S., and Y. Sharifi. Load-Carrying Capacity of Locally Corroded Steel Plate Girder Using Artificial Neural Network. *Thin-Wall Structures*, 2016. 100: 48-61.
7. Gheitasi, A., and D. Harris. Redundancy and Operational Safety of Composite Stringer Bridges with Deteriorated Girders. *Journal of Performance of Constructed Facilities,* 2015.
8. Van de Lindt, J. W., and T. M. Ahlborn. *Development of Steel Beam End Deterioration Guidelines*. Publication MDOT-RC-1454, Michigan Tech Transportation Institute, 2005.
9. Sugimoto, I., Y. Kobayashi, and A. Ichikawa. Durability Evaluation Based on Buckling Characteristics of Corroded Steel Deck Girders. *Quarterly Report of Railway Technical Research Institute*, 2006. 47: 150-155. https://www.jstage.jst.go.jp/article/rtriqr/47/3/47_3_150/_pdf/-char/en
10. Liu, C., T. Miyashita, and M. Nagai. Analytical Study on Shear Capacity of Steel I-Girders with Local Corrosion nearby Supports. *Procedia Engineering,* 2011. 14: 2276-2284.
11. Ahn, J. H., S. Kainuma, and I. T. Kim. Shear Failure Behaviors of a Web Panel with Local Corrosion Depending on Web Boundary Conditions. *Thin-Walled Structures,* 2013. 73: 302-317.
12. Kim, I. T., M. J. Lee, J. H. Ahn, and A. Kainuma. Experimental Evaluation of Shear Buckling Behaviors and Strength of Locally Corroded Web. *Journal of Constructional Steel Research,* 2013. 83: 75-89.
13. Ahn, J. H., J. H. Cheung, W. H. Lee, H. Oh, and I. T. Kim. Shear Buckling Experiments of Web Panel with Pitting and Through- Thickness Corrosion Damage. *Journal of Constructional Steel Research,* 2015. 115: 290-302.
14. Ahn, J. H., I. T. Kim, S. Kainuma, and M. J. Lee. Residual Shear Strength of Steel Plate Girder due to Web Local Corrosion. *Journal of Constructional Steel Research,* 2013. 89: 198-212.
15. Usukura, M., T. Yamaguchi, Y. Suzuki, and Y. Mitsugi. Strength Evaluation for a Corroded Damaged Steel Girder End Considering its Collapse Mechanism. *Proceedings of the 13th East Asia-Pacific Conference on Structural Engineering and Construction (EASEC),* 2013.

16. Yamaguchi, E., and T. Akagi. Degradation of Load- Carrying Capacity of Steel I-Girder End due to Corrosion. *Proceedings of the 13th East Asia-Pacific Conference on Structural Engineering and Construction (EASEC),* 2013.
17. Khurram, N., E. Sasaki, H. Katsuchi, and H. Yamada. Experimental and Numerical Evaluation of Bearing Capacity of Steel Plate Girder Affected by End Panel Corrosion. *International Journal of Steel Structures*, 2014. 14: 659-676.
18. Ahn, J. H., S. Kainuma, F. Yasuo, and I. Takehiro. Repair Method and Residual Bearing Strength Evaluation of a Locally Corroded Plate Girder at Support. *Engineering Failure Analysis,* 2013. 33: 198-418.
19. Miyashita, T., M. Nagai, D. Wakabayashi, Y. Hidekuma, A. Kobayashi, Y. Okuyama, N. Koibe, and W. Horimoto. Repair Method for Corroded Steel Girder Ends Using CFRP Sheet. Presented at IABSE – JSCE Joint Conference on Advances in Bridge Engineering- III, Bangladesh, 2015.
20. Ogami, H., K. Fujii, T. Yamada, and H. Iwasaki. Renovation of Corroded Girder End in Plate Girder Bridge with Resin and Rebars. *Implementing Innovative Ideas in Structural Engineering and Project Management,* 2015.
21. Wu, B., J. L. Cao, and L. Kang. Influence of Local Corrosion on Behavior of Steel I-Beams subjected to End Patch Loading: Experiments. *Journal of Constructional Steel Research,* 2017. 135: 150-161.
22. Wu, B., J. L. Cao, and L. Kang. End Patch Loading Behavior and Strengthening of Locally Corroded Steel I- Beams. *Journal of Constructional Steel Research,* 2018. 148: 371-382.
23. Zmetra, K. M., K. F. McMullen, A. E. Zaghi, and K. Wille. Experimental Study of UHPC Repair for Corrosion- Damaged Steel Girder Ends. *Journal of Bridge Engineering,* 2017. 22.
24. Kruszewski, D., K. Wille, and A. E. Zaghi. Push-out Behavior of Headed Shear Studs Welded on Thin Plates and Embedded in UHPC. *Engineering Structures*, 2018. 173: 429-441.
25. Kruszewski, D., K. Wille, and A. E. Zaghi. Design Considerations for Headed Shear Studs Embedded in Ultra-High Performance Concrete as Part of a Novel Bridge Repair Method. *Journal of Constructional Steel Research,* 2018. 149: 180-194.
26. Kruszewski, D., A. E. Zaghi, and K. Wille. Finite Element Study of Headed Shear Studs Embedded in Ultra-High Performance Concrete. *Engineering Structures*, 2019. 188: 538-552.
27. Kruszewski, D., A. E., Zaghi, and K. Wille. Durability Evaluation of Headed Shear Studs Embedded in Ultra-High Performance Concrete via Electrochemical Corrosion. *Journal of Bridge Engineering*, 2019. 24.
28. *Code of Federal Regulations*. https://www.gpo.gov/fdsys/pkg/CFR-2012-title23-vol1/pdf/CFR-2012-title23-vol1-sec650-311.pdf. Accessed July 13, 2019.
29. MassDOT. *MassDOT Bridge Inspection Handbook.* Boston, MA: Massachusetts Department of Transportation Highway Division Bridge Section, 2015.
30. MassDOT. *Draft LRFD Bridge Manual Part I.* Boston, MA: Massachusetts Department of Transportation Highway Division Bridge Section, 2019.
31. MassDOT. *Structures Inspection Field Report Routine & Special Member Inspection.* Structure No C18028-0KQ-DOT-NBI, 2017.
32. *PocketMike, Operating Manual*. GE Inspection Technologies, Lewistown, PA.

33. ASTM Standard E8/E8M. *Standard Test Methods for Tension Testing of Metallic Materials.* West Conshohocken, PA: ASTM International, 2011.
34. *Abaqus, User's Guide.* Dassault Systemes Simulia Corporation, Providence, RI, 2014.

This page left blank intentionally.

12.0 Appendices

12.1 Appendix A: Detailed Data and Processing Graphs for Beam Ends without Diaphragm

12.1.1 Introduction

The data was divided in two main categories: beam ends with diaphragm and beam ends without diaphragm. All the graphs in this part of the document represent the second case. The histogram contains the frequency of each of the defined corrosion patterns (the total number of times each pattern appears in the reports).

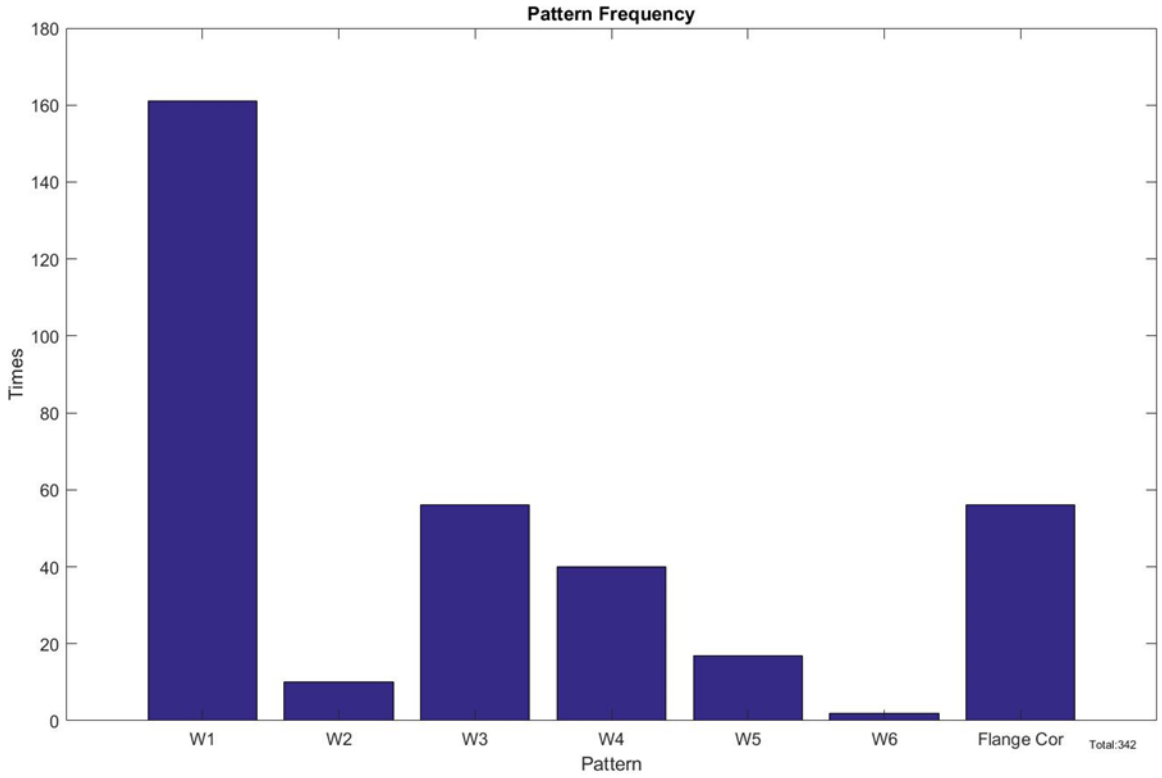

Figure 12.1: Web corrosion patterns distribution for beams without diaphragm.

For each web corrosion pattern, the authors have normalized the characteristic dimensions (CH_1, CH_2, CH_3, CL_1, CL_2, CL_3) with the height H_0, where $H_0 = H - 2t_f$.

12.1.2 Pattern W1

Web corrosion

The distribution of CH_1 is shown in Fig. 12.2. From this histogram, two main trends are noticed: either (a) full height corrosion, or (b) corrosion up to 30% of H_0.

$$CH_1 \in \begin{cases} (0, 0.3H] \\ [0.9H, H] \end{cases}$$

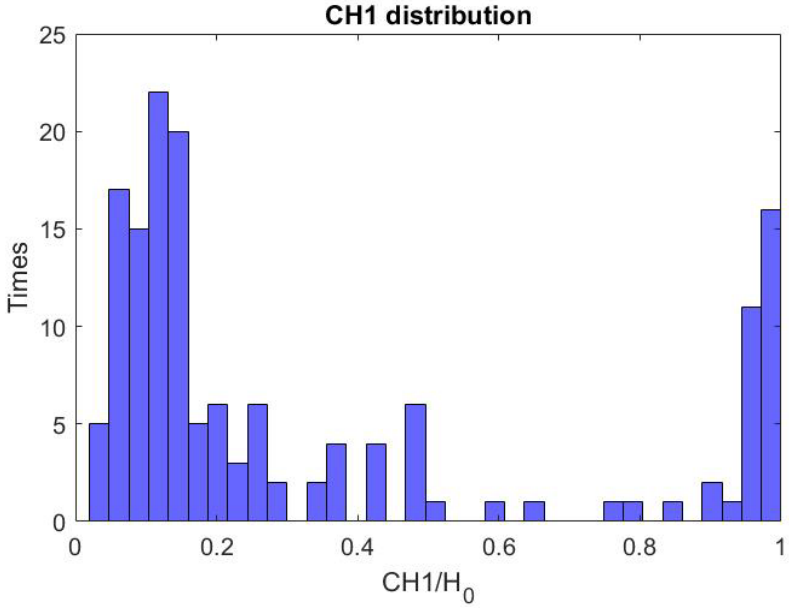

Figure 12.2: CH_1 distribution of W1 pattern for beams without diaphragm.

Similarly, the CL_1 distribution is shown in Fig. 12.3. From this histogram, it is safe to say that most of the web corrosion lengths are up to 1.5 times the H_0.

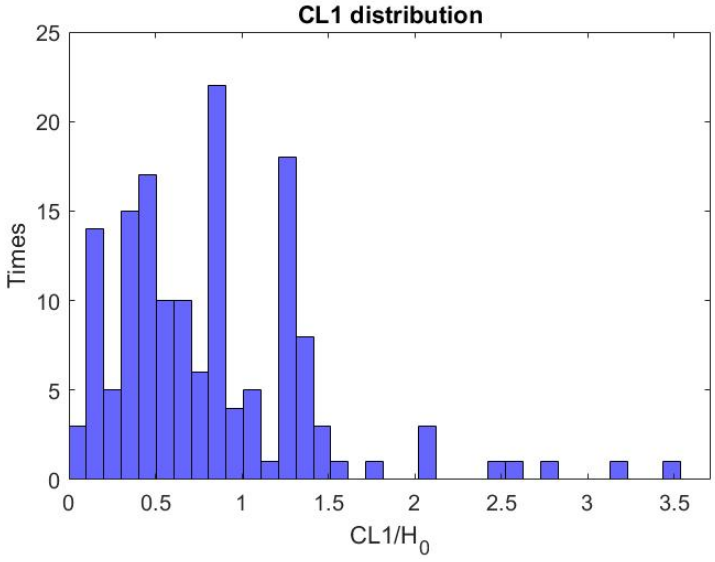

Figure 12.3: CL_1 distribution of W1 pattern for beams without diaphragm.

Fig. 12.4 shows the ratio of CL_1/CH_1 which indicates that in general, the length of the corroded area is greater than its height. Fig. 12.5 focuses on the range 0-15 for the same distribution.

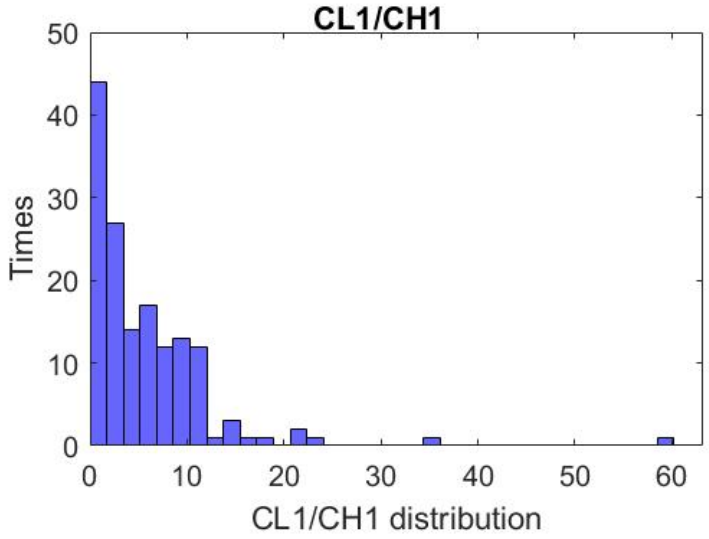

Figure 12.4: Ratio of corrosion length (CL_1) to corrosion height (CH_1) of W1 pattern for beams without diaphragm.

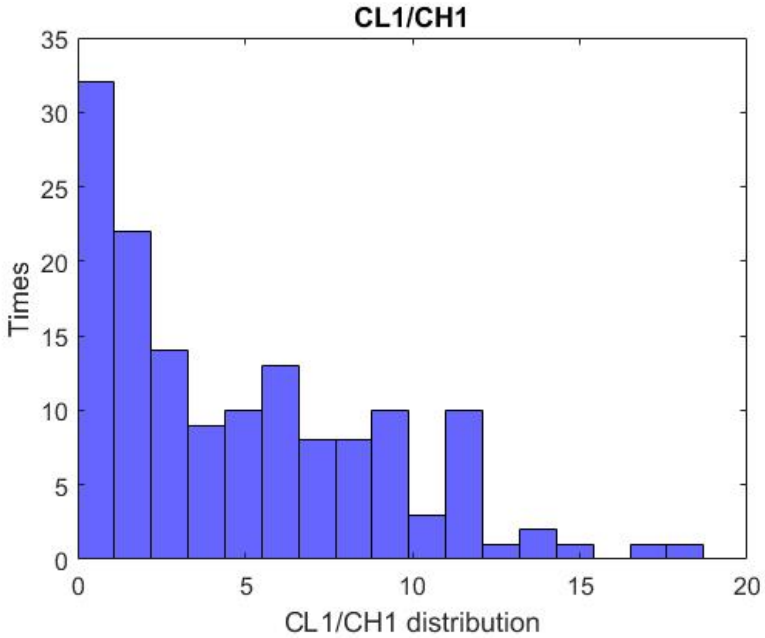

Figure 12.5: Ratio of corrosion length (CL_1) to corrosion height (CH_1) of W1 pattern for beams without diaphragm (range 0-15).

As an additional step, the corrosion length and the web thickness loss distribution for each of the two cases of CH_1 were plotted (a) for $CH_1 < 0.3H_o$ (Fig. 12.6); and (b) for $CH_1 > 0.9H_o$ (Fig. 12.9).

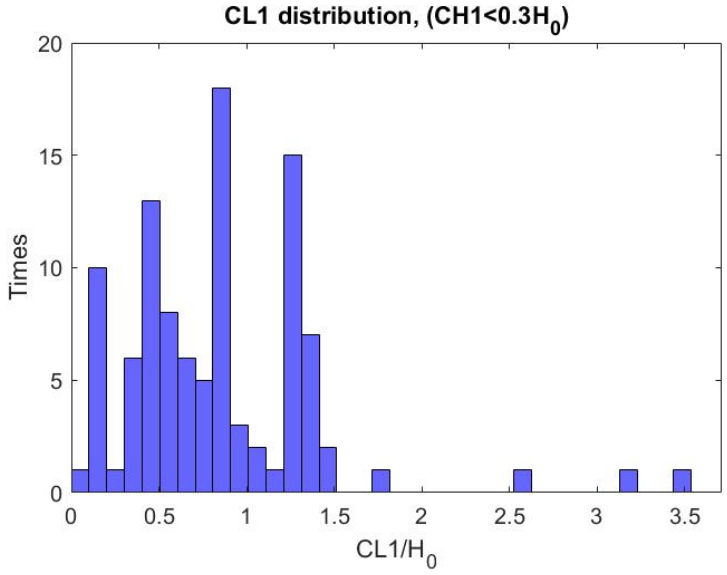

Figure 12.6: CL1 distribution of W1 web corrosion pattern, with corrosion height up to 30% of H_0 for beams without diaphragm.

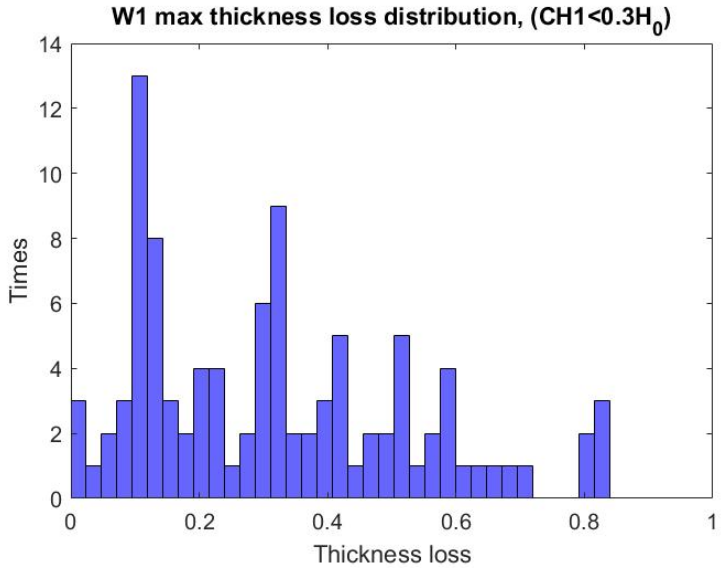

Figure 12.7: Max thickness loss distribution of W1 web corrosion pattern, with corrosion height up to 30% of H_0 for beams without diaphragm.

Based on Fig. 12.6, the team can define as extreme case the following, which covers 103 out of the 161 W1 without diaphragm cases:

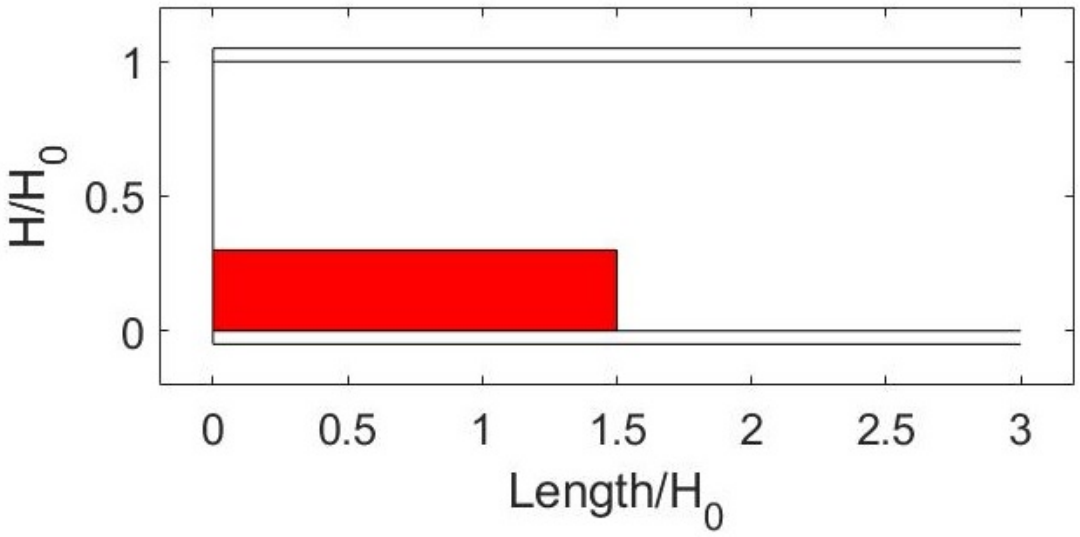

Figure 12.8: First extreme W1 web corrosion pattern, with corrosion height up to 30% of H_0 for beams without diaphragm.

Based on Fig. 12.7, the values for the web thickness loss are: $\frac{t_{loss}}{t_{web}} \in \{0.2, 0.4, 0.6, 0.8\}$

Fig. 12.9 shows the distribution of CL_1 for the case when $CH_1 > 0.9H_o$.

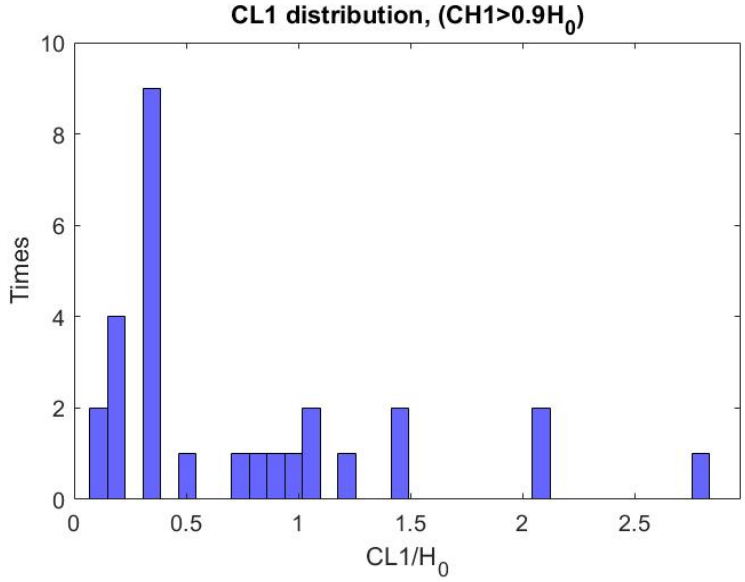

Figure 12.9: CL_1 distribution of W1 web corrosion pattern with corrosion greater than 90% of H_o for beams without diaphragm.

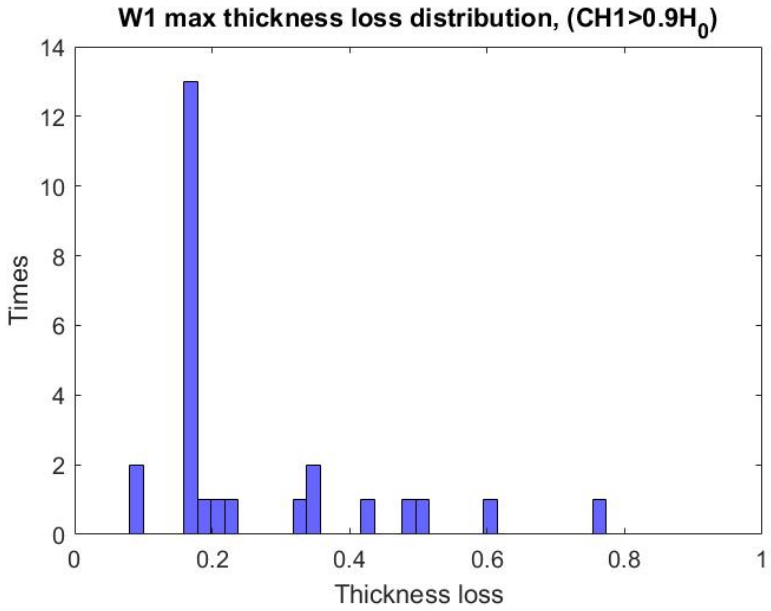

Figure 12.10: Max thickness loss distribution of W1 web corrosion pattern with corrosion height greater than 90% of H_o for beams without diaphragm.

Fig. 12.10 shows the maximum thickness loss distribution for the same groups of beams. Therefore, for the full height corrosion (> $0.9H_o$), two different cases are identified as shown in Figs. 12.11 and 12.12.

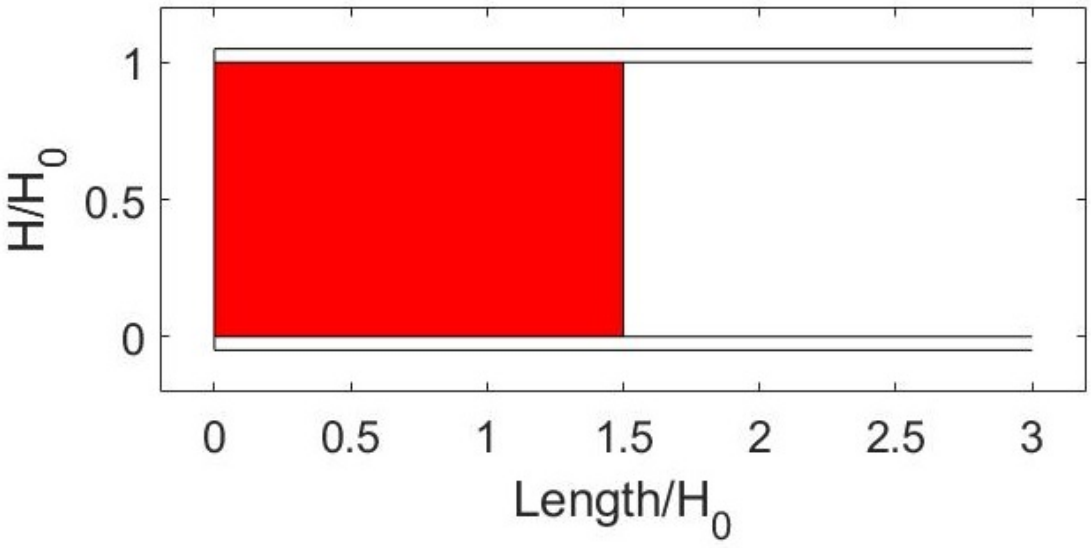

Figure 12.11: Second extreme W1 web corrosion pattern, with corrosion height greater than 90% of H_o for beams without diaphragm.

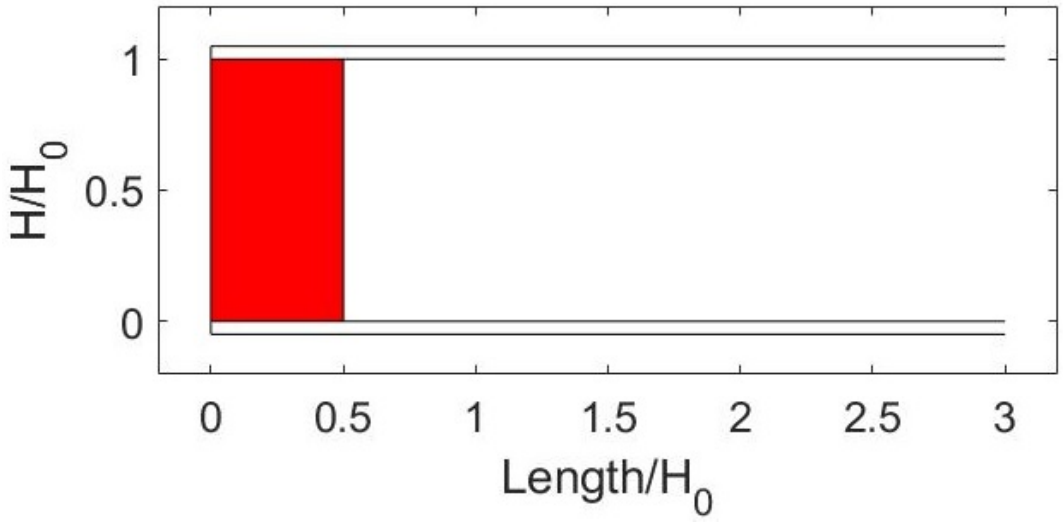

Figure 12.12: Third extreme W1 web corrosion pattern, with corrosion height greater than 90% of H_o for beams without diaphragm.

From Fig. 12.10, one can conclude that the web thickness loss for this case is: $\frac{t_{loss}}{t_{web}} \in \{0.2, 0.8\}$.

Flange corrosion

For each of the three cases (Figs. 12.8, 12.11, and 12.12) the ratio of the length of the corroded flange over the length of the corroded web was plotted (Figs. 12.13, 12.14, and 12.15).

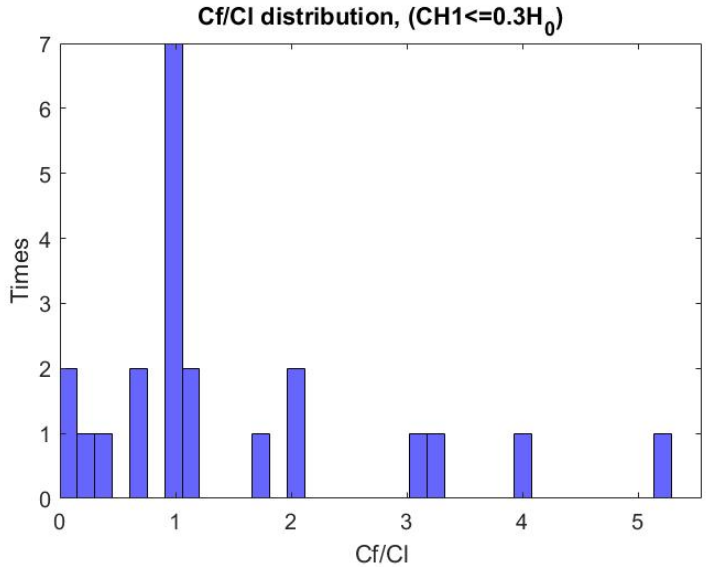

Figure 12.13: Ratio of flange to web corrosion length distribution of W1 web corrosion pattern with corrosion height up to 30% of H_o for beams without diaphragm.

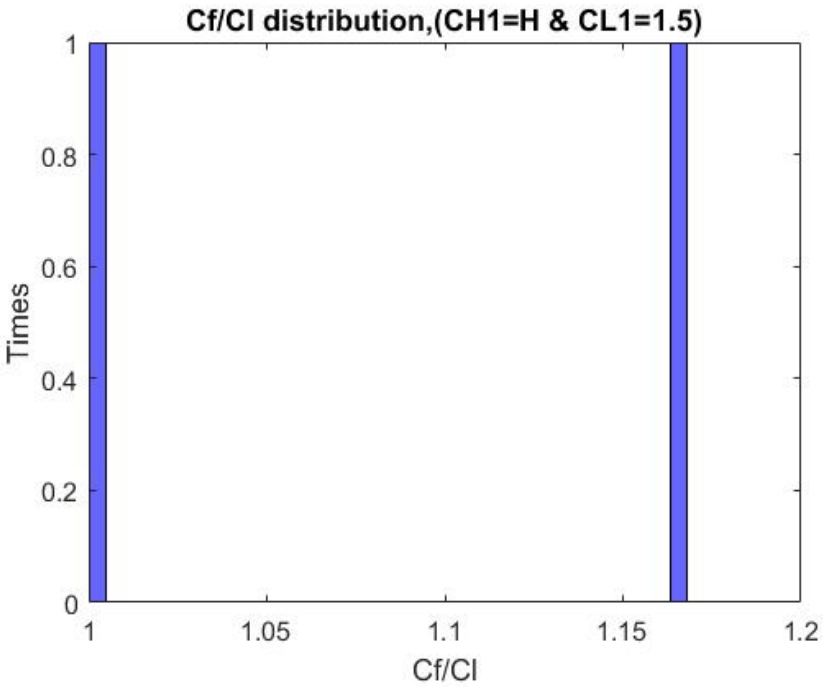

Figure 12.14: Ratio of flange to web corrosion length distribution of W1 web corrosion pattern for extreme scenario CASE B for beams without diaphragm.

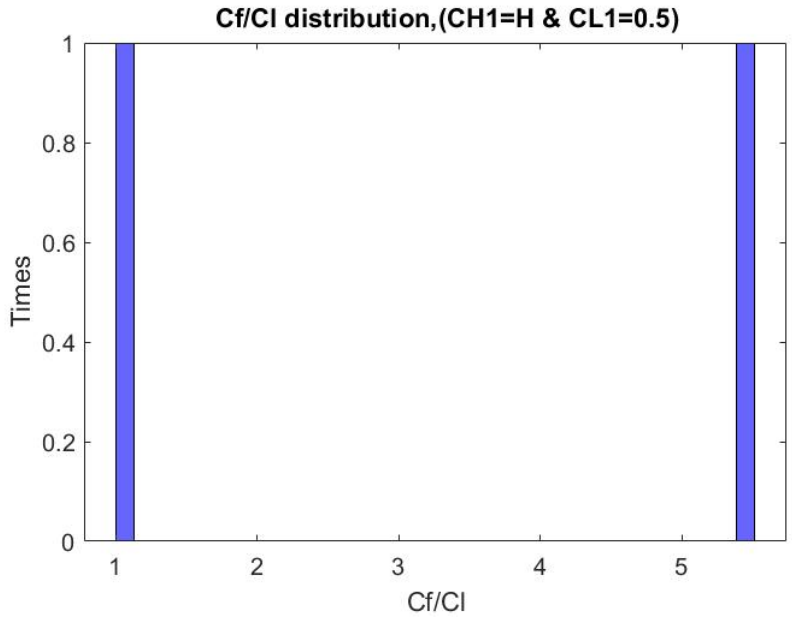

Figure 12.15: Ratio of flange to web corrosion length distribution of W1 web corrosion pattern for extreme scenario CASE C for beams without diaphragm.

The flange thickness loss is plotted in Fig. 12.16:

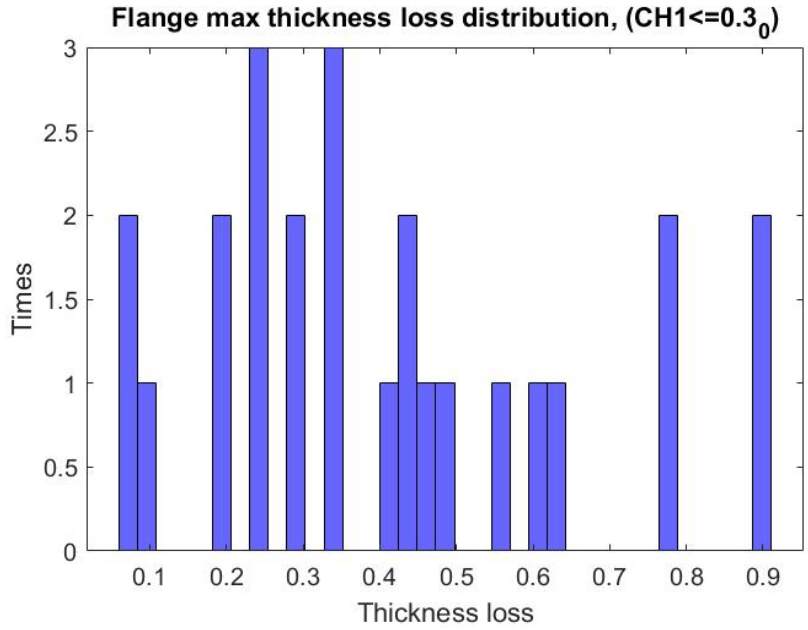

Figure 12.16: Max flange thickness loss distribution of W1 web corrosion pattern with corrosion height up to 30% of H0 for beams without diaphragm.

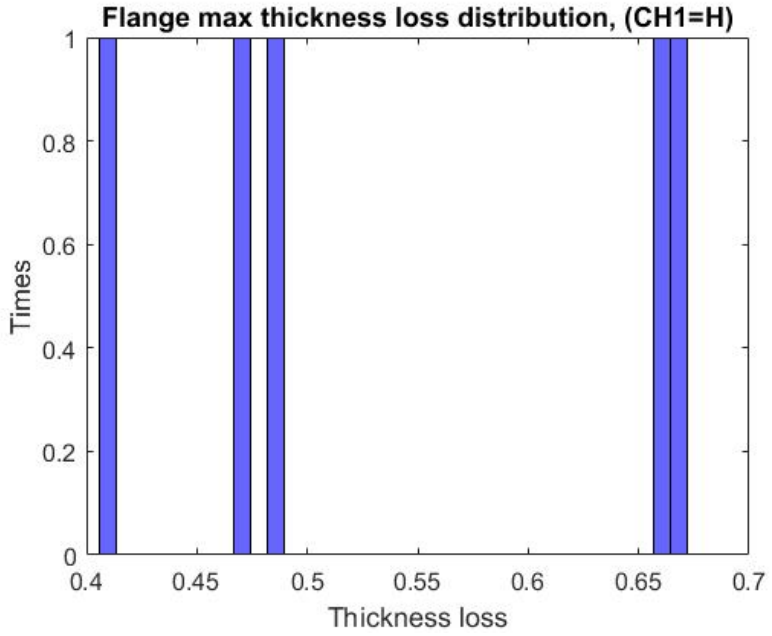

Figure 12.17: Max flange thickness loss distribution of W1 web corrosion pattern with full height corrosion for beams without diaphragm.

Thus, for Case A: $\frac{t_{loss}}{t_{flange}} \in \{0.2, 0.4, 0.6, 0.8\}$ (Fig. 12.10) and for cases B and C: $\frac{t_{loss}}{t_{flange}} \in \{0.45, 0.65\}$ (Fig. 12.16).

For all cases: $\frac{C_f}{C_l} \in [1,2]$ (Figs. 12.23, 12.24, and 12.25).

Holes

The frequency of hole appearance is shown in Table 12.1.

Table 12.1: Frequency of hole appearance for beams without diaphragm

	Frequency	No hole	M1	M2	M3	M4	M12	M13	M24
W1	161	146	9	1	3	0	0	2	0
W2	10	8	2	0	0	0	0	0	0
W3	56	44	7	0	3	1	0	1	0
W4	40	347	4	0	0	0	0	2	0
W5	17	13	3	1	0	0	0	0	0
W6	2	2	0	0	0	0	0	0	0

According to the table, the W1 pattern is combined nine times with the M1 hole pattern (not all cases provide data). The web thickness loss at these cases is shown in Fig. 12.18.

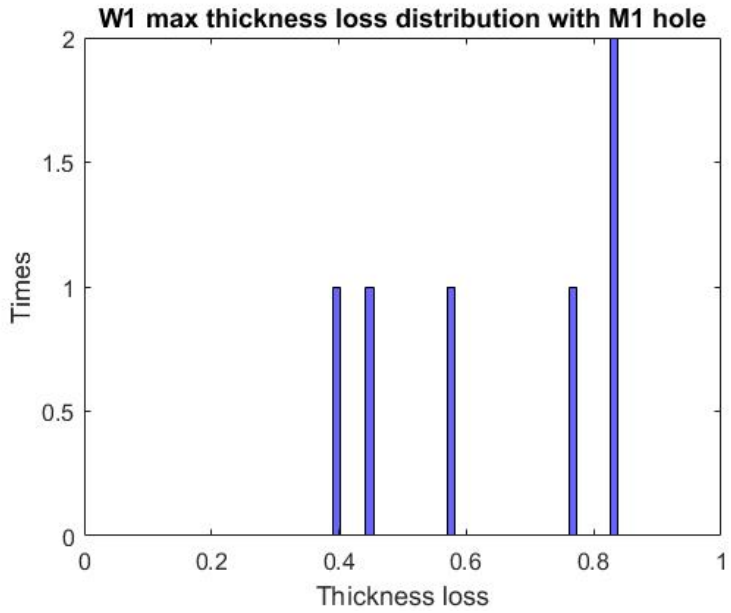

Figure 12.18: Max thickness loss distribution for W1 web corrosion patterns and M1 hole for beams without diaphragm.

Thus, it could be said that the holes appear when the web thickness loss exceeds 40%. The distribution of the hole dimensions is shown in Figs. 12.19 and 12.20:

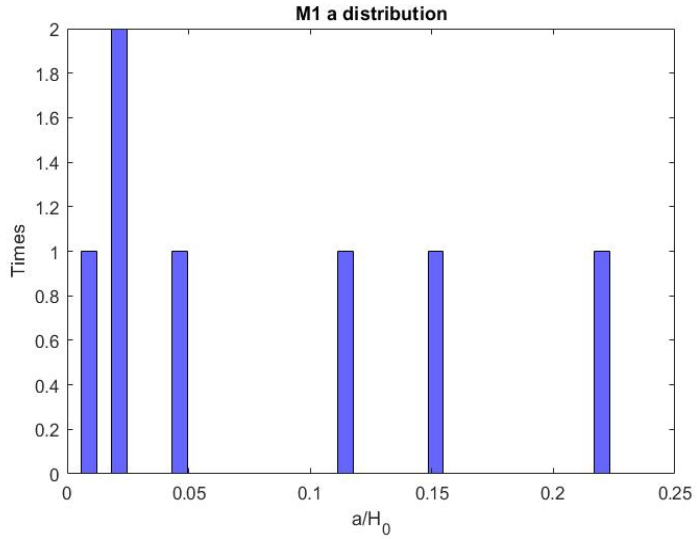

Figure 12.19: M1 web hole's pattern height distribution of W1 web corrosion pattern for beams without diaphragm.

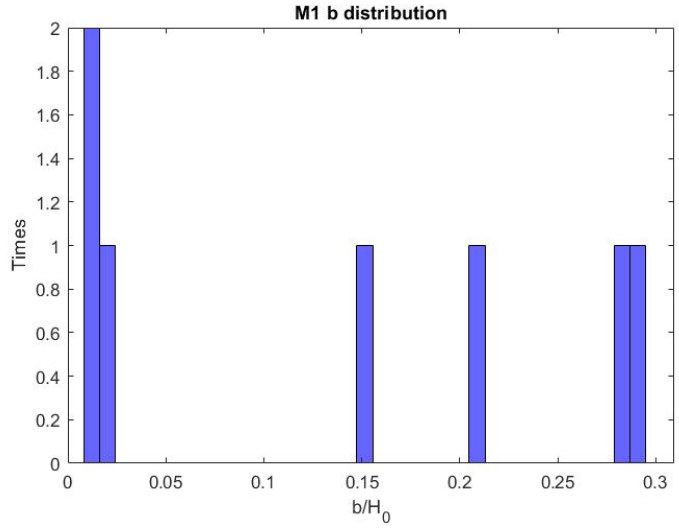

Figure 12.20: M1 web hole's pattern length distribution of W1 web corrosion pattern for beams without diaphragm.

Observing Figs. 12.19 and 12.20, it can be said that M1 appears in the form of pit holes (very small dimensions) or in a rectangular shape with the long side parallel to flange. Due to the small number of the available data for the holes, dimensions are not investigated for each case A, B, or C separately.

The extreme scenario, projected on W1 Case C with a=0.22H and b=0.3H_0, is presented in Fig. 12.21 as follows:

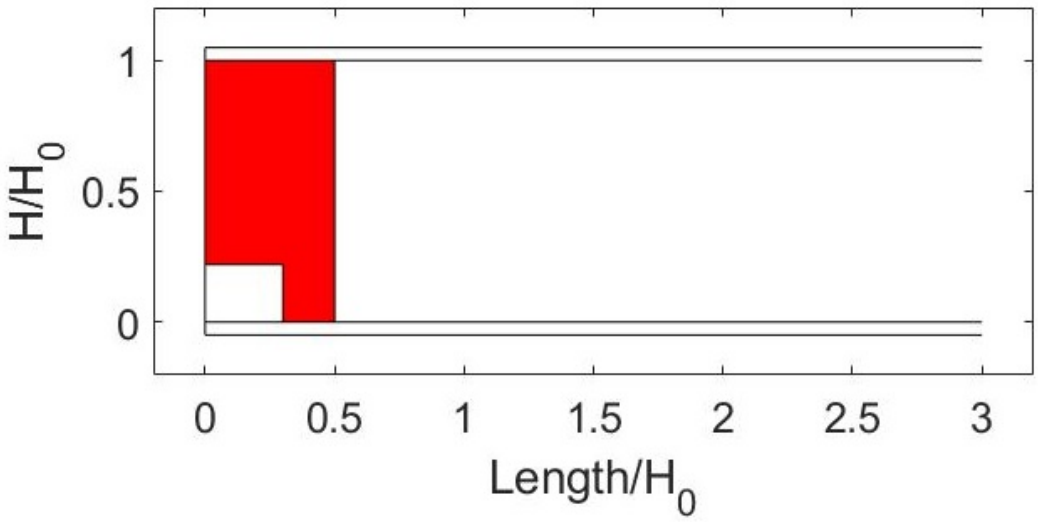

Figure 12.21: M1 extreme web hole pattern scenario of W1 web corrosion pattern, projected on W1 CASE C, for beams without diaphragm.

12.1.3 Pattern W2

Web corrosion

The W2 pattern was observed in total only 10 times. Similarly to the W1 pattern, the distributions of all normalized dimensions and web thickness loss were plotted.

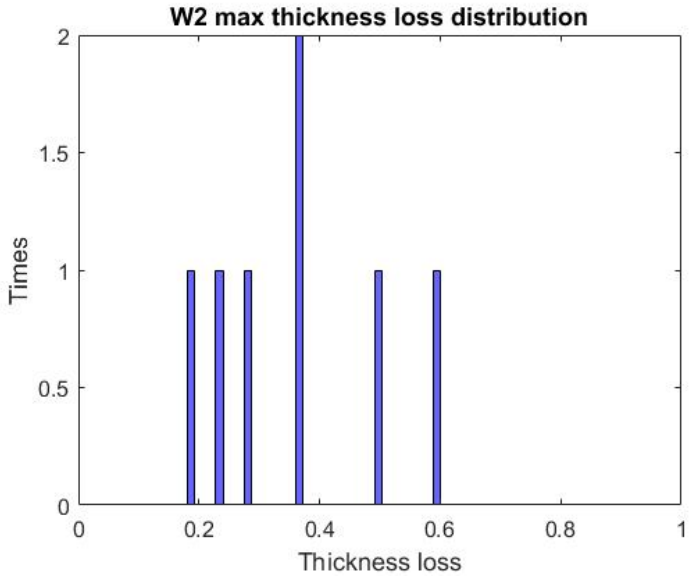

Figure 12.22: Web thickness loss distribution of W2 pattern for beams without diaphragm.

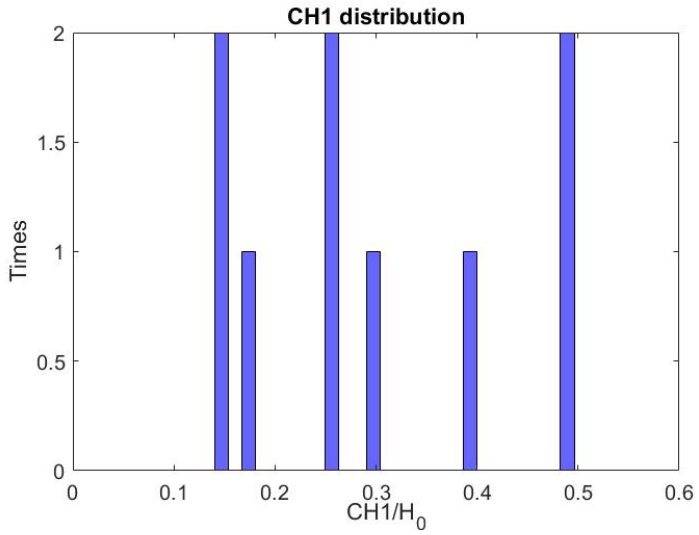

Figure 12.23: CH_1 distribution of W2 pattern for beams without diaphragm.

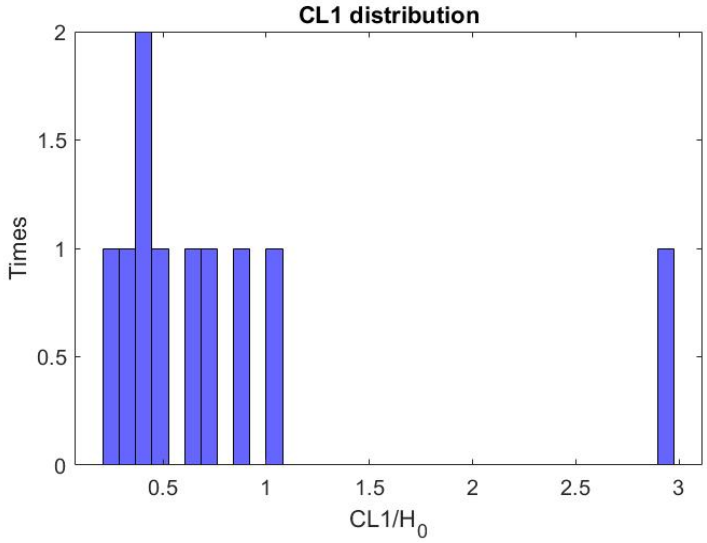

Figure 12.24: CL_1 distribution of W2 pattern for beams without diaphragm.

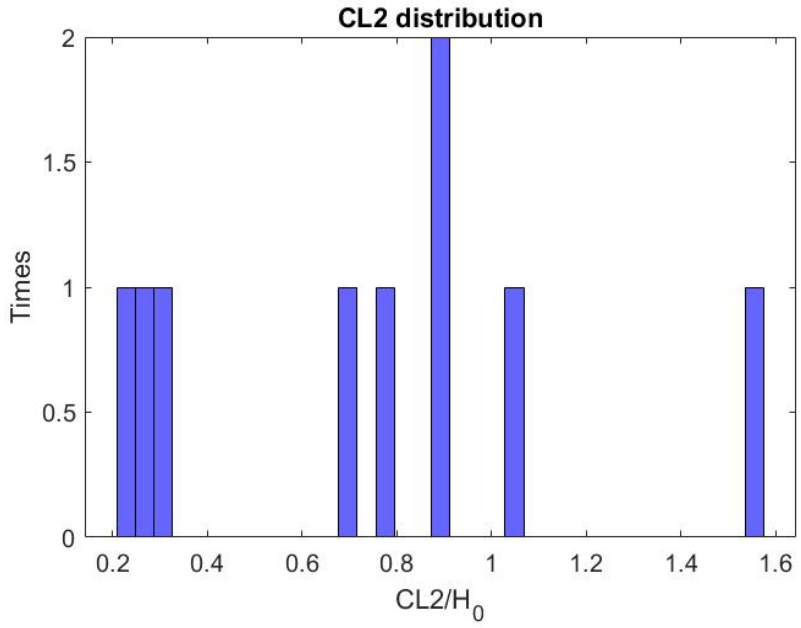

Figure 12.25: CL_2 distribution of W2 pattern for beams without diaphragm.

From Fig. 12.23 for six out of nine cases, the corrosion height is up to 0.3 H. For these cases, the web corrosion height, length, and web thickness loss is presented in Figs. 12.26-12.28.

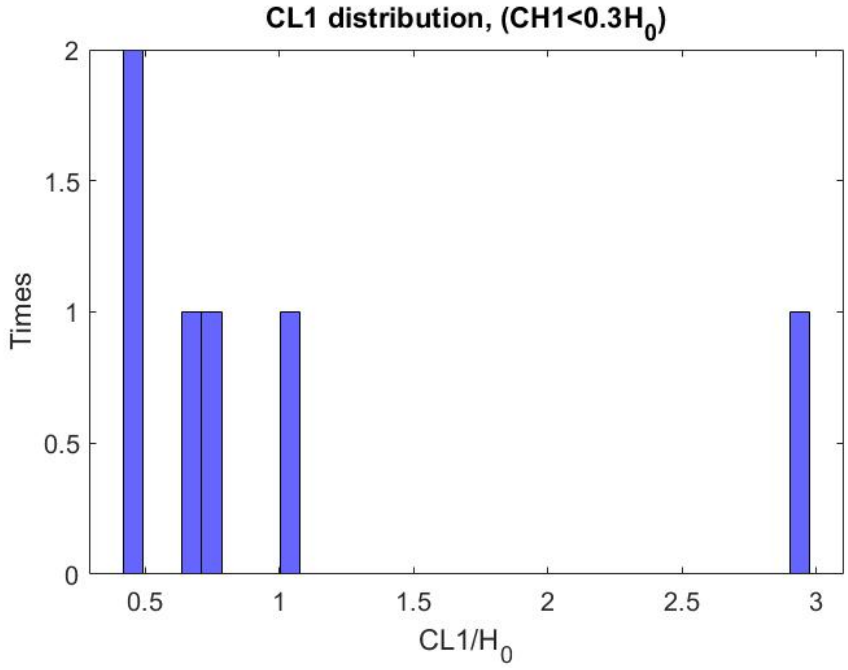

Figure 12.26: CL_1 distribution of W2 web corrosion pattern corroded up to 30% of H_0 for beams without diaphragm.

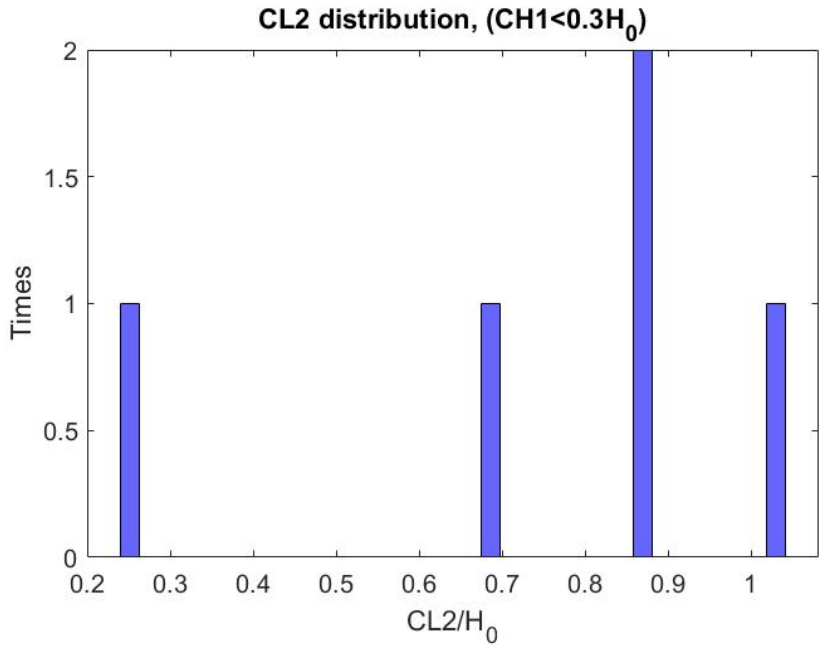

Figure 12.27: CL2 distribution of W2 web corrosion pattern corroded up to 30% of H_0 for beams without diaphragm.

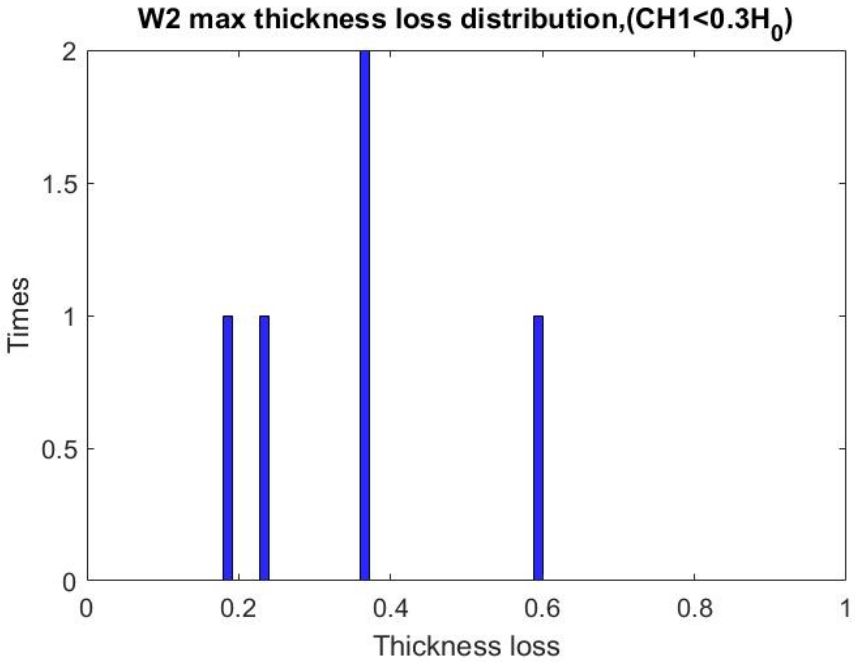

Figure 12.28: Max thickness loss distribution of W2 web corrosion pattern corroded up to 30% of H_0 for beams without diaphragm.

From Figs. 12.26 and 12.27: $CL_1 \in (0.5, 1.1H]$, $CL_2 \in (0.25, 1.2H]$, where the extreme scenario is illustrated in Fig. 12.29:

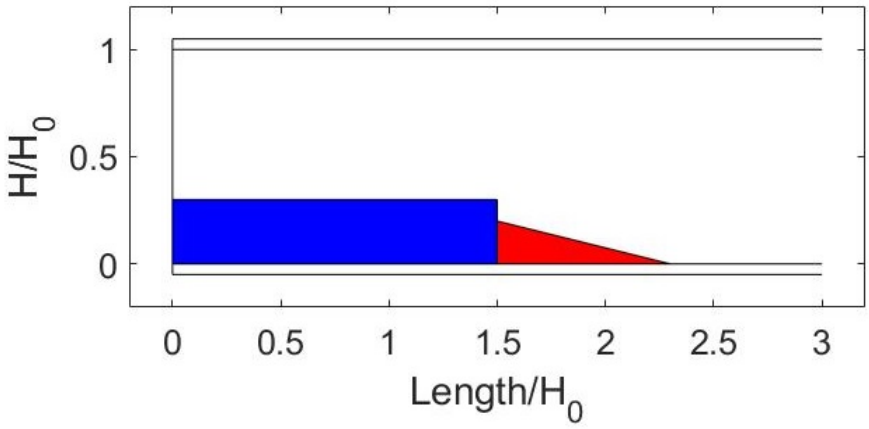

Figure 12.29: W1 CASE A extreme web corrosion scenario projected over W2 extreme web corrosion scenario.

The blue area indicates the Case A of W1 pattern, and with red the extreme W2 scenario. Since the rest of W2 cases fit in the blue shadowed area, W1 case A can be merged with W2. According to Figs. 12.7 and 12.28 , the thickness loss for W2 is in the range of Case A W1 range.

Flange corrosion

There is no analysis of flange corrosion, since the worst scenario is included in W1.

Holes

In the W2 pattern, the M1 hole appears two times, with dimensions a_1=b_1=0.05 and a_2=0.15 and b_2=0.5, which exceeds W1 M1 max hole length.

12.1.4 Pattern W3

Web corrosion

The data analysis started with the CH2 distribution:

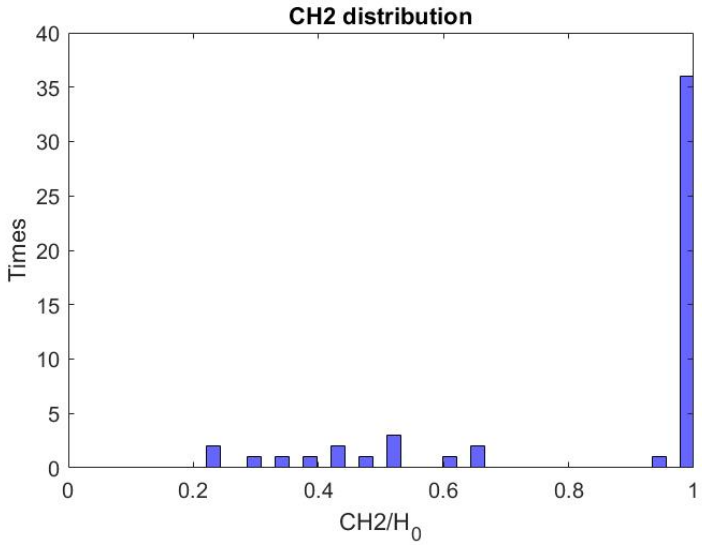

Figure 12.30: CH_2 distribution of W3 web corrosion pattern for beams without diaphragm.

From Fig. 12.30, it is obvious that the dominant scenario is the full height corroded web case. For $CH_2=H_0$ the dimension and thickness distributions are presented.

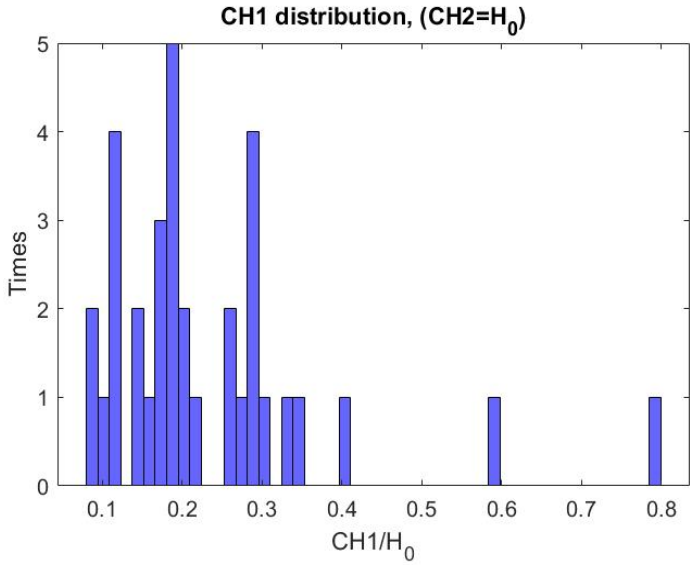

Figure 12.31: CH_1 distribution of W3 web corrosion pattern with full height corrosion for beams without diaphragm.

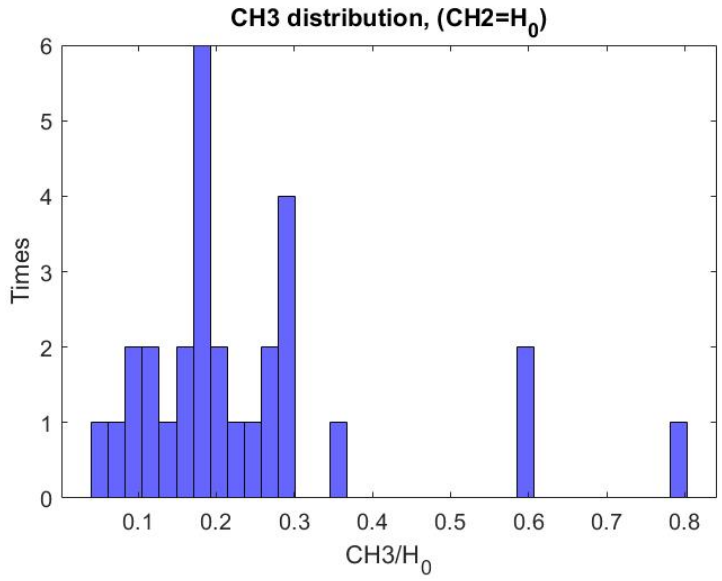

Figure 12.32: CH_3 distribution of W3 web corrosion pattern with full height corrosion for beams without diaphragm.

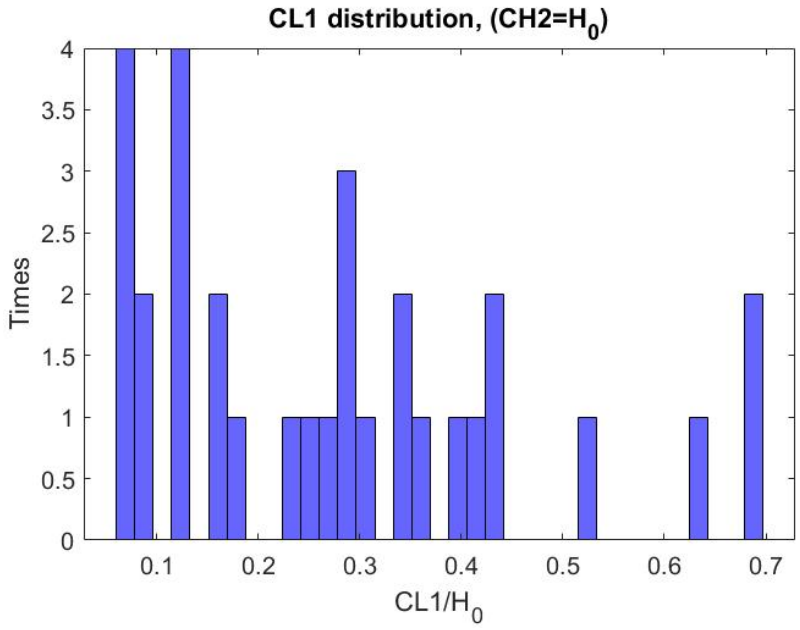

Figure 12.33: CL1 distribution of W3 web corrosion pattern with full height corrosion for beams without diaphragm.

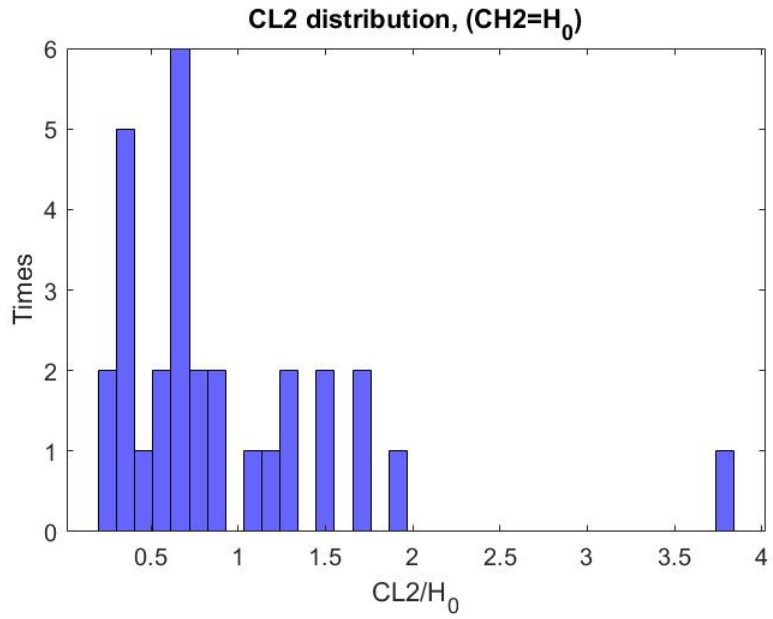

Figure 12.34: CL_2 distribution of W3 web corrosion pattern with full height corrosion for beams without diaphragm.

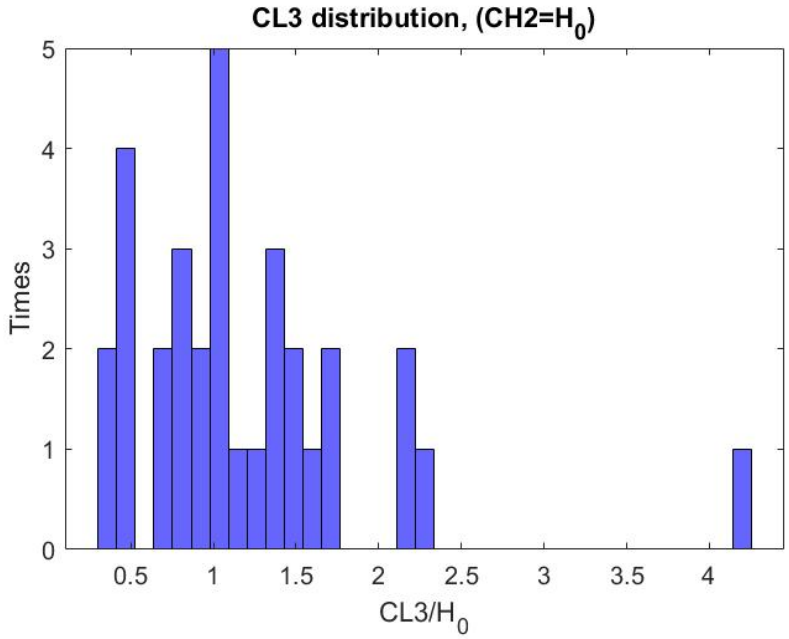

Figure 12.35: CL_3 distribution of W3 web corrosion pattern with full height corrosion for beams without diaphragm.

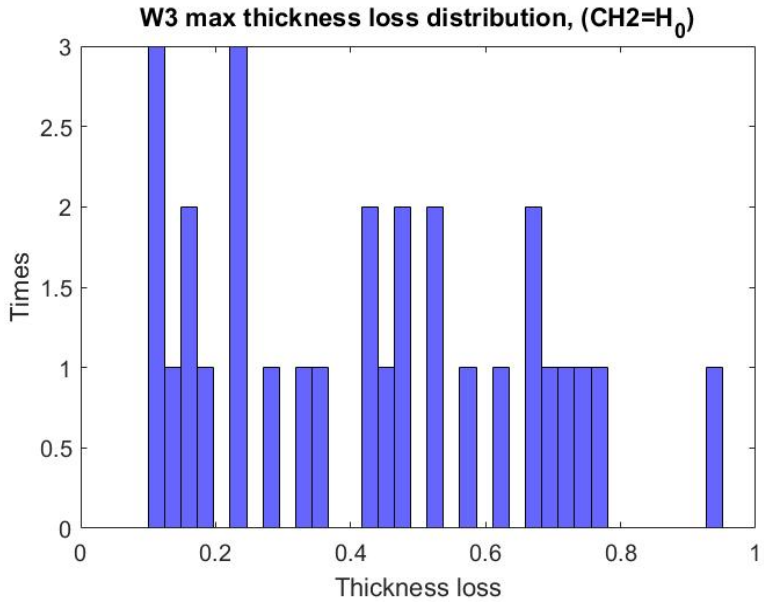

Figure 12.36: Max web thickness loss distribution of W3 web corrosion pattern with full height corrosion for beams without diaphragm.

From the last figures, one can conclude that:

$$CH_1 \in (0,0.35]$$
$$CH_3 \in (0,0.35]$$
$$CL_1 \in (0.05, 0.7]$$
$$CL_3 \in (0.5, 2.3]$$
$$\frac{t_{loss}}{t_{web}} \in \{0.1,0.2,0.3,0.4,0.5,0.6,0.7,0.8\}$$

And therefore, the extreme scenario is as follows (Fig. 12.37):

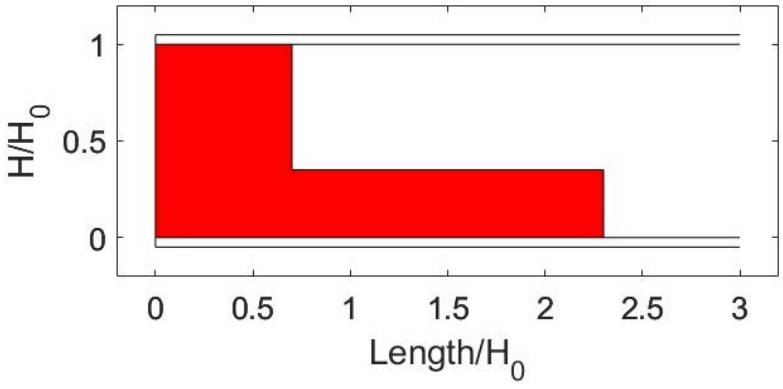

Figure 12.37: Extreme W3 web corrosion scenario for beams without diaphragm.

Flange corrosion

Based on Fig. 12.38, CF is considered equal to CL.

$$\frac{t_{loss}}{t_{flange}} \in \{0.4, 0.6, 0.8\}$$

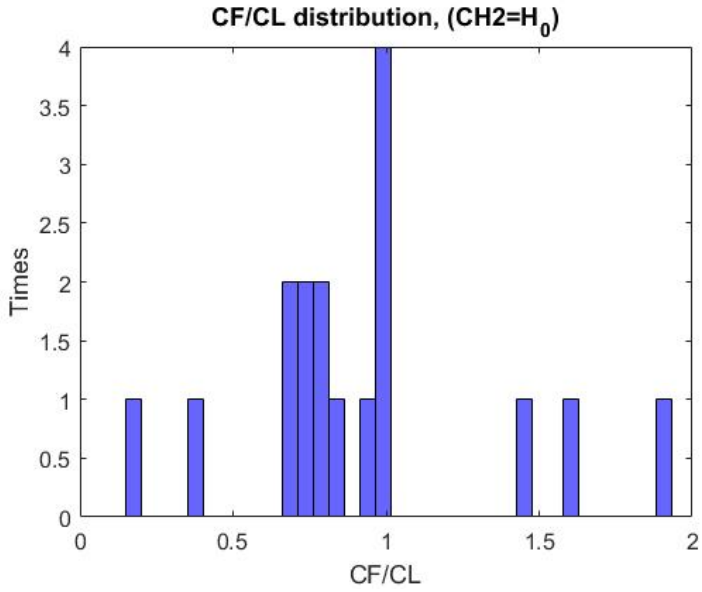

Figure 12.38: Ratio of flange to web corrosion length distribution of W3 web corrosion pattern with full height corrosion for beams without diaphragm.

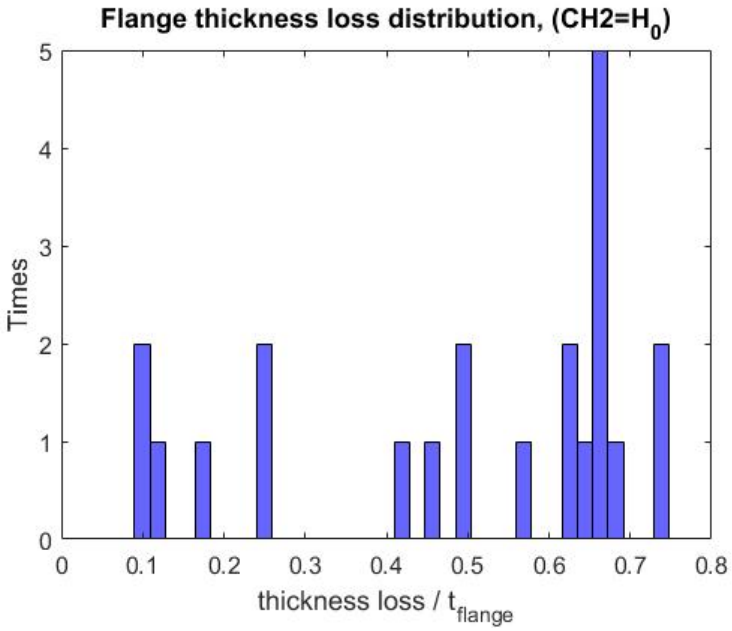

Figure 12.39: Max flange loss thickness distribution of W3 web corrosion pattern with full height corrosion for beams without diaphragm.

Holes

Holes dimensions distribution:

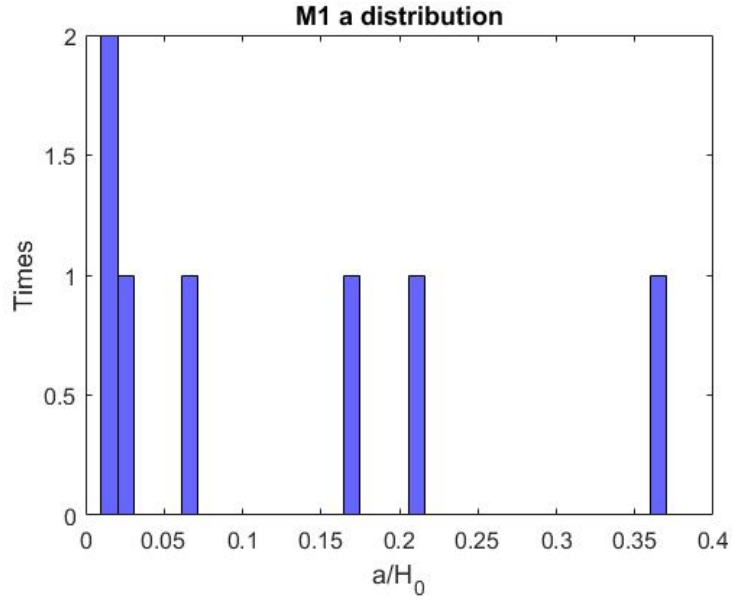

Figure 12.40: M1 web hole's pattern height distribution of W3 web corrosion pattern for beams without diaphragm.

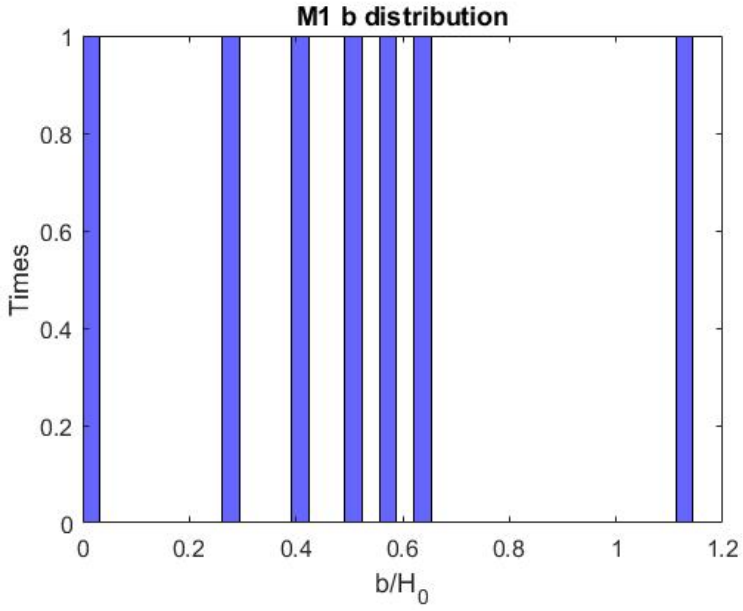

Figure 12.41: M1 web hole's pattern length distribution of W1 web corrosion pattern for beams without diaphragm.

The extreme hole scenario with a=0.21, b=0.63, is presented below, projected on W3 corroded area:

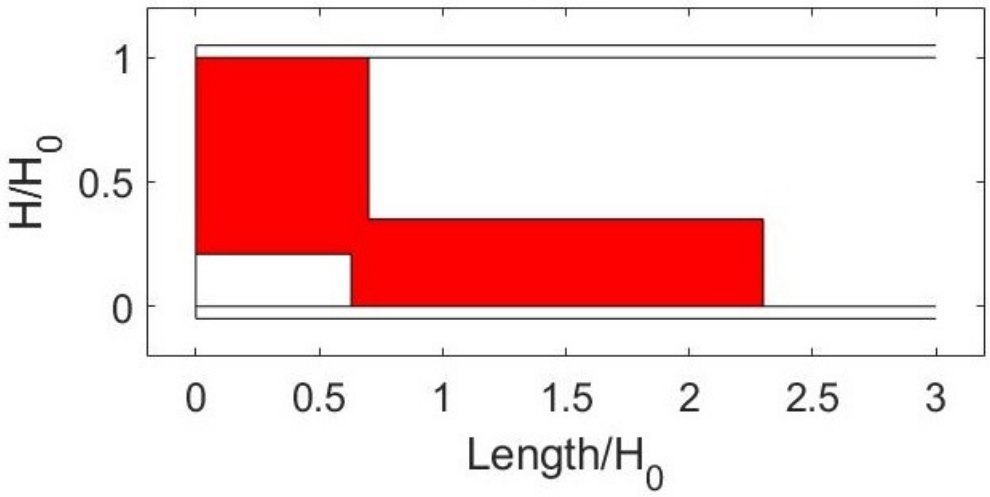

Figure 12.42: M1 extreme web hole pattern scenario of W1 web corrosion pattern, projected on W3 extreme corrosion scenario, for beams without diaphragm.

12.1.5 Pattern W4

Web corrosion

The thickness loss and the distribution of all normalized dimensions are plotted.

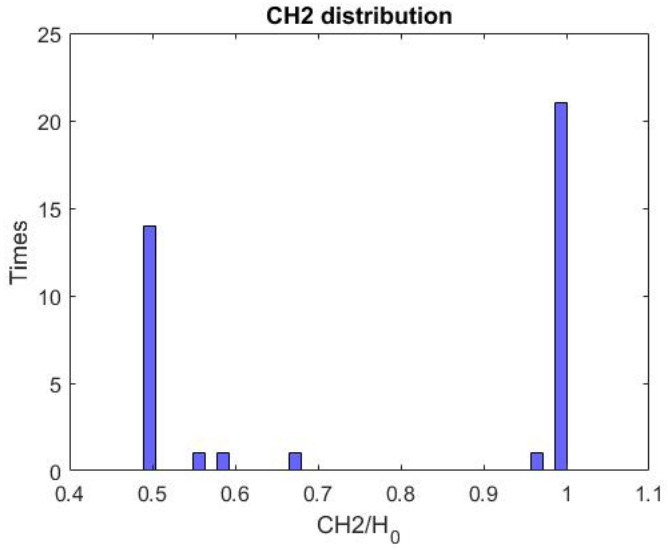

Figure 12.43: CH2 distribution of W4 web corrosion pattern for beams without diaphragm.

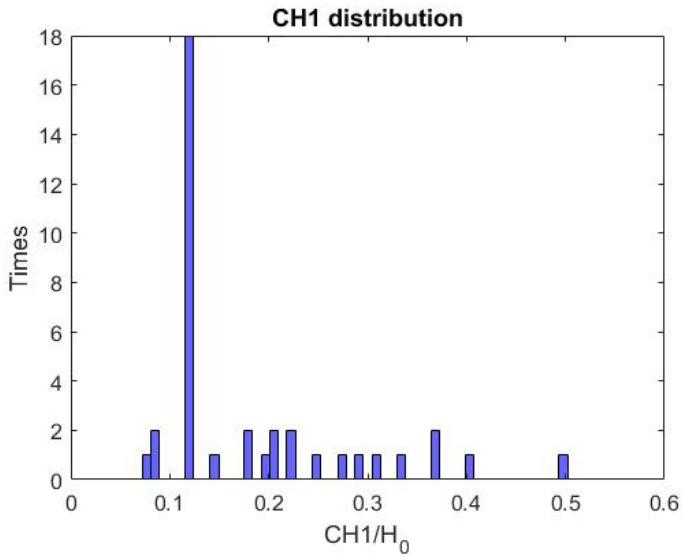

Figure 12.44: CH1 distribution of W4 web corrosion pattern for beams without diaphragm.

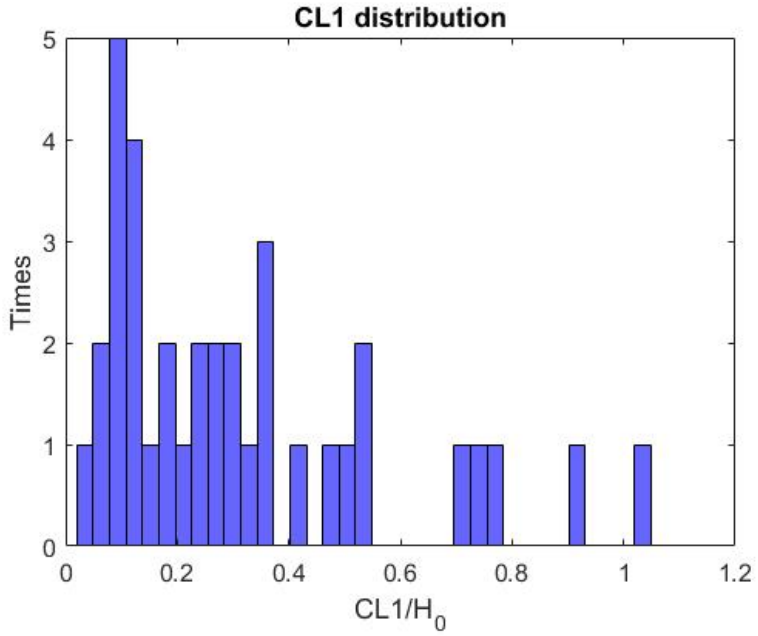

Figure 12.45: CL1 distribution of W4 web corrosion pattern for beams without diaphragm.

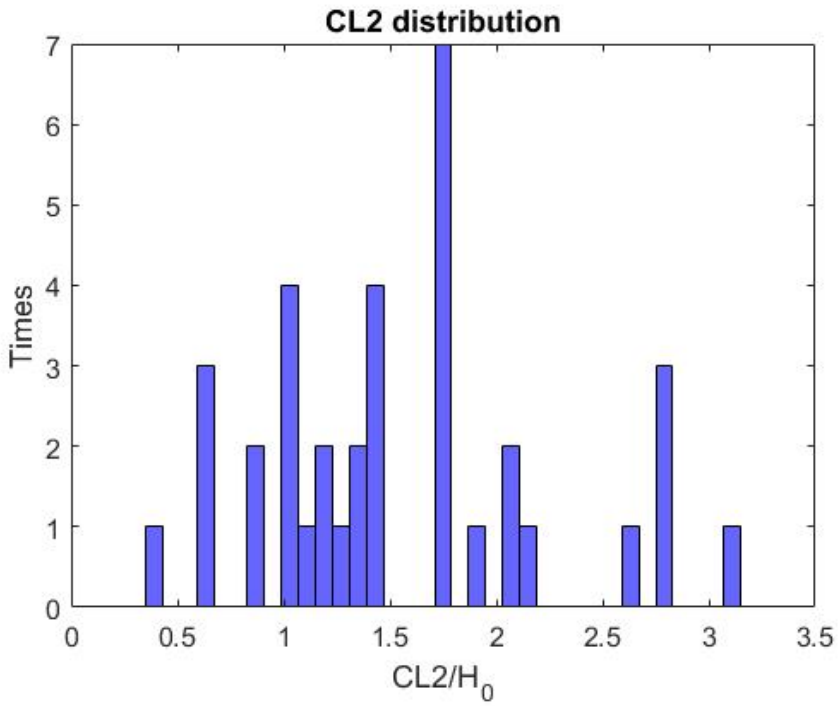

Figure 12.46: CL2 distribution of W4 web corrosion pattern for beams without diaphragm.

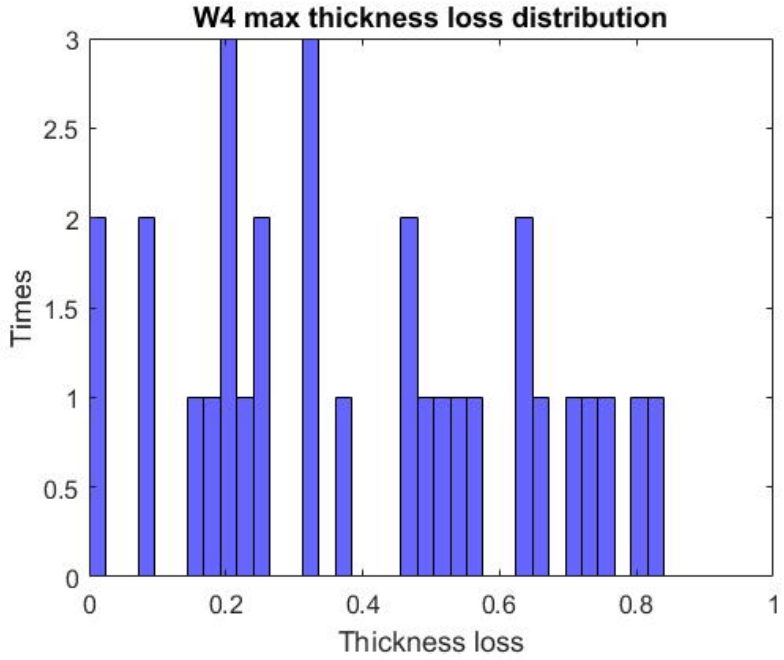

Figure 12.47: Max web thickness loss distribution of W4 web corrosion pattern for beams without diaphragm.

From the CH2 histogram (Fig. 12.43), two main trends are noticed: either (a) full height corrosion, or (b) corrosion up to 50% of H_0. As an additional step, the corrosion dimensions

(CH1, CL1, CL2, and CL3) and the web thickness loss distribution for each of the two cases of CH1 were plotted, (a) for CH1=0.5H_o and (b) for CH1=H_o.

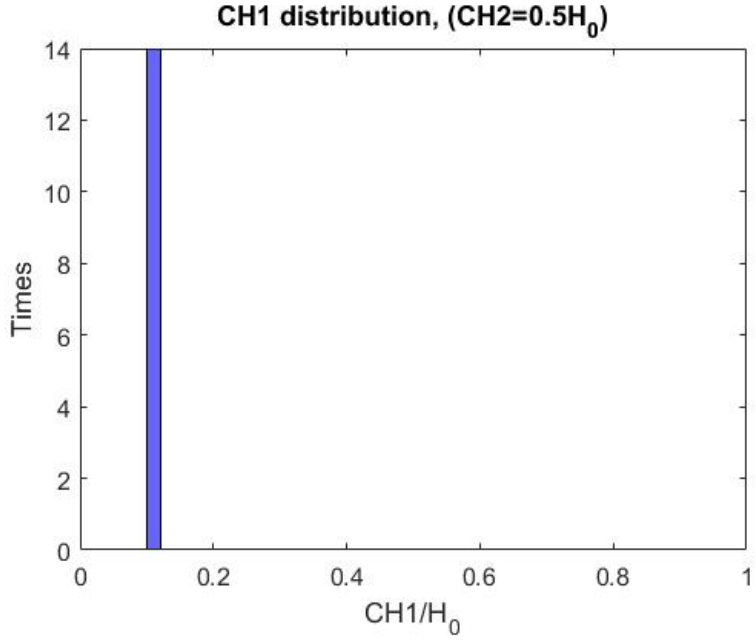

Figure 12.48: CH1 distribution of W4 web corrosion pattern, with corrosion height up to 50% of H_0 for beams without diaphragm.

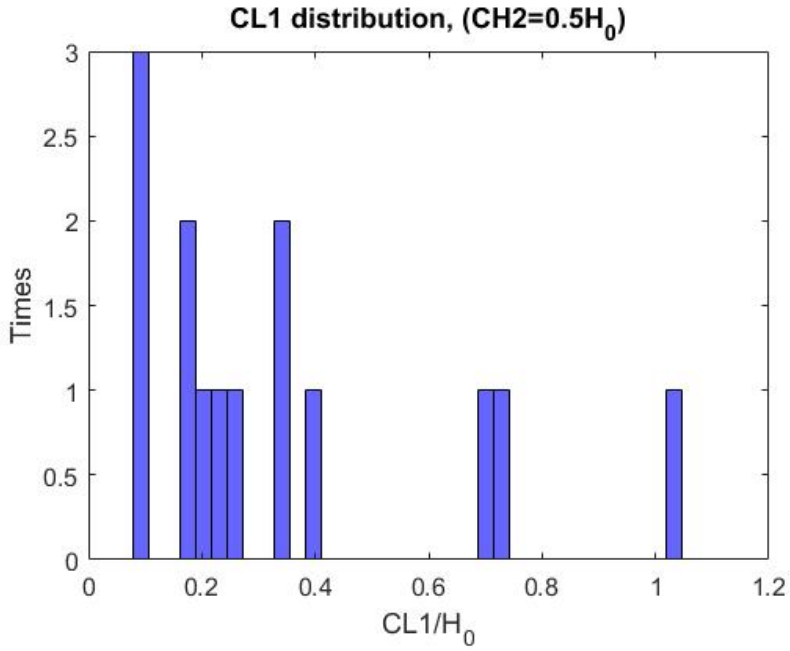

Figure 12.49: CL1 distribution of W4 web corrosion pattern, with corrosion height up to 50% of H_0 for beams without diaphragm.

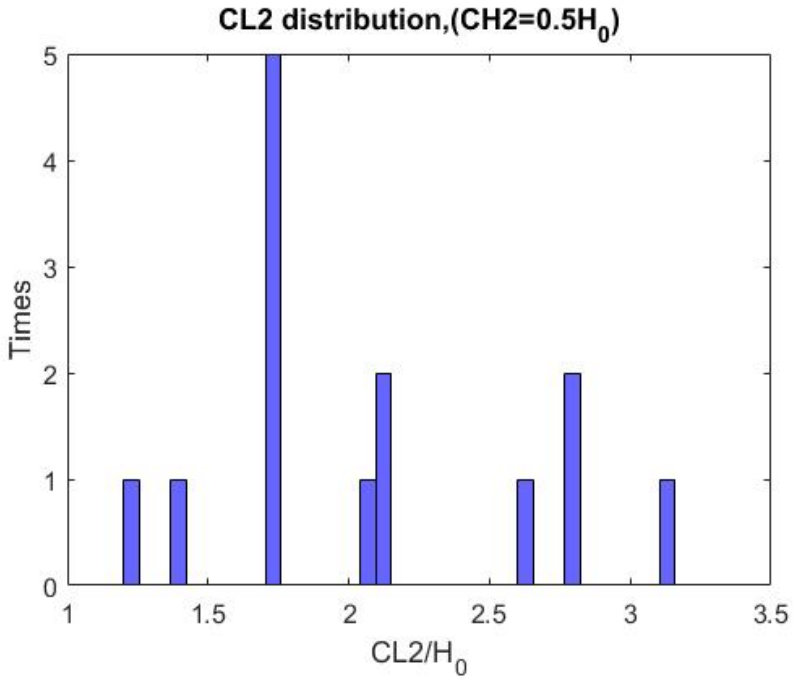

Figure 12.50: CL2 distribution of W4 web corrosion pattern, with corrosion height up to 50% of H_0 for beams without diaphragm.

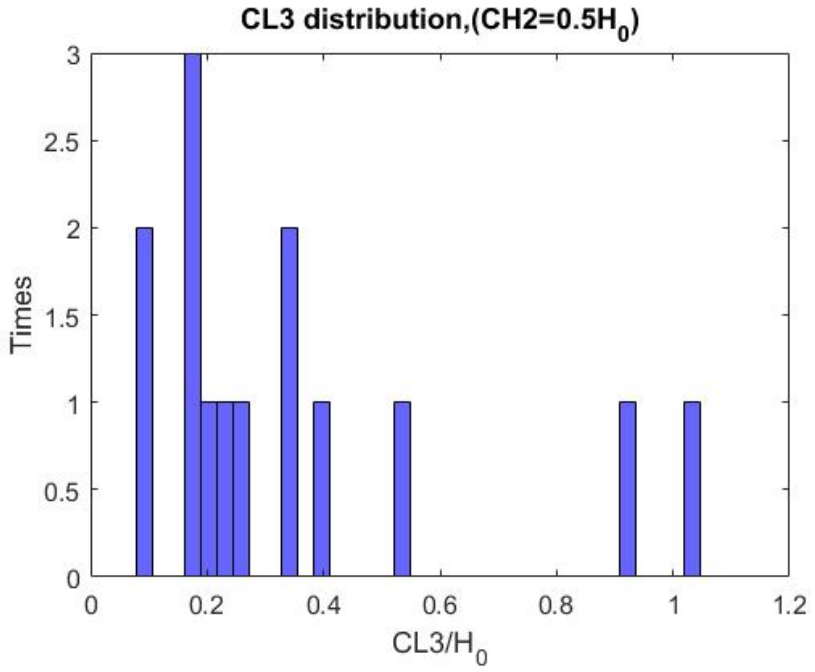

Figure 12.51: CL3 distribution of W4 web corrosion pattern, with corrosion height up to 50% of H_0 for beams without diaphragm.

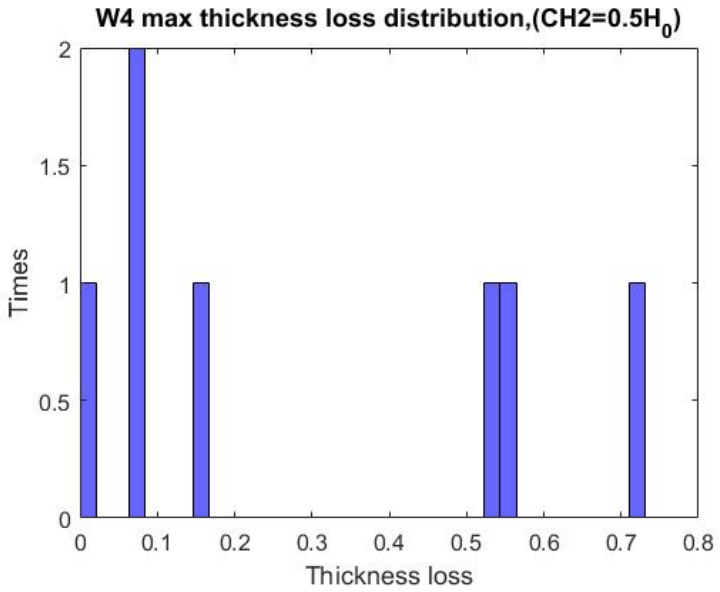

Figure 12.52: Max web thickness loss distribution of W4 web corrosion pattern, with corrosion height up to 50% of H_0 for beams without diaphragm.

Based on Figs. 12.48–12.52:

$$CH_1 = 0.12H_0$$
$$CL_2 \in [1.2,3.2]H_0$$
$$CL_1 \cong CL_3 \cong [0.2,0.4]H_0$$
$$\frac{t_{loss}}{t_{web}} \in \{0.05,0.15,0.55,0.75\}$$

The extreme scenario is:

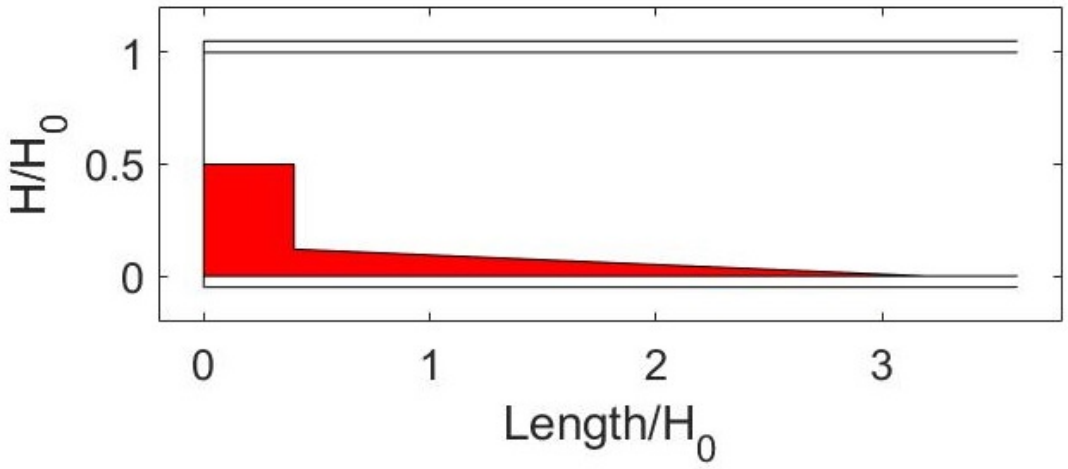

Figure 12.53: First extreme W4 web corrosion scenario for beams without diaphragm.

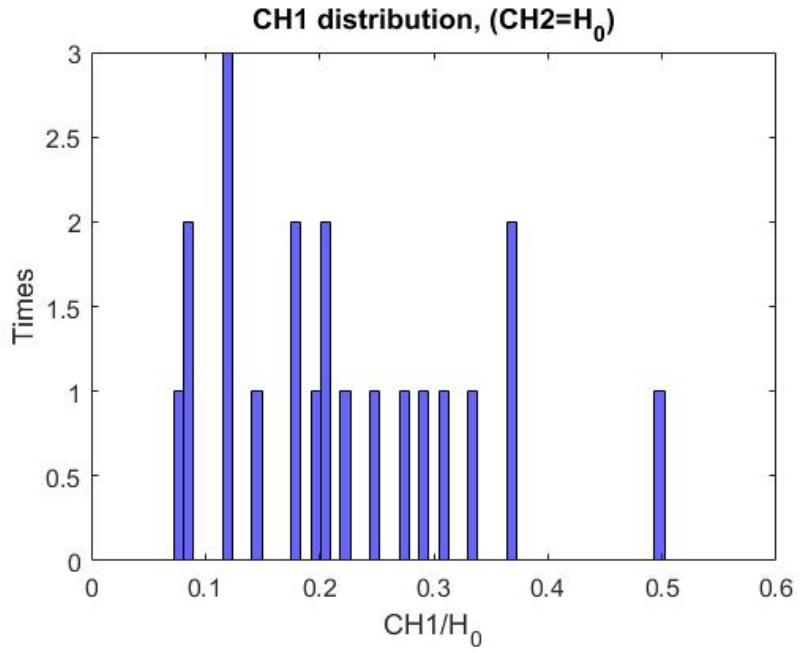

Figure 12.54: CH1 distribution of W4 web corrosion pattern, with full height corrosion for beams without diaphragm.

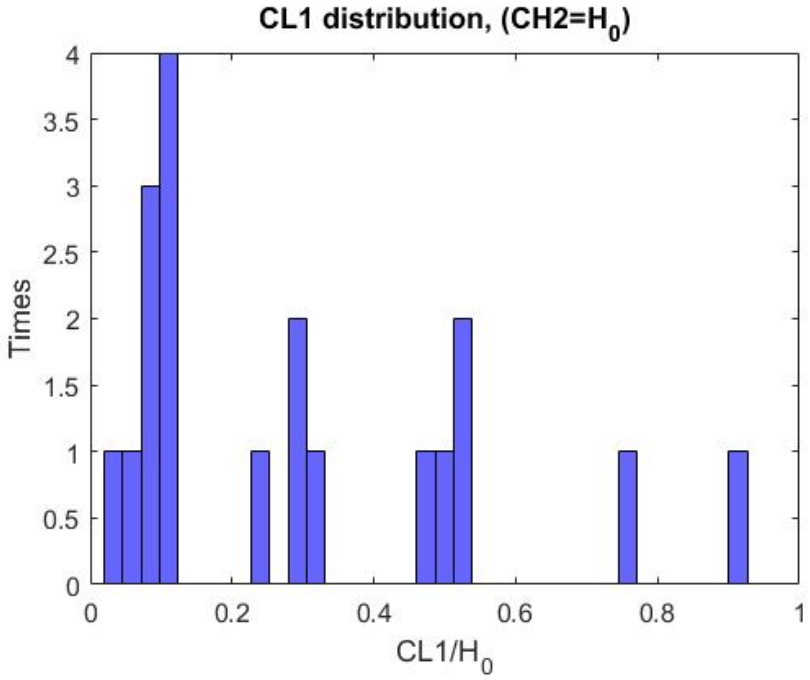

Figure 12.55: CL1 distribution of W4 web corrosion pattern, with full height corrosion for beams without diaphragm.

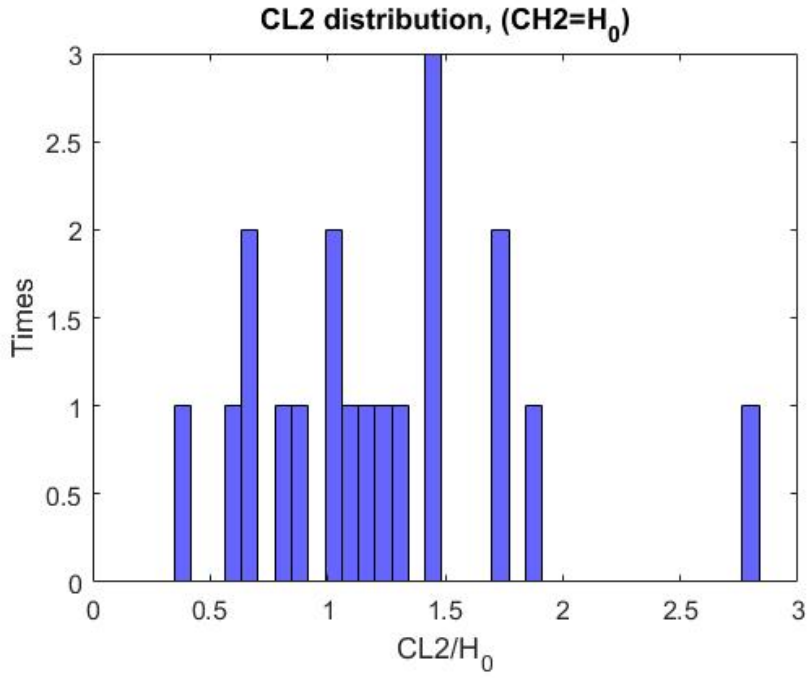

Figure 12.56: CL2 distribution of W4 web corrosion pattern, with full height corrosion for beams without diaphragm.

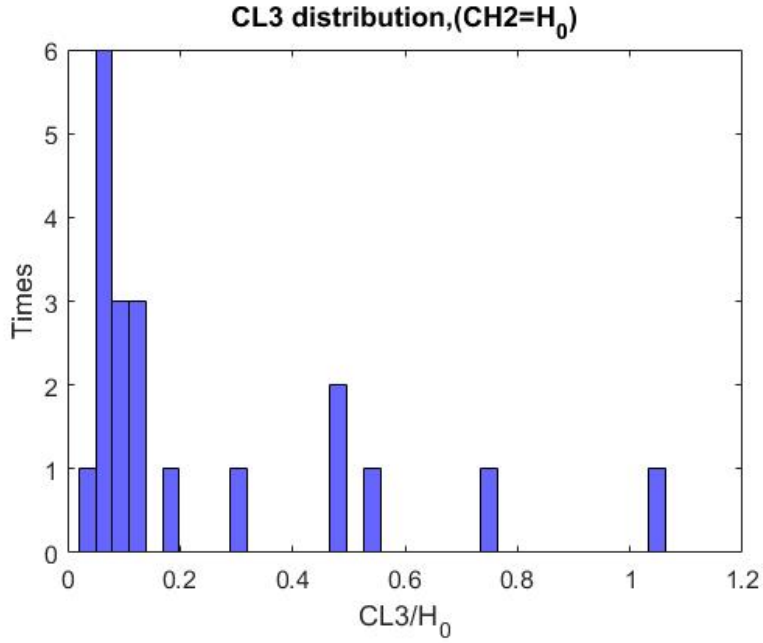

Figure 12.57: CL3 distribution of W4 web corrosion pattern, with full height corrosion for beams without diaphragm.

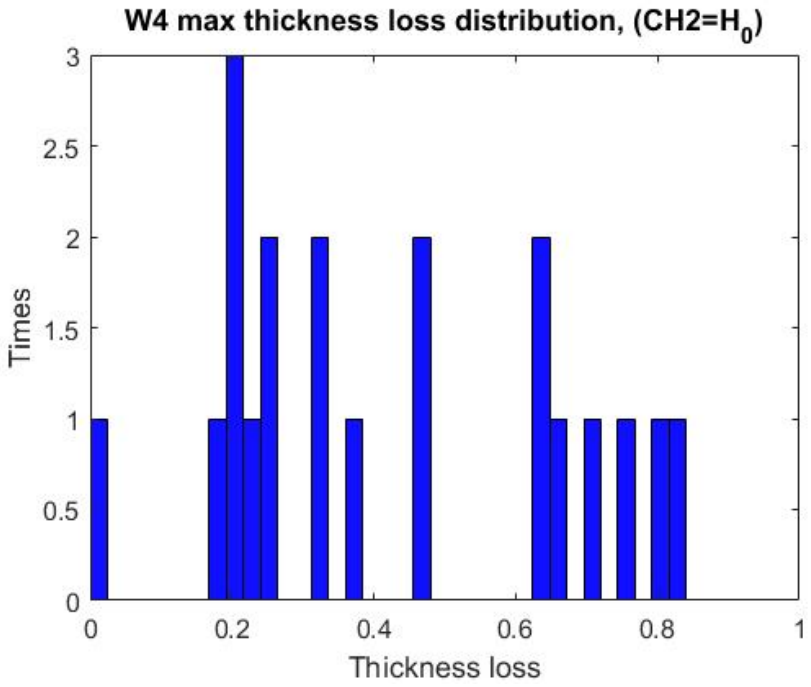

Figure 12.58: Max web thickness loss distribution of W4 web corrosion pattern, with full height corrosion for beams without diaphragm.

For the full height corrosion:

$$CH_1 = [0.1,0.5]H_0$$
$$CL_1 \in (0, 0.9]H_0$$
$$CL_2 \in [0.5, \quad 1.8]H_0$$
$$CL_3 \in (0, 0.2]H_0$$

with thickness loss:

$$\frac{t_{loss}}{t_{web}} \in \{0.2,0..4,0.6,0.8\}$$

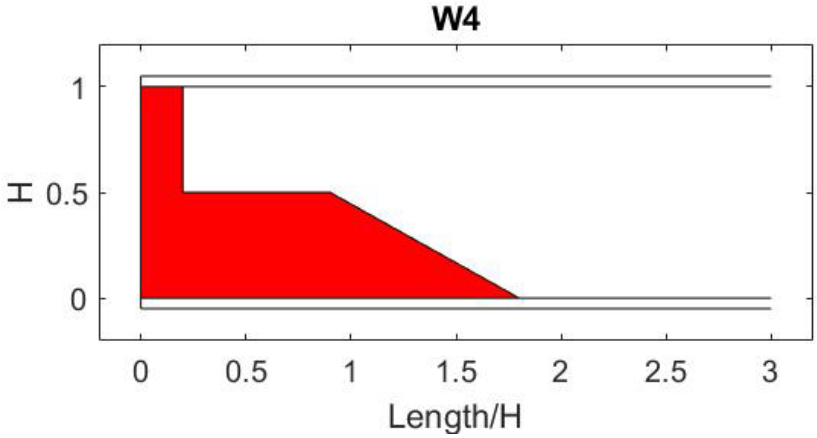

Figure 12.59: Second extreme W4 web corrosion scenario for beams without diaphragm.

The two W4 extreme scenarios are now projected over the extreme W3 scenario (blue):

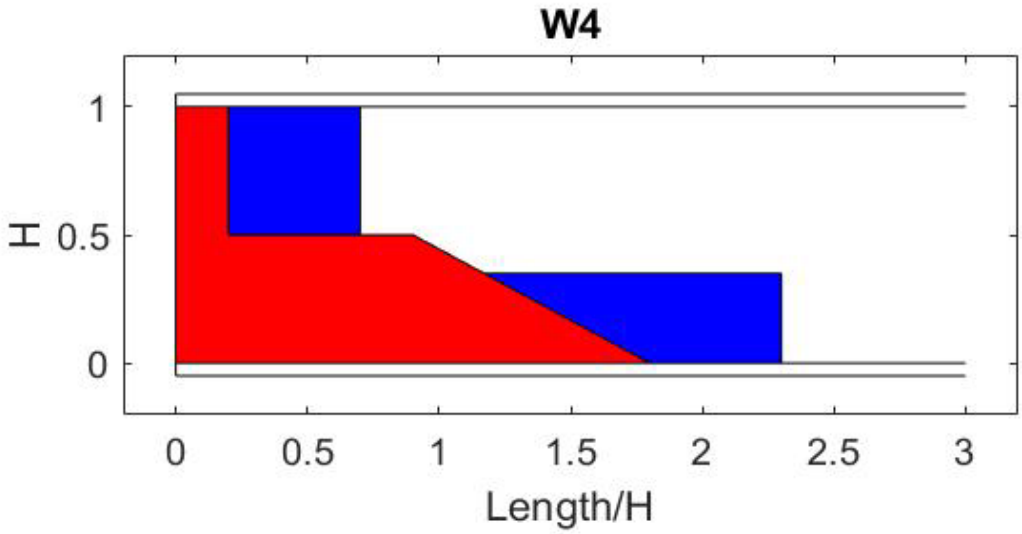

Figure 12.60: First extreme W4 scenario (red) projected over extreme W3 web corrosion scenario (blue).

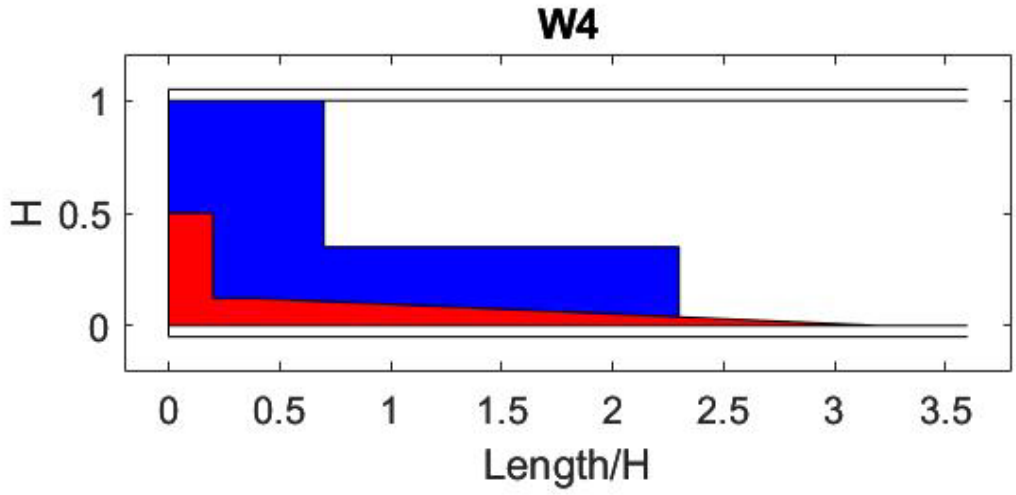

Figure 12.61: Second extreme W4 scenario (red) projected over extreme W3 web corrosion scenario (blue).

Considering the way W3 and W4 have been defined, W3 can be expressed by W4, if W4CL1=W4CL3 and W4CH3≠0. Figures 12.60 and 12.61 demonstrate that W3 includes the extreme W4 scenarios, thus W3 and W4 could be merged to one pattern.

Flange corrosion

There is no analysis of flange corrosion, since the worst scenario is included in W3.

Holes

Table 12.2 shows the frequency of hole appearance. Considering the way W3 and W4 have been defined, W3 can be expressed by W4, if W4CL1=W4CL3 and W4CH3≠0. Graphs 12.62 and 12.63 demonstrate that W3 includes the extreme W4 scenarios, thus W3 and W4 could be merged to one pattern.

Table 12.2: Frequency of hole appearance for beams without diaphragm

	Frequency	No hole	M1	M2	M3	M4	M12	M13	M24
W1	161	146	9	1	3	0	0	2	0
W2	10	8	2	0	0	0	0	0	0
W3	56	44	7	0	3	1	0	1	0
W4	40	347	4	0	0	0	0	2	0
W5	17	13	3	1	0	0	0	0	0
W6	2	2	0	0	0	0	0	0	0

According to Table 12.2, the W4 pattern is combined four times with the M1 hole pattern. The available data are not enough to extract conclusions about the web thickness loss at these cases. Holes dimension distribution:

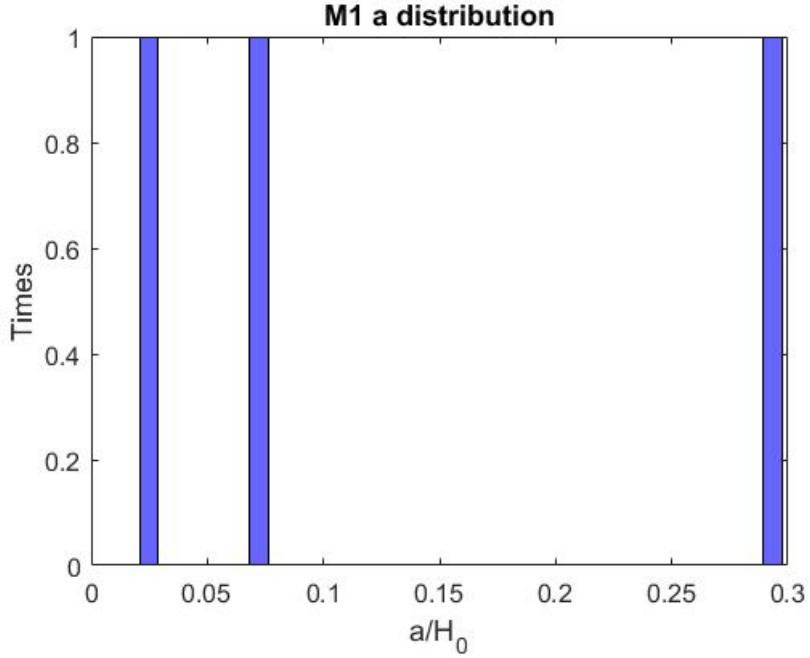

Figure 12.62: M1 web hole's pattern height distribution of W4 web corrosion pattern for beams without diaphragm.

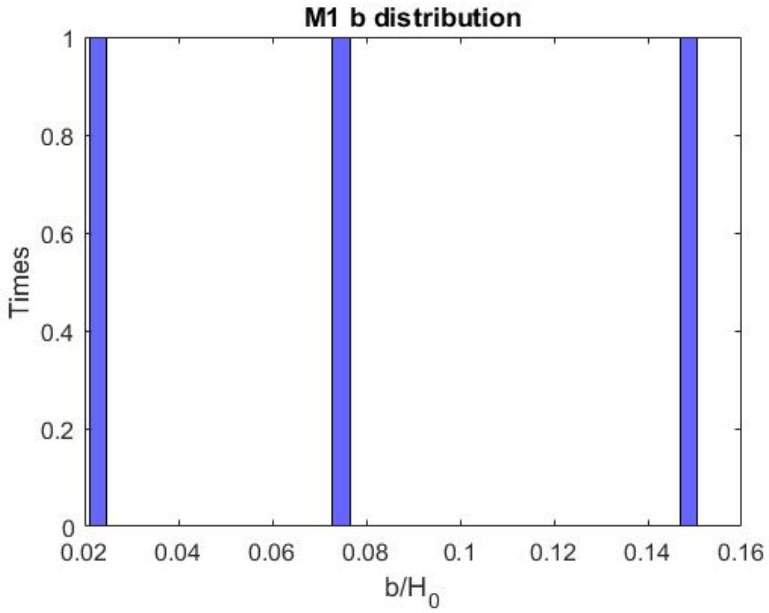

Figure 12.63: M1 web hole's pattern length distribution of W3 web corrosion pattern for beams without diaphragm.

Holes extreme cases belong in the range of W3 M1 holes.

12.1.6 Pattern W5

Web corrosion

The W5 pattern was observed in total only 17 times. The normalized dimensions and the web thickness loss are presented in Figs. 12.64-12.67.

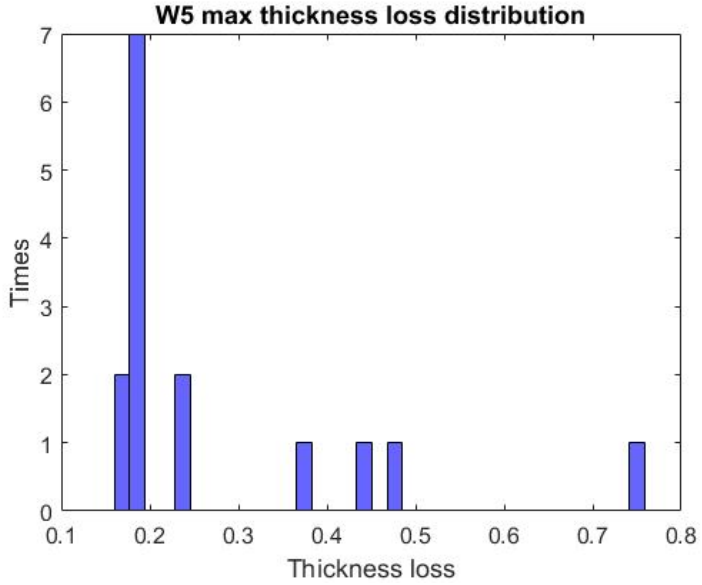

Figure 12.64: Max web thickness loss distribution of W5 web corrosion pattern for beams without diaphragm.

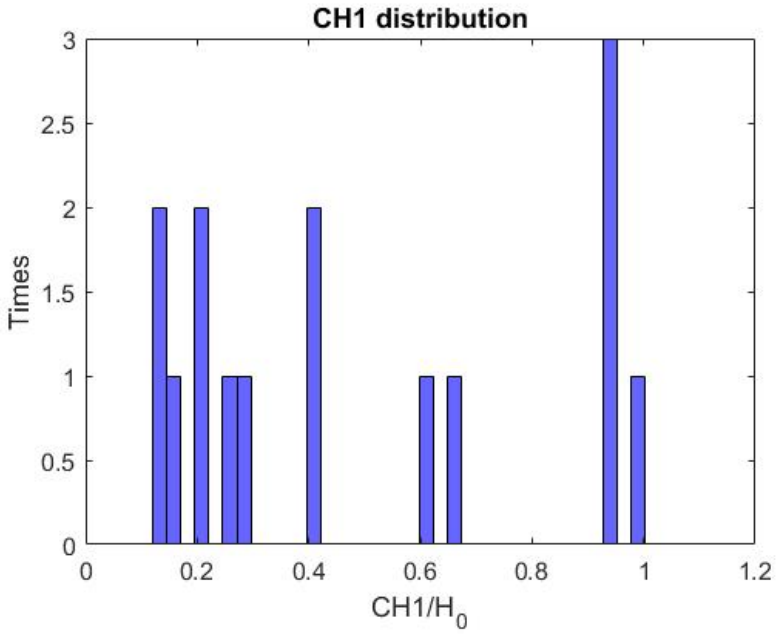

Figure 12.65: CH2 distribution of W5 web corrosion pattern for beams without diaphragm.

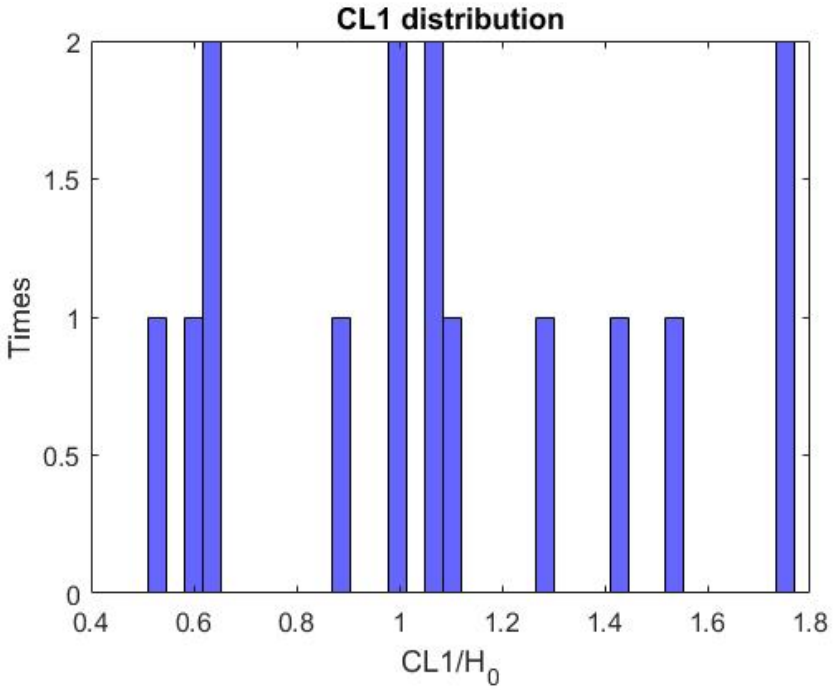

Figure 12.66: Max web thickness loss distribution of W5 web corrosion pattern for beams without diaphragm.

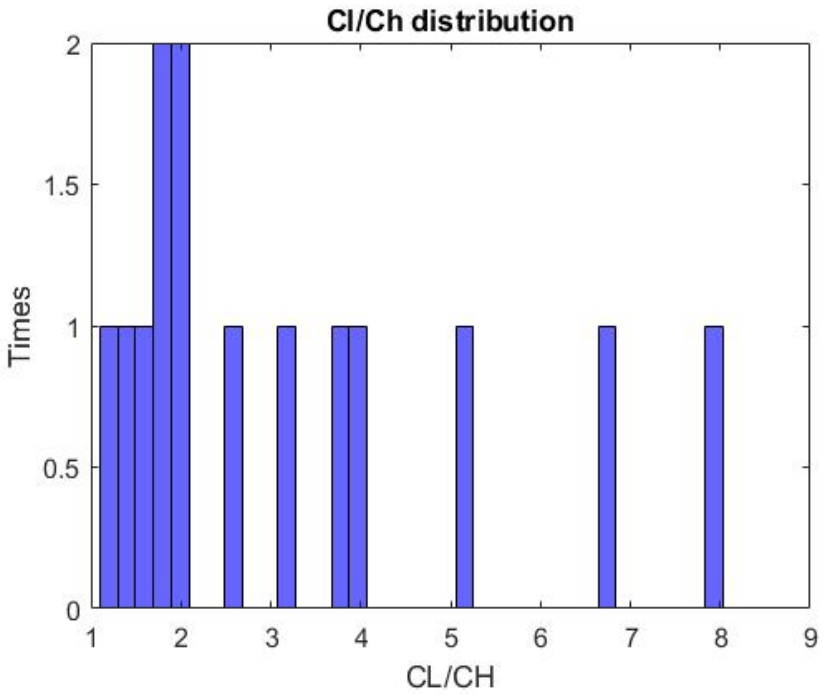

Figure 12.67: Ratio of corrosion length to height of W1 web corrosion pattern for beams without diaphragm.

From Fig. 12.64: $CH_1 = [0.15,\ 1]H_0$

From Fig. 12.65: $\mathrm{CL}_1 = [0.5,\ 1.8]\mathrm{H}_0$, with thickness loss: $\frac{t_{loss}}{t_{web}} \in \{0.2, 0.5\}$

The extreme case:

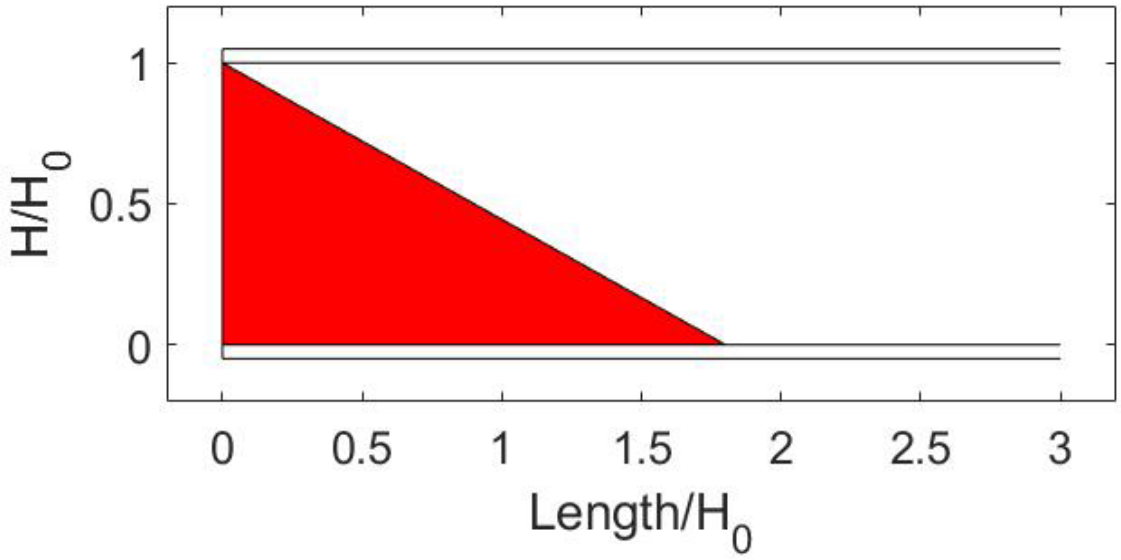

Figure 12.68: Extreme W4 web corrosion scenario for beams without diaphragm.

According to Fig. 12.67, the examined cases should have a ratio $\frac{CL}{CH} \in [1,4]$.

Flange corrosion

The ratio of the length of the corroded flange over the length of the corroded web was plotted.

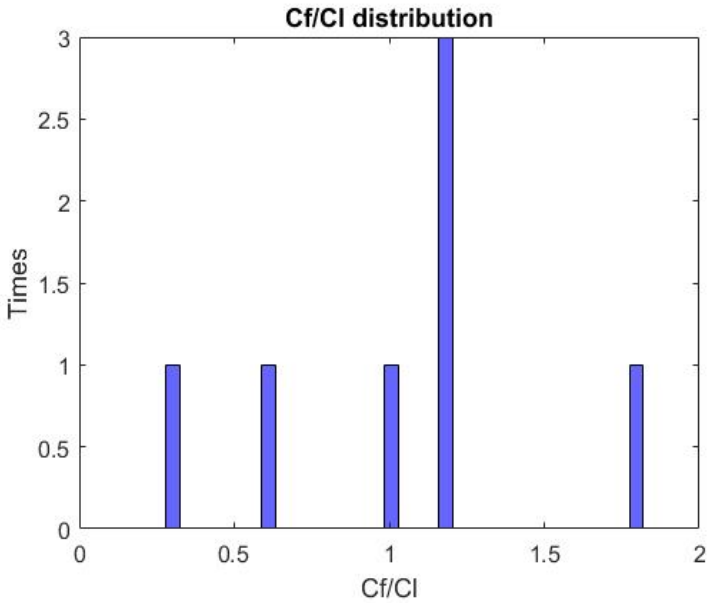

Figure 12.69: Ratio of flange to web corrosion length distribution of W5 web corrosion pattern for beams without diaphragm.

Thus, $\frac{Cf}{Cl} \in [1,1.8]$

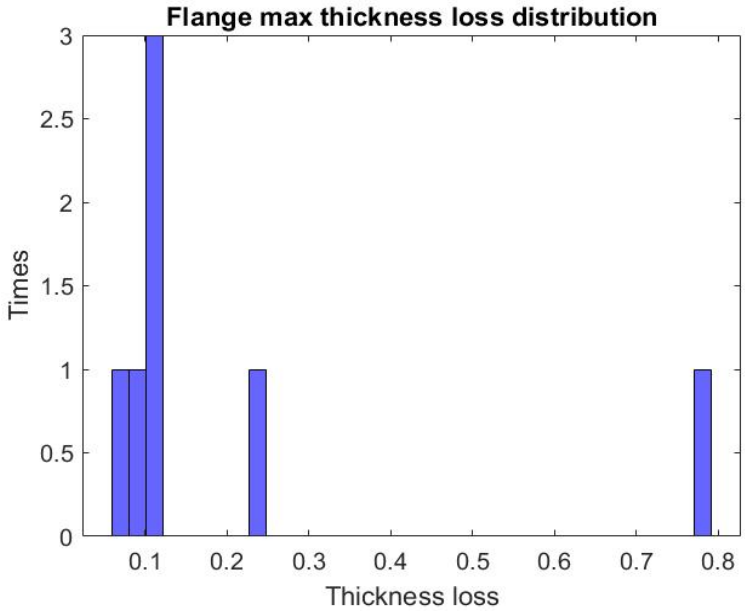

Figure 12.70: Max flange thickness loss distribution of W5 web corrosion pattern for beams without diaphragm.

Holes

The cases with holes are very few and are disregarded.

12.2 Appendix B: Detailed Data and Processing Graphs for Beam Ends with Diaphragm

12.2.1 Introduction

The data was divided in two main categories: beam ends with diaphragm and beam ends without diaphragm. All the graphs in Appendix B represent the first case. The histogram in Fig. 12.71 contains the frequency of each of the defined corrosion patterns (the total number of times each pattern appears in the reports).

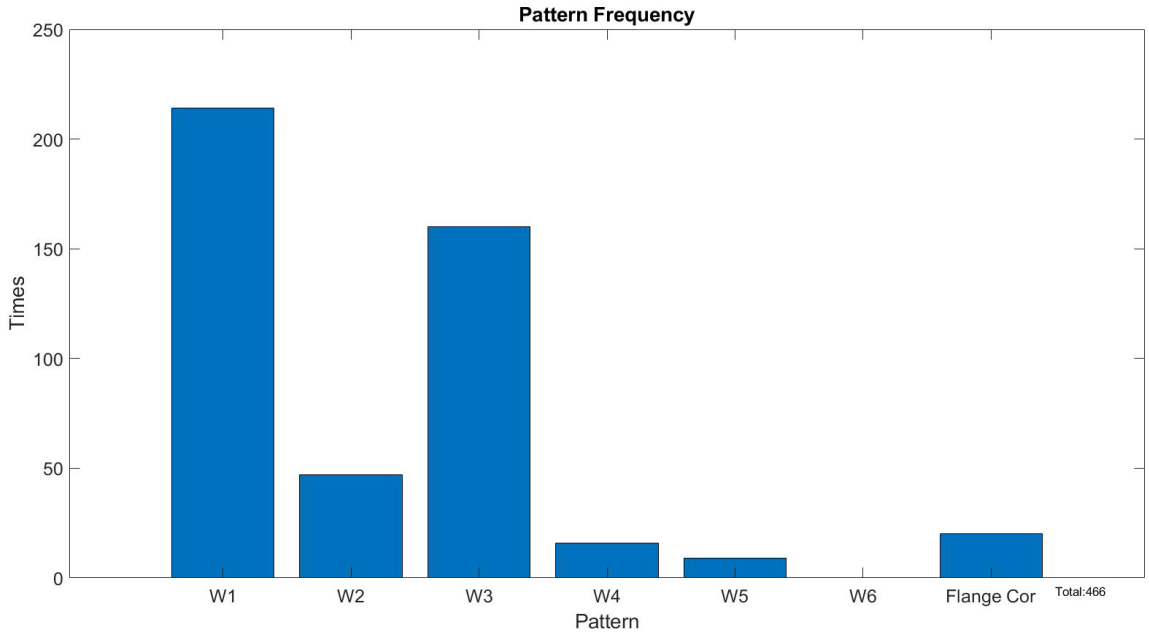

Figure 12.71: Web corrosion patterns distribution for beams with diaphragm.

For each web corrosion pattern, the team normalized the characteristic dimensions (CH1, CH2, CH3, CL1, Cl2, CL3) with the height H_0, where $H_0 = H - 2t_f$.

12.2.2 Pattern W1

Web corrosion

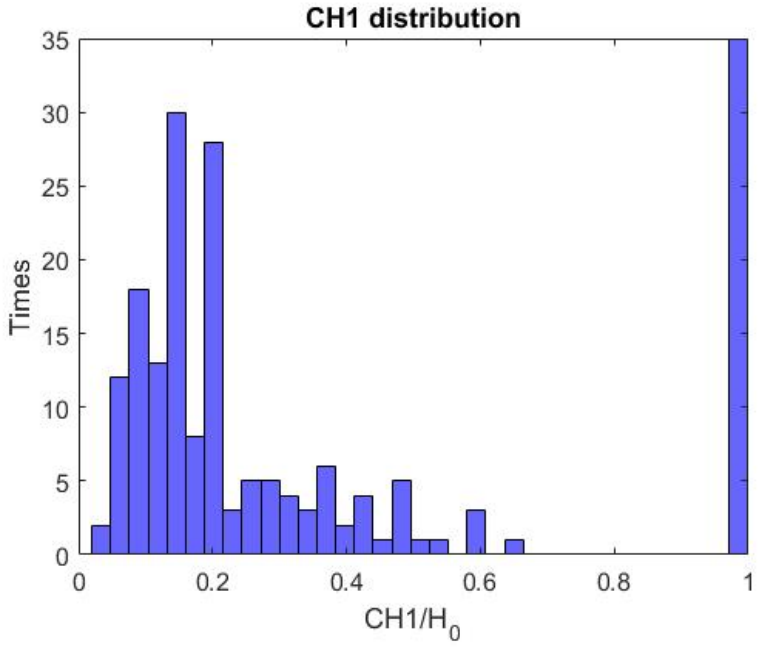

Figure 12.72: CH1 distribution of W1 web pattern for beams with diaphragm (total = 189).

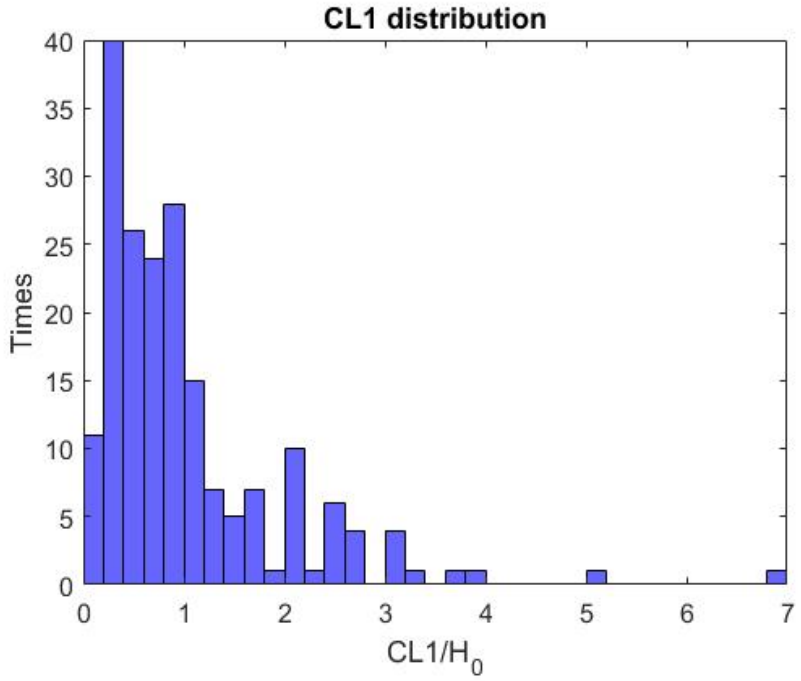

Figure 12.73: CL1 distribution of W1 web corrosion pattern for beams with diaphragm.

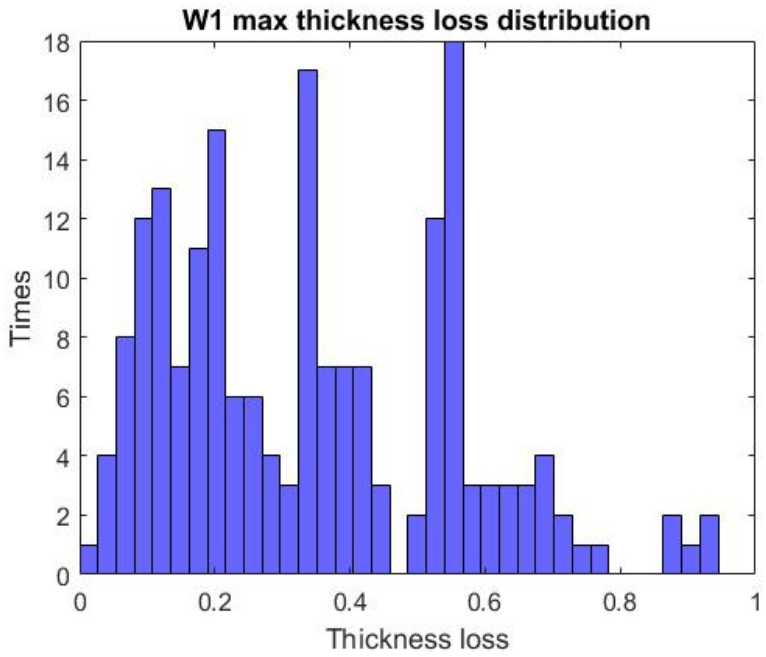

Figure 12.74: Max thickness loss distribution of W1 web corrosion pattern for beams with diaphragm.

From the CH1 histogram (Fig. 12.72), two main trends are noticed, which cover almost 85% of cases (158 out of 189): either (a) full height corrosion, or (b) corrosion up to 30% of H_0.

$$CH_1 \in \begin{cases} (0, 0.3H_0] \\ H_0 \end{cases}$$

For full height:

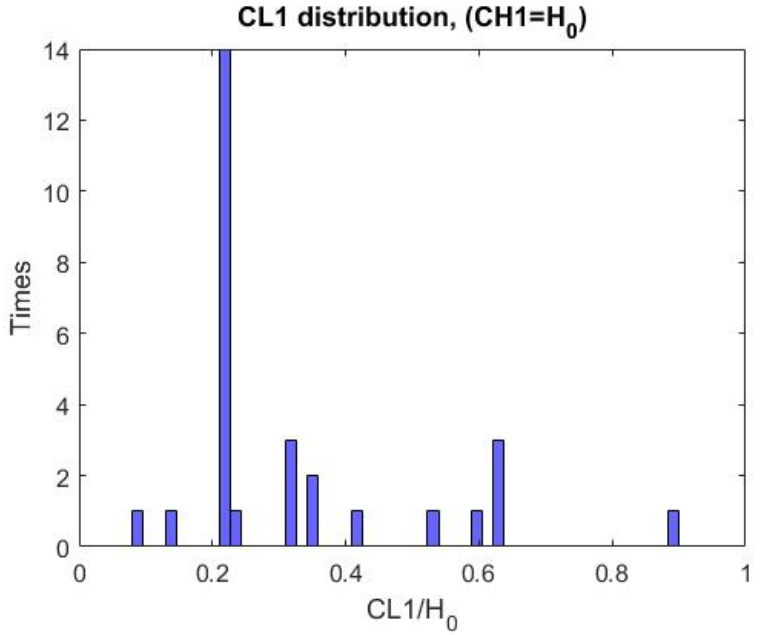

Figure 12.75: CL1 distribution of full height W1 web corrosion pattern for beams with diaphragm.

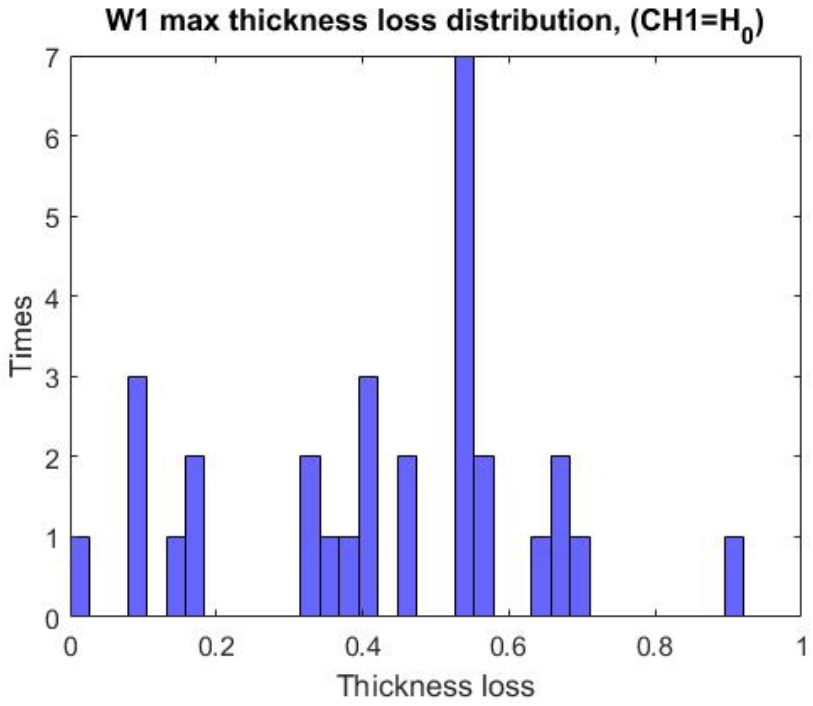

Figure 12.76: Max thickness loss distribution of full height W1 web corrosion pattern for beams with diaphragm.

Observing the figure for full height corrosion and CL <= 0.35H:

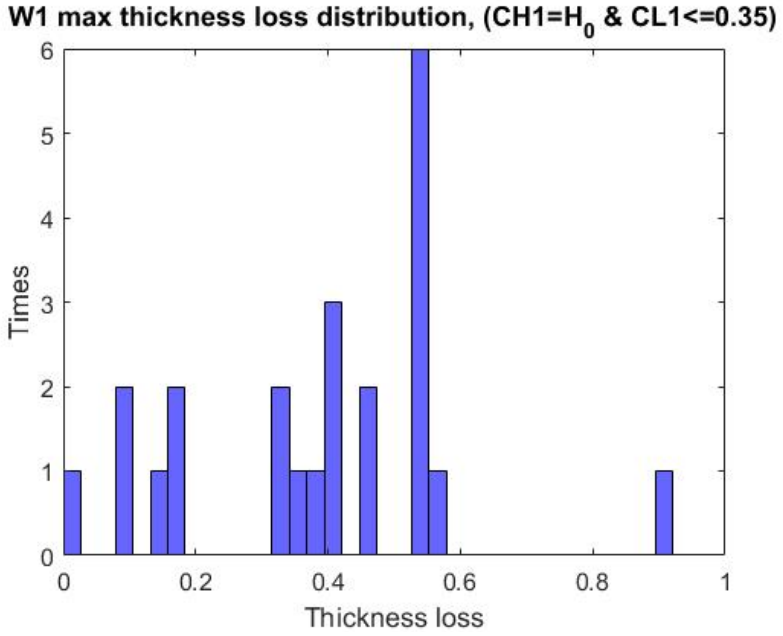

Figure 12.77: Max web thickness loss distribution of W1 web corrosion pattern, with corrosion height up to 35% of H_0, for beams with diaphragm.

For the full height corrosion case, one case is identified: **CASE A**

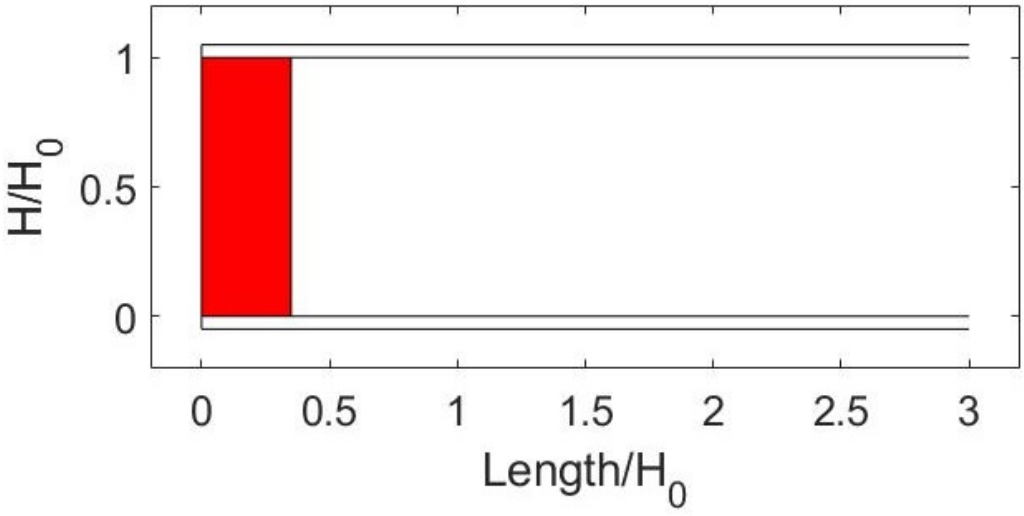

Figure 12.78: First extreme W1 web corrosion pattern, with full height corrosion for beams with diaphragm.

With web thickness loss $\frac{t_{loss}}{t_{web}} \in \{0.2, 0.4, 0.6\}$ (Fig. 12.77).

Flange corrosion CASE A

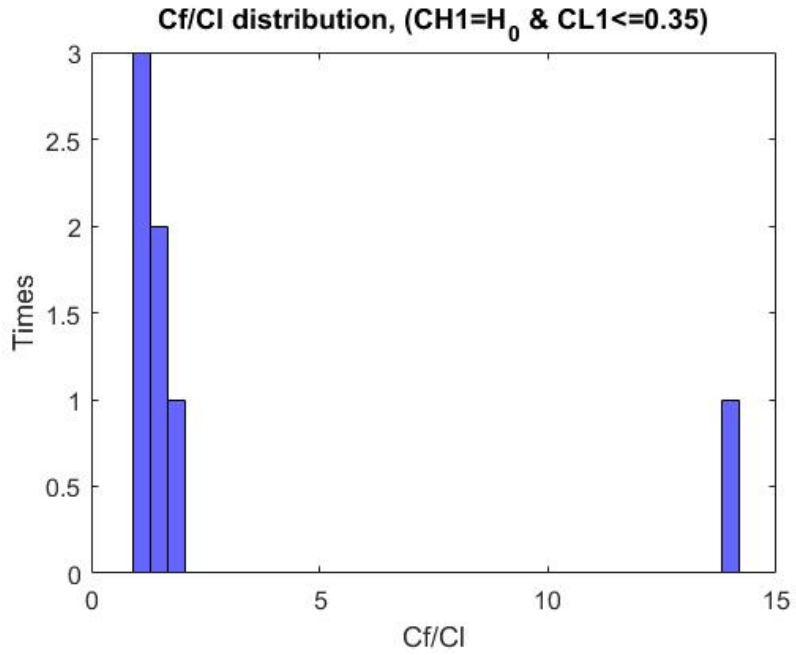

Figure 12.79: Ratio of flange to web corrosion length distribution of W1 web corrosion pattern, with full height corrosion and up to 35% of H_0 length, for beams with diaphragm.

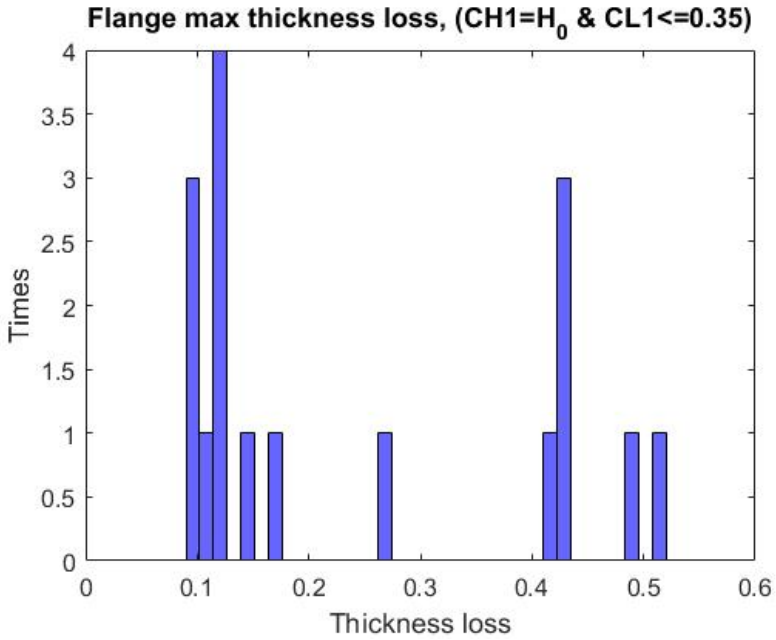

Figure 12.80: Max flange thickness loss distribution of W1 web corrosion pattern, with full height corrosion and up to 35% of H_0 length, for beams with diaphragm.

Thus, for Case A: $\frac{t_{loss}}{t_{flange}} \in \{0.15, 0.45\}$ (Fig. 12.80). The ratio of the length of the corroded flange over the length of the corroded web $\frac{Cf}{Cl} \in [1, 1.7]$

For $CH_1 \in (0, 0.3]$

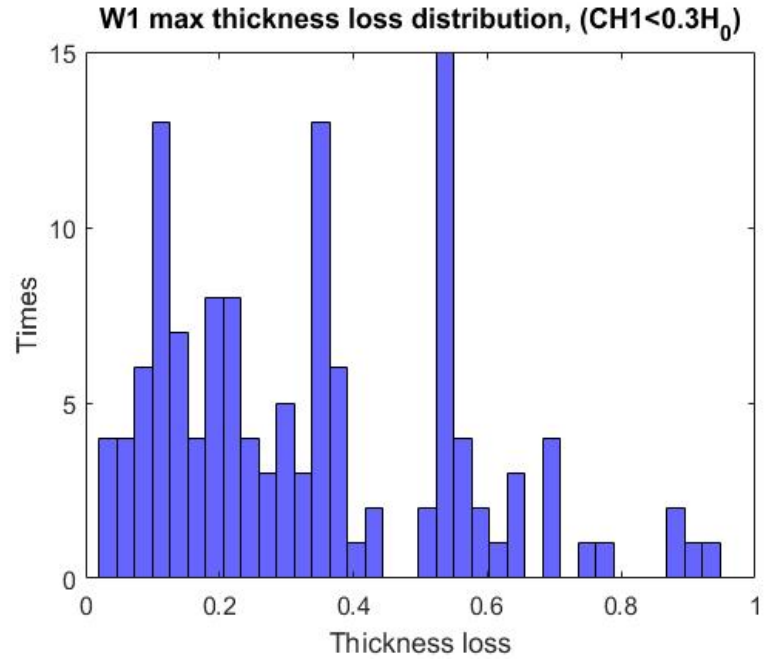

Figure 12.81: Max web thickness loss distribution of W1 web corrosion pattern with corrosion height up to 30% of H_0 for beams with diaphragm.

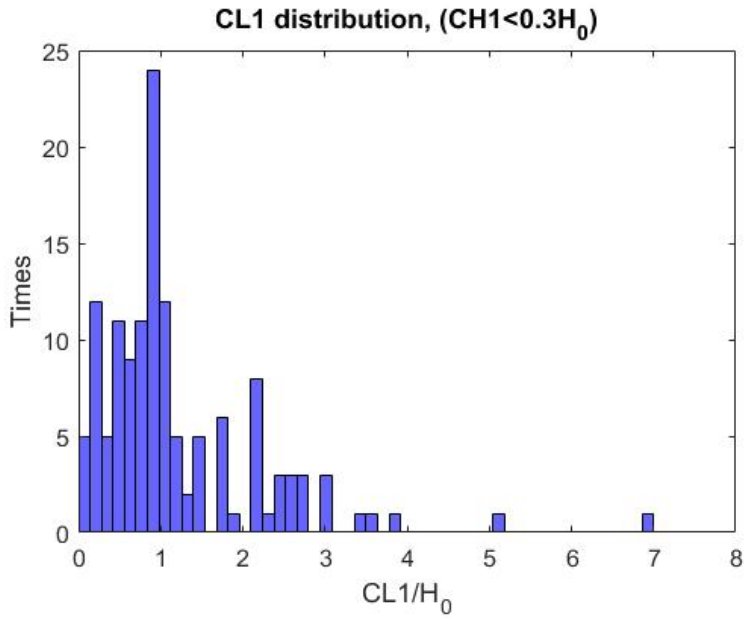

Figure 12.82: CL1 thickness loss distribution of W1 web corrosion pattern with corrosion height up to 30% of H_0 for beams with diaphragm.

From Fig. 12.82: $CL_1 \in (0, 2.5]$, with web thickness loss $\frac{t_{loss}}{t_{web}} \in \{0.2,0.4,0.6,0.8\}$.

CASE B

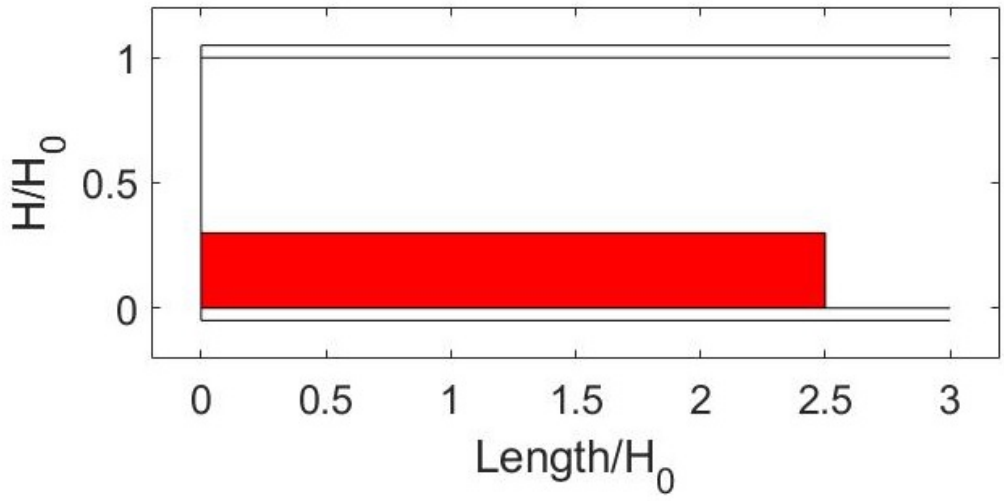

Figure 12.83: Second extreme W1 web corrosion pattern, with corrosion height up to 30% of H_0 for beams with diaphragm.

For case B: $\frac{t_{loss}}{t_{flange}} \in \{0.2,0.4,0.6,0.8\}$. The ratio of the length of the corroded flange over the length of the corroded web is $\frac{Cf}{Cl} \in (0,1]$.

Flange corrosion CASE B

For CH1 < $0.3H_0$

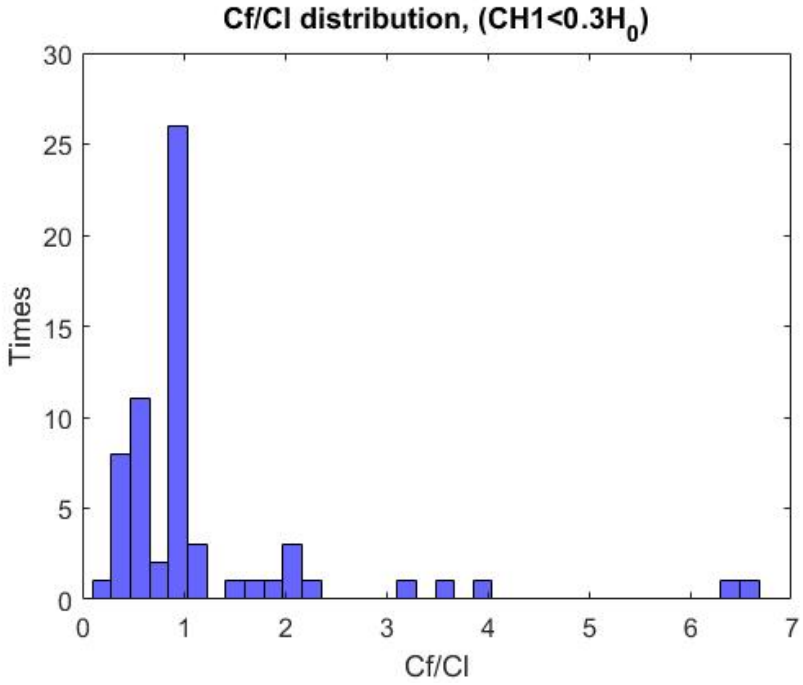

Figure 12.84: Ratio of flange to web corrosion length distribution of W1 web corrosion pattern with corrosion height up to 30% of H_0 for beams with diaphragm.

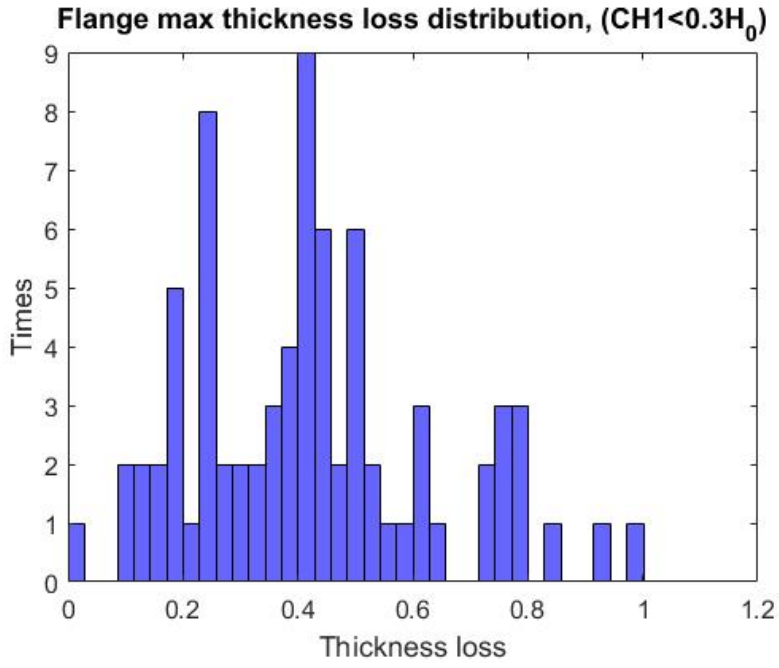

Figure 12.85: Max flange thickness loss distribution of W1 web corrosion pattern with corrosion height up to 30% of H_0 for beams with diaphragm.

Holes

The W1 pattern is combined 11 times with the M1 hole pattern. The web thickness loss, holes dimensions, and corrosion height at these cases are given as:

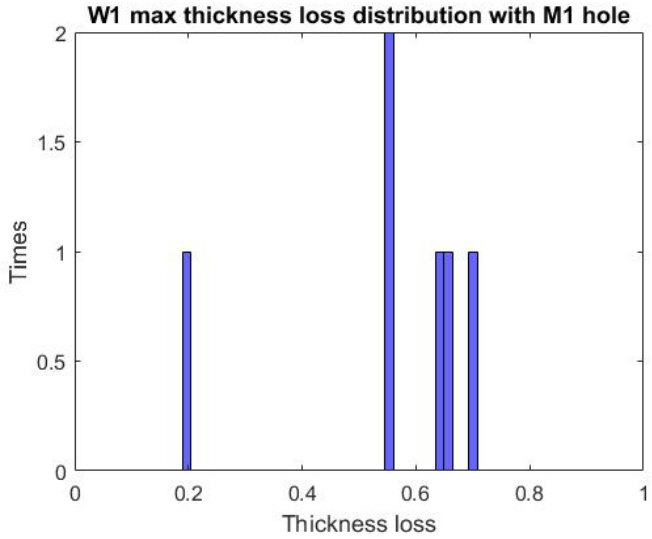

Figure 12.86: Max thickness loss distribution for W1 web corrosion patterns and M1 hole for beams with diaphragm.

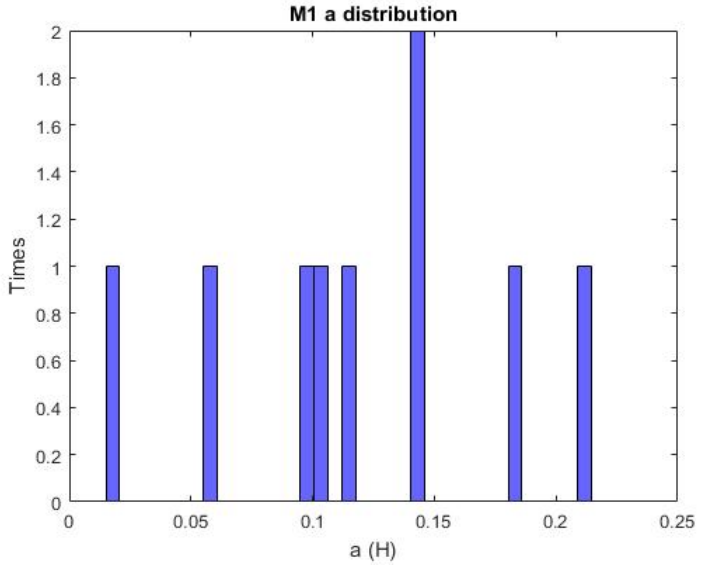

Figure 12.87: M1 web hole's pattern height distribution of W1 web corrosion pattern for beams with diaphragm.

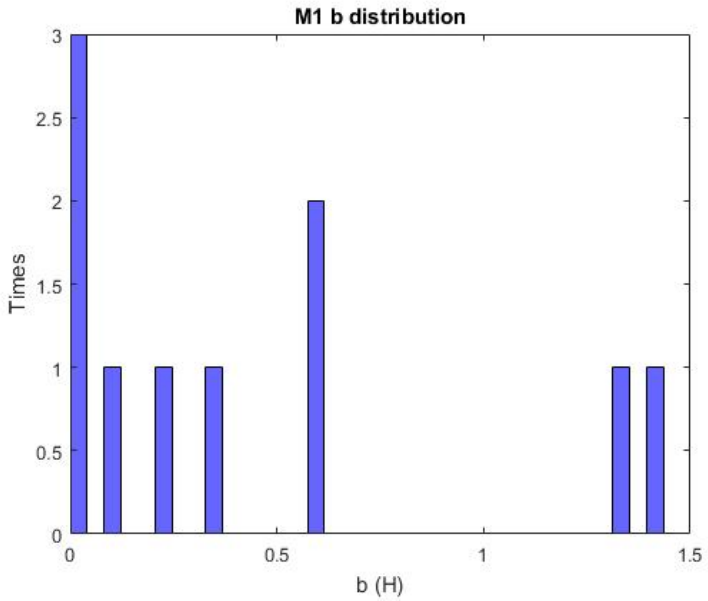

Figure 12.88: M1 web hole's pattern length distribution of W1 web corrosion pattern for beams with diaphragm.

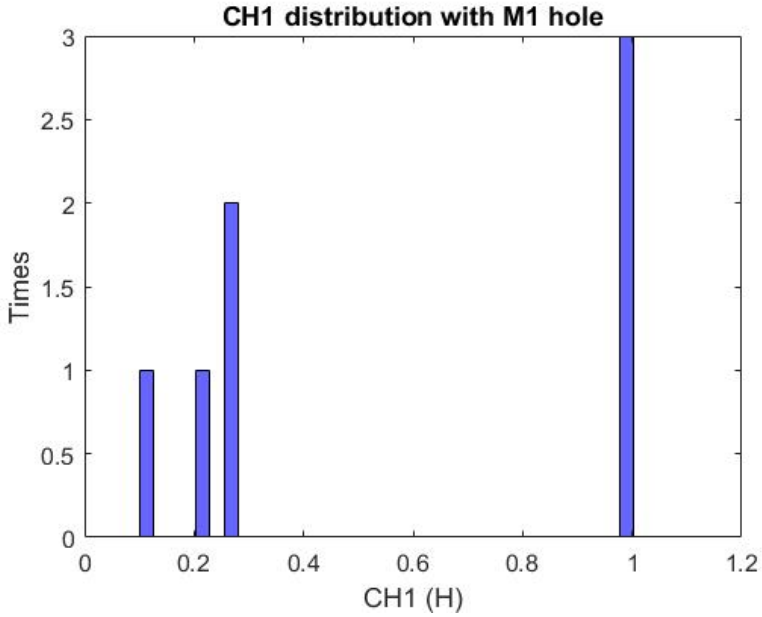

Figure 12.89: CH1 distribution for beams with M1 hole and W1 web corrosion pattern and diaphragm.

From Fig. 12.86, one can conclude that holes are equally distributed between web corrosion scenarios CASE A and CASE B. It is worth mentioning that there are two cases of long parallel to flange holes (Fig. 12.88). The two longest holes (1.3 H_0 and 1.4 H_0) are the same with the greatest height (0.18 and 0.21, respectively). As a result, an extreme hole case is considered the following (projected on Case B web corrosion scenario):

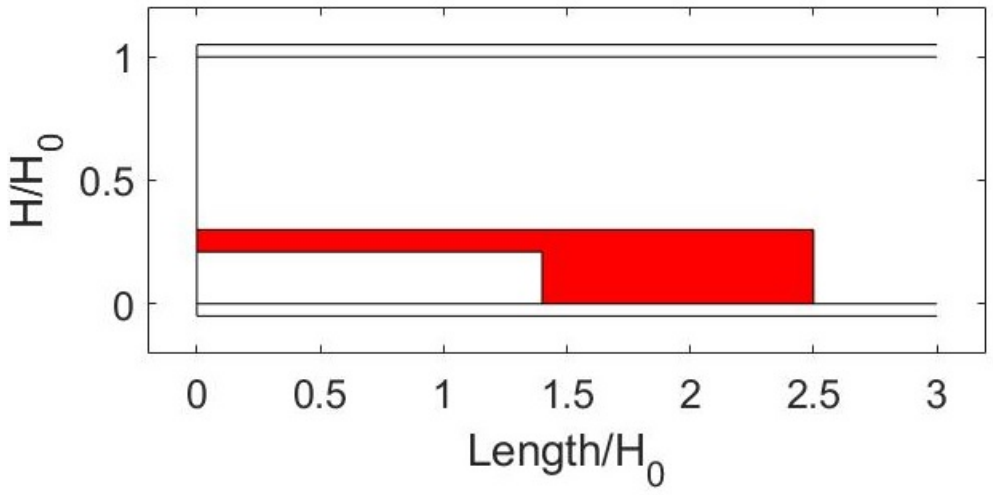

Figure 12.90: M1 extreme web hole pattern scenario of W1 web corrosion pattern, for beams with diaphragm.

There are also four cases of M2 hole pattern. The web thickness loss, hole dimensions, and corrosion height of these cases are given as:

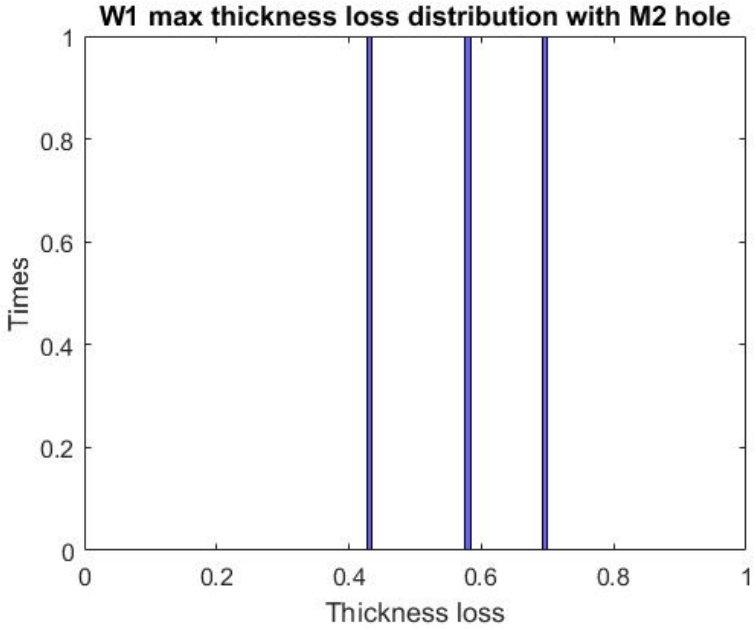

Figure 12.91: Max thickness loss distribution for W1 web corrosion patterns and M2 hole for beams with diaphragm.

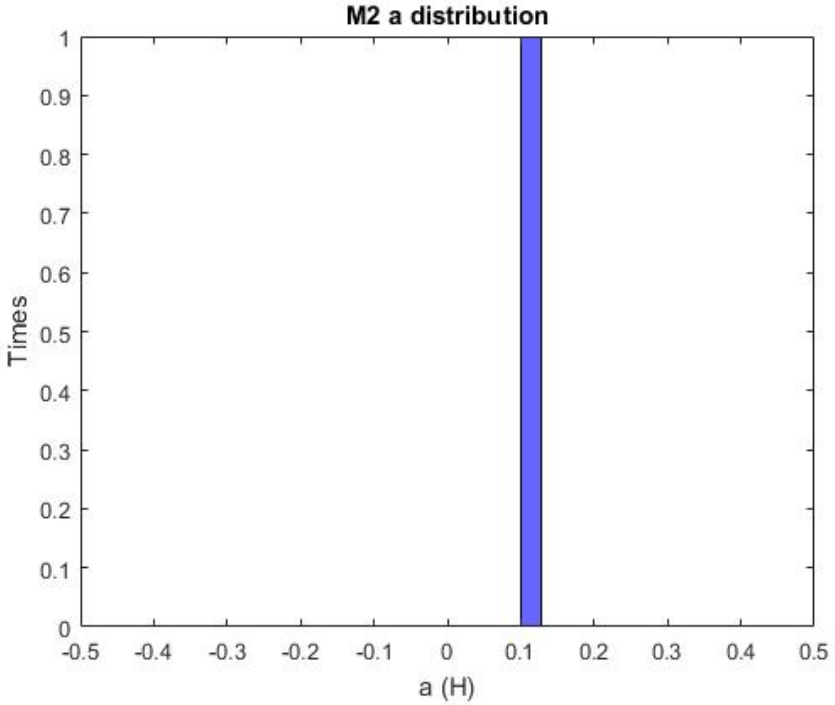

Figure 12.92: M2 web hole's pattern height distribution of W1 web corrosion pattern for beams with diaphragm.

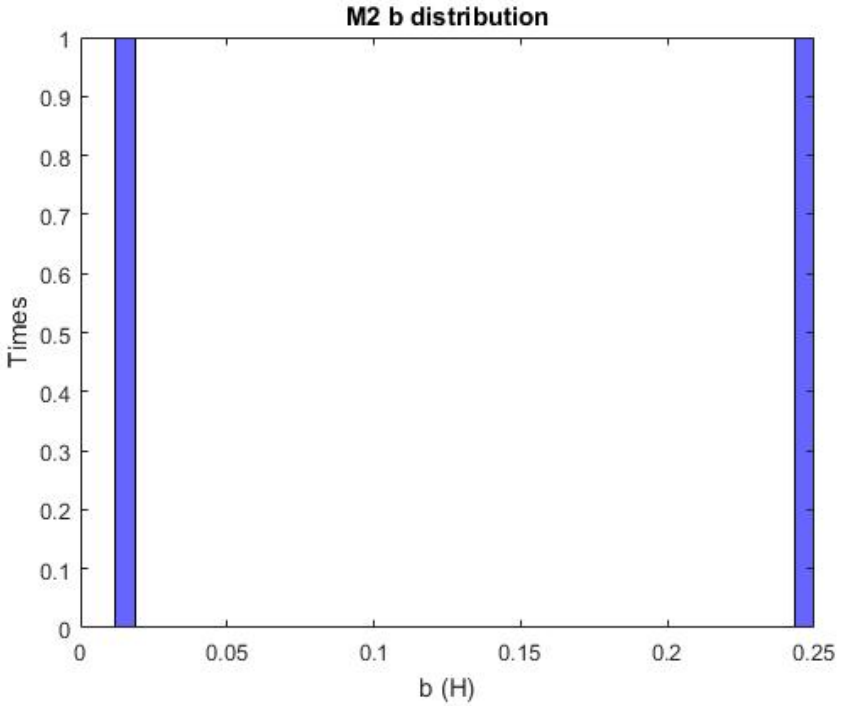

Figure 12.93: M2 web hole's pattern length distribution of W1 web corrosion pattern for beams with diaphragm.

The sample is too small to extract conclusions.

12.2.3 Pattern W2

Web corrosion

The W2 pattern was observed in total only 47 times.

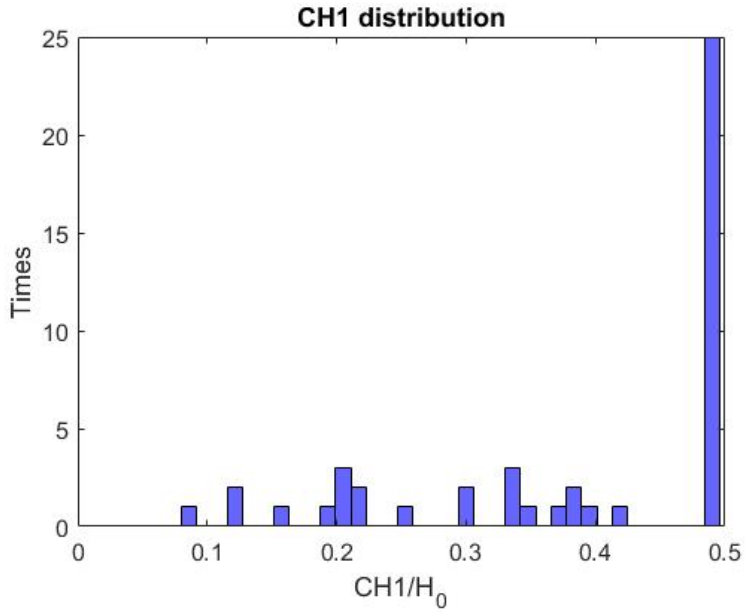

Figure 12.94: CH1 distribution of W2 pattern for beams with diaphragm.

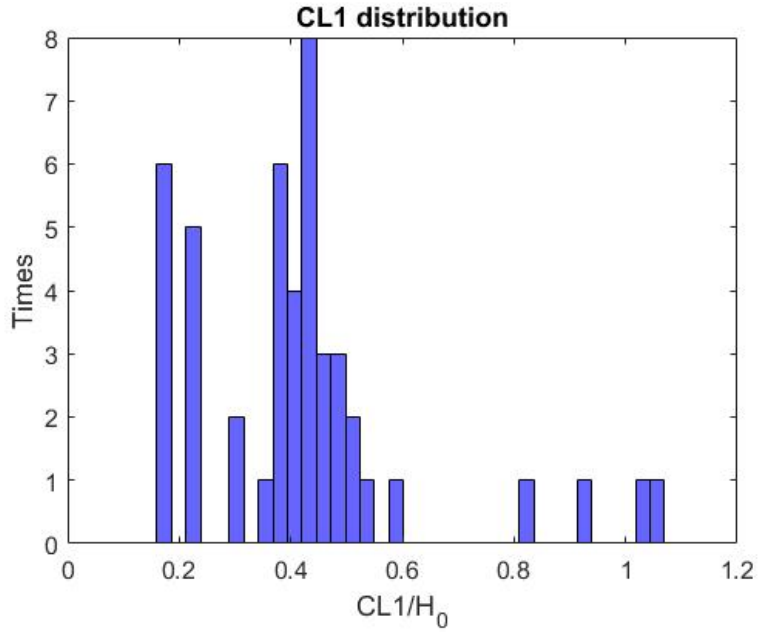

Figure 12 95: CL1 distribution of W2 pattern for beams with diaphragm.

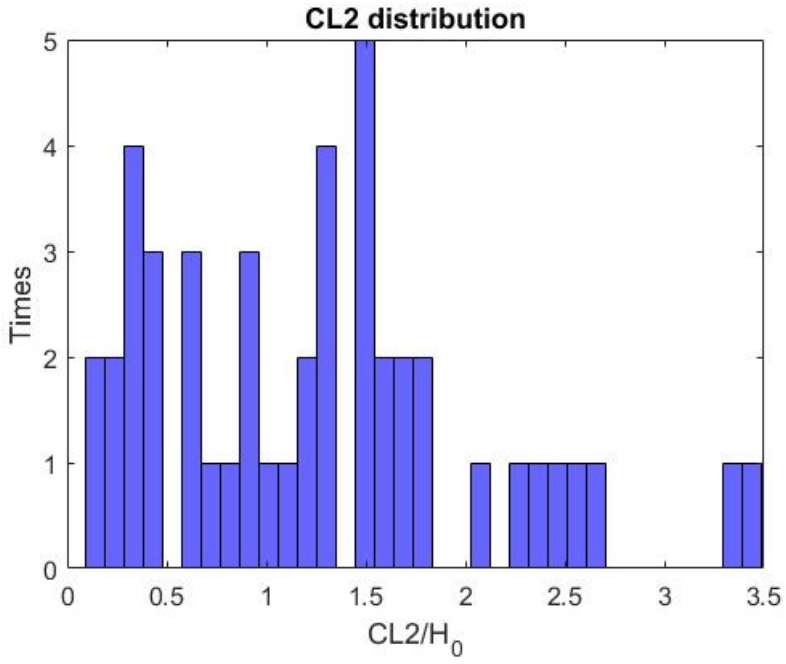

Figure 12.96: CL2 distribution of W2 pattern for beams with diaphragm.

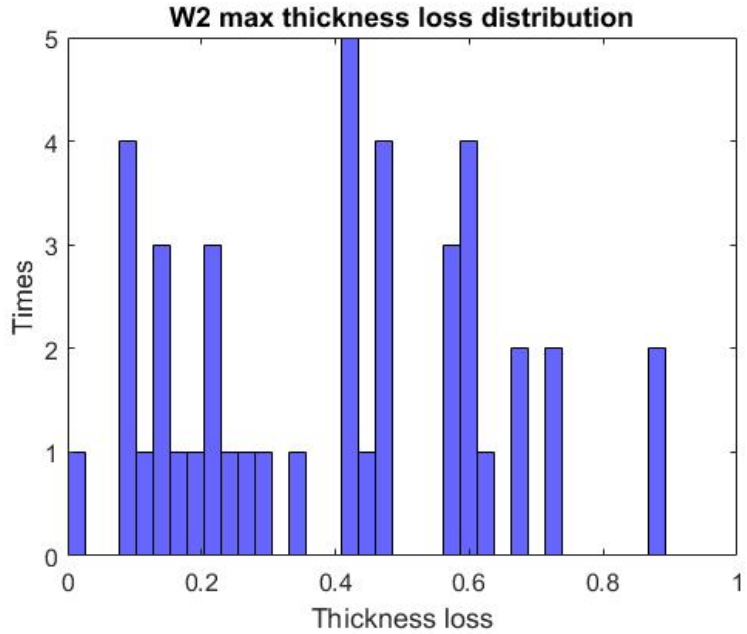

Figure 12.97: Web thickness loss distribution of W2 pattern for beams with diaphragm.

From the above:

$$CH_1 \in (0,0.5H_0]$$
$$CL_1 \in (0,0.6H_0]$$
$$CL_2 \in (0,1.8H_0]$$
$$\frac{t_{loss}}{t_{web}} \in \{0.2,0.4,0.6,0.8\}$$

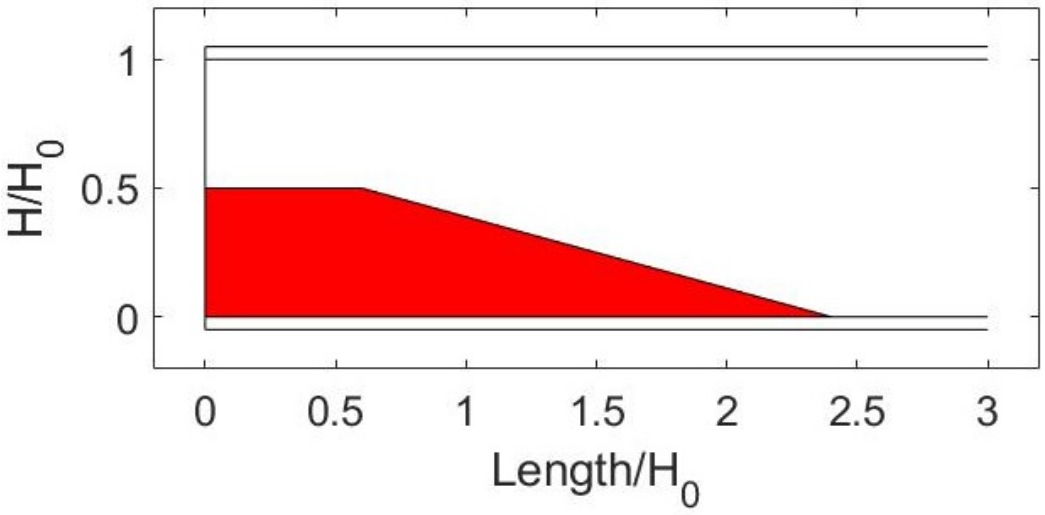

Figure 12.98: Extreme W2 web corrosion pattern for beams with diaphragm.

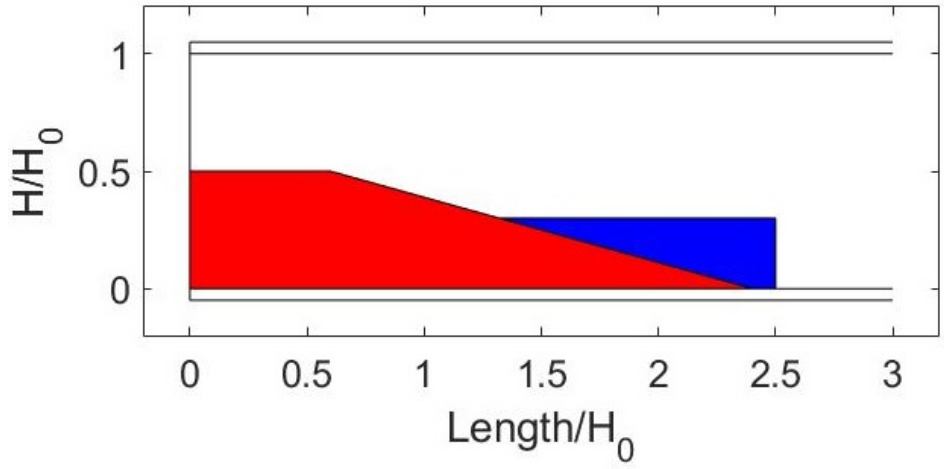

Figure 12.99: W2 extreme web corrosion scenario (with red color) projected over W1 CASE B extreme web corrosion scenario (with blue color).

W1 can be concerned as a case of W2 with CL2 equal to zero.

Flange corrosion

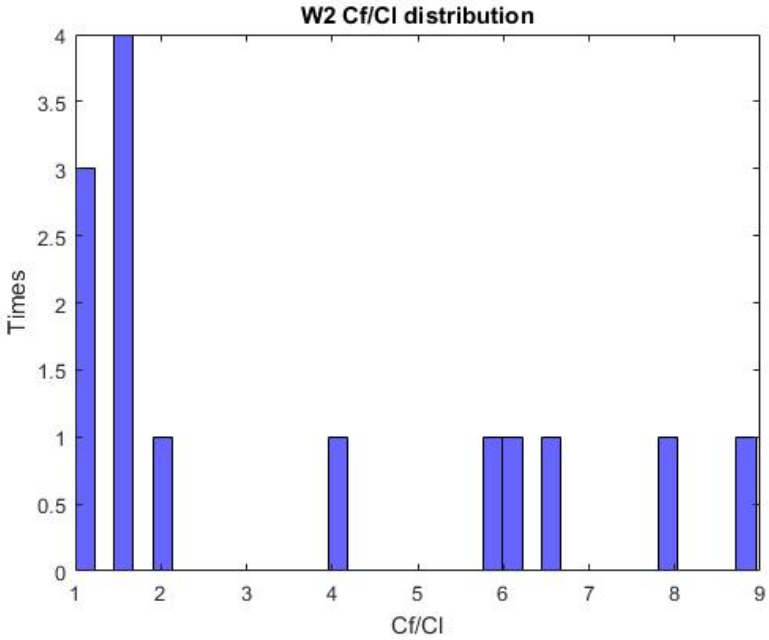

Figure 12.100: Ratio of flange to web corrosion length distribution of W2 web corrosion pattern corrosion for beams with diaphragm.

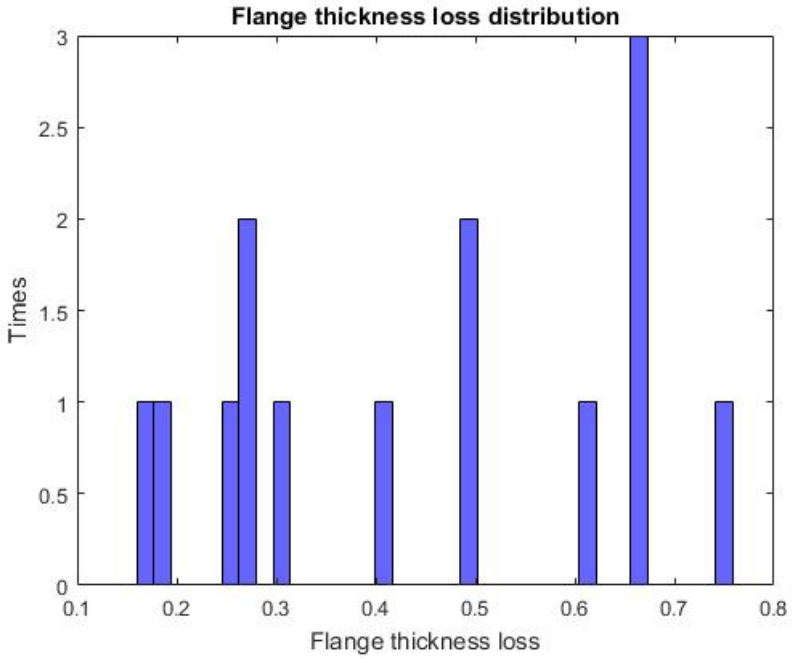

Figure 12.101: Max flange loss thickness distribution of W2 web corrosion pattern for beams without diaphragm.

Holes

Table 12.3: Hole frequency for beams with diaphragm.

	Frequency	No hole	M1	M2	M3	M4	M12	M13	M24
W1	214	190	11	4	5	2	2	0	0
W2	47	41	1	4	0	0	1	0	0
W3	160	112	23	5	6	2	7	4	1
W4	16	13	1	2	0	0	0	0	0
W5	9	9	0	0	0	0	0	0	0
W6	0	0	0	0	0	0	0	0	0

According to the table above, the W2 pattern is combined once with M1 and four times with M2. As was mentioned, W2 and W1 were taken as one pattern. Thus, for M1, the team checked if the dimensions of the unique hole belonged in the range of W1 M1. The unique hole with $a=0.089H_0$ and $b=0.31H_0$ satisfies the limits of Figure 12.90.

For the M2 hole pattern, the sample for W1 was very small. Thus, the team was not able to extract conclusions, so M2 for both W1 and W2 were processed together:

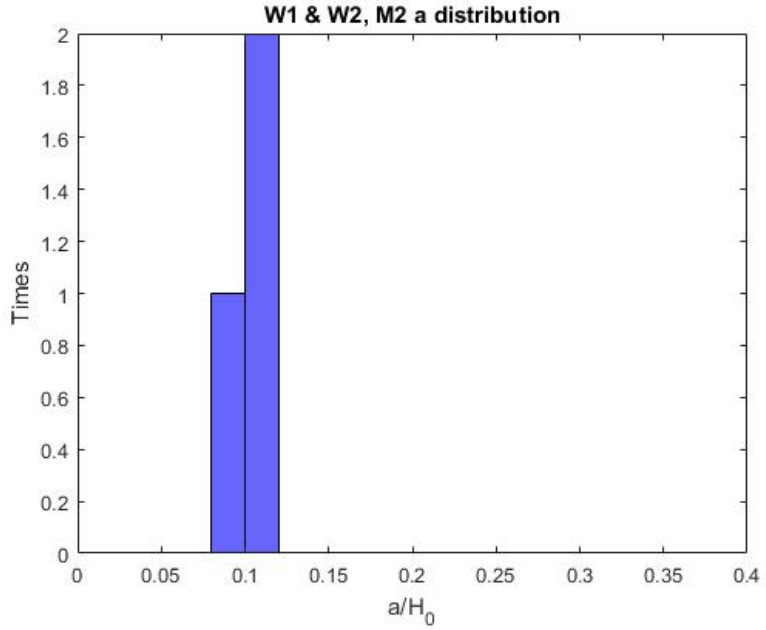

Figure 12.102: M2 web hole's pattern height distribution of W1 and W2 web corrosion patterns for beams with diaphragm.

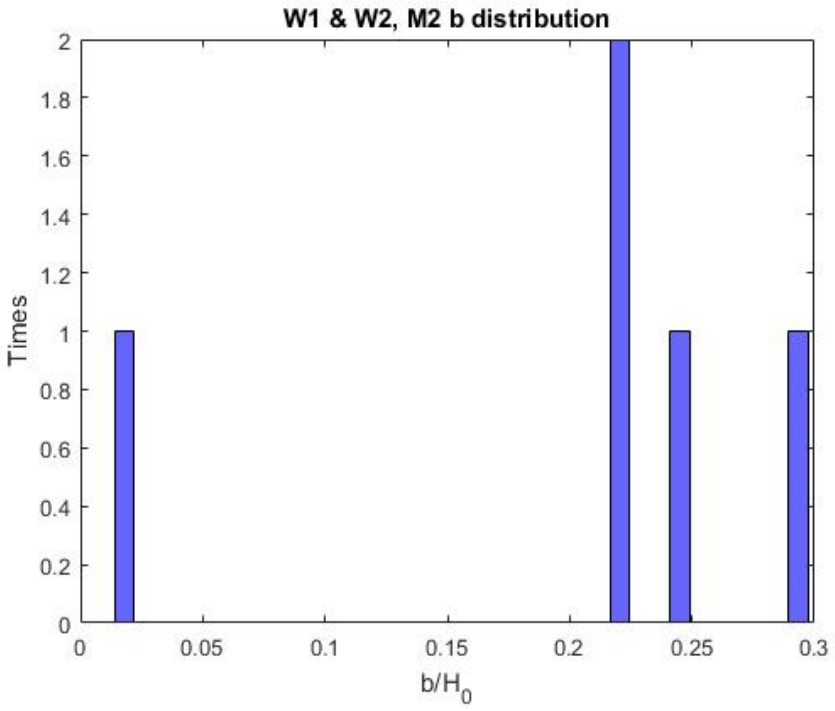

Figure 12.103: M2 web hole's pattern length distribution of W1 and W2 web corrosion patterns for beams with diaphragm.

The sample remains very small (three values for M2a, and five for M2b), but one could assume that M2 holes are thin and long 100% material loss areas underneath the diaphragm:

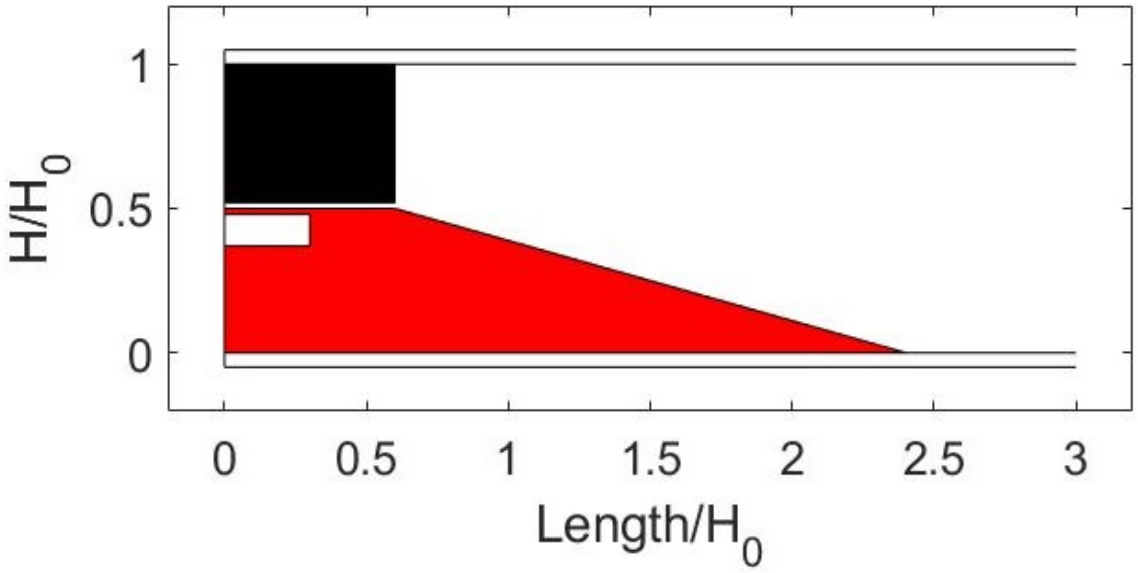

Figure 12.104: M2 hole pattern projected on the extreme W2 web corrosion pattern. With black color is illustrated the diaphragm that could be found with these patterns.

With a<=0.11, and b<=0.3

12.2.4 Pattern W3

Web corrosion

The data analysis started with the CH2 distribution.

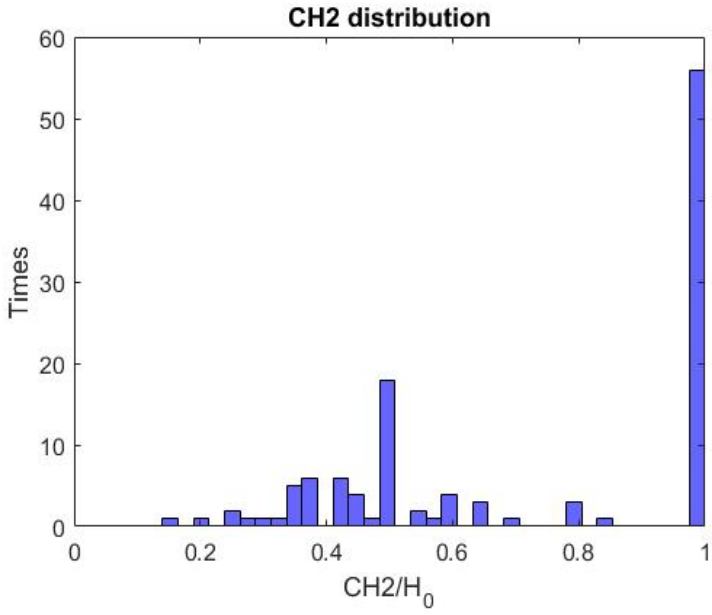

Figure 12.105: CH2 distribution of W3 web corrosion pattern for beams with diaphragm.

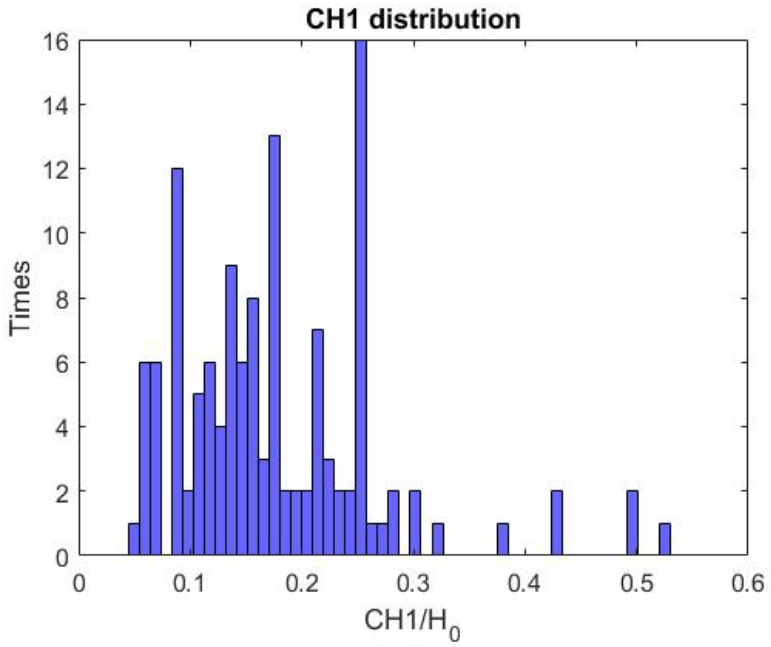

Figure 12.106: CH1 distribution of W3 web corrosion pattern for beams with diaphragm.

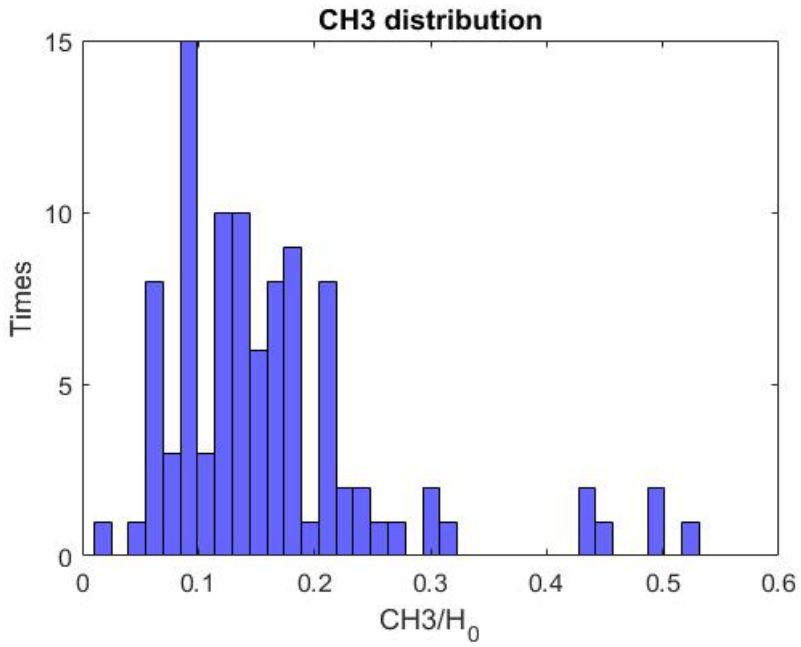

Figure 12.107: CH3 distribution of W3 web corrosion pattern for beams with diaphragm.

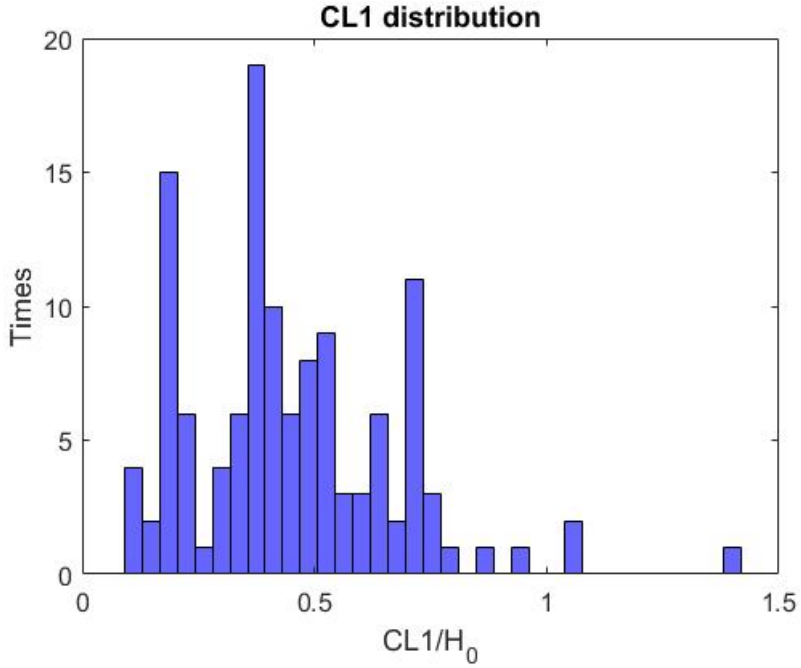

Figure 12.108: CL1 distribution of W3 web corrosion pattern for beams with diaphragm.

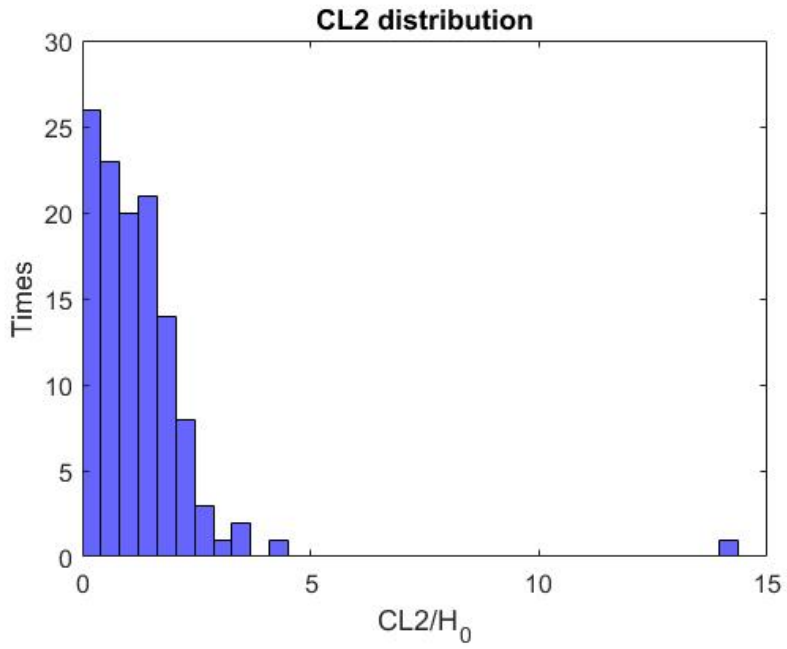

Figure 12.109: CL2 distribution of W3 web corrosion pattern for beams with diaphragm.

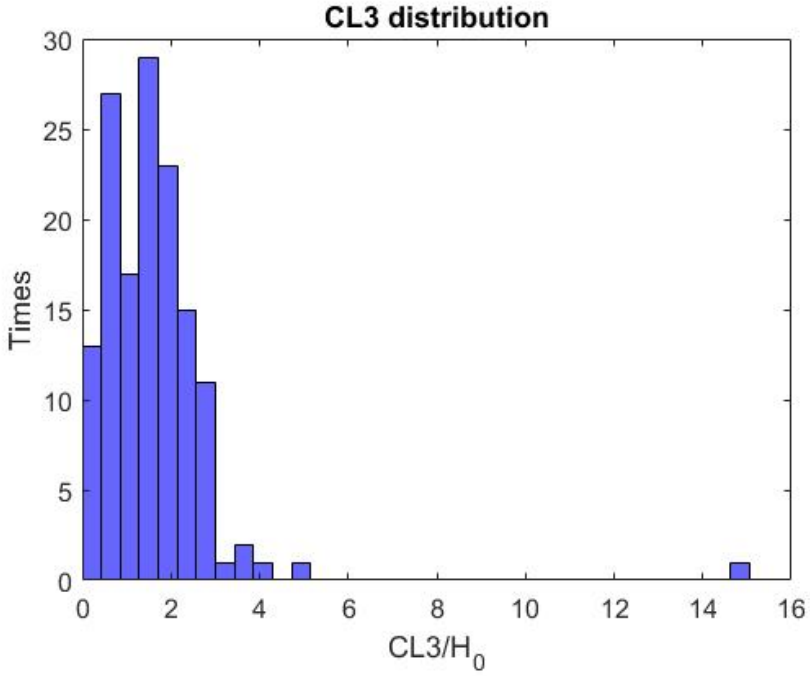

Figure 12.110: CL3 distribution of W3 web corrosion pattern for beams with diaphragm.

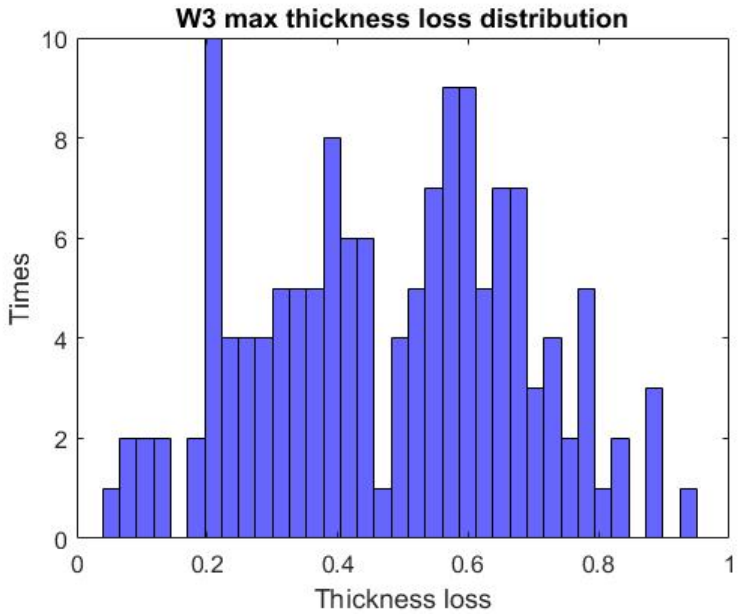

Figure 12.111: Max web thickness loss distribution of W3 web corrosion pattern for beams with diaphragm.

From the CH2 histogram (Fig. 12.105), two main trends are noticed, either (a) full height corrosion, or (b) corrosion up to 50% of H_0.

$$CH_2 \in \begin{cases} (0, 0.5H_0] \\ H_0 \end{cases}$$

For full height corrosion:

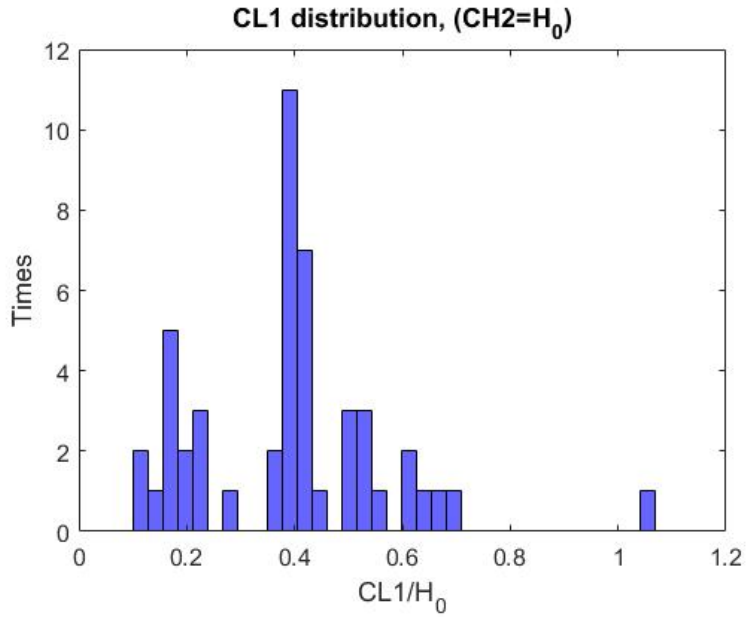

Figure 12.112: CL1 distribution of W3 web corrosion pattern with full height corrosion for beams with diaphragm.

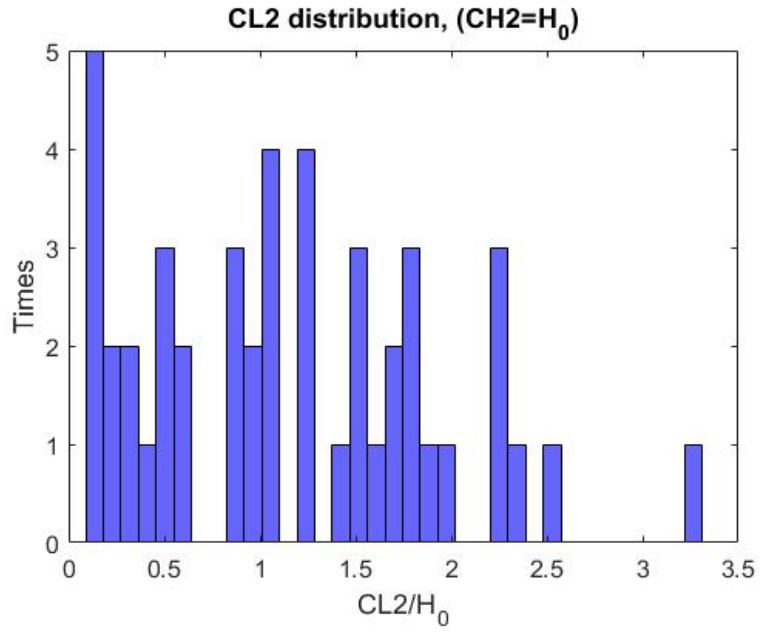

Figure 12.113: CL2 distribution of W3 web corrosion pattern with full height corrosion for beams with diaphragm.

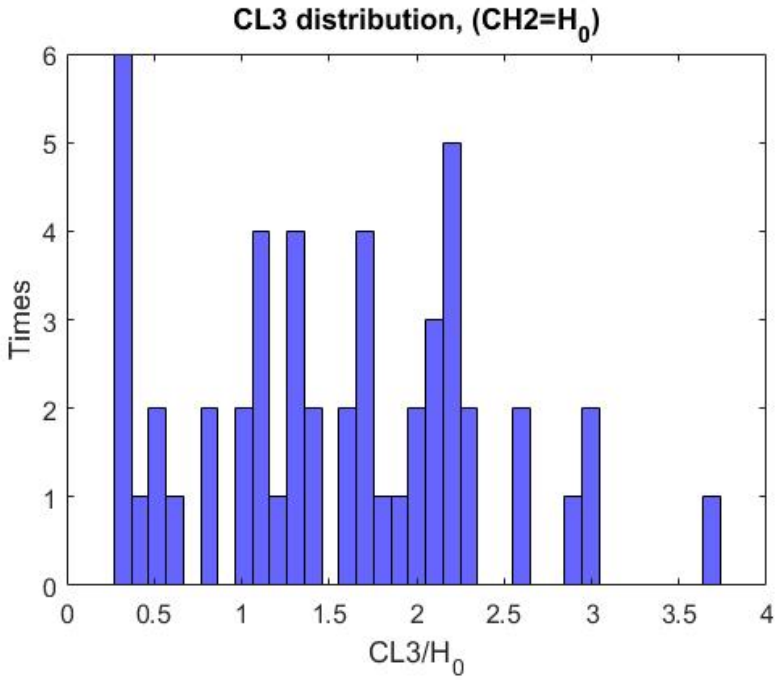

Figure 12.114: CL3 distribution of W3 web corrosion pattern with full height corrosion for beams with diaphragm.

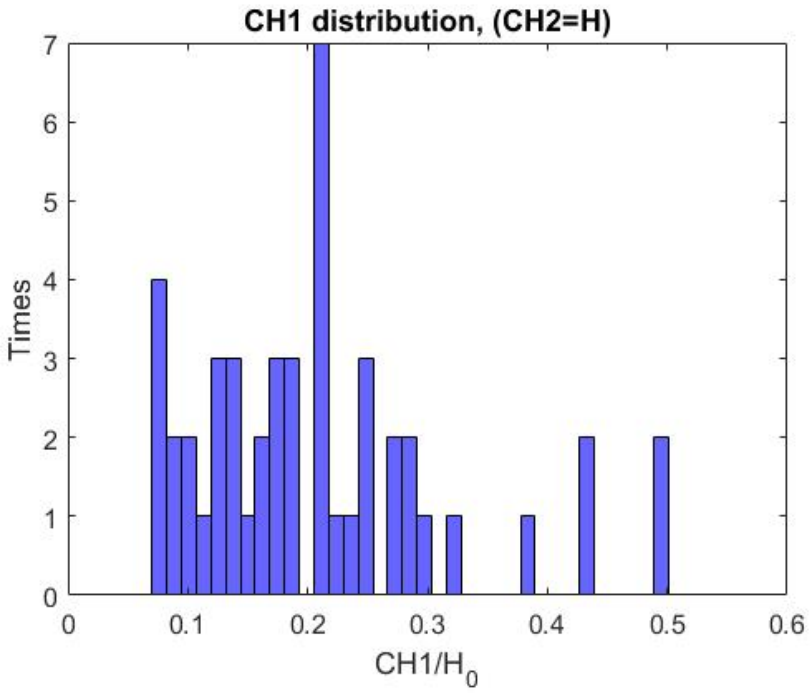

Figure 12.115: CH1 distribution of W3 web corrosion pattern with full height corrosion for beams with diaphragm.

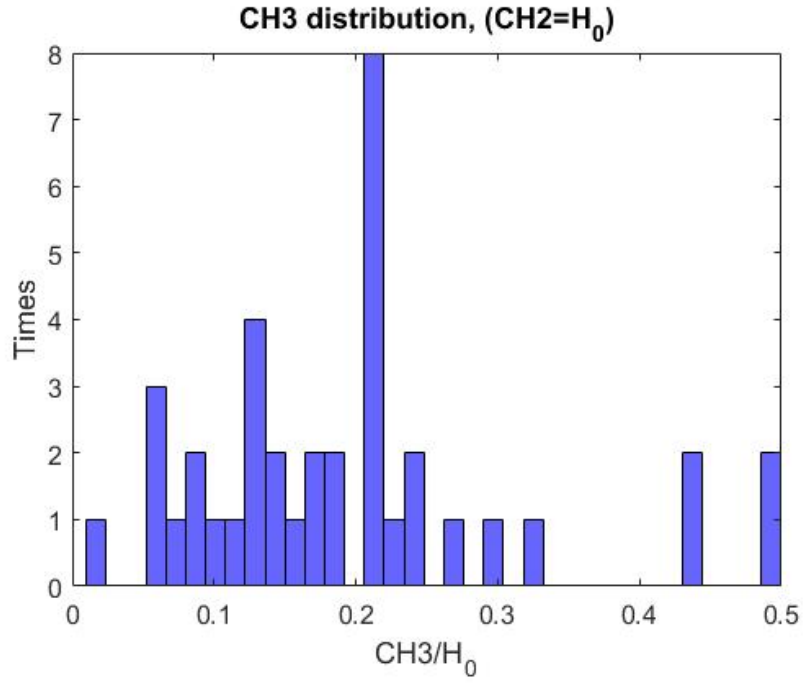

Figure 12.116: CH3 distribution of W3 web corrosion pattern with full height corrosion for beams with diaphragm.

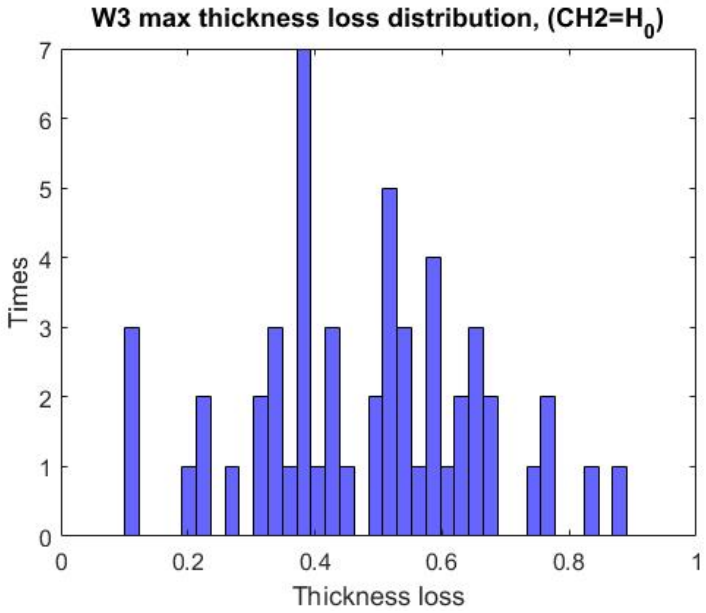

Figure 12.117: Max web thickness loss distribution of W3 web corrosion pattern with full height corrosion for beams with diaphragm.

From the CL3 histogram (Fig. 12.114), two main trends are noticed:

$$CL_3 \in \begin{cases} (0.25, 0.6]H_0 \\ (0.6, 2.25]H_0 \end{cases}$$

For full height corrosion and CL3$\in (0.25, 0.6]H_0$

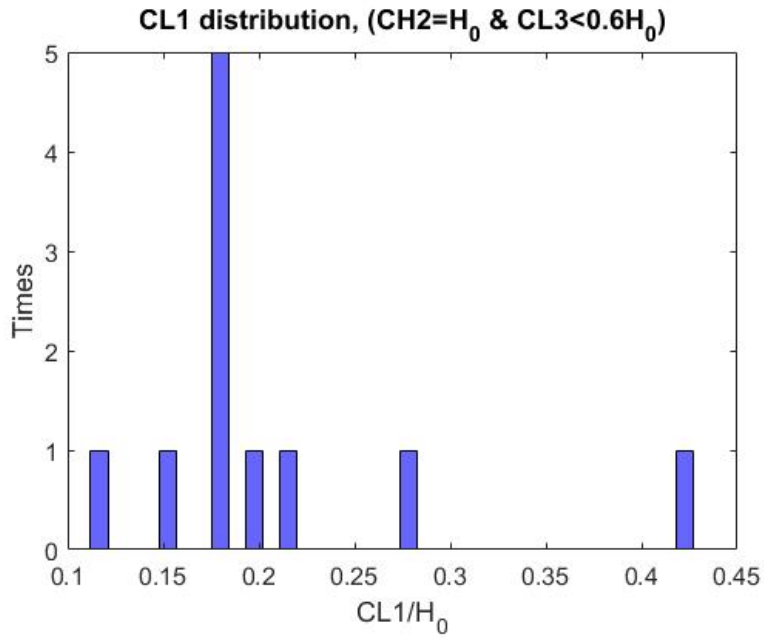

Figure 12.118: : CL1 distribution of W3 web corrosion pattern with full height corrosion and deteriorated length up to 60% of H_0 for beams with diaphragm.

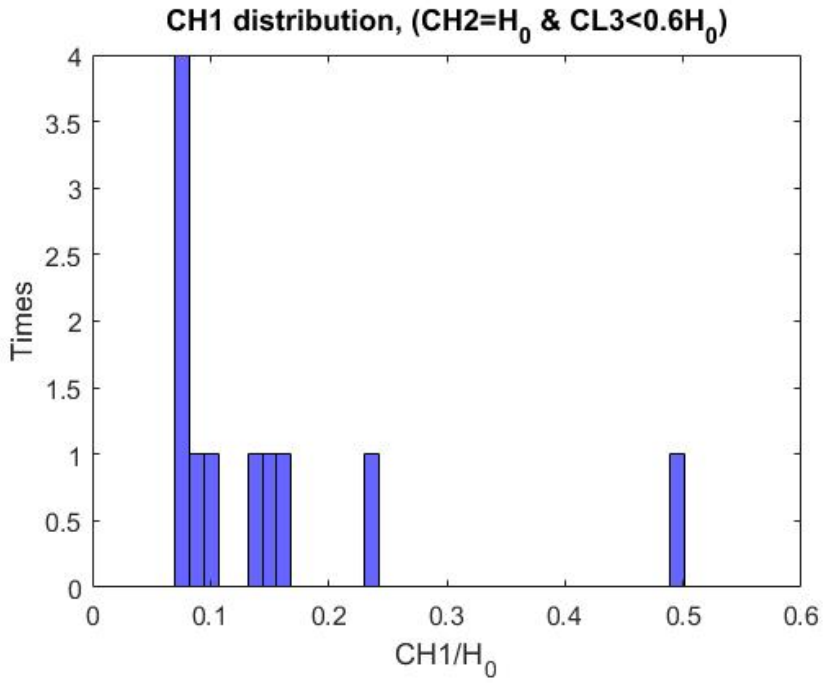

Figure 12.119: CH1 distribution of W3 web corrosion pattern with full height corrosion and deteriorated length up to 60% of H_0 for beams with diaphragm.

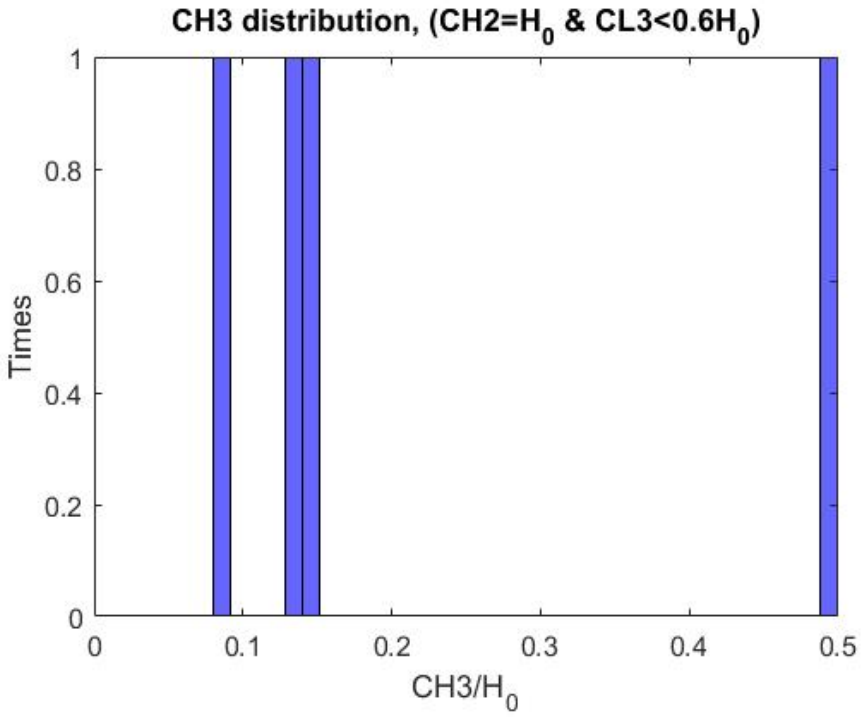

Figure 12.120: CH3 distribution of W3 web corrosion pattern with full height corrosion and deteriorated length up to 60% of H_0 for beams with diaphragm.

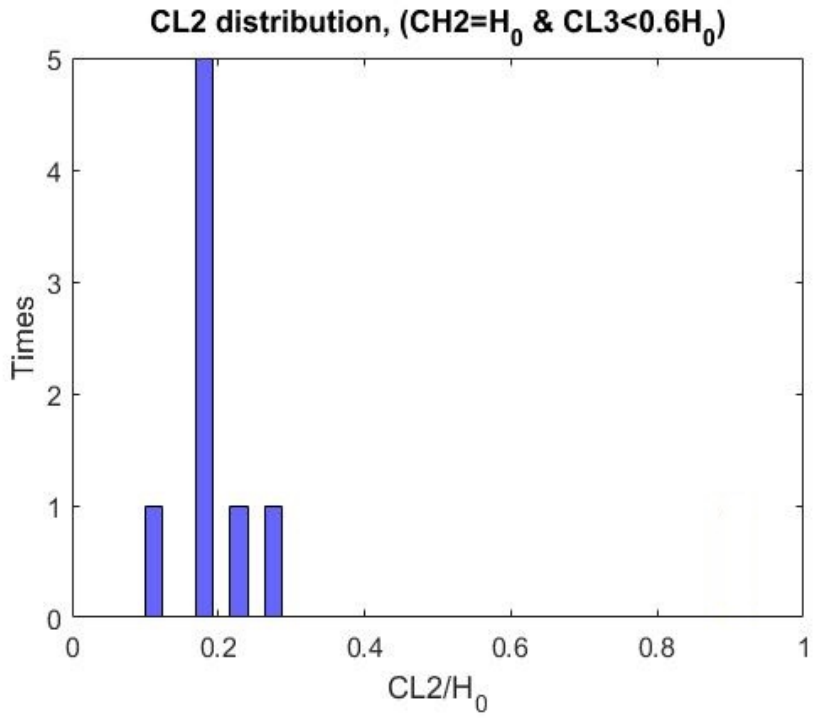

Figure 12.121: CL2 distribution of W3 web corrosion pattern with full height corrosion and deteriorated length up to 60% of H_0 for beams with diaphragm.

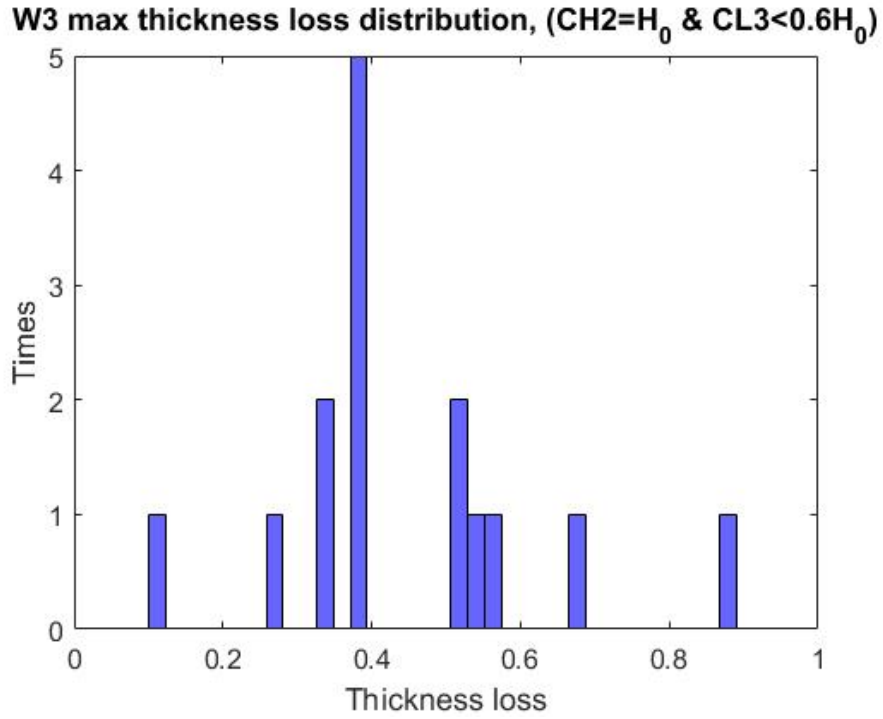

Figure 12.122: Max web thickness loss distribution, of W3 web corrosion pattern, with full height corrosion and deteriorated length up to 60% of H_0 for beams with diaphragm.

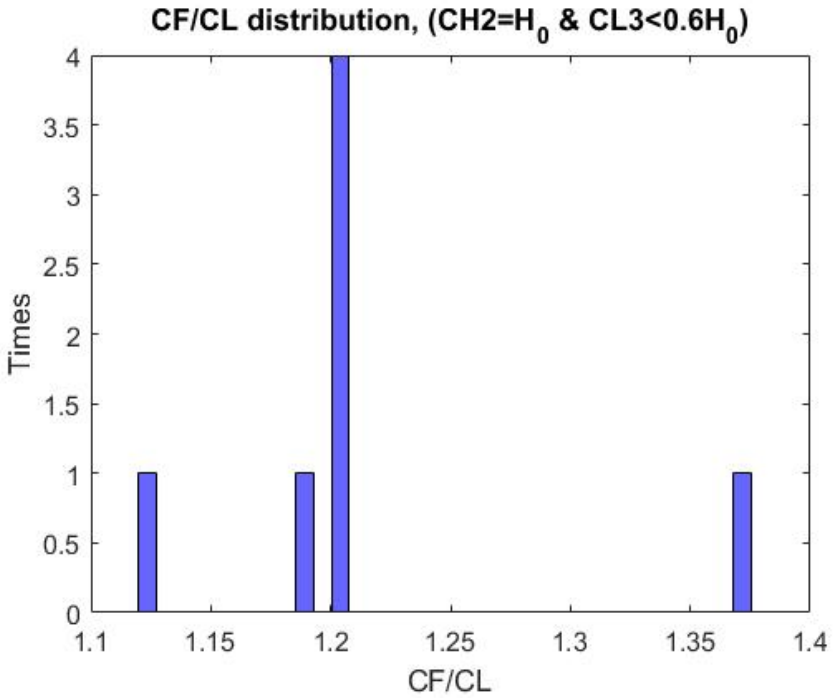

Figure 12.123: Ratio of flange to web corrosion length distribution, of W3 web corrosion pattern, with full height corrosion and deteriorated length up to 60% of H_0 for beams with diaphragm.

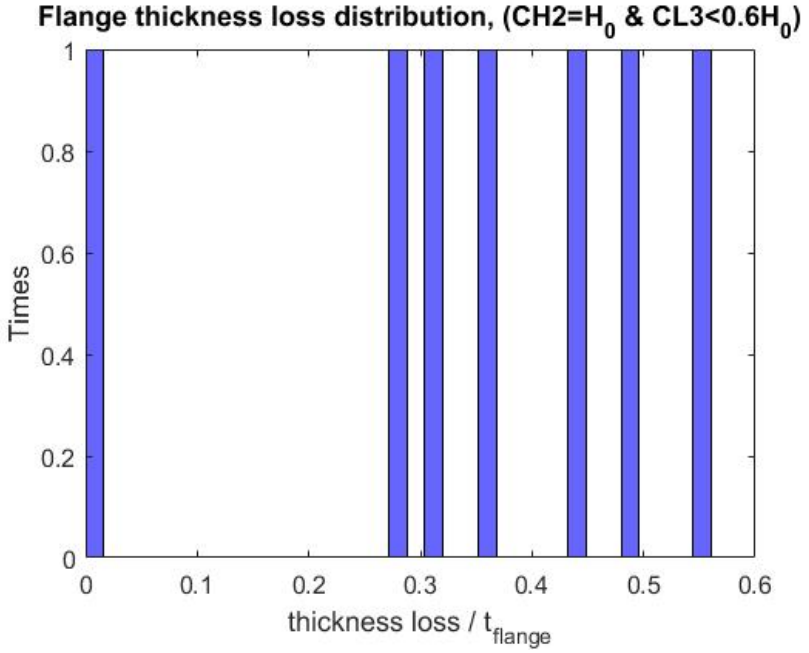

Figure 12.124: Max flange loss thickness distribution, for beams with W3 web corrosion pattern, with full height corrosion, deteriorated length up to 60% of H_0 and with diaphragm.

$$CL_3 \in (0.25,0.6]H_0$$

$CL_1 \in (0.1,0.2]H_0$

$$CL_1 \in (0.1,0.2]H_0$$

$$CH_1 = CH_3 \in (0.06,0.16]H_0$$

$\frac{t_{loss}}{t_{web}} \in \{0.4,0.6\}$

$\frac{Cf}{Cl} = 1.2$ and

$\frac{t_{loss}}{t_{flange}} \in \{0.3,0.6\}$

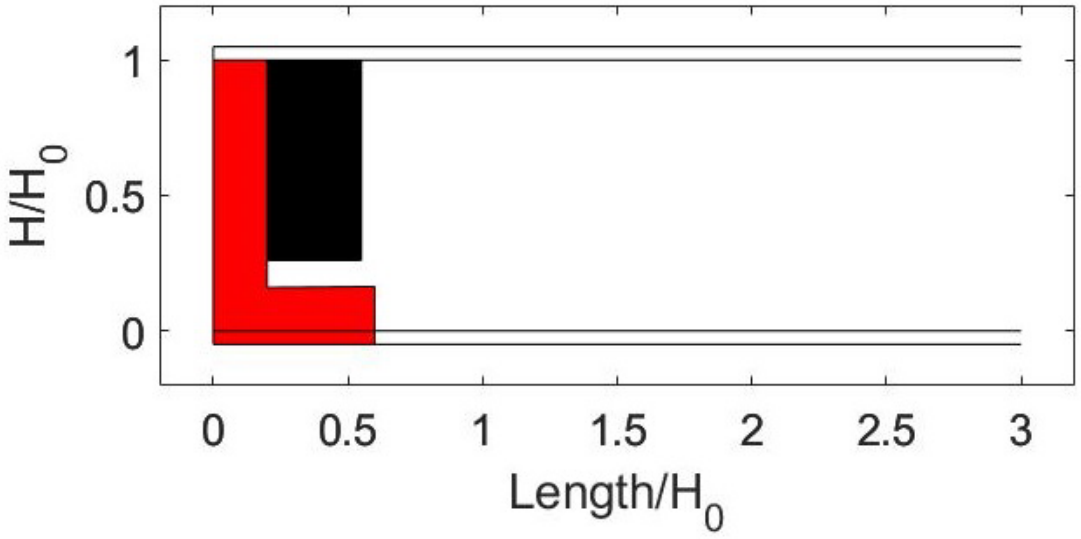

Figure 12.125: First extreme flange and W3 web corrosion scenario for beams with diaphragm.

For full height corrosion and CL3<=2.3:

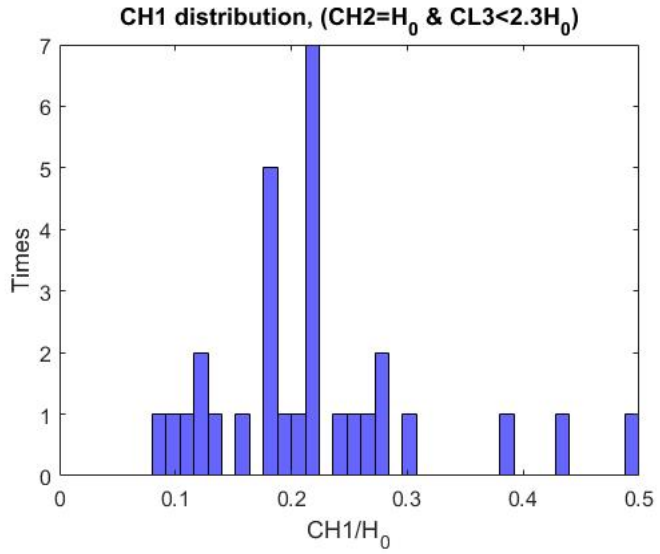

Figure 12.126: CH1 distribution of W3 web corrosion pattern, with full height corrosion and deteriorated length up to 230% of H_0, for beams with diaphragm.

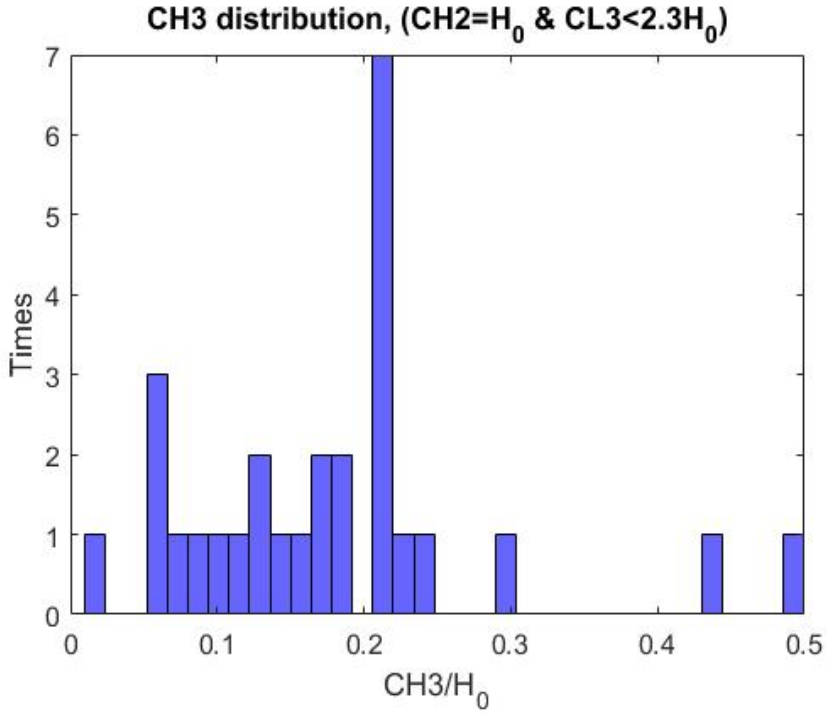

Figure 12.127: CH3 distribution of W3 web corrosion pattern, with full height corrosion and deteriorated length up to 230% of H_0, for beams with diaphragm.

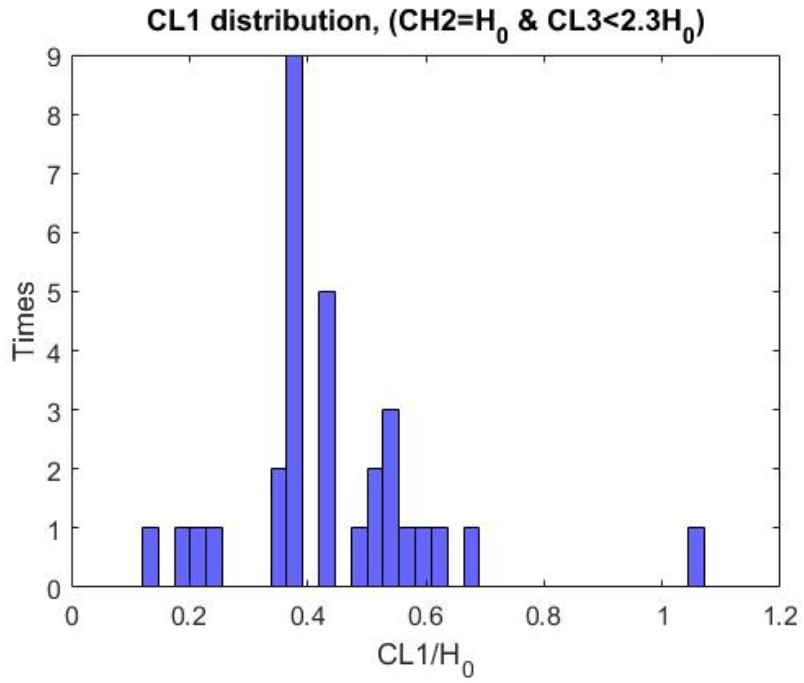

Figure 12.128: CL1 distribution of W3 web corrosion pattern, with full height corrosion and deteriorated length up to 230% of H_0, for beams with diaphragm.

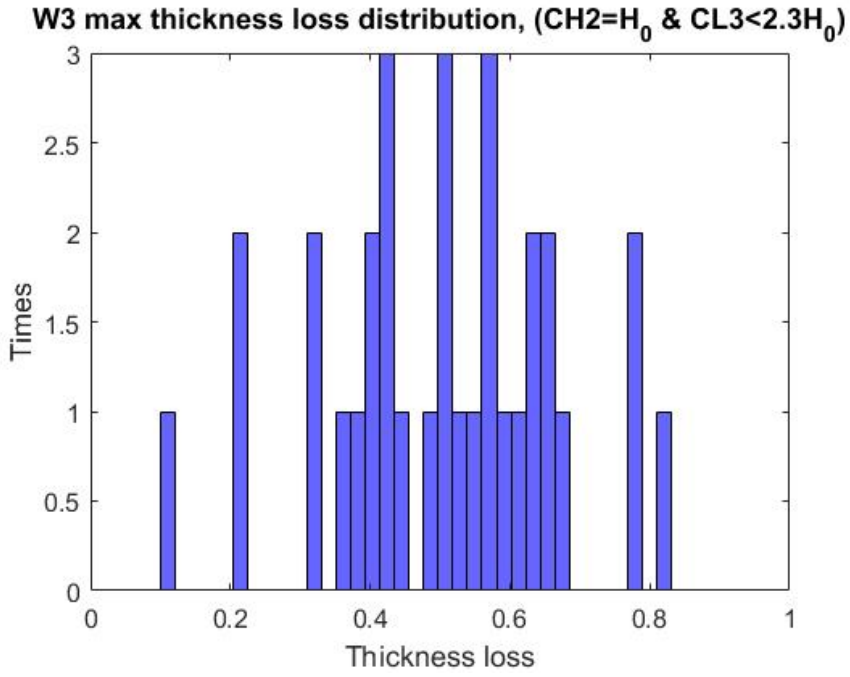

Figure 12.129: Max web thickness loss distribution, of W3 web corrosion pattern, with full height corrosion and deteriorated length up to 230% of H_0, for beams with diaphragm.

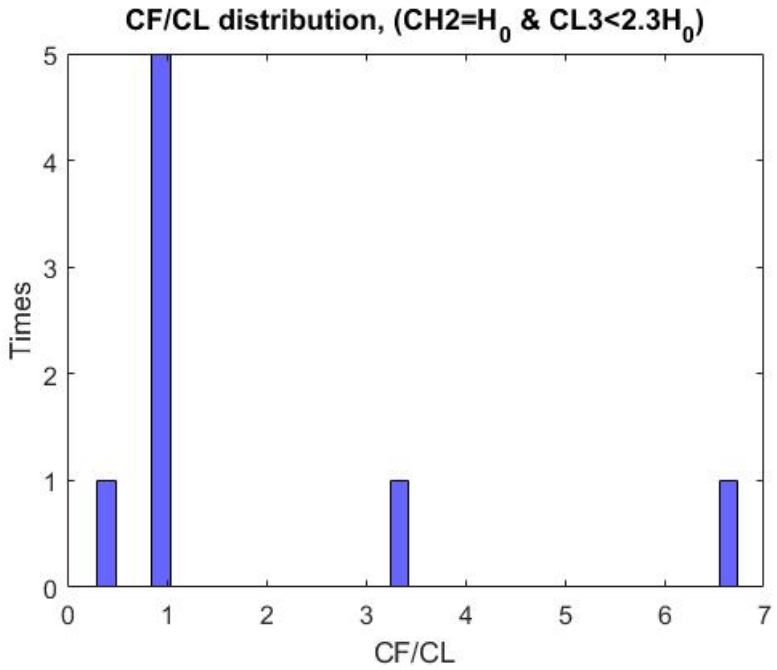

Figure 12.130: Ratio of flange to web corrosion length distribution, of W3 web corrosion pattern, with full height corrosion and deteriorated length up to 230% of H_0 for beams with diaphragm.

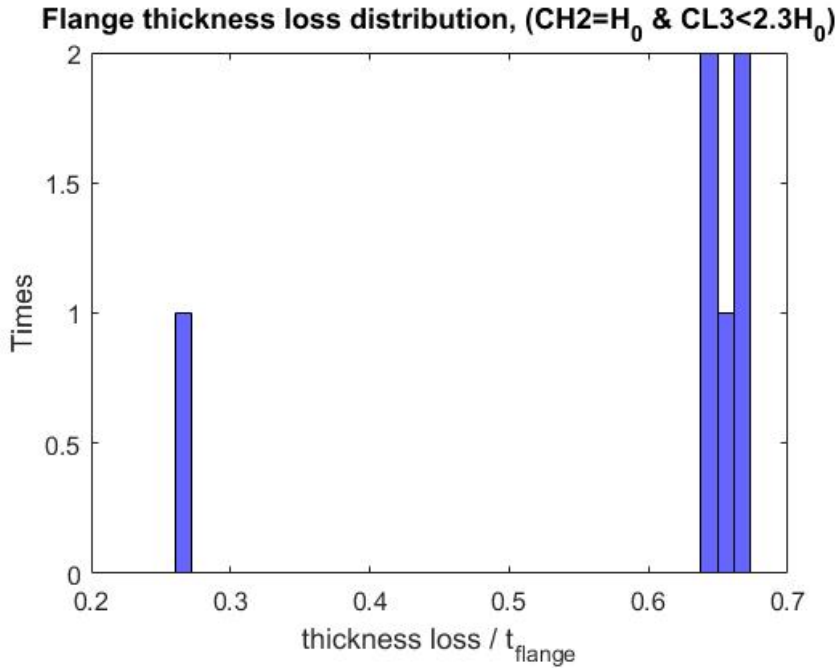

Figure 12.131: Max flange loss thickness distribution, for beams with W3 web corrosion pattern, with full height corrosion, deteriorated length up to 230% of H_0 and with diaphragm.

$$CL_3 \in (0.6,2.3]H_0$$
$$CL_1 \in (0.2,0.6]H_0$$
$$CH_1 = CH_3 \in (0.05,0.30]H_0$$
$$\frac{t_{loss}}{t_{web}} \in \{0.4,0.6,0.8\}$$
$$\frac{Cf}{Cl} = 1 \text{ and}$$
$$\frac{t_{loss}}{t_{flange}} \in \{0.65\}$$

Extreme scenario:

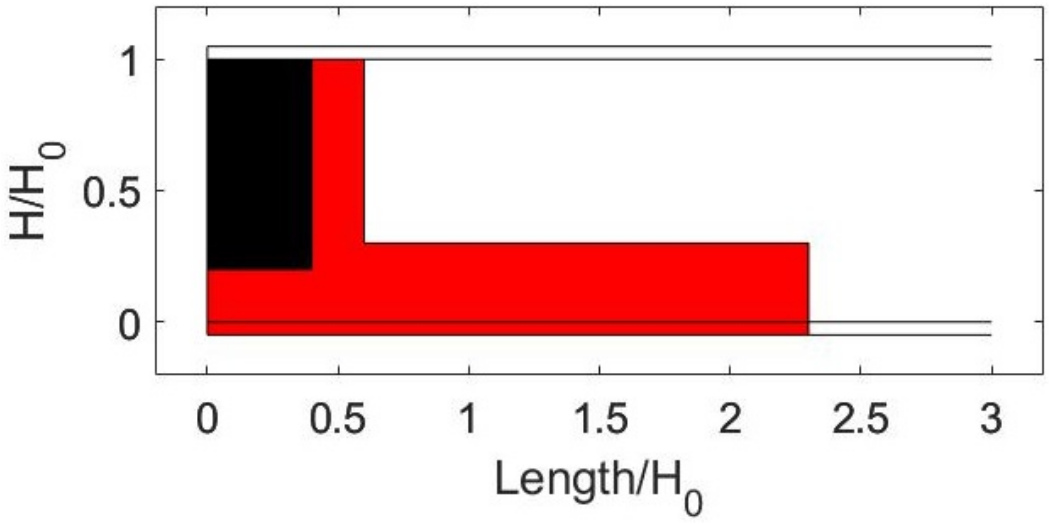

Figure 12.132: Second extreme flange and W3 web corrosion scenario for beams with diaphragm.

For height <= $0.5H_0$

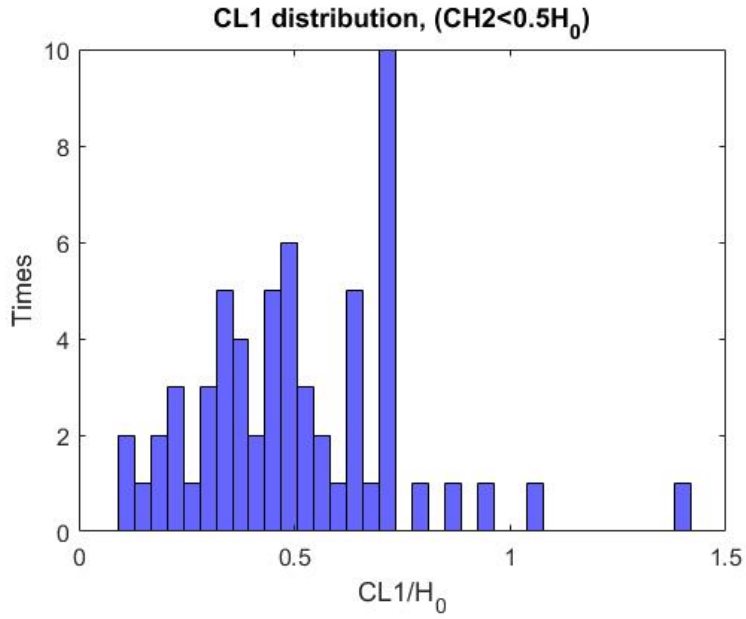

Figure 12.133: CL1 distribution of W3 web corrosion pattern, with corrosion height up to 50% of H_0, for beams with diaphragm.

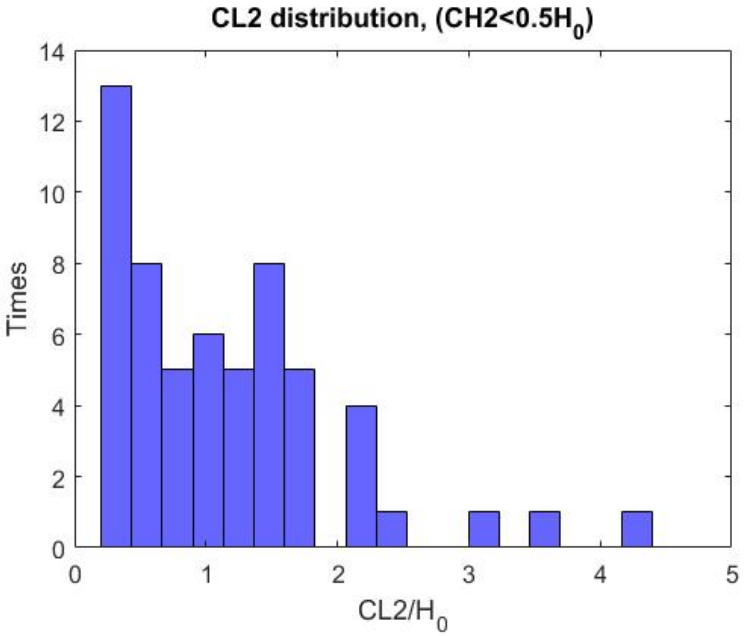

Figure 12.134: CL2 distribution of W3 web corrosion pattern, with corrosion height up to 50% of H_0, for beams with diaphragm.

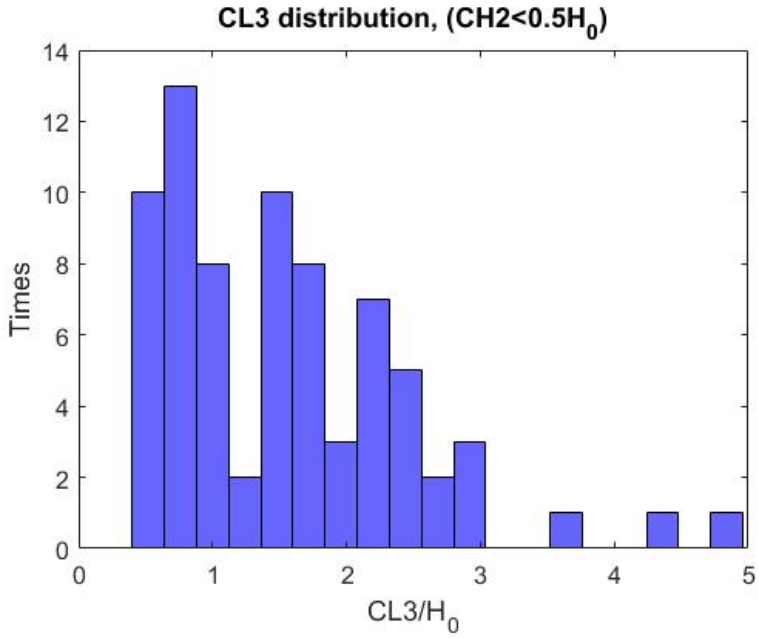

Figure 12.135: CL3 distribution of W3 web corrosion pattern, with corrosion height up to 50% of H_0, for beams with diaphragm.

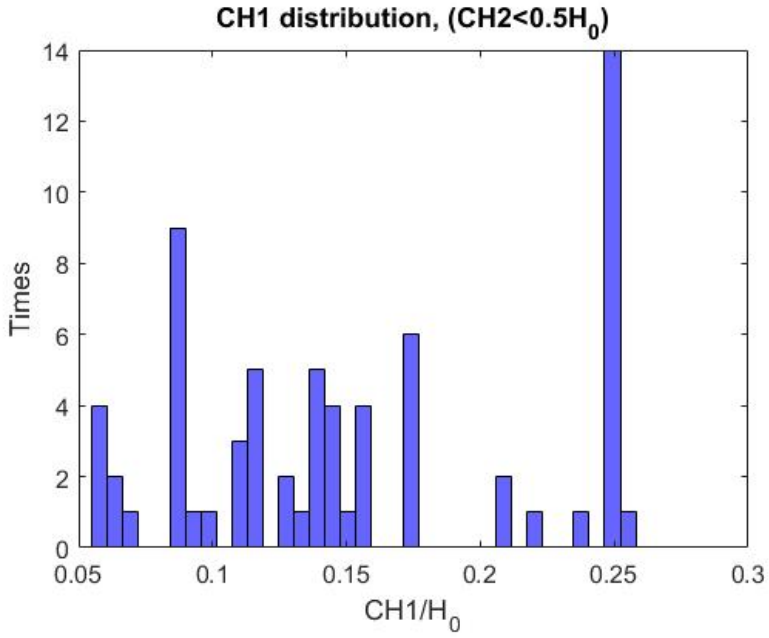

Figure 12.136: CH1 distribution of W3 web corrosion pattern, with corrosion height up to 50% of H_0, for beams with diaphragm.

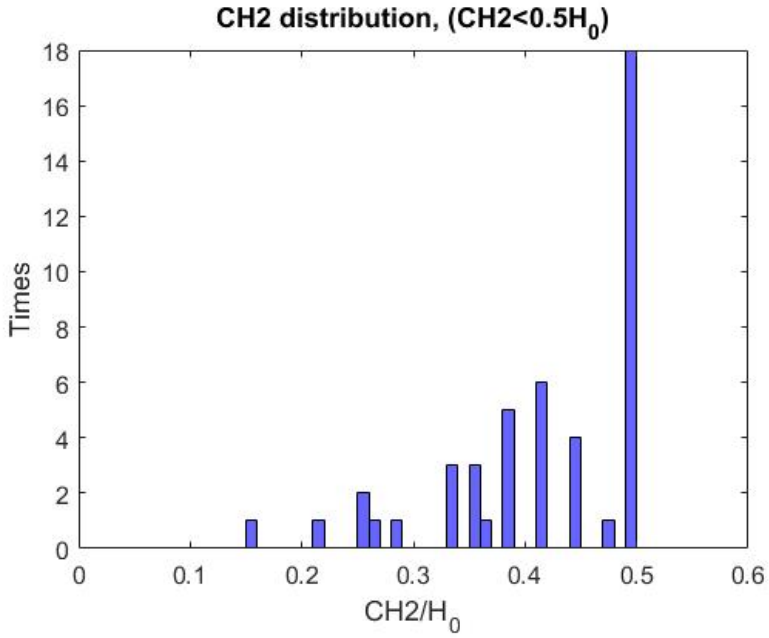

Figure 12.137: CH2 distribution of W3 web corrosion pattern, with corrosion height up to 50% of H_0, for beams with diaphragm.

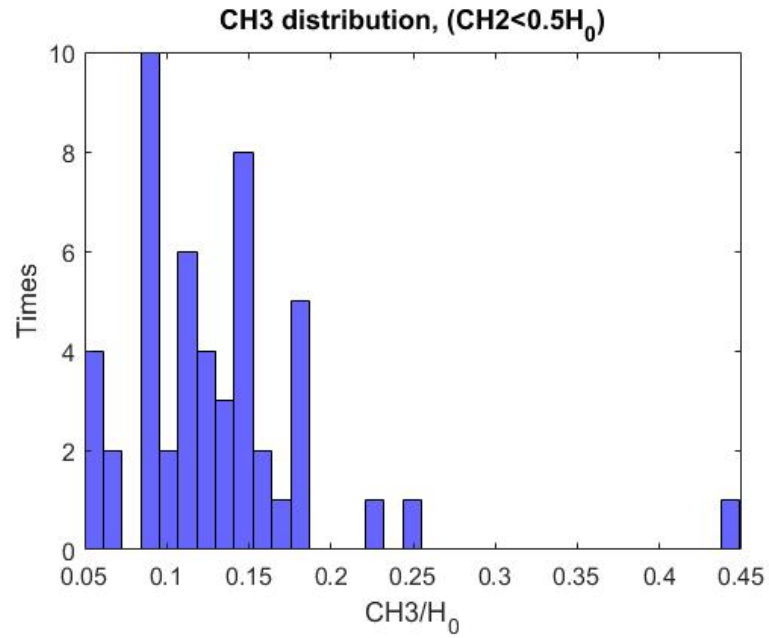

Figure 12.138: CH3 distribution of W3 web corrosion pattern, with corrosion height up to 50% of H0, for beams with diaphragm.

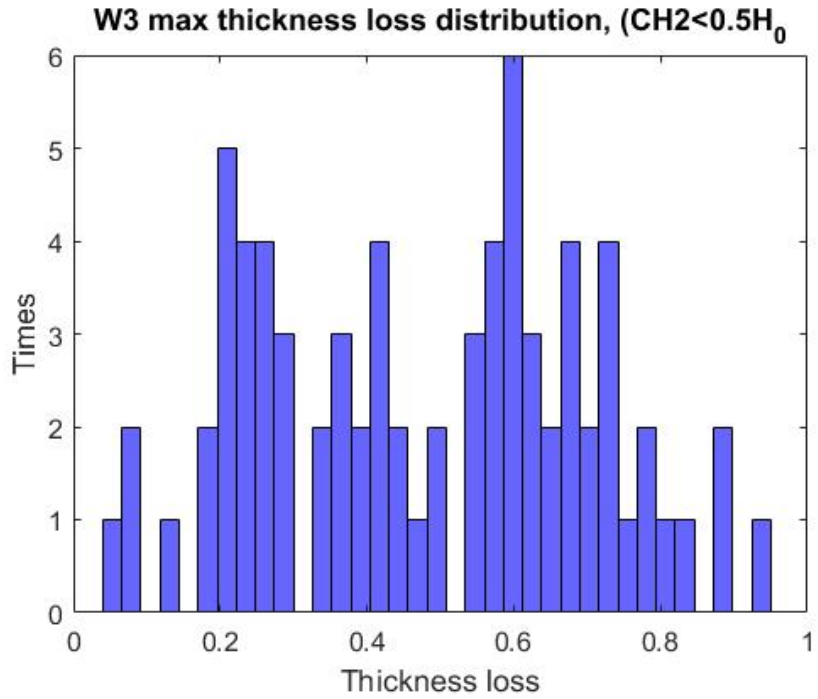

Figure 12.139: Max web thickness loss distribution of W3 web corrosion pattern, with corrosion height up to 50% of H_0, for beams with diaphragm.

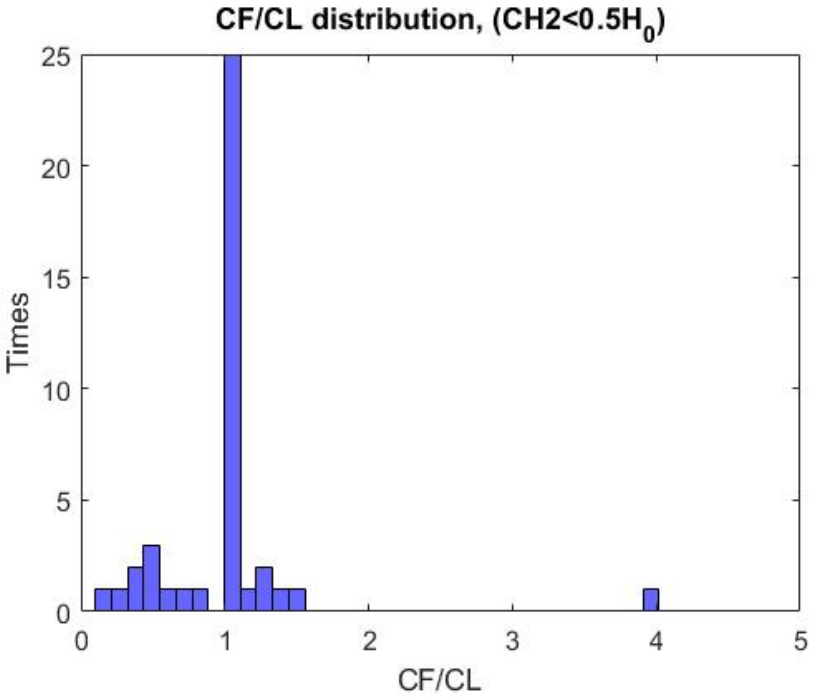

Figure 12.140: Ratio of flange to web corrosion length distribution, of W3 web corrosion pattern, with corrosion height up to 50% of H_0, for beams with diaphragm.

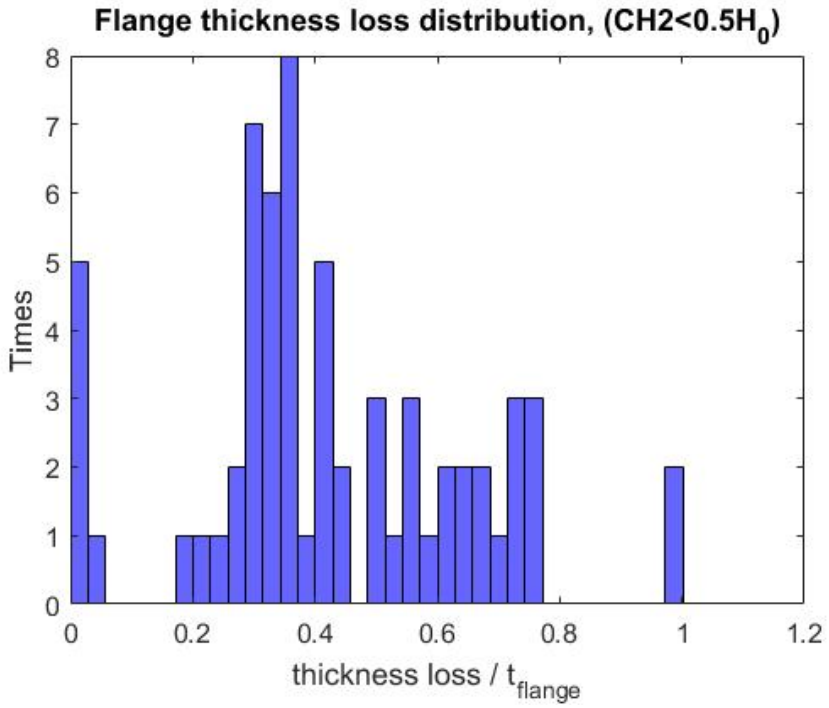

Figure 12.141: Max flange loss thickness distribution, for beams with W3 web corrosion pattern, with corrosion height up to 50% of H_0, for beams with diaphragm.

$$CL_3 \in (0.5,3]H_0$$
$$CL_1 \in (0.1,0.75]H_0$$
$$CH_1 = \in (0.05,0.25]H_0$$
$$CH_3 \in (0.05,0.18]H_0$$
$$\frac{t_{loss}}{t_{web}} \in \{0.4,0.6,0.8\}$$
$$\frac{Cf}{Cl} = 1 \text{ and}$$
$$\frac{t_{loss}}{t_{flange}} \in \{0.3,0.6,0.8\}$$

Extreme scenario:

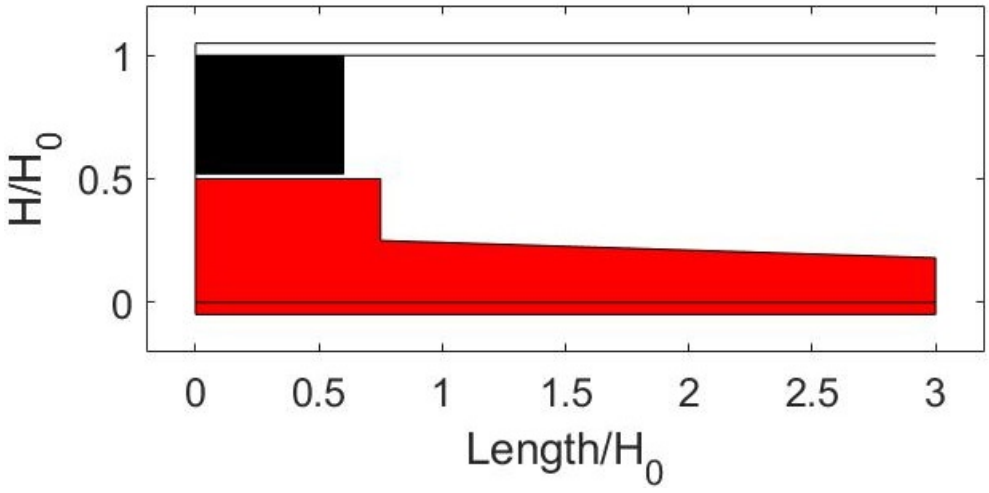

Figure 12.142: Third extreme flange and W3 web corrosion scenario for beams with diaphragm.

Holes

Holes dimensions distribution for M1:

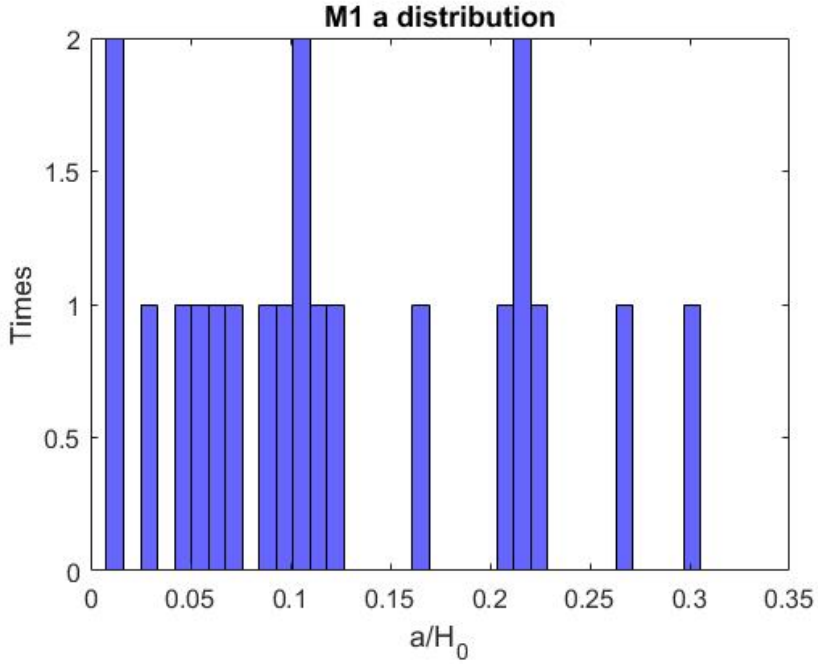

Figure 12.143: M1 web hole's pattern height distribution of W3 web corrosion pattern for beams with diaphragm.

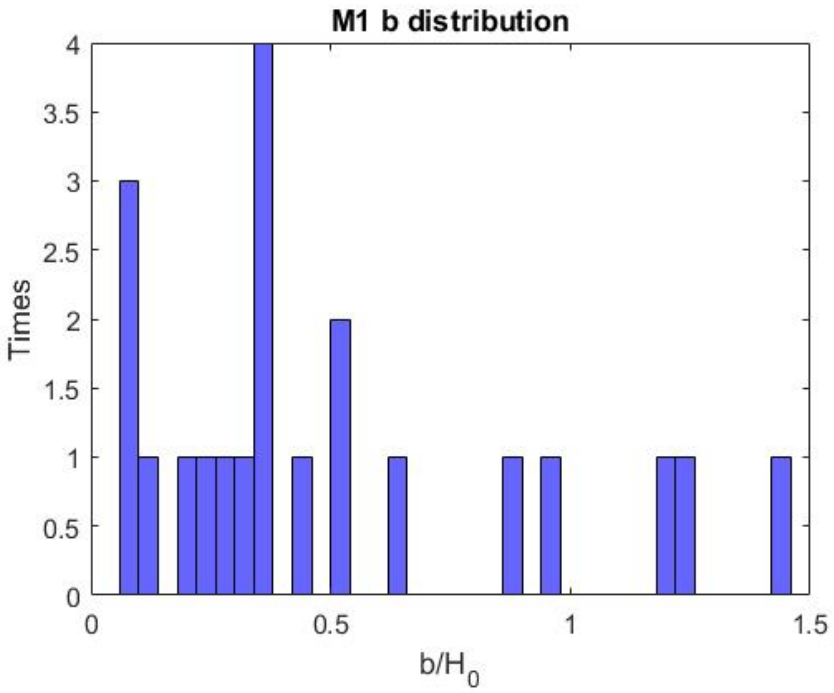

Figure 12.144: M1 web hole's pattern length distribution of W3 web corrosion pattern for beams with diaphragm.

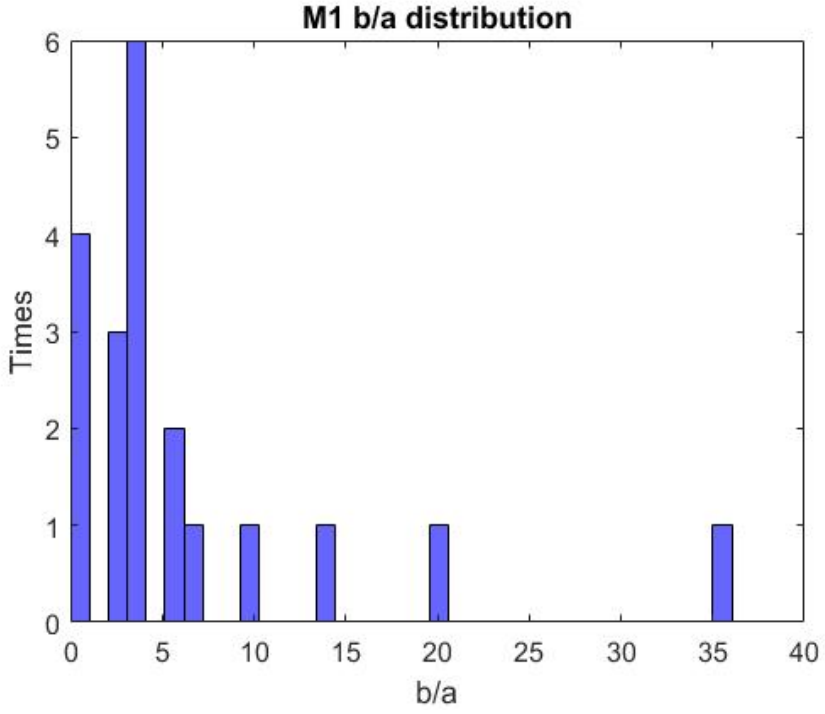

Figure 12.145: M1 web hole's ratio length to height distribution of W3 web corrosion pattern for beams with diaphragm.

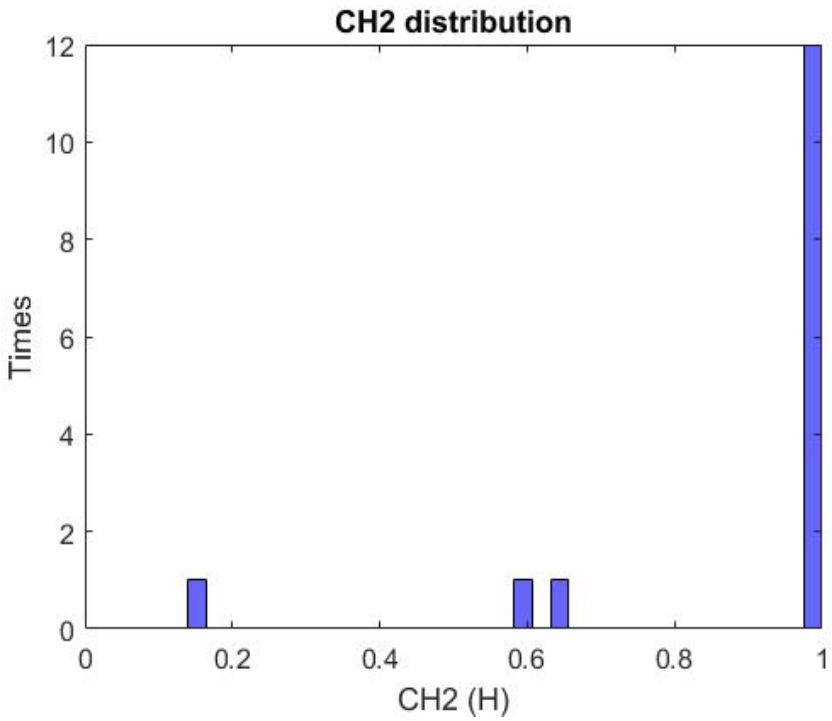

Figure 12.146: Max corrosion height distribution of W3 pattern with M1 hole, for beams with diaphragm.

From Fig. 12.146, holes appear to be mainly at full height corroded web. Holes seem to be mainly thin and long across the web. From Fig. 12.145, most of the cases have a ratio of hole length to height up to 6. From Fig. 12.144, length up to 50% of H_o. Thus, for the extreme hole scenario, the hole's height is considered as 0.083.

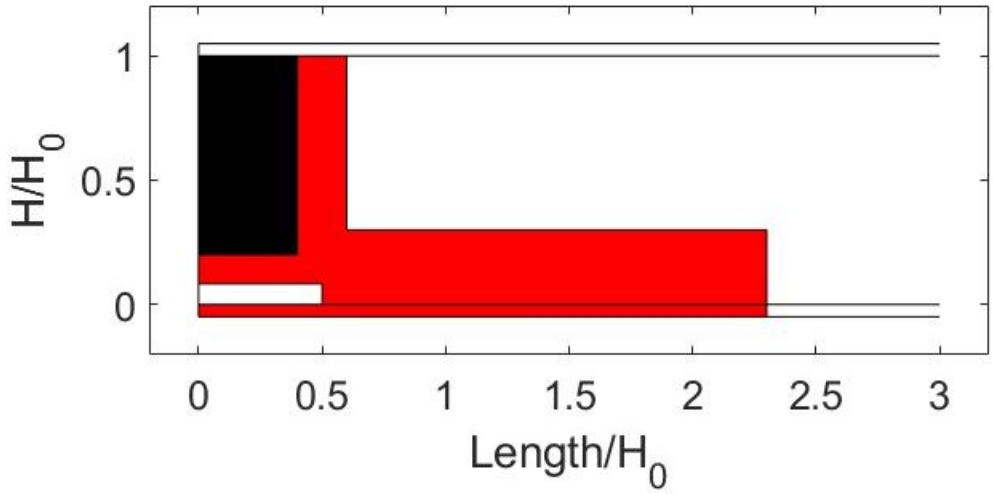

Figure 12.147: M1 hole pattern projected on the second extreme W3 web corrosion pattern scenario. Black illustrates the diaphragm that could be found with these patterns.

12.2.5 Pattern W4

Web corrosion

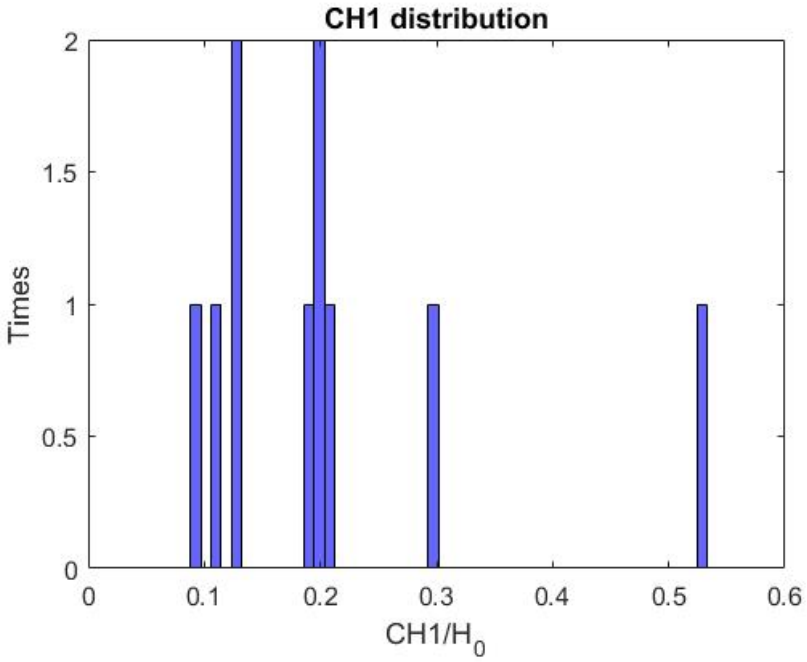

Figure 12.148: CH1 distribution of W4 web corrosion pattern for beams with diaphragm.

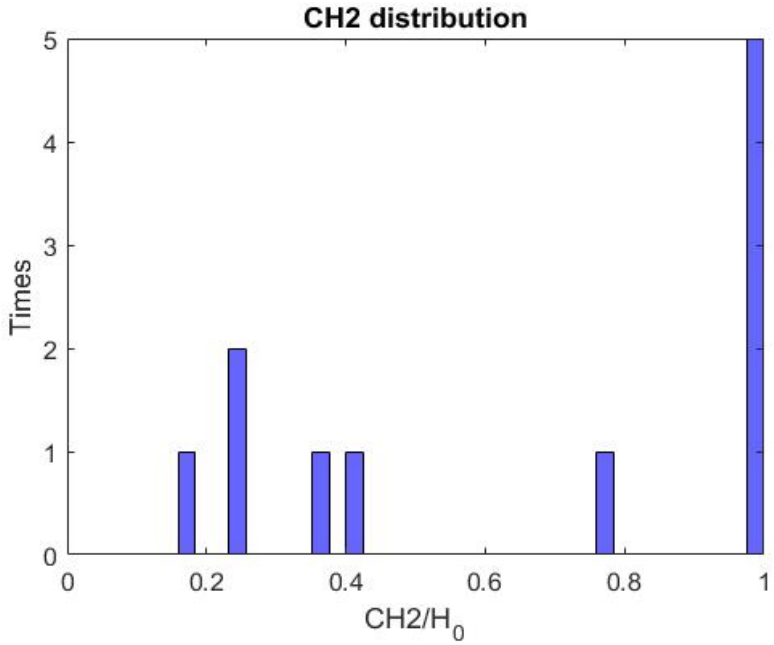

Figure 12.149: CH2 distribution of W4 web corrosion pattern for beams with diaphragm.

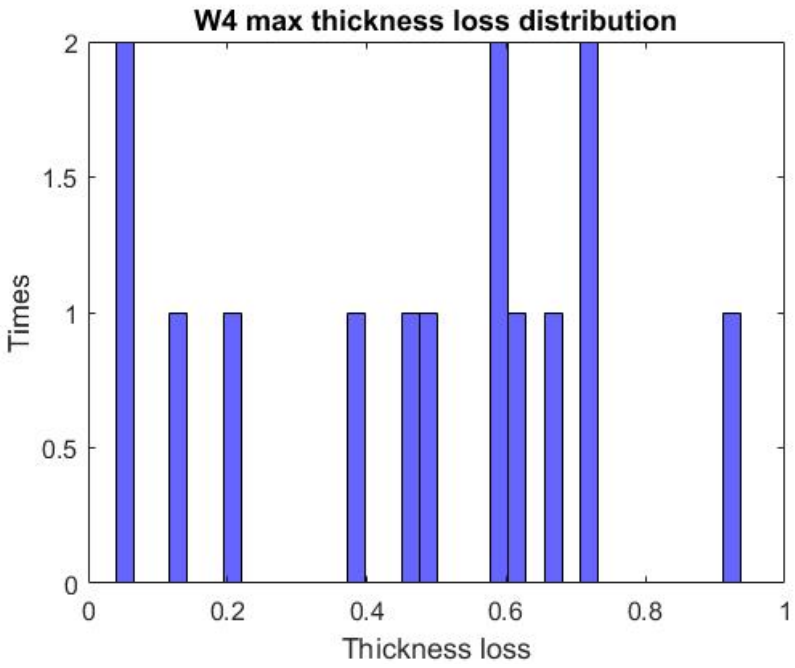

Figure 12.150: Max web thickness loss distribution of W4 web corrosion pattern for beams with diaphragm.

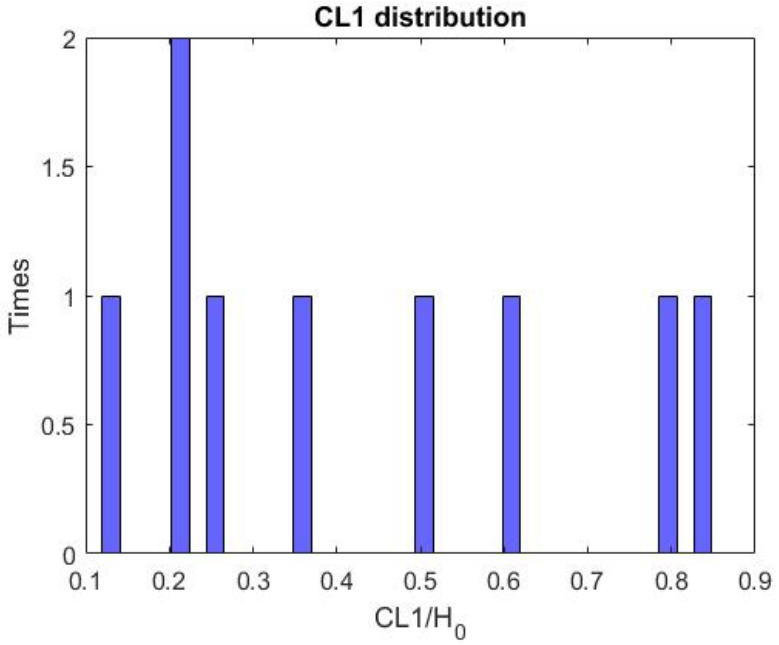

Figure 12.151: CL1 distribution of W4 web corrosion pattern for beams with diaphragm.

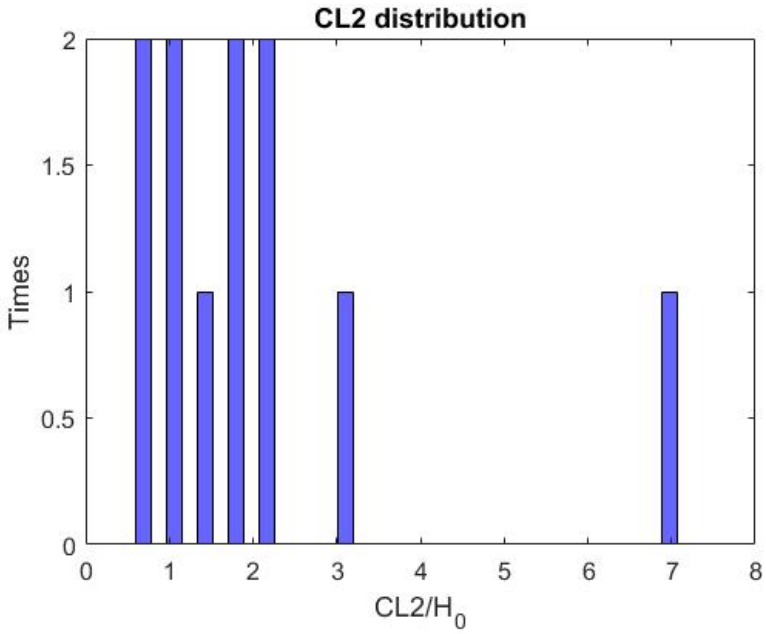

Figure 12.152: CL2 distribution of W4 web corrosion pattern for beams with diaphragm.

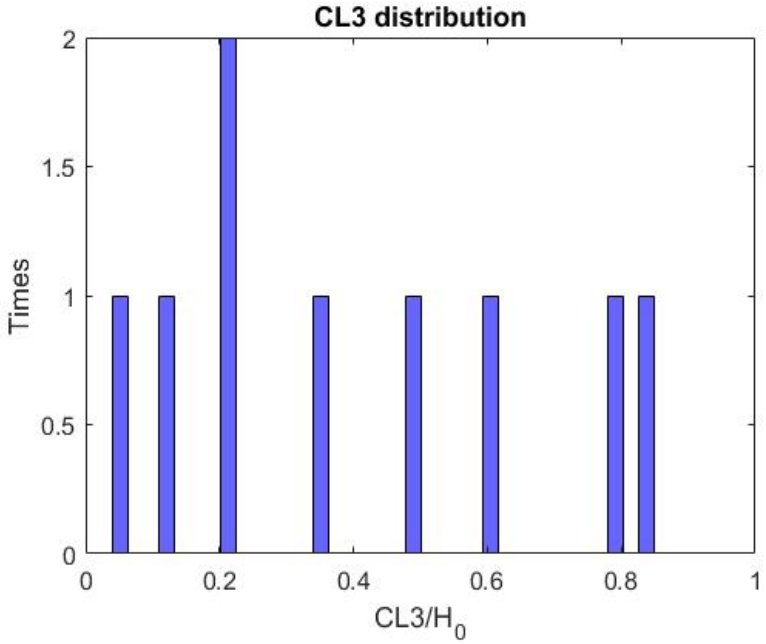

Figure 12.153: CL3 distribution of W4 web corrosion pattern for beams with diaphragm.

As in W3 patterns, two trends are observed: (a) full height corrosion and (b) up to 40% H_o.

For full height corrosion:

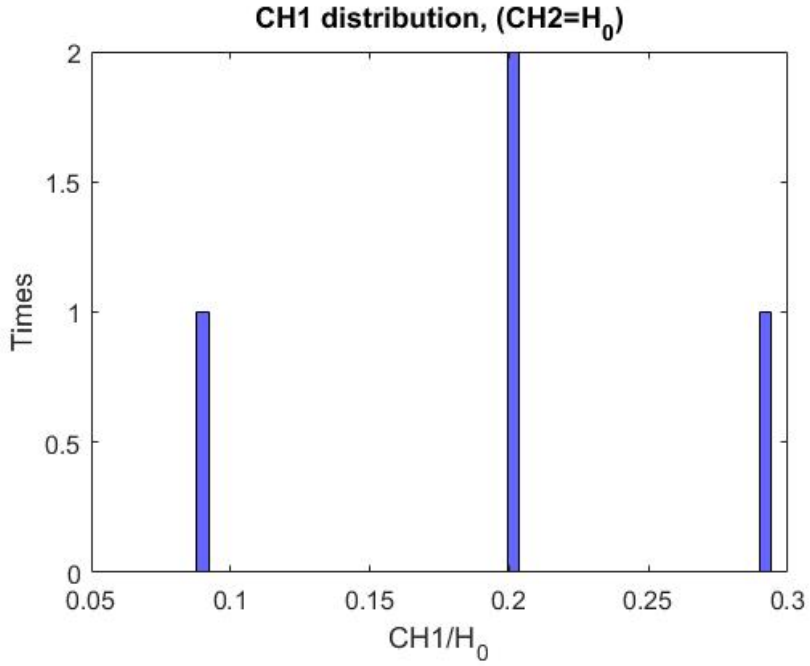

Figure 12.154: CH1 distribution of W4 web corrosion pattern with full height corrosion for beams with diaphragm.

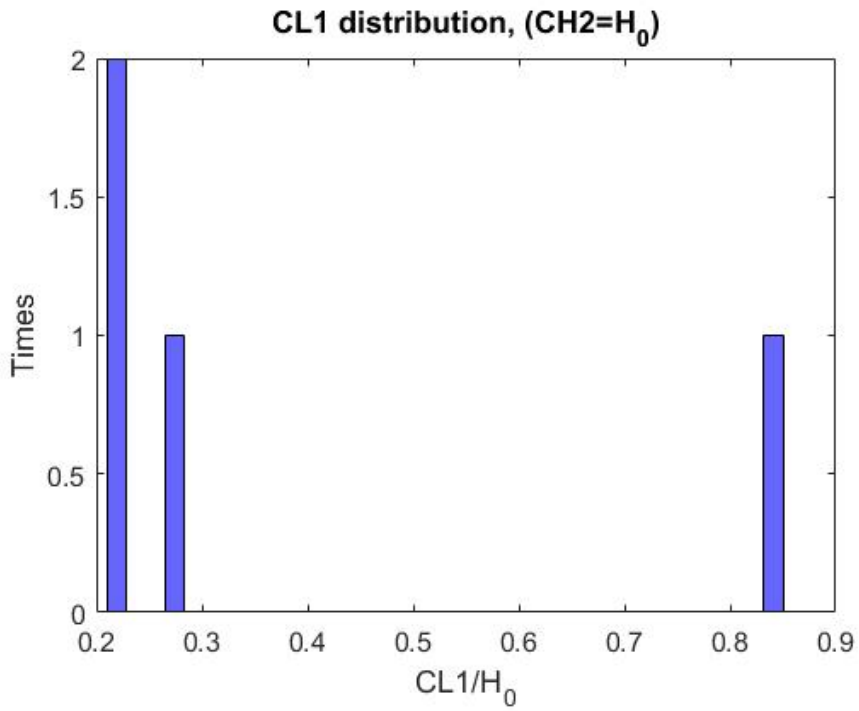

Figure 12.155: CL1 distribution of W4 web corrosion pattern with full height corrosion for beams with diaphragm.

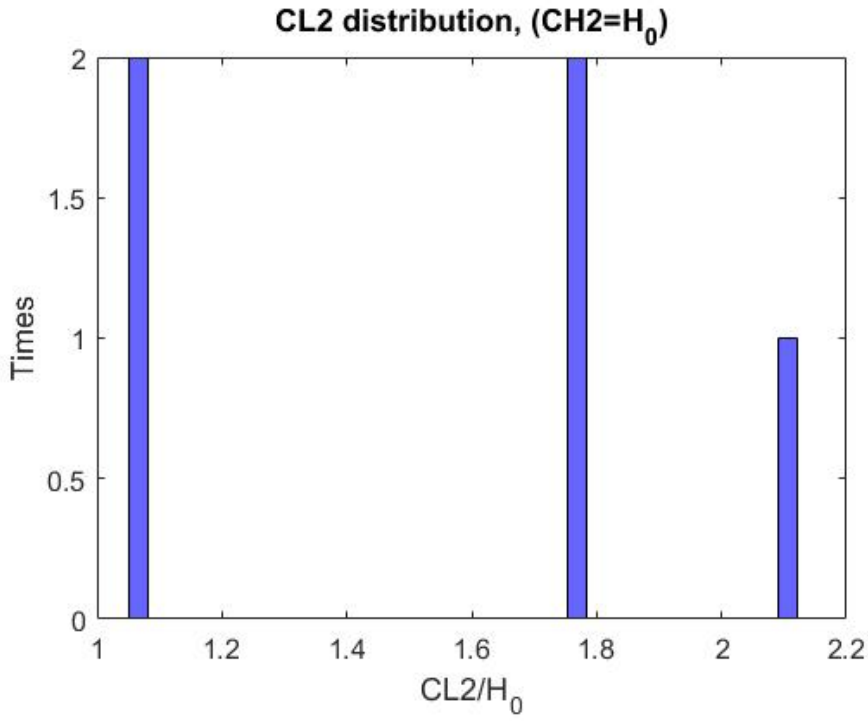

Figure 12.156: CL2 distribution of W4 web corrosion pattern with full height corrosion for beams with diaphragm.

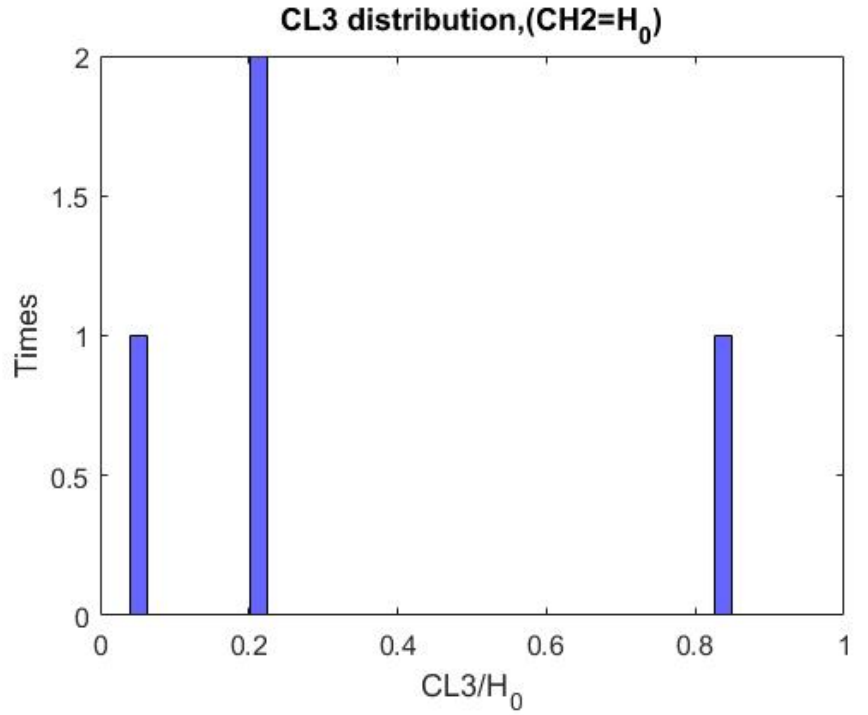

Figure 12.157: CL3 distribution of W4 web corrosion pattern with full height corrosion for beams with diaphragm.

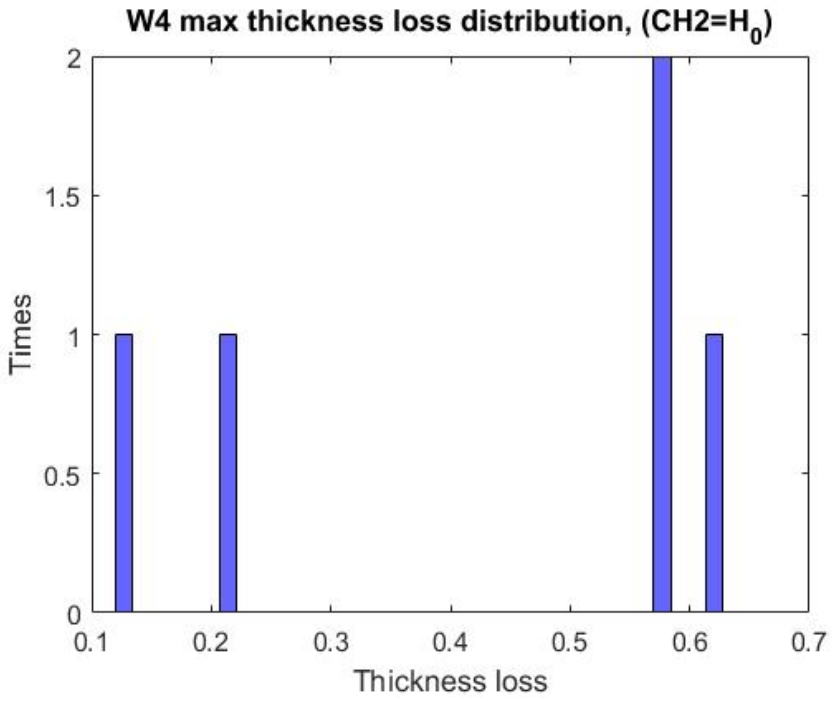

Figure 12.158: Max web thickness loss distribution of W4 web corrosion pattern with full height corrosion for beams with diaphragm.

Even the sample is small:

$$CL_1 \in (0.2,0.8)H_0$$
$$CL_2 \in [1,2.1]H_0$$
$$CL_3 \in (0.2,0.8)H_0$$
$$CH_1 = \in (0.1,0.3]H_0$$
$$\frac{t_{loss}}{t_{web}} \in \{0.1,0.2,0.6\}$$

The extreme scenario is shown in Fig. 12.159:

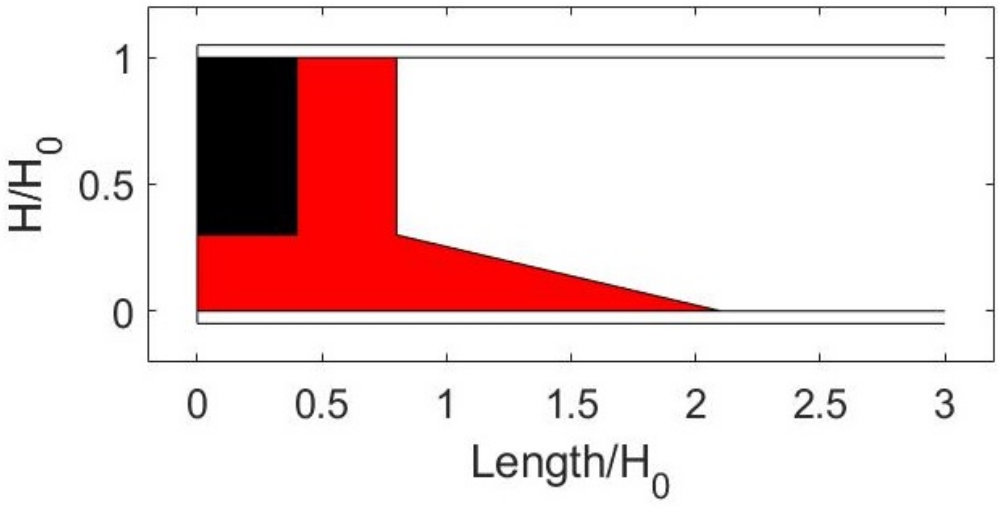

Figure 12.159: First extreme W4 web corrosion scenario for beams with diaphragm.

Even the small sample, W4 with full height corrosion, seems to follow the corresponding W3 pattern.

For Ch2<=0.4H:

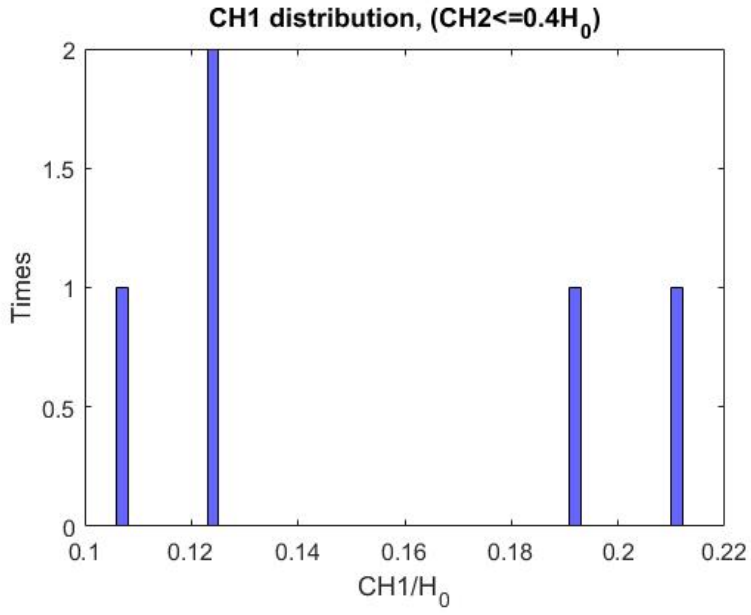

Figure 12.160: CH1 distribution of W4 web corrosion pattern, with corrosion height up to 40% of H_0, for beams with diaphragm.

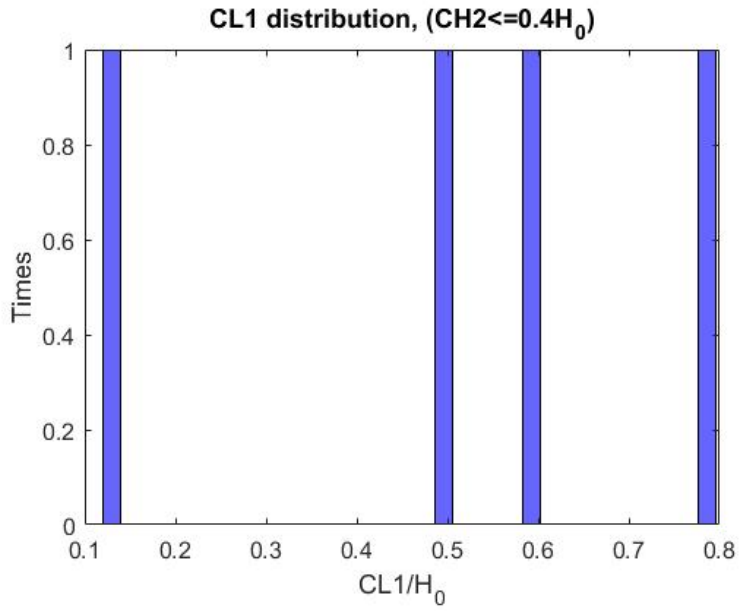

Figure 12.161: CL1 distribution of W4 web corrosion pattern, with corrosion height up to 40% of H_0, for beams with diaphragm.

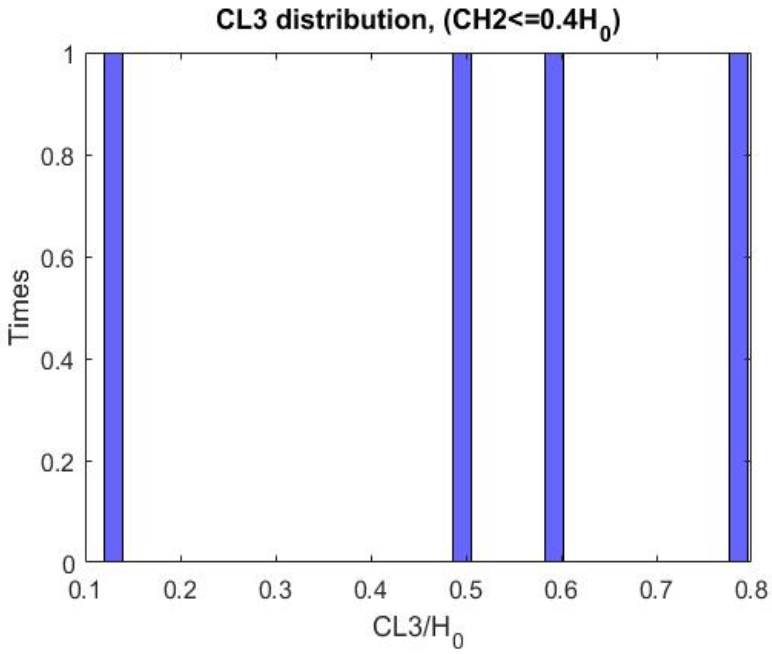

Figure 12.162: CL3 distribution of W4 web corrosion pattern, with corrosion height up to 40% of H_0, for beams with diaphragm.

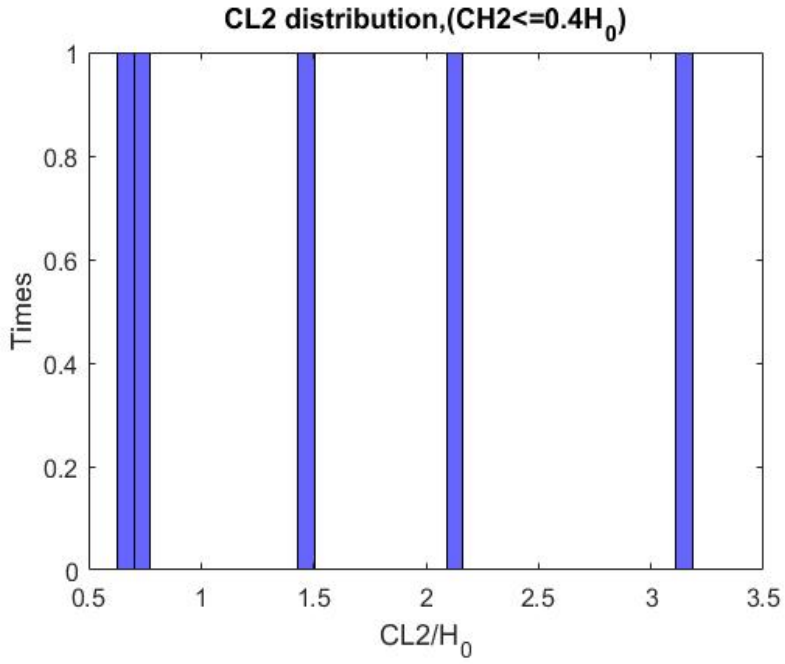

Figure 12.163: CL2 distribution of W4 web corrosion pattern, with corrosion height up to 40% of H_0, for beams with diaphragm.

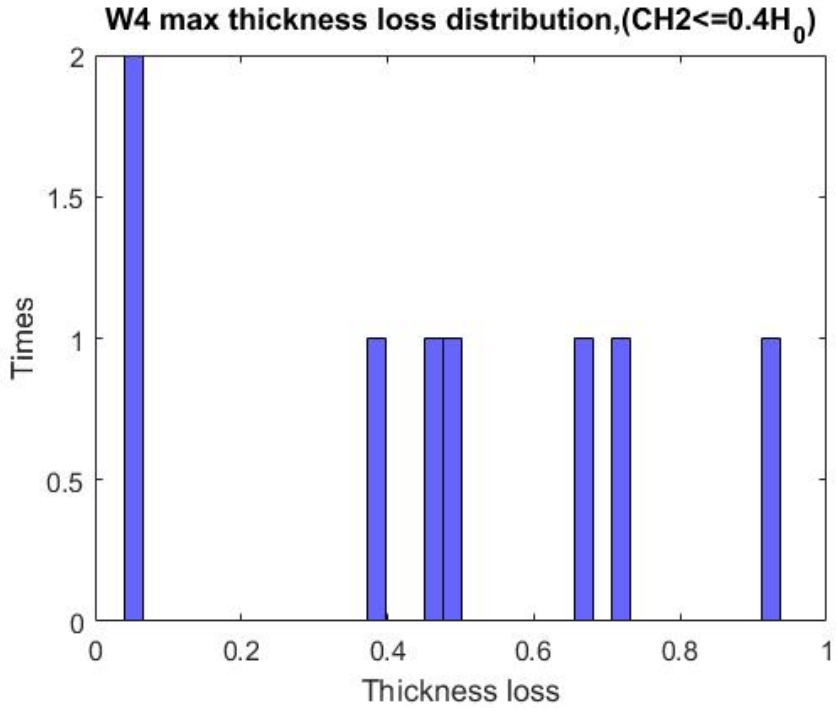

Figure 12.164: Max web thickness loss distribution of W4 web corrosion pattern, with corrosion height up to 40% of H_0, for beams with diaphragm.

$$CL_1 \in (0.1,0.8]H_0$$
$$CL_2 \in (0.6,3.1]H_0$$
$$CL_3 \in (0.1,0.8]H_0$$

$CH_1 = (0.1,0.2]H_0$

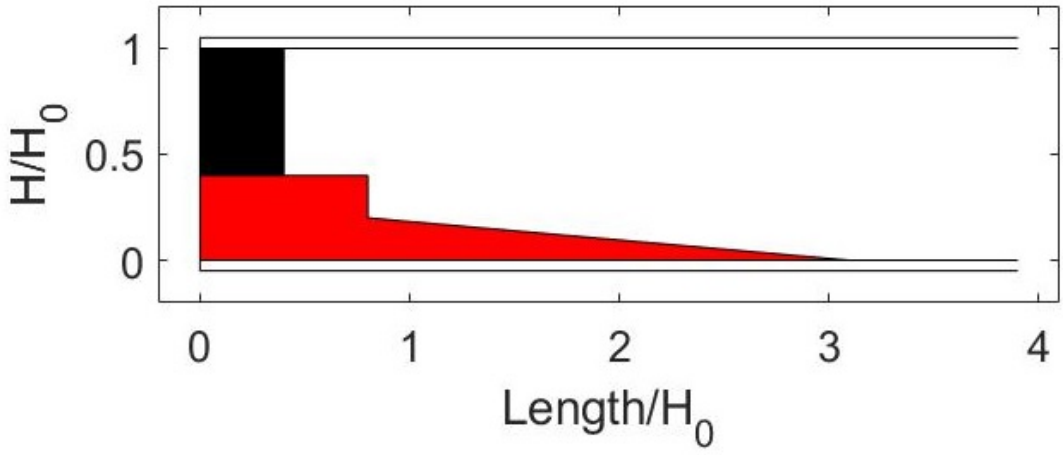

Figure 12.165: Second extreme W4 web corrosion scenario for beams with diaphragm.

The W3 pattern seems to follow the corresponding W4 pattern.

Holes

The M1 pattern is found only once, and it appears as a pit hole (0.0044*0.0044). The M2 pattern is combined with W3 M2 holes.

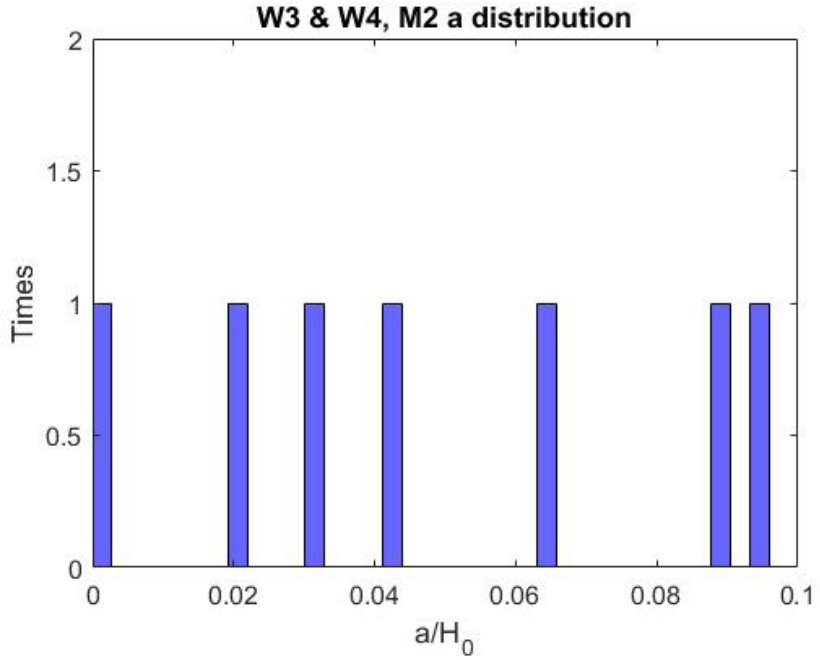

Figure 12.166: M2 web hole's pattern height distribution of W3 and W4 web corrosion pattern for beams with diaphragm.

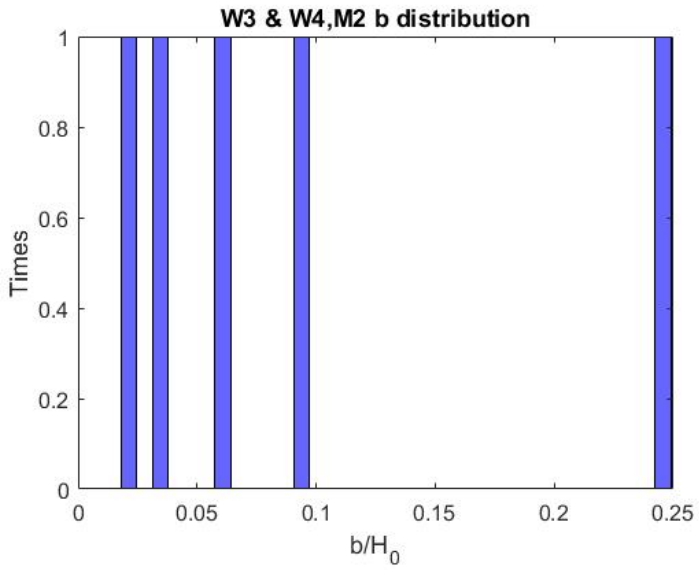

Figure 12.167: M2 web hole's pattern length distribution of W3 and W4 web corrosion pattern for beams with diaphragm.

The worst-case scenario is: a=0.1, b=0.25.

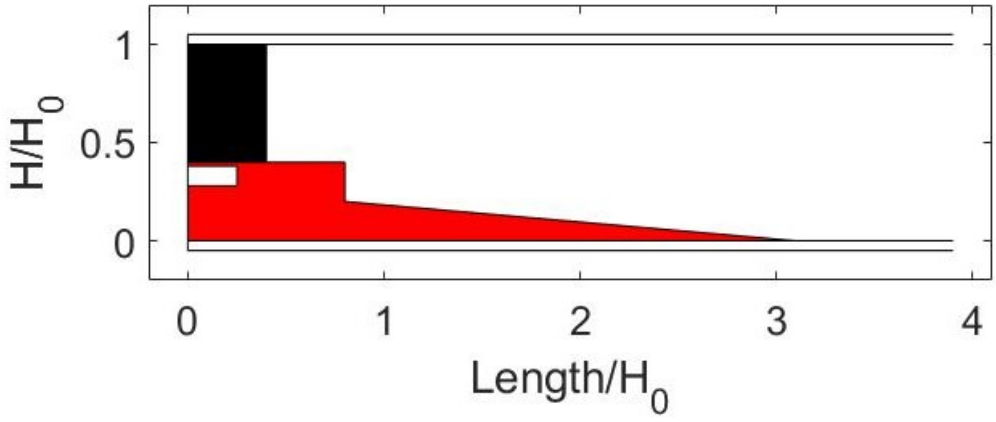

Figure 12.168: Extreme M2 hole pattern scenario projected on second extreme W4 web corrosion scenario for beams with diaphragm.

12.2.6 Pattern W5

Web corrosion

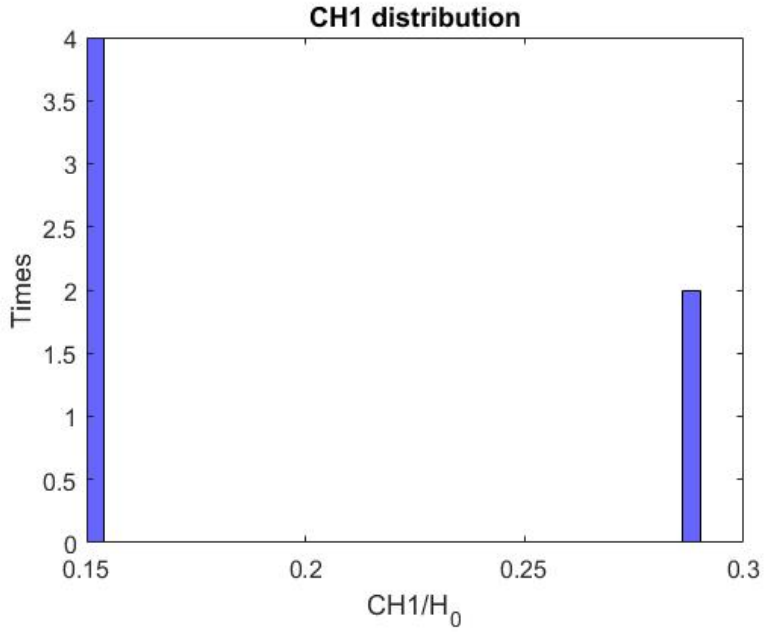

Figure 12.169: CH1 distribution of W5 web corrosion pattern for beams with diaphragm.

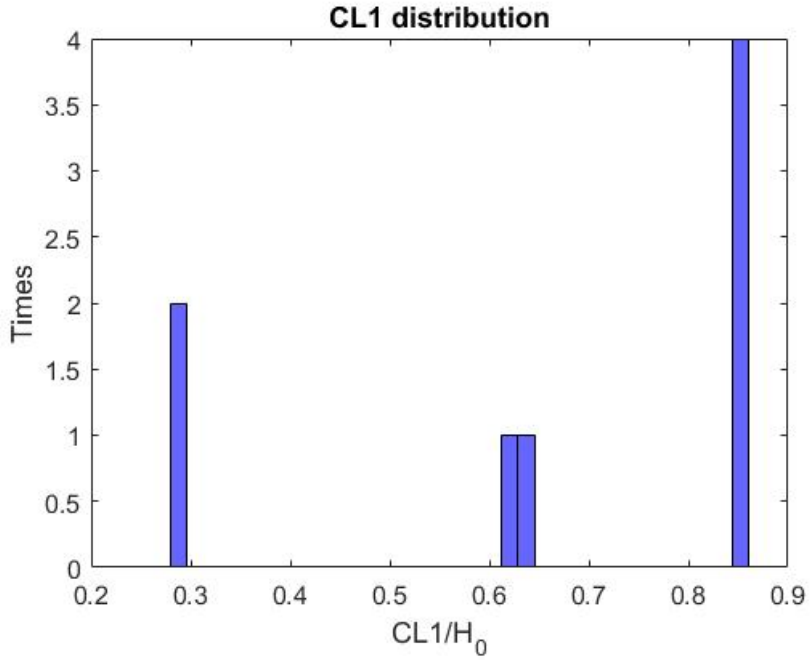

Figure 12.170: CL1 distribution of W4 web corrosion pattern for beams with diaphragm.

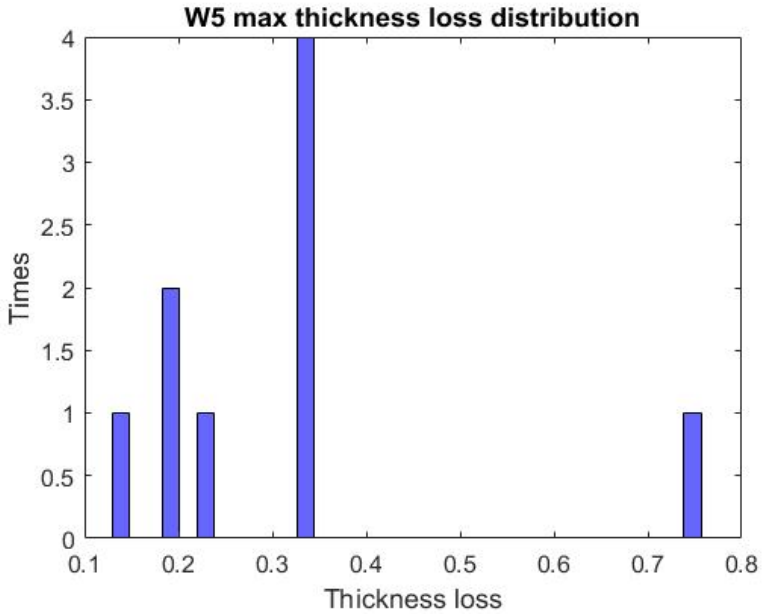

Figure 12.171: Max web thickness loss distribution of W5 web corrosion pattern for beams with diaphragm.

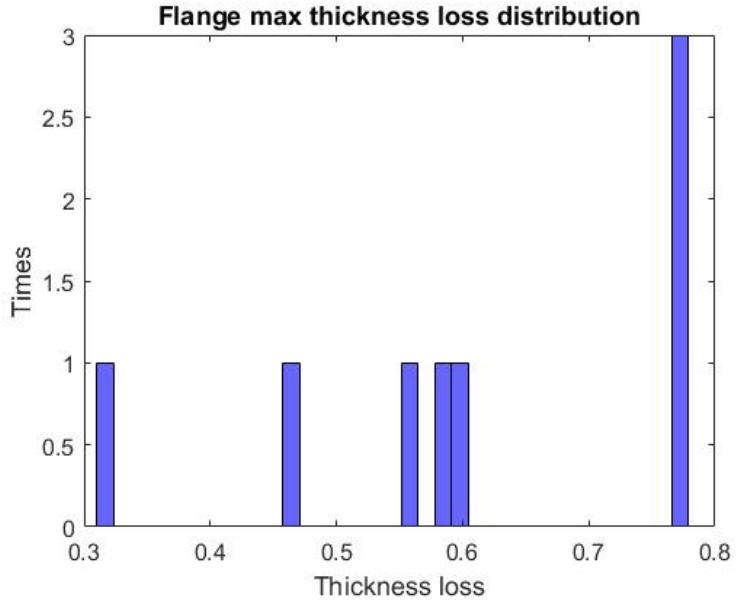

Figure 12.172: Max flange thickness loss of beams with W5 web corrosion pattern for beams with diaphragm.

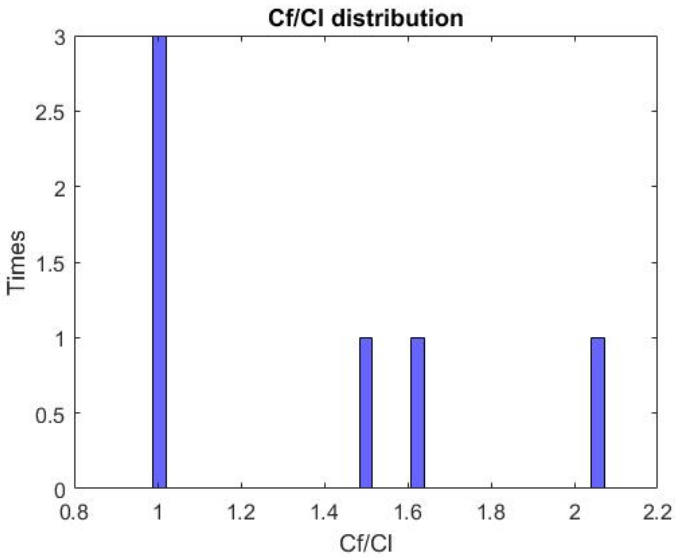

Figure 12.173: Ratio of flange to web corrosion length distribution, of W5 web corrosion pattern for beams with diaphragm.

$$CL_1 \in [0.3,0.85]H_0$$
$$CH_1 = (0.15,0.30]H_0$$
$$\frac{t_{loss}}{t_{web}} \in \{0.35\}$$
$$\frac{t_{loss}}{t_{flange}} \in \{0.3,0.6,0.8\} \text{ with } \frac{C_f}{C_l} \in \{1,1.6\}$$

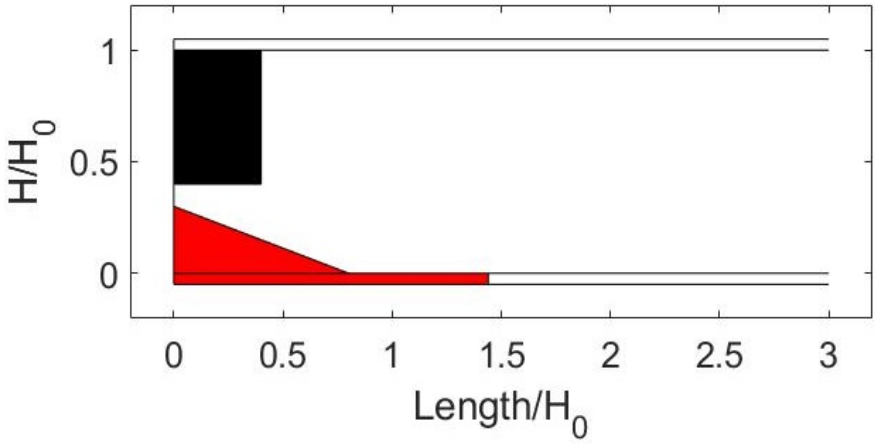

Figure 12.174: Extreme W5 web corrosion scenario for beams with diaphragm.